UNIVERSITÀ DEGLI STUDI DI ROMA "TOR VERGATA"

FACOLTA' DI INGEGNERIA

DOTTORATO DI RICERCA IN
INGEGNERIA DELL'ENERGIA-AMBIENTE

XXII CICLO DEL CORSO DI DOTTORATO

New Transport Equations for Turbulent flow with variable Transport Properties. Biomedical Applications of Non-Newtonian Blood Flow in Coronary Stent and Stenosed Carotid Artery

Andrea Boghi

A.A. 2009/2010

Docente Guida/Tutor: Prof. Fabio Gori

Coordinatore: Prof. Fabio Gori

“Big whirls have little whirls, That feed on their velocity,
and little whirls have lesser whirls,
and so on to viscosity.”

Lewis F. Richardson, Weather Prediction by Numerical Process, 1920

Contents

Abstract

Transport properties such as thermal conductivity, mass diffusivity and viscosity of aqueous solutions are important in many industrial processes, scientific applications such as biological processes of living organisms, and in prediction of heat and mass-transfer coefficients under turbulent regimes. Available theoretical models frequently cannot describe real systems as they are met in practice. Better predictive models can be developed based on reliable experimental information on thermodynamic and transport properties. Only few works have dealt with the variability of physical properties in turbulent flow. In the previous models the equations are deduced with the assumption of constant physical properties and later the dependence on the transported variable is introduced. The present paper is aimed to investigate the influence of the variability of physical properties on the transport equations of mean variables and second order moments in turbulent flow. We focus on heat, mass and momentum transfer. As well established in Non-Newtonian fluid mechanics, besides the Reynolds ones, new terms, depending of the variability of physical properties, appear which are involved in energy transfer between large and small scales of turbulence. Concerning mass and heat transfer properties these new terms are achieved, modelled and a FORTRAN Finite Volume code is written to give the order of magnitude of the influence of these terms. Concerning the momentum transfer a new transport equation for turbulent kinetic energy dissipation rate is proposed. In the last two sections we show two examples of Non-Newtonian fluid momentum transfer: blood flow in coronary stent and carotid artery solved by commercial code FLUENT. Despite in the last problem we have turbulent flow, we have treated it in laminar regime because a closure for the turbulent dissipation rate equation proposed in this work is lacking yet.

Keywords: *Turbulent Flow, Mass Diffusivity, Thermal Conductivity, Non-Newtonian, Carotid Artery, Stent*

Chapter 1:

Introduction

1.1 Variable Physical Properties

Transport properties (thermal conductivity, mass diffusivity and viscosity) of aqueous solutions are important in many industrial processes such as material transport, solid deposition, corrosion in steam generators, and electrical power boilers, and scientific applications such as calculation of design parameters, developments and utilization of geothermal and ocean thermal energy, efficient operation of high-temperature energy-generating systems, geology and mineralogy, hydrothermal synthesis, biological processes of living organisms, and in prediction of heat and mass-transfer coefficients under both laminar and turbulent regimes. Knowledge of pressure, temperature, and composition dependence of transport properties of aqueous electrolyte solutions are essential to understand a variety of problems in a number of technological and engineering applications as: chemical processes, desalination processes, geochemistry, calculation of design parameters, development and utilization of geothermal and ocean thermal energy, geology and mineralogy, prediction of heat and mass-transfer coefficients, environmental applications, and treatment of wastewater.

To understand and to control the processes using electrolyte solutions, requires the knowledge of their thermodynamic and transport properties. Thermal conductivity and viscosity of electrolyte solutions are also of research interest because the long-range electrostatic interactions (coulomb forces between ions) can cause difficulty in describing the behaviour of

such systems. Electrostatic interactions govern thermodynamic and transport properties of ionic electrolyte solutions.

Available theoretical models frequently cannot describe real systems as they are met in practice. Better predictive models can be developed based on reliable experimental information on thermodynamic and transport properties. However, measurements of thermal conductivity and viscosity of aqueous salt solutions have so far been limited to rather narrow ranges of temperature, pressure, and concentration with less than satisfactory accuracy [1.1].

1.2 Turbulence Modeling

Much of the efforts in developments of turbulence models focus on ensuring a strict compliance with physical constraints and mathematical formalism, which are "per se" supposed to ensure a higher degree of model generality. Physical constraints are in part identified with the compliance with turbulence asymptotic and limiting states (infinite and vanishing Reynolds numbers, two-dimensional turbulence and others). The ability to reproduce the behavior of individual terms in transport equations for turbulent stresses and scale-supplying variable in various flows is also regarded as a criterion for the validation of physical foundation of the modeling concept.

Some of the mathematical constraints, such as coordinate invariance, are ensured by most second-moment closures. A strict fulfillment of others, such as frame indifference, or various realizable constraints, often imposes a degree of model complexity which aggravates the application of the models to the computation of real flows, although the conditions in which these constraints may come into prominence, are rarely encountered in such flows. The true validation of turbulence models is in their ability to reproduce and predict a wide range of real flows with acceptable accuracy. A compromise is often needed between the strict compliance

with various constraints and computational sturdiness, which will allow the model to be incorporated into an efficient numerical algorithm and applied to the solution of real flows [1.2].

1.3 Second Order Turbulence Closures

Second-order or second-moment turbulence closures which originated with the work of Rotta [1.3], have been extensively used for the numerical simulation of turbulent flows. With turbulence models of this type, the second-moment correlations representing the turbulent transport of momentum, heat or any other scalar are found directly from their own (necessarily approximate) transport equations [1.4]. The approach may be contrasted with the usual phenomenological treatment in which, by analogy with molecular transport, models are devised for the effective turbulent viscosity and effective turbulent Prandtl or Schmidt number.

The transport equations for the second-moments, which serve as the basis for all one-point closures, including eddy-viscosity models, describe in essence the dynamics of large scales, energy-containing motion: the second-moments are of the same order of magnitude as the kinetic energy, providing thus information on the overall characteristic turbulent velocity scale. In order to close the unknown terms in these equations, it is necessary to introduce another scale, in length or time. The most common choice is the scalar dissipation rate of turbulence kinetic energy ε (or a combination of k and ε, such as $\omega = \varepsilon/k$), because this quantity appears as a sink term in the kinetic energy equation, and its physical interpretation is straightforward. The entire turbulent field is then described by a unique set of the characteristic time and spatial scales. This is one of the major assumptions underlining the one-point statistical turbulence closures.

Most popular turbulence models, irrespective of the closure level, invoke at some stage of derivation the assumption of local energy equilibrium both in physical and spectral space. Such

assumptions are inherent in modeling some of the terms in transport equations, or are invoked when defining some of the model coefficients. This implicitly assumes that all spatial information can be given by a unique length scale for the whole spectrum and that various eddy and the major processes associated with them are linked together by a spectral transfer of energy at a constant rate. Therefore, the dissipation process, acting on small eddies, is assumed to respond with the same characteristic time to any change imposed or occurring on the energy containing eddies located in the large-scale spectrum range. Despite this obvious oversimplification of the realistic spectral dynamics, such an assumption seems to be satisfactory for a wide range of flows of practical interest. That is why the single-scale modeling approach has been so successful ever since the early development.

There are, however, many flows where such a spectral equilibrium is not attained. Typical examples include several non-equilibrium flows, attached and with separation and reattachment, flow impingement and stagnation, longitudinal vortices, secondary motion, swirl, system rotation. These models cannot reproduce satisfactorily the evolution of any flow which departs significantly from equilibrium conditions. Indeed, the rudimentary forms of modeled transport equations with single source and sink terms, tuned in equilibrium flows, do not offer much flexibility. However, the full second-moment closure in differential form may still serve as a sound basis for accounting for the dynamics of each individual stress component. Handling extreme cases when the flow is subjected to strong time or space variation or abrupt changes of external conditions requires further extension of the model to account for various specific phenomena, as well as further refinements of the current models for each term. In order to capture the non-equilibrium dynamics of such flows, it is necessary to introduce different scales by which to describe eddies of different sizes, their evolution and mutual interaction.

Several multiple-scale approaches within the one-point methodology have been proposed in the literature aimed at distinguishing different scales associated with various processes in the dynamics of turbulence. The statistical two-point description of turbulence has been regarded as a convenient mathematical framework for better understanding and modeling of the one-point quantities allowing deriving a transport equation for the Reynolds stress tensor and others second moments, transport equations for the length-scale tensor, providing a better insight in the closure of the classical one-point dissipation equation and develop multiple-scale models. The reason for preferring a second-moment model is that the turbulent interactions which generate the turbulent stresses and heat fluxes can be treated exactly: moreover, for those processes which cannot be so handled, a more rational and systematic set of approximations can be devised than for schemes founded on the notion of effective turbulent transport coefficients.

Nomenclature for Second Order Moments Equations

Symbol	Definition	SI Unit
Latin		
$k = \langle u_i' u_i' \rangle / 2$	Turbulent kinetic energy	$m^2 \cdot s^{-2}$
$k' = u_i' u_i' / 2$	Instantaneous turbulent kinetic energy	$m^2 \cdot s^{-2}$
P	Mean pressure	Pa
p'	Fluctuating pressure	Pa
$\langle S_{ij} \rangle = \frac{1}{2}\left(\frac{\partial U_i}{\partial x_j} + \frac{\partial U_j}{\partial x_i} \right) - \frac{1}{3}\frac{\partial U_k}{\partial x_k}\delta_{ij}$	ij-component of mean rate of shear tensor	s^{-1}

$S'_{ij} = \frac{1}{2}\left(\frac{\partial u'_i}{\partial x_j} + \frac{\partial u'_j}{\partial x_i}\right) - \frac{1}{3}\frac{\partial u'_k}{\partial x_k}\delta_{ij}$	ij-component of fluctuating rate of shear tensor	s^{-1}
t	Time	s
U_i	i mean velocity component	$m \cdot s^{-1}$
u'_i	i fluctuating velocity component	$m \cdot s^{-1}$
$T_{R,ij} = -\left\langle \rho u'_i u'_j \right\rangle$	ij-component of Reynolds stress tensor	Pa
$T'_{R,ij} = -\rho u'_i u'_j$	ij-component of instantaneous Reynolds stress tensor	Pa
x_i	i coordinate	m

Greek

Γ	Passive Scalar Diffusivity	$m^2 \cdot s^{-1}$
$\varepsilon = 2\nu\langle S'_{ij} S'_{ij} \rangle$	Turbulent dissipation rate	$m^2 \cdot s^{-3}$
$\varepsilon' = 2\nu S'_{ij} S'_{ij}$	Instantaneous turbulent dissipation rate	$m^2 \cdot s^{-3}$
ν	Molecular kinematic viscosity	$m^2 \cdot s^{-1}$
ρ	Density	$kg \cdot m^{-3}$
$\langle \phi \rangle$	Mean passive scalar	
ϕ'	Fluctuating passive scalar	
$\sqrt{\langle \phi' \phi' \rangle}$	Passive Scalar root Mean Square	
$\langle \Omega_{ij} \rangle = \frac{1}{2}\left(\frac{\partial U_i}{\partial x_j} - \frac{\partial U_j}{\partial x_i}\right)$	ij-component of mean rotation rate tensor	s^{-1}

$\Omega'_{ij} = \frac{1}{2}\left(\frac{\partial u'_i}{\partial x_j} - \frac{\partial u'_j}{\partial x_i}\right)$	ij-component of fluctuating rotation rate tensor	s^{-1}

1.4 Second Order Moments equations

In this section we will list the mainly used Second Order Moments equations for an incompressible non-Newtonian fluid in their exact form.

Turbulent Kinetic Energy Conservation equation:

$$\frac{\partial k}{\partial t} + U_j \frac{\partial k}{\partial x_j} = P_k - \frac{\partial T_{k,j}}{\partial x_j} - \varepsilon$$

$$\begin{cases} P_k = \dfrac{1}{\rho} T_{R,ij} \langle S_{ij} \rangle \\ T_{k,j} = \langle k' u'_j \rangle + \langle \dfrac{p'}{\rho} u'_j \rangle - \nu \dfrac{\partial k}{\partial x_j} - \nu \dfrac{1}{\rho} \dfrac{\partial T_{R,ij}}{\partial x_i} \\ \varepsilon = 2\nu \langle S'_{ij} S'_{ij} \rangle \end{cases} \tag{1.1}$$

Turbulent Dissipation Rate Conservation equation:

$$\frac{\partial \varepsilon}{\partial t} + U_j \frac{\partial \varepsilon}{\partial x_j} = P_\varepsilon - \frac{\partial T_{\varepsilon,j}}{\partial x_j} - D_\varepsilon$$

$$\begin{cases} P_\varepsilon = -4\nu \langle \dfrac{1}{\rho} \dfrac{\partial p'}{\partial x_j} \dfrac{\partial S'_{kj}}{\partial x_k} \rangle - 8\nu \left(\langle S'_{ik} S'_{ij} \rangle \langle S_{kj} \rangle - \langle S'_{ik} \Omega'_{ij} \rangle \langle \Omega_{kj} \rangle \right) + \\ -4\nu \left(\langle S'_{ik} S'_{ij} S'_{kj} \rangle - \langle S'_{ik} \Omega'_{ij} \Omega'_{kj} \rangle \right) - 4\nu \langle u'_j S'_{ik} \rangle \dfrac{\partial \langle S_{ik} \rangle}{\partial x_j} + \\ T_{\varepsilon,j} = 4\nu \langle S'_{jk} \dfrac{1}{\rho} \dfrac{\partial p'}{\partial x_k} \rangle + \langle u'_j \varepsilon' \rangle - \nu \dfrac{\partial \varepsilon}{\partial x_j} \\ D_\varepsilon = \langle 2\nu \dfrac{\partial S'_{ik}}{\partial x_j} 2\nu \dfrac{\partial S'_{ik}}{\partial x_j} \rangle + \end{cases} \tag{1.2}$$

Reynolds Stresses Conservation equation:

$$\frac{\partial \langle u_i' u_k' \rangle}{\partial t} + U_j \frac{\partial \langle u_i' u_k' \rangle}{\partial x_j} = P_{\langle u_i' u_k' \rangle} + D_{\langle u_i' u_k' \rangle} - \frac{\partial T_{\langle u_i' u_k' \rangle, j}}{\partial x_j} - \varepsilon_{\langle u_i' u_k' \rangle}$$

$$\begin{cases} P_{\langle u_i' u_k' \rangle} = -\langle u_k' u_j' \rangle \dfrac{\partial U_i}{\partial x_j} - \langle u_i' u_j' \rangle \dfrac{\partial U_k}{\partial x_j} + \dfrac{1}{\rho} \left\langle 2 p' S_{ki}' \right\rangle \\ D_{\langle u_i' u_k' \rangle} = -\dfrac{1}{\rho} \dfrac{\partial \left\langle u_k' p' \right\rangle}{\partial x_i} - \dfrac{1}{\rho} \dfrac{\partial \left\langle u_i' p' \right\rangle}{\partial x_k} \\ T_{\langle u_i' u_k' \rangle, j} = \langle u_j' u_i' u_k' \rangle - \nu \dfrac{\partial \langle u_i' u_k' \rangle}{\partial x_j} \\ \varepsilon_{\langle u_i' u_k' \rangle} = 2\nu \left\langle \dfrac{\partial u_i'}{\partial x_j} \dfrac{\partial u_k'}{\partial x_j} \right\rangle \end{cases} \tag{1.3}$$

Passive Scalar Variance Conservation equation:

$$\frac{\partial}{\partial t}\left(\frac{\langle \phi' \phi' \rangle}{2} \right) + U_j \frac{\partial}{\partial x_j}\left(\frac{\langle \phi' \phi' \rangle}{2} \right) = P_\phi - \frac{\partial T_{\phi, j}}{\partial x_j} - \varepsilon_\phi$$

$$\begin{cases} P_\phi = -\left\langle \phi' u_j' \right\rangle \dfrac{\partial \langle \phi \rangle}{\partial x_j} \\ T_{\phi, j} = \left\langle u_j' \dfrac{\phi' \phi'}{2} \right\rangle - \Gamma \dfrac{\partial}{\partial x_j}\left(\dfrac{\langle \phi' \phi' \rangle}{2} \right) \\ \varepsilon_\phi = \Gamma \left\langle \dfrac{\partial \phi'}{\partial x_j} \dfrac{\partial \phi'}{\partial x_j} \right\rangle \end{cases} \tag{1.4}$$

Passive Scalar Variance Dissipation Rate Conservation equation:

$$\frac{\partial \varepsilon_\phi}{\partial t} + U_j \frac{\partial \varepsilon_\phi}{\partial x_j} = P_{\varepsilon_\phi} - \frac{\partial T_{\varepsilon_\phi, j}}{\partial x_j} - \varepsilon_{\varepsilon_\phi}$$

$$\begin{cases} P_{\varepsilon_\phi} = -2\Gamma \left\langle \frac{\partial \phi'}{\partial x_j} \frac{\partial \phi'}{\partial x_k} \frac{\partial u_j'}{\partial x_k} \right\rangle - 2\Gamma \left\langle \frac{\partial \phi'}{\partial x_j} \frac{\partial \phi'}{\partial x_k} \right\rangle \frac{\partial U_j}{\partial x_k} + \\ -2\Gamma \left\langle u_j' \frac{\partial \phi'}{\partial x_k} \right\rangle \frac{\partial}{\partial x_j} \left(\frac{\partial \langle \phi \rangle}{\partial x_k} \right) - 2\Gamma \left\langle \frac{\partial u_j'}{\partial x_k} \frac{\partial \phi'}{\partial x_k} \right\rangle \frac{\partial \langle \phi \rangle}{\partial x_j} \\ T_{\varepsilon_\phi, j} = \left\langle u_j' \varepsilon_\phi' \right\rangle - \Gamma \frac{\partial \varepsilon_\phi}{\partial x_j} \\ \varepsilon_{\varepsilon_\phi} = 2\Gamma \left\langle \frac{\partial}{\partial x_j} \left(\frac{\partial \phi'}{\partial x_k} \right) \frac{\partial}{\partial x_j} \left(\frac{\partial \phi'}{\partial x_k} \right) \right\rangle \end{cases} \tag{1.5}$$

Passive Scalar Turbulent Flux Conservation equation:

$$\frac{\partial \langle u_i' \phi' \rangle}{\partial t} + U_j \frac{\partial \langle u_i' \phi' \rangle}{\partial x_j} = P_{\langle u_i' \phi' \rangle} + D_{\langle u_i' \phi' \rangle} - \frac{\partial T_{\langle u_i' \phi' \rangle, j}}{\partial x_j} - \varepsilon_{\langle u_i' \phi' \rangle}$$

$$\begin{cases} P_{\langle u_i' \phi' \rangle} = -\langle u_j' \phi' \rangle \frac{\partial U_i}{\partial x_j} - \langle u_j' u_i' \rangle \frac{\partial \langle \phi \rangle}{\partial x_j} + \frac{1}{\rho} \left\langle p' \frac{\partial \phi'}{\partial x_i} \right\rangle \\ D_{\langle u_i' \phi' \rangle} = -\frac{1}{\rho} \frac{\partial \langle \phi' p' \rangle}{\partial x_i} \\ T_{\langle u_i' \phi' \rangle, j} = \langle u_j' u_i' \phi' \rangle - \Gamma \left\langle u_i' \frac{\partial \phi'}{\partial x_j} \right\rangle - \nu \left\langle \phi' \frac{\partial u_i'}{\partial x_j} \right\rangle \\ \varepsilon_{\langle u_i' \phi' \rangle} = (\nu + \Gamma) \left\langle \frac{\partial u_i'}{\partial x_j} \frac{\partial \phi'}{\partial x_j} \right\rangle \end{cases} \tag{1.6}$$

1.5 Computational Methods

Confidence in CFD can be gained only by proving that basic errors of numerical simulations are efficiently reduced, i.e. iteration, discretization and modeling errors. The discretization error, which is the difference between the exact solution of the differential equations and the exact solution of discretized algebraic system of equations, can be reduced by grid refinement and by employing more accurate approximations. The iteration error, which is the difference between the iterative and the exact solution of the algebraic equation systems, can also be reduced to negligible levels. On the modeling side, turbulence models appear to be the largest and the most common source of error in numerical simulation of Reynolds-averaged Navier–Stokes (RANS) equations, because flows in practice are predominantly turbulent.

Therefore to date, the most common turbulence models implemented in CFD codes are of the eddy viscosity type, e.g. standard $k-\varepsilon$, non-linear $k-\varepsilon$ and $k-\omega$ models. Even though limitations of these models are very well known, they are used due to numerical robustness and the fact that parametric studies do not often require absolute accuracy but rather calculation of relative differences, caused by specific parametric variations [1.5].

Differential second-moment (Reynolds-stress) turbulence closure models (DSM) have long been expected to replace the currently popular eddy viscosity models (EVM) as the industrial standard for Computational Fluid Dynamics (CFD). Yet, despite almost three decades of development and indisputable progress, only a few commercial CFD vendors offer DSM as a modeling option. Even fewer industrial users recognize the natural superiority of the DSM. These models, used and researched mainly within academic community, are still viewed as a development target rather than as a proven and mature technique for solving complex flow phenomena. Moreover, the second-moment closure require careful use and deeper understanding

of the basic features of flows, e.g. many oscillating convergence behaviors during steady state calculations may be related to capturing some transient phenomena and not to the model's numerical instability, and hence transient calculations are required to obtain numerically and physically accurate results. However, more reliable and refined turbulence models than those of the eddy-viscosity type are clearly required. In the case of the second-moment closure, attempts of using it for complex industrial applications have been reported, but commercial CFD vendors still do not recommend it for 'everyday' applications. It seems that so far, a robust numerical algorithm is not available for the second-moment closure.

In the last decade, a number of papers have been reported on the implementation of the second-moment closure in finite volume codes. The starting point of most of the work in this area is the set of governing Reynolds-Averaged Navier–Stokes equations solved for dependent variables in Cartesian co-ordinates and by using collocated variable arrangements. The same approach is also used in many commercial CFD codes, e.g. STAR-CD, FLUENT, CFX, AVL FIRE/SWIFT, etc. The advantages of this approach, like having a single set of computational cells covering a non-orthogonal calculation domain, easier implementation of boundary conditions and general simplicity without diminishing the accuracy of simulations, encourage many CFD developers to follow such practice. Numerical algorithms based on the control volume method often differ in interpolation techniques employed which allow for different types of grids [1.5].

References of Chapter 1

[1.1] I. M. Abdulagatov and N. D. Azizov, Thermal Conductivity and Viscosity of Aqueous K2SO4 Solutions at Temperatures from 298 to 575K and at Pressures up to 30MPa International Journal of Thermophysics, Vol. 26, No. 3, May 2005

[1.2] B. Basara, Employment of the second-moment turbulence closure on arbitrary unstructured grids Int. J. Numer. Meth. Fluids 2004; 44:377–407

[1.3] J. Rotta, Turbulent boundary layers in incompressible flow, in *Progress in Aeronautical Science,* Vol. 2. Pergamon, Oxford (1962). 37.

[1.4] B. E. Launder and D. S. A. Samaraweera Application of A Second-Moment Turbulence Closure To Heat And Mass Transport In Thin Shear Flows-I. Two-Dimensional Transport Inf J Hmr, Muss Trunsfir. Vol. 22. Pp 1631-1643

[1.5] A. Cadiou, K. Hanjalić, K. Stawiarski, A two-scale second-moment turbulence closure based on weighted spectrum integration Theoret. Comput. Fluid Dynamics (2004) 18: 1–26

Chapter 2:

Numerical Method

2.1 Finite Volume Method (FVM) in a two-dimensional flow.

Let list the equations involved in Cartesian coordinates for a Newtonian incompressible fluid with variable diffusivity. The equations have the following form

$$\frac{\partial \phi}{\partial t} + div\left(\vec{u}\phi\right) = div\left(\Gamma \nabla \phi\right) + S_{\phi} \tag{2.1}$$

The finite volume discretization is treated first in steady case and its generalization to unsteady case is simple. At first the equations are discretized in a FVM approach and the algorithm to solve the pressure-velocity coupling is choosen later. In a FVM approach the integration over a control volume,in a rectangular mesh, gives

$$\frac{\partial}{\partial t}\left(\int_{\Omega} \phi dV\right) + \int_{\partial\Omega} \phi \vec{u} \cdot \hat{n} dA = \int_{\partial\Omega} \Gamma \nabla \phi \cdot \hat{n} dA + \int_{\Omega} S_{\phi} dV \tag{2.2}$$

Replacing the average on boundaries and control volume

$$
\begin{aligned}
&\frac{\partial}{\partial t}\left(\int_{\Omega}\phi dV\right)=\frac{\partial}{\partial t}\left(\phi\delta x\delta y\delta z\right)_{I,J,K}\\
&\int_{\partial\Omega}\phi\vec{u}\cdot\hat{n}dA=\left(u_i\phi\delta x_j\delta x_k\right)_{I-\frac{1}{2},J,K}-\left(u_i\phi\delta x_j\delta x_k\right)_{I+\frac{1}{2},J,K}=\\
&\left(u_{i_p+1,J,K}\delta x_j\delta x_k\right)\left(\frac{\phi_{I+1,J,K}+\phi_{I,J,K}}{2}\right)-\left(u_{i_p,J,K}\delta x_j\delta x_k\right)\left(\frac{\phi_{I,J,K}+\phi_{I-1,J,K}}{2}\right)\\
&\int_{\partial\Omega}\Gamma\nabla\phi\cdot\hat{n}dA=\left(\Gamma\frac{\partial\phi}{\partial x_i}\delta x_j\delta x_k\right)_{I-\frac{1}{2},J,K}-\left(\Gamma\frac{\partial\phi}{\partial x_i}\delta x_j\delta x_k\right)_{I+\frac{1}{2},J,K}=\\
&\left(\frac{\Gamma_{I+1,J,K}+\Gamma_{I,J,K}}{2}\delta x_j\delta x_k\right)\left(\frac{\phi_{I+1,J,K}-\phi_{I,J,K}}{\delta x_i}\right)-\left(\frac{\Gamma_{I-1,J,K}+\Gamma_{I,J,K}}{2}\delta x_j\delta x_k\right)\left(\frac{\phi_{I,J,K}-\phi_{I-1,J,K}}{\delta x_i}\right)+\\
&\int_{\Omega}S_{\phi}dV=\left(S_{\phi}\delta x\delta y\delta z\right)_{I,J,K}
\end{aligned}
\tag{2.3}
$$

The scheme is a second-order Central Difference with the variables calculated on the edges of the control volume with a linear interpolation and a dummy node is considered on the edge, Fig. 2.1. Following Patankar [2.1], the staggered grid is adopted, due to the natural grid for a fluid dynamic problem. For x-velocity, Fig. 2.2, the cell contours in y direction coincide with those of the scalar one, while the contours along x direction are moved to mid-cell along x. For y-velocity, Fig. 2.3, the cell contours along x direction coincide with those of the scalar one, while the contours along y direction are moved to mid-cell along y. For the velocity components a fictitious grid is used, the longitudinal middle column is shifted forward and between the nodes $\left(j_p,i_p\right)$ and $\left(J,I+1\right)$ is present the node $\left(J,i_p+1\right)$. The transverse node is shifted of a half-forward line between the nodes $\left(j_p,i_p\right)$ and $\left(J+1,I\right)$, i.e.the node is $\left(j_p+1,I\right)$.

The discretized equations [2.1-2.2] are then

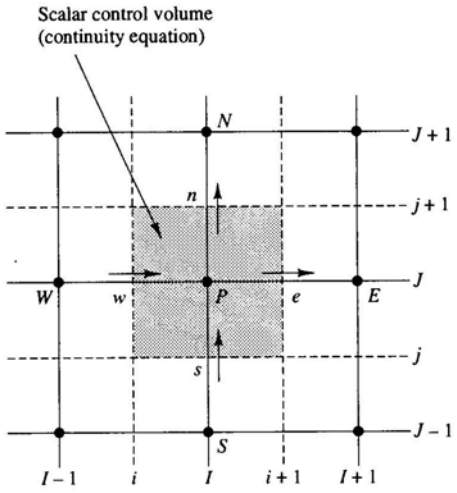

Figure 2.1 Control volume for scalar variables.

$$
\begin{aligned}
a_{\phi,e} &= \left(D_{\phi,e} - \frac{F_{\phi,e}}{2} \right); D_{\phi,e} = \left(\frac{\Gamma_{I+1,J} + \Gamma_{I,J}}{2\left(x_{I+1} - x_I\right)} \left(y_{j_p+1} - y_{j_p} \right) \right); F_{\phi,e} = u_{i_p+1,J} \left(y_{j_p+1} - y_{j_p} \right) \\
a_{\phi,w} &= \left(D_{\phi,w} + \frac{F_{\phi,w}}{2} \right); D_{\phi,w} = \left(\frac{\Gamma_{I,J} + \Gamma_{I-1,J}}{2\left(x_I - x_{I-1}\right)} \left(y_{j_p+1} - y_{j_p} \right) \right); F_{\phi,w} = u_{i_p,J} \left(y_{j_p+1} - y_{j_p} \right) \\
a_{\phi,n} &= \left(D_{\phi,n} - \frac{F_{\phi,n}}{2} \right) D_{\phi,n} = \left(\frac{\Gamma_{I,J+1} + \Gamma_{I,J}}{2\left(y_{J+1} - y_J\right)} \left(x_{i_p+1} - x_{i_p} \right) \right); F_{\phi,n} = v_{I,j_p+1} \left(x_{i_p+1} - x_{i_p} \right) \\
a_{\phi,s} &= \left(D_{\phi,s} + \frac{F_{\phi,s}}{2} \right); D_{\phi,s} = \left(\frac{\Gamma_{I,J} + \Gamma_{I,J-1}}{2\left(y_J - y_{J-1}\right)} \left(x_{i_p+1} - x_{i_p} \right) \right); F_{\phi,s} = v_{I,j_p} \left(x_{i_p+1} - x_{i_p} \right) \\
a_{\phi,p} &= a_{\phi,e} + a_{\phi,w} + a_{\phi,n} + a_{\phi,s} + \left(F_{\phi,e} - F_{\phi,w} + F_{\phi,n} - F_{\phi,s} \right) \\
a_{\phi,p}\phi_{I,J,K} &= a_{\phi,e}\phi_{I+1,J,K} + a_{\phi,w}\phi_{I-1,J,K} + a_{\phi,n}\phi_{I,J+1,K} + a_{\phi,s}\phi_{I,J-1,K} + S_\phi \left(x_{i_p+1} - x_{i_p} \right) \left(y_{j_p+1} - y_{j_p} \right)
\end{aligned}
\tag{2.4}
$$

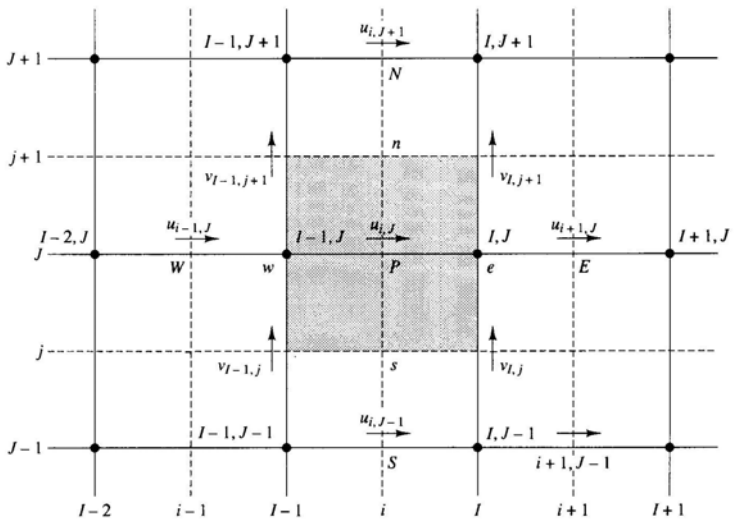

Figure 2.2 Control volume for the velocity component (u).

$$a_{u,w}=\left(D_{u,w}+\frac{F_{u,w}}{2}\right);D_{u,w}=\left(\frac{\mu_{I-1,J}}{\left(x_{i_p}-x_{i_p-1}\right)}\left(y_{j_p+1}-y_{j_p}\right)\right);F_{u,w}=\rho\left(\frac{u_{i_p,J}+u_{i_p-1,J}}{2}\right)\left(y_{j_p+1}-y_{j_p}\right);$$

$$a_{u,e}=\left(D_{u,e}-\frac{F_{u,e}}{2}\right);D_{u,e}=\left(\frac{\mu_{I,J}}{\left(x_{i_p+1}-x_{i_p}\right)}\left(y_{j_p+1}-y_{j_p}\right)\right);F_{u,e}=\rho\left(\frac{u_{i_p,J}+u_{i_p+1,J}}{2}\right)\left(y_{j_p+1}-y_{j_p}\right);$$

$$a_{u,s}=\left(D_{u,s}+\frac{F_{u,s}}{2}\right);D_{u,s}=\left(\frac{\mu_{I-1,J}+\mu_{I,J}+\mu_{I-1,J-1}+\mu_{I,J-1}}{4\left(y_J-y_{J-1}\right)}\left(x_I-x_{I-1}\right)\right);F_{u,s}=\rho\left(\frac{v_{I-1,j_p}+v_{I,j_p}}{2}\right)\left(x_I-x_{I-1}\right);$$

$$a_{u,n}=\left(D_{u,n}-\frac{F_{u,n}}{2}\right);D_{u,n}=\left(\frac{\mu_{I-1,J+1}+\mu_{I,J+1}+\mu_{I-1,J}+\mu_{I,J}}{4\left(y_{J+1}-y_J\right)}\left(x_I-x_{I-1}\right)\right);F_{u,n}=\rho\left(\frac{v_{I-1,j_p+1}+v_{I,j_p+1}}{2}\right)\left(x_I-x_{I-1}\right);\quad(2.5)$$

$$b_u=D_{u,e}\left(u_{i_p+1,J}-u_{i_p,J}\right)-D_{u,w}\left(u_{i_p,J}-u_{i_p-1,J}\right)+D_{u,n}\left(v_{I,j_p+1}-v_{I-1,j_p+1}\right)-D_{u,s}\left(v_{I,j_p}-v_{I-1,j_p}\right);$$

$$a_{u,p}=\left(a_{u,e}+a_{u,w}+a_{u,n}+a_{u,s}+\left(F_{u,e}-F_{u,w}\right)+\left(F_{u,n}-F_{u,s}\right)\right);$$

$$a_{u,p}u_{i_p,J}=a_{u,w}u_{i_p-1,J}+a_{u,e}u_{i_p+1,J}+a_{u,s}u_{i_p,J-1}+a_{u,n}u_{i_p,J+1}+b_u-\left(p_{I,J}-p_{I-1,J}\right)\left(y_{j_p+1}-y_{j_p}\right)$$

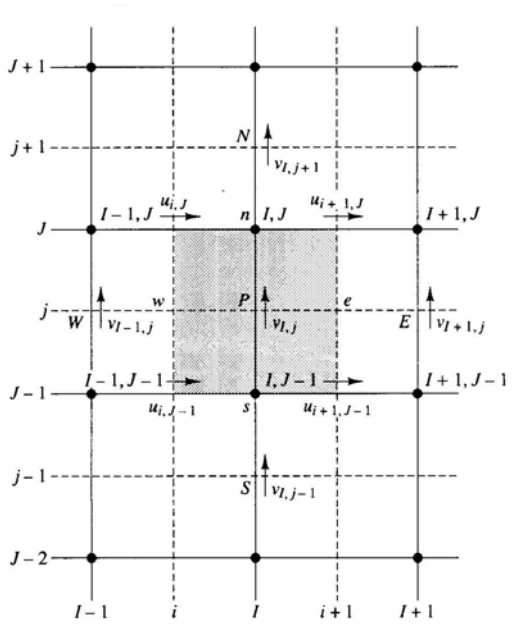

Figure 2.3 Control volume for the velocity component (v).

$$a_{v,w}=\left(D_{v,w}+\frac{F_{v,w}}{2}\right);D_{v,w}=\left(\frac{\mu_{I-1,J-1}+\mu_{I,J-1}+\mu_{I-1,J}+\mu_{I,J}}{4\left(x_I-x_{I-1}\right)}\left(y_J-y_{J-1}\right)\right);F_{v,w}=\rho\left(\frac{u_{J-1,i_p}+u_{i_p,J}}{2}\right)\left(y_J-y_{J-1}\right);$$

$$a_{v,e}=\left(D_{v,e}-\frac{F_{v,e}}{2}\right);D_{v,e}=\left(\frac{\mu_{I,J-1}+\mu_{I+1,J-1}+\mu_{I,J}+\mu_{I+1,J}}{4\left(x_I-x_{I-1}\right)}\left(y_J-y_{J-1}\right)\right);F_{v,e}=\rho\left(\frac{u_{J-1,i_p+1}+u_{i_p+1,J}}{2}\delta y\right)\left(y_J-y_{J-1}\right);$$

$$a_{v,s}=\left(D_{v,s}+\frac{F_{v,s}}{2}\right);D_{v,s}=\left(\frac{\mu_{I,J-1}}{\left(y_{j_p}-y_{j_p-1}\right)}\left(x_{i_p+1}-x_{i_p}\right)\right);F_{v,s}=\rho\left(\frac{v_{I,j_p-1}+v_{I,j_p}}{2}\right)\left(x_{i_p+1}-x_{i_p}\right);$$

$$a_{v,n}=\left(D_{v,n}-\frac{F_{v,n}}{2}\right);D_{v,n}=\left(\frac{\mu_{I,J}}{\left(y_{j_p+1}-y_{j_p}\right)}\left(x_{i_p+1}-x_{i_p}\right)\right);F_{v,n}=\rho\left(\frac{v_{I,j_p}+v_{I,j_p+1}}{2}\right)\left(x_{i_p+1}-x_{i_p}\right);\qquad(2.6)$$

$$b_v=D_{v,e}\left(u_{i_p+1,J}-u_{J-1,i_p+1}\right)-D_{v,w}\left(u_{i_p,J}-u_{J-1,i_p}\right)+D_{v,n}\left(v_{I,j_p+1}-v_{I,j_p}\right)-D_{v,s}\left(v_{I,j_p}-v_{I,j_p-1}\right);$$

$$a_{v,p}=\left(a_{v,e}+a_{v,w}+a_{v,n}+a_{v,s}+\left(F_{v,e}-F_{v,w}\right)+\left(F_{v,n}-F_{v,s}\right)\right);$$

$$a_{v,p}v_{I,j_p}=a_{v,e}v_{I+1,j_p}+a_{v,w}v_{I-1,j_p}+a_{v,n}v_{I,j_p+1}+a_{v,s}v_{I,j_p}+b_v-\left(p_{I,J}-p_{I,J-1}\right)\left(x_{i_p+1}-x_{i_p}\right)$$

2.2 Boundary Conditions

Implementation of boundary conditions is complicated by the presence of the staggered grid, because many nodes do not coincide with the actual physical boundary of the grid. It is then necessary to borrow the given conditions on the physical boundary-free nodes, i.e. those in the middle between nodes. The presence of staggered grids introduced phantom nodes, where the values of the variables do not need to be calculated.

Boundaries of the passive scalar mesh coincides with the physical contour of the control volume, and nodes surrounding the edges are used for the boundary conditions. It follows that the boundary conditions are introduced changing the discretized equations relative to the nodes adjacent to walls, deleting the link with the boundary nodes and inserting appropriate source terms S_p and S_u. The coefficient of the equation is equal to zero in its boundary and the flow that comes from there, exact or linearly approximated, is introduced through S_p and S_u. This is usually done when the flow at a given cell is imposed, but can also be done when is necessary to capture the value in internal nodes of a domain, as, for example, in presence of an obstacle. In that case an arbitrarily large value, like 10^{30}, is imposed to S_p and S_u 10^{30} is multiplied by the value of the variable required on that node.

2.2.1. Entry conditions: VELOCITY INLET

The velocity distribution at the entrance of the duct must be specified and the equations must be solved from $I = 1,\ i_p = 2$. Axial velocity can be imposed by setting the profile

$$u_{J,2} = u_{imposed,J} \tag{2.7}$$

The transverse velocity is more complicated because no velocity is present on that node and the source equivalent to the equation $I = 1$ must be solved. In this case it is not necessary to calculate

the velocity as the average between a cell and an adjacent one because the value in the middle of the cell is the value to be imposed as boundary conditions. The diffusive and convective terms, relative to the cell, are altered. The convective term is substituted by a fixed flow, and the diffusive term by the gradient calculated on the middle of the cell. Three terms are altered in the equation for v on the node $I = 1$.

$$
\begin{aligned}
&S_{u,v,j_p,1} = 0;\\
&S_{p,v,j_p,1} = -\left(2\left(\frac{\mu_{in,J-1} + \mu_{in,J}}{2} \right) \frac{\left(y_{j_p+1} - y_{j_p} \right)}{\left(x_{i_p+1} - x_{i_p} \right)} + \rho \left(\frac{u_{in,J-1} + u_{in,J}}{2} \right) \left(y_{j_p+1} - y_{j_p} \right) \right);\\
&b_{v,(1,j_p)} = D_{v,e}\left(u_{2,J} - u_{2,J-1} \right) - \left(\frac{\mu_{in,J-1} + \mu_{in,J}}{2\left(x_{i_p+1} - x_{i_p} \right)} \right) \left(u_{1,J} - u_{1,J-1} \right) + \\
&D_{v,n}\left(v_{1,j_p+1} - v_{1,j_p} \right) - D_{v,s}\left(v_{1,j_p} - v_{1,j_p-1} \right) + \frac{S_{u,v,j_p,1}}{\left(x_{i_p+1} - x_{i_p} \right)};\\
&a_{v,w,j_p,1} = 0;\\
&a_{v,p} = a_{v,e} + a_{v,w} + a_{v,n} + a_{v,s} - S_{p,v} + \left(F_{v,e} - F_{v,w} \right) + \left(F_{v,n} - F_{v,s} \right);
\end{aligned}
\tag{2.8}
$$

Let write the conditions for scalar variables considering two different ones for the passive scalar, i.e. Dirichlet or Neuman type condition.

$$
\begin{aligned}
&S_{p,\phi} = -\left(2\Gamma_{in} \left(\frac{\left(y_{j_p+1} - y_{j_p} \right)}{\left(x_{i_p+1} - x_{i_p} \right)} \right) + u_{in} \left(y_{j_p+1} - y_{j_p} \right) \right);\\
&S_{u,\phi} = -S_{p,\phi}\phi_{in};\\
&a_{\phi,w} = 0;\\
&a_{\phi,p} = a_{\phi,e} + a_{\phi,w} + a_{\phi,n} + a_{\phi,s} - S_{p,\phi} + \left(F_{\phi,e} - F_{\phi,w} \right) + \left(F_{\phi,n} - F_{\phi,s} \right);\\
&a_{\phi,p}\phi_{1,J} = a_{\phi,e}\phi_{2,J} + a_{\phi,n}\phi_{1,J+1} + a_{\phi,s}\phi_{1,J-1} + S_{u,\phi};
\end{aligned}
\tag{2.9}
$$

2.2.2. Condition of wall: WALL

The most common boundary condition for the two walls, the first for $j_p = 1$ and the second for $j_p = Ny + 1$. As far as the transverse velocity on the wall is concerned, the boundary conditions are

$$v_{1,I} = v_{wall,1,I} \tag{2.10}$$

$$v_{Ny+1,I} = v_{wall,Ny+1,I} \tag{2.11}$$

As far as the longitudinal velocity is concerned the equation for $J = 1$ needs to be altered in order to take into account of the value on the wall .

$$\begin{aligned}
&S_{u,u,1,i_p} = 0;\\
&S_{p,u,1,i_p} = -\left(2\left(\frac{\mu_{wall,I-1} + \mu_{wall,I}}{2\left(y_{j_p+1} - y_{j_p} \right)} \right)\left(x_{i_p+1} - x_{i_p} \right) \right);\\
&b_u = D_{u,e}\left(u_{1,i_p+1} - u_{2,i_p} \right) - D_{u,w}\left(u_{1,i_p} - u_{2,i_p-1} \right) + D_{u,n}\left(v_{I,2} - v_{I-1,2} \right) + \frac{S_{u,u,1,i_p}}{\left(y_{j_p+1} - y_{j_p} \right)};\\
&a_{u,s,1,i_p} = 0;\\
&a_{u,p} = a_{u,e} + a_{u,w} + a_{u,n} + a_{u,s} - S_{p,u} + \left(F_{u,e} - F_{u,w} \right) + \left(F_{u,n} - F_{u,s} \right);
\end{aligned} \tag{2.12}$$

Let write the conditions for scalar variables.

$$\begin{aligned}
&S_{u,\phi} = J_{wall,I}\left(x_{i_p+1} - x_{i_p} \right);\\
&S_{p,\phi} = 0;\\
&a_{\phi,s,1,I} = 0;\\
&a_{\phi,p} = a_{\phi,e} + a_{\phi,w} + a_{\phi,n} + a_{\phi,s} - S_{p,\phi} + \left(F_{\phi,e} - F_{\phi,w} \right) + \left(F_{\phi,n} - F_{\phi,s} \right);\\
&a_{\phi,p}\phi_{I,1} = a_{\phi,e}\phi_{I+1,1} + a_{\phi,w}\phi_{I-1,1} + a_{\phi,n}\phi_{I,2} + S_{u,\phi};
\end{aligned} \tag{2.13}$$

2.2.3. Output condition: OUTFLOW

If the output is far from disturbances of geometric type, and the fluid reachs a fully developed flow, the exit condition of type OUTFLOW is implemented. The gradients of all the flow variables are zero in the direction of the main flow except the pressure gradient. The output is placed on the nodes $i_p = Nx+1$, which are immediately following $I = Nx$. The calculations then proceed to $i_p = Nx+1$ and $I = Nx$, which are the nodes where the equations require a modification.

$$u_{J,Nx+1} = u_{J,Nx} \tag{2.14}$$

The transverse velocity is

$$\begin{aligned}
&S_{u,v} = 0;\\
&S_{p,v} = 0;\\
&b_v = \left(\frac{\mu_{out,J-1} + \mu_{out,J}}{2\left(x_{i_p+1} - x_{i_p}\right)}\right)\left(u_{Nx,J} - u_{Nx,J-1}\right) - D_{v,w}\left(u_{Nx,J} - u_{Nx,J-1}\right) +\\
&D_{v,n}\left(v_{Nx,j_p+1} - v_{Nx,j_p}\right) - D_{v,s}\left(v_{Nx,j_p} - v_{Nx,j_p-1}\right) + \frac{S_{u,v}}{\left(x_{i_p+1} - x_{i_p}\right)};\\
&a_{v,e} = 0;\\
&a_{v,p} = a_{v,e} + a_{v,w} + a_{v,n} + a_{v,s} - S_{p,v} + \left(F_{v,e} - F_{v,w}\right) + \left(F_{v,n} - F_{v,s}\right);
\end{aligned} \tag{2.15}$$

$$\begin{aligned}
&S_{u,\phi} = 0;\\
&S_{p,\phi} = 0;\\
&a_{\phi,e} = 0;\\
&a_{\phi,p} = a_{\phi,e} + a_{\phi,w} + a_{\phi,n} + a_{\phi,s} - S_{p,\phi} + \left(F_{\phi,e} - F_{\phi,w}\right) + \left(F_{\phi,n} - F_{\phi,s}\right);\\
&a_{\phi,p}\phi_{Nx,J} = a_{\phi,w}\phi_{Nx-1,J} + a_{\phi,n}\phi_{Nx,J+1} + a_{\phi,s}\phi_{Nx,J-1} + S_{u,\phi};
\end{aligned} \tag{2.16}$$

2.2.4. Pressure condition imposed: CONSTANT PRESSURE

The boundary condition requiring imposition of pressure is used when the values of the pressure boundary are known. Typical problems of this kind are flows on outer surfaces, around objects, free surfaces, buoyancy-driven flows, natural convection, flames propagation, internal flows with multiple outputs. A convenient method of treating this condition is to determine the pressure just inside the edge of the physical domain, that is $I = 1$, $I = Nx$.

The axial velocity equation is solved from $i_p = 2$ to $i_p = Nx$, and the other scalar variables from $I = 1$ to $I = Nx$. The main problem is the calculation of the longitudinal velocity because the entry value is determined by the conditions within the domain. This difficulty is resolved by generating a velocity boundary that satisfies the continuity equation.

2.2.5. Treatment of Edges

In dealing with the boundary conditions we must be very careful to what happens in the points of different boundaries, i.e. the edges.

2.3 Resolution of The System of Equations

There are two families of methods: direct ones, which belong to the method of inversion with the Cramer Gauss elimination, and iterative ones. In a direct method the number of operations to solve a system of N equations in N unknowns is of the order of N^3, because is required the simultaneous storage in memory of all the N^2 variables, the matrix coefficients, for N times..

The iterative methods are based on the repetition of a relatively simple algorithm that leads to convergence after a certain number of calculations. Examples are the algorithms of

Jacobi and Gauss-Seidel. The total number of iterations is N times the number of iterations, not predictable in advance. It is guaranteed in advance the convergence of iterative method, unless meeting certain assumptions. The main advantage of iterative methods is that only non-zero coefficients of the system must be stored in memory, because most of the factors that resolve the system with a direct method are zeros. The methods of Jacobi and Gauss-Seidel are simple to implement, but can lead to slow convergence. In 1949, Thomas proposed a technique to solve tridiagonal systems, called tri-diagonal matrix algorithm (TDMA), which is a direct method for one-dimensional problems, but can be used also for two and three dimensions iteratively. From the computational point of view is very economical and requires a minimum number of variables stored in memory.

The Thomas algorithm consists of two steps: forward-elimination, which consists of eliminating the unknown node's previous system of equations, and back-substitution of a node according to the values of the unknown in the next node.

$$\begin{aligned}
&\phi_{I,J} = A_{\phi I,J}\phi_{I,J+1} + C'_{\phi,I,J} \\
&A_{\phi,I,J} = \frac{a_{\phi,n}}{a_{\phi,p} - a_{\phi,s}A_{\phi,I,J-1}} \\
&C'_{\phi I,J} = \frac{a_{\phi,s}C'_{\phi,I,J-1} + C_{\phi,I,J}}{a_{\phi,p} - a_{\phi,s}A_{\phi,I,J-1}} \\
&C_{\phi,I,J} = a_{\phi,e}\phi_{I+1,J} + a_{\phi,w}\phi_{I-1,J} + S_{u,\phi}
\end{aligned} \tag{2.17}$$

In this system, the boundary conditions must be given. Iterations proceed from $J = 2$ to $J = Ny - 1$, and along x from $i_p = 2$, $i_p = Nx$, [2.2].

$$\begin{aligned}
&A_{\phi,I,1} = 0 \\
&C'_{\phi,I,1} = 0 \\
&A_{\phi,I,Ny} = 0 \\
&C'_{\phi,I,Ny} = 0
\end{aligned} \tag{2.18}$$

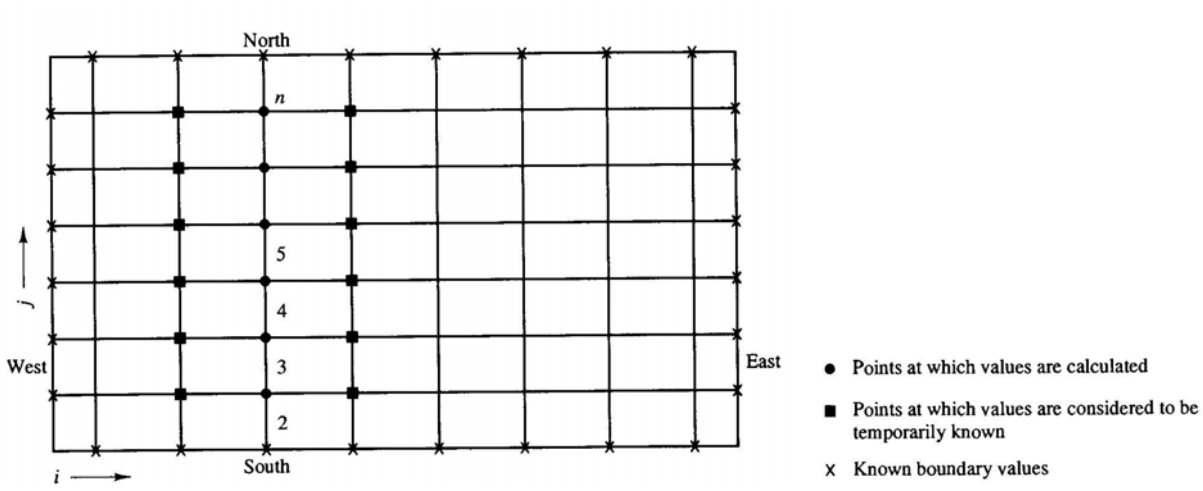

Figure 2. 4 Thomas Algorithm.

2.4 Pressure-Velocity Coupling

In this way a system of N equations in $N+1$ unknown is written,missing the pressure conservation equation, which is not exhisting. The calculation of pressure, which is a state variable, can be done by the knowledge of other state variables as density and temperature. For example in the case of ideal gases

$$p = \rho RT \tag{2.19}$$

or for a Van der Waals equation of state

$$p = \frac{\rho RT}{1 - b'\rho} - a''\rho^2 \tag{2.20}$$

During the iterative calculation the pressure can be obtained once density and temperature are calculated.

For incompressible flow the density is constant and cannot be linked to the pressure and a system of N equations in N unknowns is present. The problems associated with non-linear equations and the coupling between pressure and velocity can be solved by adopting an iterative procedure like that proposed with the SIMPLE algorithm, Patankar and Spalding (1972). In this

algorithm and its later developments, the coefficients of the system are evaluated according to the guessed-variables, which translate into those evaluated during the previous iteration. In this way the coefficients can be calculated and a linear system must be solved. The pressure needs to be estimated in order to make the calculation of velocity, and the pressure correction equation is obtained from the continuity one. The pressure correction equation is used to update pressure and velocity components and the algorithm proceeds until convergence. The estimated variables are marked with an asterisk:

$$\begin{aligned} a_{u,p}u^*_{i_p,J} &= a_{u,w}u^*_{i_p-1,J} + a_{u,e}u^*_{i_p+1,J} + a_{u,s}u^*_{i_p,J-1} + a_{u,n}u^*_{i_p,J+1} + b_u - \left(p^*_{I,J} - p^*_{I-1,J}\right)\left(y_{j_p+1} - y_{j_p}\right) \\ a_{v,p}v^*_{I,j_p} &= a_{v,e}v^*_{I+1,j_p} + a_{v,w}v^*_{I-1,j_p} + a_{v,n}v^*_{I,j_p+1} + a_{v,s}v^*_{I,j_p-1} + b_v - \left(p^*_{I,J} - p^*_{I,J-1}\right)\left(x_{i_p+1} - x_{i_p}\right) \\ a_{\phi,p}\phi^*_{I,J} &= a_{\phi,e}\phi^*_{I+1,J} + a_{\phi,w}\phi^*_{I-1,J} + a_{\phi,n}\phi^*_{I,J+1} + a_{\phi,s}\phi^*_{I,J-1} + S_{u,\phi} \end{aligned} \qquad (2.21)$$

2.5 The SIMPLE Algorithm

The acronym SIMPLE, standing for Semi-Implicit Method for Pressure-Linked Equation, was introduced by Patankar and Spalding in 1972 and is essentially a guess-and-correct procedure.

The variable correction is defined as the difference between the true value of the variable and the variable estimated, therefore

$$\begin{aligned} p &= p^* + p' \\ u &= u^* + u' \\ v &= v^* + v' \end{aligned} \qquad (2.22)$$

Substituting the correct pressure field equation the correct velocity is obtained. Subtracting Eq. (2.5) to (2.21) and Eq. (2.6) to (2.22) the transport equation linking the variables is obtained

$$a_{u,p}u'_{i_p,J} = a_{u,w}u'_{i_p-1,J} + a_{u,e}u'_{i_p+1,J} + a_{u,s}u'_{i_p,J-1} + a_{u,n}u'_{i_p,J+1} + b_u - \left(p'_{I,J} - p'_{I-1,J}\right)\left(y_{j_p+1} - y_{j_p}\right)$$
$$a_{v,p}v'_{I,j_p} = a_{v,e}v'_{I+1,j_p} + a_{v,w}v'_{I-1,j_p} + a_{v,n}v'_{I,j_p+1} + a_{v,s}v'_{I,j_p-1} + b_v - \left(p'_{I,J} - p'_{I,J-1}\right)\left(x_{i_p+1} - x_{i_p}\right) \quad (2.23)$$

The main approximation of the SIMPLE algorithm is done supposing that the contribution of these terms is negligible as compared to the pressure correction, by writing

$$u'_{i_p,J} \approx -\frac{\left(p'_{I,J} - p'_{I-1,J}\right)\left(y_{j_p+1} - y_{j_p}\right)}{a_{u,p}}$$
$$v'_{I,j_p} \approx -\frac{\left(p'_{I,J} - p'_{I,J-1}\right)\left(x_{i_p+1} - x_{i_p}\right)}{a_{v,p}} \quad (2.24)$$

Substituting the expressions into the continuity equation it is obtained a linear equation for the pressure correction.

$$a_{p',p}p'_{I,J} = a_{p',w}p'_{I-1,J} + a_{p',e}p'_{I+1,J} + a_{p',s}p'_{I,J-1} + a_{p',n}p'_{I,J+1} + b'_{I,J} \quad (2.25)$$

The coefficients are defined as follows:

$$b'_{I,J} = -\rho\left(u^*_{i_p+1,J} - u^*_{i_p,J}\right)\left(y_{j_p+1} - y_{j_p}\right) - \rho\left(v^*_{I,j_p+1} - v^*_{I,j_p}\right)\left(x_{i_p+1} - x_{i_p}\right);$$
$$a_{p',w} = \frac{\rho\left(y_{j_p+1} - y_{j_p}\right)^2}{a_{u,p,J,i_p}}; a_{p',e} = \frac{\rho\left(y_{j_p+1} - y_{j_p}\right)^2}{a_{u,p,J,i_p+1}};$$
$$a_{p',s} = \frac{\rho\left(x_{i_p+1} - x_{i_p}\right)^2}{a_{v,p,j_p,I}}; a_{p',n} = \frac{\rho\left(x_{i_p+1} - x_{i_p}\right)^2}{a_{v,p,j_p+1,I}}; \quad (2.25)$$
$$a_{p',p} = a_{p',w} + a_{p',e} + a_{p',s} + a_{p',n};$$

Note that if the estimated variables are correct, the continuity equation is automatically satisfied, and therefore the source of the pressure correction equation is zero, which means that it is correct. Finally, the simplification made in Eqs. (2.24) does not influence the final solution, because in a convergent solution pressure and velocity must be zero. This simplification is due to

the need to calculate an unknown variable as a function of known variables (guessed ones).

$$\begin{aligned} p^{new} &= p^{*} + \alpha_p p' \\ u^{new} &= \alpha_u \left(u^{*} + u'\right) + \left(1-\alpha_u\right) u^{old} \\ v^{new} &= \alpha_v \left(v^{*} + v'\right) + \left(1-\alpha_v\right) v^{old} \end{aligned} \tag{2.26}$$

The α are the coefficients of under-relaxation which are between 0 and 1 and cannot be known in advance. This value must be close to unity for faster convergence, but far away from the unit to have a stable solution [2.1-2.2].

2.6 The SIMPLER Algorithm

The algorithm SIMPLER (SIMPLE Revised), Patankar (1980), is an improved version of SIMPLE. The continuity equation is used to derive a transport equation for the pressure, that will calculate a pressure field satisfying the interim continuity equation. This is done through a different arrangement of the momentum equation. Let

$$\begin{aligned} u_{i_p,J} &= \hat{u}_{i_p,J} - \frac{\left(\hat{p}_{I,J} - \hat{p}_{I-1,J}\right)\left(y_{j_p+1} - y_{j_p}\right)}{a_{u,p}} \\ v_{I,j_p} &= \hat{v}_{I,j_p} - \frac{\left(\hat{p}_{I,J} - \hat{p}_{I,J-1}\right)\left(x_{i_p+1} - x_{i_p}\right)}{a_{v,p}} \end{aligned} \tag{2.27}$$

$$\begin{aligned} \hat{u}_{i_p,J} &= \frac{a_{u,w}u^{*}_{i_p-1,J} + a_{u,e}u^{*}_{i_p+1,J} + a_{u,s}u^{*}_{i_p,J-1} + a_{u,n}u^{*}_{i_p,J+1} + b_u}{a_{u,p}} \\ \hat{v}_{I,j_p} &= \frac{a_{v,e}v^{*}_{I+1,j_p} + a_{v,w}v^{*}_{I-1,j_p} + a_{v,n}v^{*}_{I,j_p+1} + a_{v,s}v^{*}_{I,j_p-1} + b_v}{a_{v,p}} \end{aligned} \tag{2.28}$$

Requiring that velocities satisfy the continuity equation

$$\rho\left(u_{i_p+1,J} - u_{i_p,J}\right)\left(y_{j_p+1} - y_{j_p}\right) + \rho\left(v_{I,j_p+1} - v_{I,j_p}\right)\left(x_{i_p+1} - x_{i_p}\right) = 0 \tag{2.29}$$

substituting equations (2.28) and (2.29) we obtain

$$a_{p',p}\hat{p}_{I,J} = a_{p',w}\hat{p}_{I-1,J} + a_{p',e}\hat{p}_{I+1,J} + a_{p',s}\hat{p}_{I,J-1} + a_{p',n}\hat{p}_{I,J+1} + \hat{b}_{I,J} \tag{2.30}$$

and

$$\hat{b}_{I,J} = -\rho\left(\hat{u}_{i_p+1,J} - \hat{u}_{i_p,J}\right)\left(y_{j_p+1} - y_{j_p}\right) - \rho\left(\hat{v}_{I,j_p+1} - \hat{v}_{I,j_p}\right)\left(x_{i_p+1} - x_{i_p}\right); \tag{2.31}$$

The coefficients appearing are the same for the equation of pressure correction, and have not to be redefined. The last thing to do is to update the pressure

$$p^*_{I,J} = \hat{p}_{I,J} \tag{2.32}$$

At this point the SIMPLER algorithm is proceeding as SIMPLE.

2.7 The SIMPLEC Algorithm

The SIMPLEC algorithm (SIMPLE-Consistent), Van Doormal and Raithby (1984), follows the same steps of the SIMPLE algorithm, with the difference that the equations for momentum are handled in such a way that corrections to the terms of the velocity they fail are less significant than in SIMPLE [2.2].

2.8 The PISO Algorithm

The PISO algorithm (Pressure Implicit with Splitting Operator), Issa (1986), is a pressure-velocity coupling algorithm originally developed to provide non-iterative methods in unsteady compressible fluids and for iterative methods in steady state. PISO provides a sequence of prediction and two corrections and can be seen as an extension of SIMPLE where there is a subsequent step correction. The algorithm proceeds identical to SIMPLE, but after the upgrade there is a new step correction [2.2].

2.9 Boundary Conditions For Pressure Correction Equation

Having introduced an equation for the pressure correction, it seems only natural to ask what boundary conditions to satisfy this equation. We must always remember that the correct pressure is a term that is added to the pressure and estimated that the total sum of the two has to reflect the boundary conditions imposed on the pressure when they are invoked explicitly. In fact perhaps the main advantage of the staggered grid lies in the fact that it is not necessary to know the boundary conditions for pressure. Since at the ghost cells pressure correction is assumed to be zero, because they are outside the physical domain, we begin to see the boundary conditions one by one [2.1-2.2].

2.9.1 Entry condition: VELOCITY INLET

The velocity is imposed on the entrance, so that the correction on the longitudinal velocity is zero. In this equation does not appear a corrected pressure on the node west and the corresponding factor is zero.

2.9.2 Condition of wall: WALL

The transverse velocity is imposed and there is no correction on the transverse velocity on the walls.

2.9.3 Output condition: OUTFLOW

This condition is unique because velocity is not imposed and the derivatives in the longitudinal direction are zero. Therefore, the source will not contain terms in u.

2.9.4 Pressure condition imposed: CONSTANT PRESSURE

The last condition to be discussed is the pressure imposed on the boundary. This condition is easy because pressure is imposed

$$p'(boundary) = 0 \tag{2.33}$$

The calculations will proceed with the index.

2.10 Comparison of Pressure Velocity Coupling Methods

The SIMPLE algorithm is relatively simple to implement and has been successfully implemented in most CFD programs. Subsequent versions of SIMPLE can produce savings in computational effort due to improved convergence. The SIMPLE algorithm produces a satisfactory correction in the momentum equations, but not in the correct pressure.

The SIMPLER algorithm for pressure correction is used only to correct velocity. Separate equation and a more effective pressure correction equation is solved to obtain the correct pressure field. Since there was no omission in the equation discretized in SIMPLER the resulting pressure field is the computed velocity field, as the correct velocity field gives the proper pressure range, which does not happen in SIMPLE. Although the number of calculations in SIMPLER algorithm increases of 30% the corresponding convergence rate increases of the 30-50%. SIMPLEC, PISO and SIMPLER showed an equal efficiency but is not clear which is the most efficient. Comparisons between different algorithms have shown that the efficiency depends on the specific flow conditions and the coupling with the scalar variables. PISO seems more efficient in problems where there is a tight coupling between velocity and scalar variables while SIMPLER in the other two cases [2.1-2.2].

2.11 Properties of discretisation schemes

The numerical results will only be physically realistic when the discretisation scheme has certain fundamental properties: Conservativeness, Boundedness and Transportiveness

2.11.1 Conservativeness

Flux consistency ensures conservation of φ over the entire domain for the central difference formulation of the diffusion flux. In consistent flux interpolation formulae give rise to unsuitable schemes that do not satisfy overall conservation. The flux values calculated at the east face of control volume I and the west face of control volume I+1 may be unequal if the gradient of the two curves are different at the cell face. If this is the case, the two fluxes do not cancel out when summed and overall conservation is not satisfied.

2.11.2 Boundedness

When solving a set of algebraic equations, normally iterative numerical techniques are used. Scarborough (1958) has shown that a sufficient condition for a convergent iterative method can be expressed in terms of the values of the coefficient of the discretised equations:

$$\frac{\sum|a_{nb}|}{|a'_p|}\begin{cases} \leq 1 & \textit{at all nodes} \\ < 1 & \textit{at one node at least} \end{cases} \tag{2.34}$$

a'_p is the net coefficient of the central node P (i.e. $a'_p = a_p - S_p$) and the summation in the numerator is taken over all the neighboring nodes (nb). If the differencing scheme produces coefficients that satisfy the criterion, the resulting matrix of coefficients is diagonally dominated.

For diagonally dominance, we need large values of net coefficient a'_p (i.e. the linearization practice of source terms should ensure that S_P is negative). Diagonal dominance

states that in the absence of sources the internal nodal values of the property φ should be bounded by its boundary values. Another essential requirement for boundedness is that all coefficients of the discretised equations should have the same sign.

2.11.3 Transportiveness

Define the non-dimensional cell Peclet number as a measure of the relative strengths of convection and diffusion:

$$Pe = F/D \tag{2.35}$$

Two extreme cases: (1) no convection and pure diffusion ($Pe = 0$) and (2) no diffusion and pure convection ($Pe \rightarrow \infty$). It is very important that the relationship between the magnitude of the Peclet number and the directionality of influencing, known as the transportiveness, is borne out in the discretisation scheme.

2.11.4 Assessment of the central differencing scheme

The central differencing scheme uses consistent expressions to evaluate convective and diffusive fluxes at the control volume faces. The expression for a_p which satisfies the Scarborough criterion if the continuity equation is satisfied. Given that $F_w > 0$ and $F_e > 0$ (i.e. the flow is unidirectional), for a_E to be positive: $F_e/D_e = Pe_e < 2$. The central differencing scheme does not possess the transportiveness property at $Pe > 2$ and gives unrealistic solutions. For given values of ρ and Γ, it is only possible to satisfy the condition if the velocity is small, hence in diffusion-dominated low Reynolds number flows, or if the grid spacing is small. Owing to this limitation central differencing is not a suitable discretisation practice for general purpose flow calculations.

2.11.5 UPWIND, HYBRID and POWER-LAW Schemes

Discretisation scheme that posses conservativeness, boundedness and transportiveness give physically realistic results and stable iterative solutions. Upwind, hybrid and power-law differencing scheme possess conservativeness, boundedness and transportiveness and are highly stable, but suffer from false diffusion in multi-dimensional flows if the velocity vectors is not parallel to one of the co-ordinate directions.

UPWIND

$$\begin{cases} a_w = D_w + \max\left(F_w, 0\right) \\ a_e = D_e + \max\left(-F_e, 0\right) \end{cases} \tag{2.36}$$

HYBRID

$$\begin{cases} a_w = \max\left(F_w, \left(D_w + F_w/2\right), 0\right) \\ a_e = \max\left(-F_e, \left(D_e - F_e/2\right), 0\right) \end{cases} \tag{2.37}$$

POWER-LAW

$$\begin{cases} a_w = D_w \max\left(0, \left(1 - 0.1\left|F_w/D_w\right|\right)^5\right) + \max\left(F_w, 0\right) \\ a_e = D_e \max\left(0, \left(1 - 0.1\left|F_e/D_e\right|\right)^5\right) + \max\left(-F_e, 0\right) \end{cases} \tag{2.38}$$

2.12 Turbulence modelling

Equations (1.1-1.6) contain terms that can be modelled specifying the approach to solve the turbulent flow. The model chosen in the present work is the *k*-*ε* turbulence model improved by Nagano and Tagawa [2.6] (referred to as NT model in the following) which reproduces strictly the limiting behaviour of wall and free turbulence. In the NT model, the eddy viscosity relation $\nu_T \propto k^{1/2} l$ (being l large-scale) holds far from the wall where is determined by large

scale energy-containing eddies, while the relation is $\nu_T \propto k^{1/2}\eta$ (being η is the Kolmogorov micro-scale) close to the wall where is determined by small-scale eddies, dominating mainly the dissipation process. Constants and relations used in the NT model are summarized

Nomenclature for k-ε Model

Symbol	Definition	SI Unit
Latin		
k	Turbulent kinetic energy	$m^2 \cdot s^{-2}$
P	Mean pressure	Pa
$\langle S_{ij} \rangle$	ij-component of mean rate of shear tensor	s^{-1}
t	Time	s
$u_\tau = \sqrt{\tau_w / \rho}$	Friction velocity	$m \cdot s^{-1}$
U_i	i-mean velocity component	$m \cdot s^{-1}$
x_i	i-coordinate	m
Greek		
ε	Turbulent dissipation rate	$m^2 \cdot s^{-3}$
ν	Molecular kinematic viscosity	$m^2 \cdot s^{-1}$
$\nu_T = C_\mu f_\mu k^2 / \varepsilon$	Turbulent kinematic viscosity	$m^2 \cdot s^{-1}$
ρ	Density	$kg \cdot m^{-3}$

Dimensionless

$\begin{cases} C_{1,\varepsilon} = 1.45 \\ C_{2,\varepsilon} = 1.90; \\ C_{\mu} = 0.09 \end{cases} \begin{cases} \sigma_{\varepsilon} = 1.3 \\ \sigma_{k} = 1.4; \\ \sigma_{T} = 1.0 \end{cases}$ Constants of the turbulent model

$\begin{cases} f_{1,\varepsilon} = 1.0 \\ f_{2,\varepsilon} = \left(1 - 0.3e^{-(\mathrm{Re}_{\tau}/6.5)^2}\right)\left(1 - e^{-y^+/6}\right)^2 \\ f_{\mu} = \left(1 - e^{-y^+/26}\right)\left(1 + 4.1/\mathrm{Re}_{\tau}^{3/4}\right) \end{cases}$ Functions of the turbulent model

$k^+ = k/u_{\tau}^2$ Turbulent kinetic energy

$P^+ = P/\left(\rho u_{\tau}^2\right)$ Mean pressure

$\mathrm{Re}_{\tau} = k^2/(\nu\varepsilon)$ Turbulent Reynolds Number

$S_{ij}^+ = \left(\nu/u_{\tau}^2\right)\langle S_{ij}\rangle$ ij-component of mean rate of shear tensor

$t^+ = t/\left(\nu/u_{\tau}^2\right)$ Time

$U_i^+ = U_i/u_{\tau}$ i-mean velocity component

$x_i^+ = x_i/\left(\nu/u_{\tau}\right)$ i-coordinate

$\varepsilon^+ = \varepsilon/\left(u_{\tau}^4/\nu\right)$ Turbulent dissipation rate

y^+ Wall coordinate

2.13 Equations

The equations to be solved are the following. The continuity equation

$$\frac{\partial U_i^+}{\partial x_i^+} = 0 \tag{2.39}$$

The momentum equation

$$\frac{\partial U_j^+}{\partial t^+} + U_i^+ \frac{\partial U_j^+}{\partial x_i^+} = -\frac{\partial P^+}{\partial x_j^+} - \frac{2}{3}\frac{\partial k^+}{\partial x_j^+} + \frac{\partial}{\partial x_i^+}\left(2\left(1+\nu_T^+\right)S_{ij}^+\right) \tag{2.40}$$

The equation for turbulent kinetic energy

$$\frac{\partial k^+}{\partial t^+} + U_i^+ \frac{\partial k^+}{\partial x_i^+} = 2\nu_T^+ S_{ij}^+ S_{ij}^+ + \frac{\partial}{\partial x_i^+}\left(\left(1+\frac{\nu_T^+}{\sigma_k}\right)\frac{\partial k^+}{\partial x_i^+}\right) - \varepsilon^+ \tag{2.41}$$

The equation for turbulent dissipation rate

$$\frac{\partial \varepsilon^+}{\partial t^+} + U_i^+ \frac{\partial \varepsilon^+}{\partial x_i^+} = C_{1,\varepsilon} f_{1,\varepsilon} \frac{\varepsilon^+}{k^+} 2\nu_T^+ S_{ij}^+ S_{ij}^+ + \frac{\partial}{\partial x_i^+}\left(\left(1+\frac{\nu_T^+}{\sigma_\varepsilon}\right)\frac{\partial \varepsilon^+}{\partial x_i^+}\right) - C_{2,\varepsilon} f_{2,\varepsilon} \frac{\varepsilon^+}{k^+}\varepsilon^+ \tag{2.42}$$

The case investigated in the present paper is relative to fully developed turbulent flow between parallel plates.

Boundary conditions at the wall ($y^+=0$) for U_i^+, k^+ and ε^+ are:

$$\begin{cases} U_i^+ = 0, \forall i \\ k^+ = 0 \\ \varepsilon^+\big|_w = 2\left(\partial\sqrt{k^+}\,/\,\partial x_i^+\right)^2\Big|_w \end{cases} . \tag{2.43}$$

2.14 Grid

As requested by the Finite Volume Method the entire domain is discretized into a number N of elementary volumes. A natural approach is to solve the equations on a uniform grid, i.e. equally spaced and separated by a distance which represents the ratio between the length of the domain and the number of nodes. This discretization has the advantage of being very simple but is very inefficient because the computational effort is equally distributed on all nodes, while there is a greater demand of accuracy where the gradients of variables are higher, i.e. the walls. A variable grid is then chosen with very small values near the walls and very large at the centre of the duct. An hyperbolic tangent function has been chosen and the following Figure 2.5 shows the relationship between nodes and grid coordinates while Fig. 2.6 and between grid dimension and coordinates.

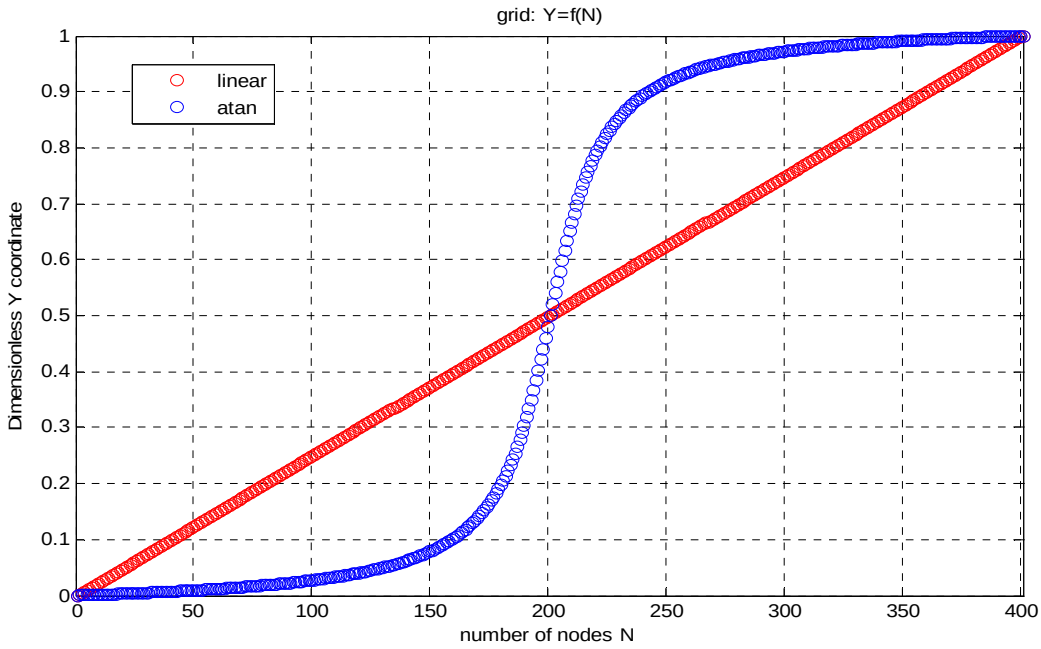

Figure 2.5: dimensionless y-coordinate vs. number of nodes.

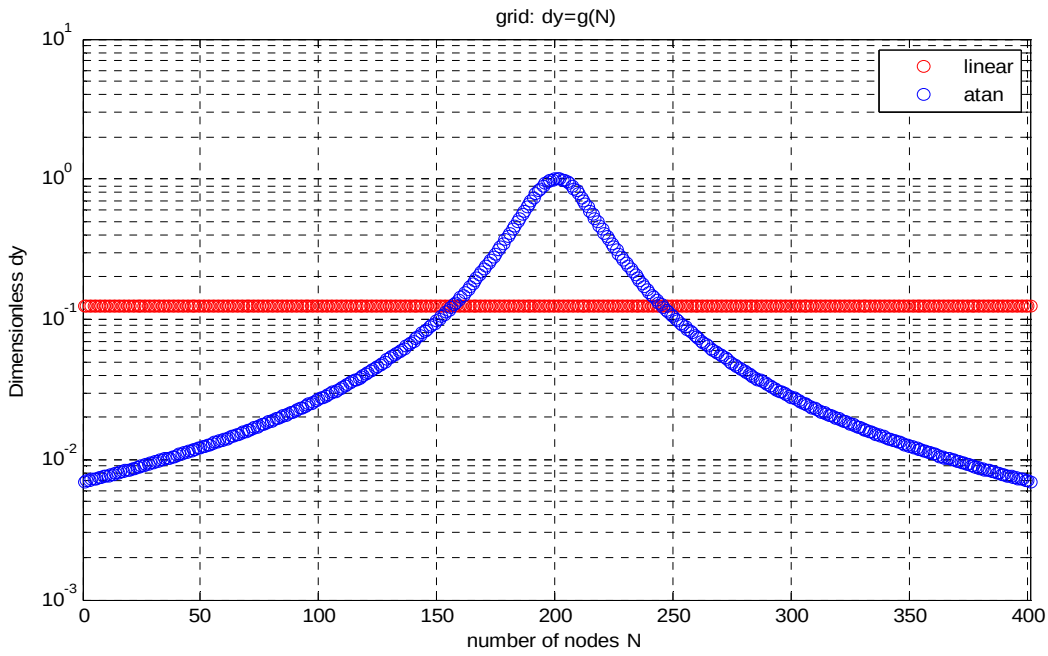

Figure 2.6: dimensionless dy vs. number of nodes.

2.15 Results

Numerical simulations are carried on for fully developed turbulent flow between parallel plates, at different Reynolds numbers. Results of mean velocity profile in the turbulent boundary layer are presented in Figure 2.7, together with the universal velocity profile. Comparison is good in the viscous sub-layer, although the logarithmic law is not fitted exactly elsewhere, in agreement to [2.6-2.8], because Reynolds number is comparatively low.

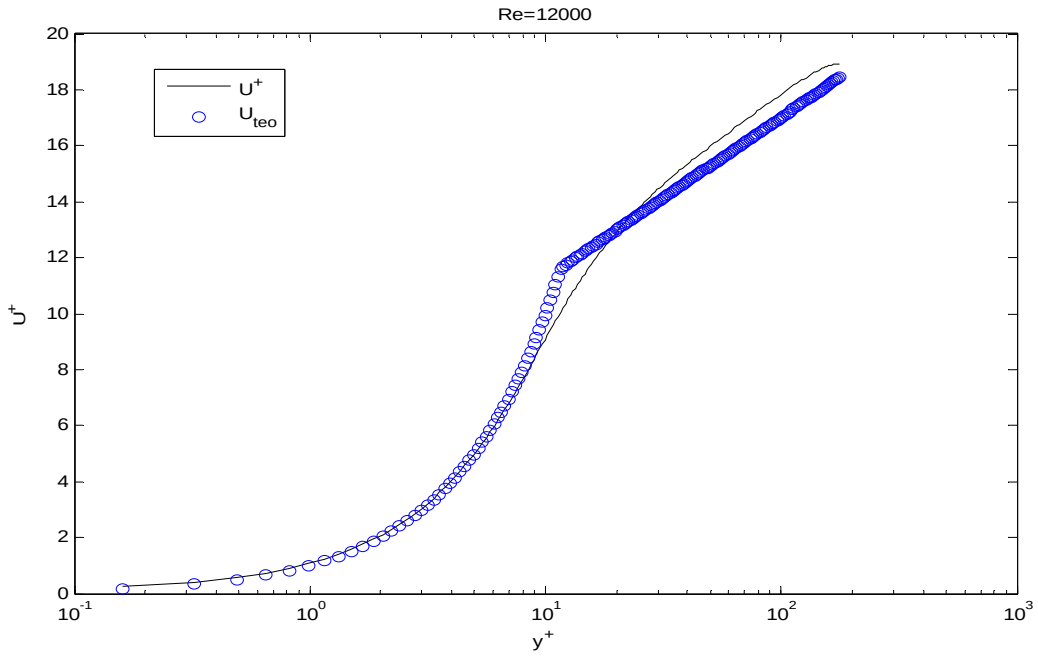

Figure 2.7: Mean velocity profile at Re=12,000.

Figure 2.8 presents results of Dimensionless shear stresses as laminar, turbulent and total one, i.e. sum of the two. Total stress is a linear function of wall distance.

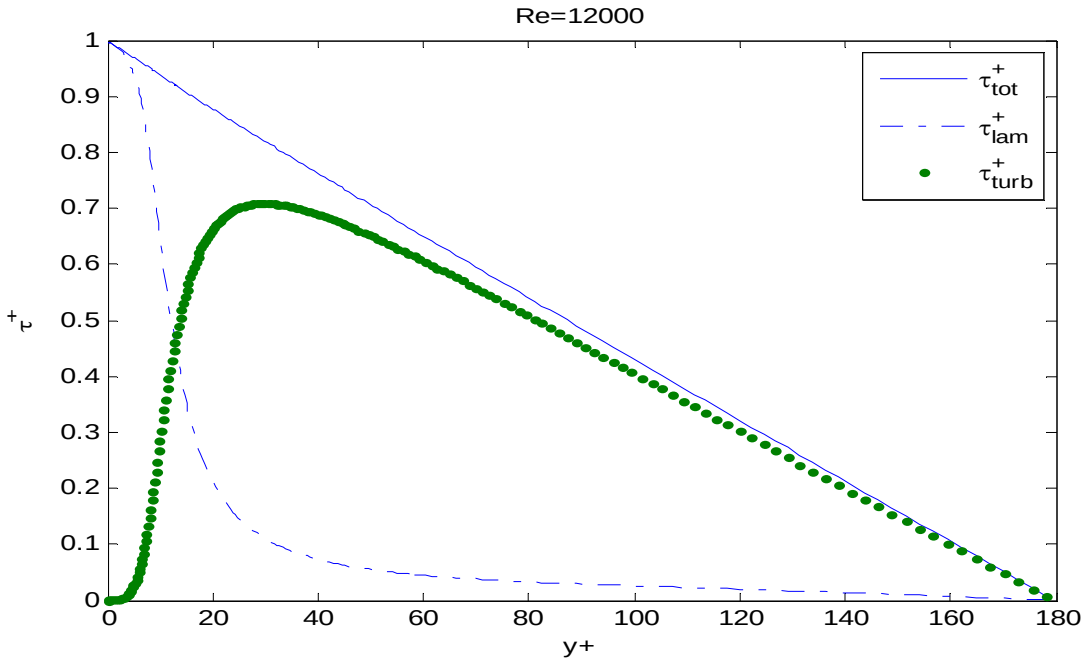

Figure 2.8: Non dimensional shear stresses at Re=12,000.

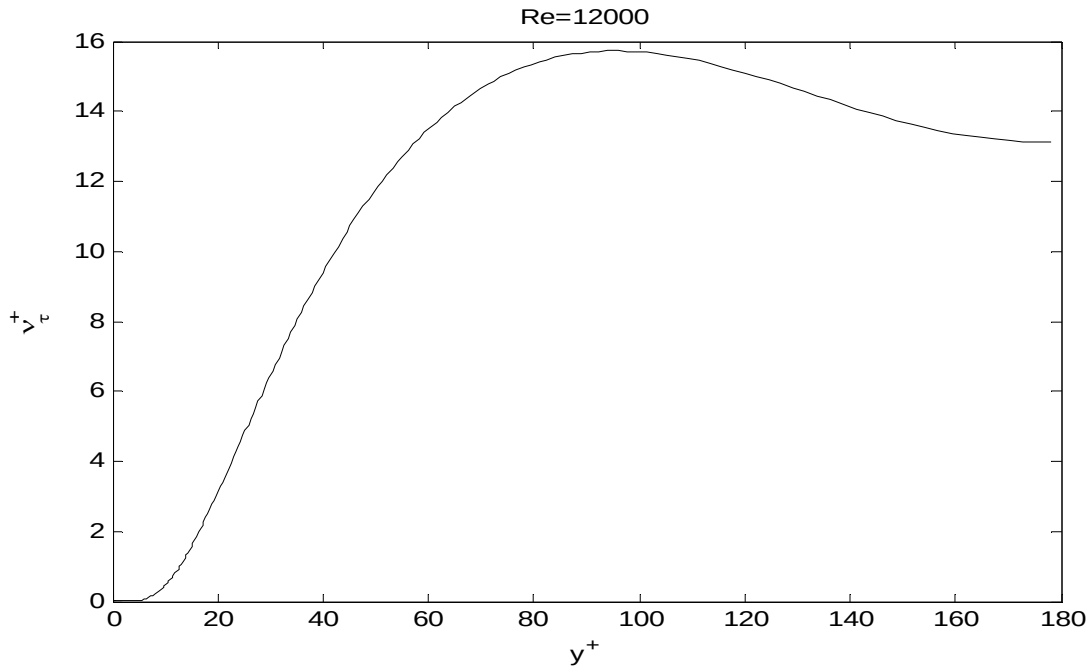

Figure 2.9: Dimensionless turbulent viscosity at Re=12,000.

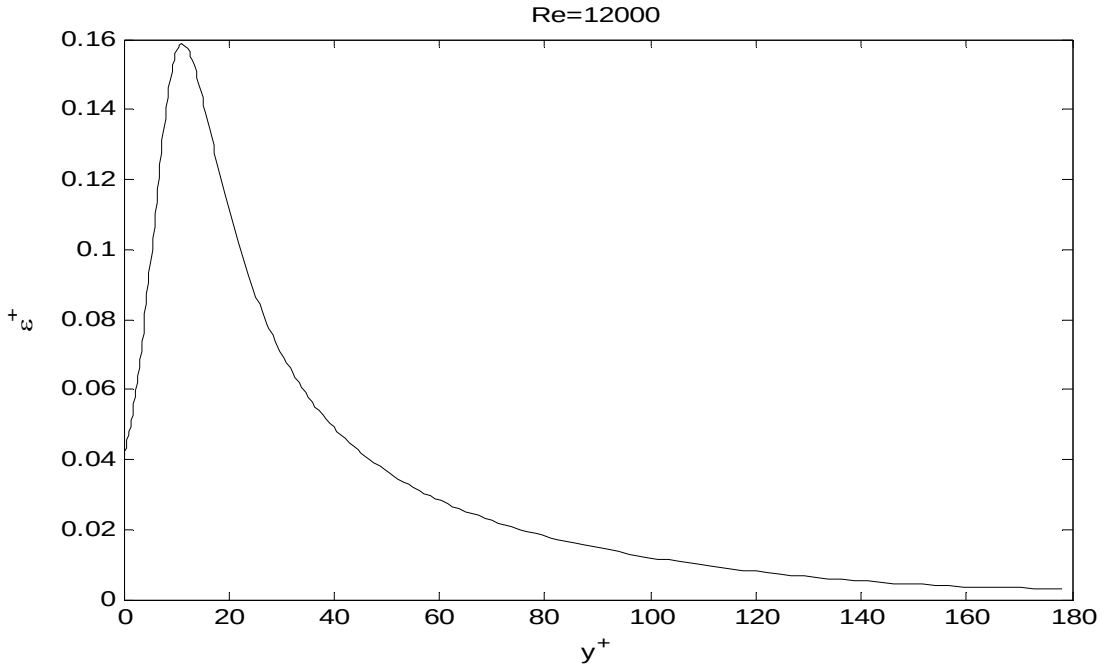

Figure 2.10: Dimensionless turbulent dissipation rate at Re=12,000.

Figure 2.10 presents the results for Dimensionless turbulent dissipation rate and Figure 2.11 those for Dimensionless turbulent kinetic energy, both comparable with [2.6-2.8].

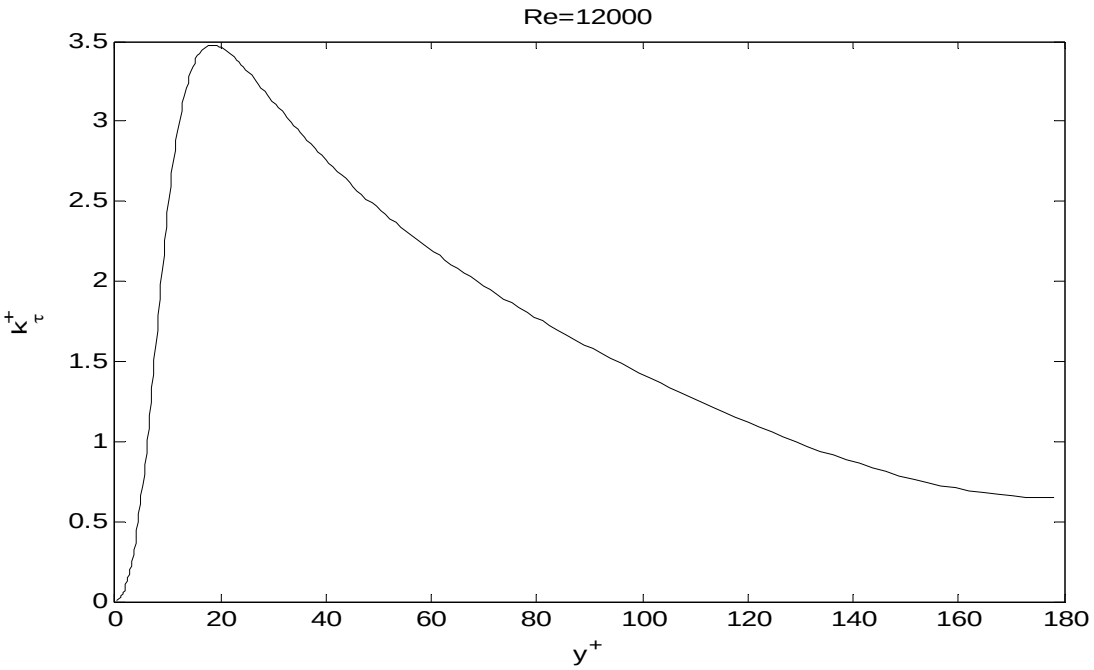

Figure 2.11: Dimensionless turbulent kinetic energy at Re=12,000.

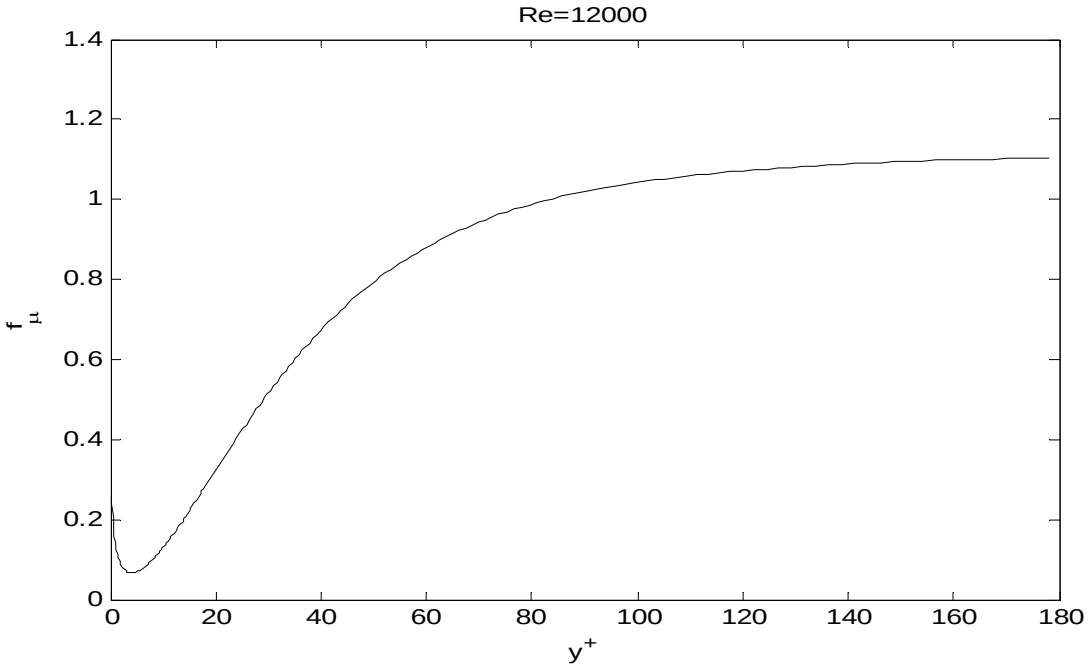

Figure 2.12: fmu at Re=12,000.

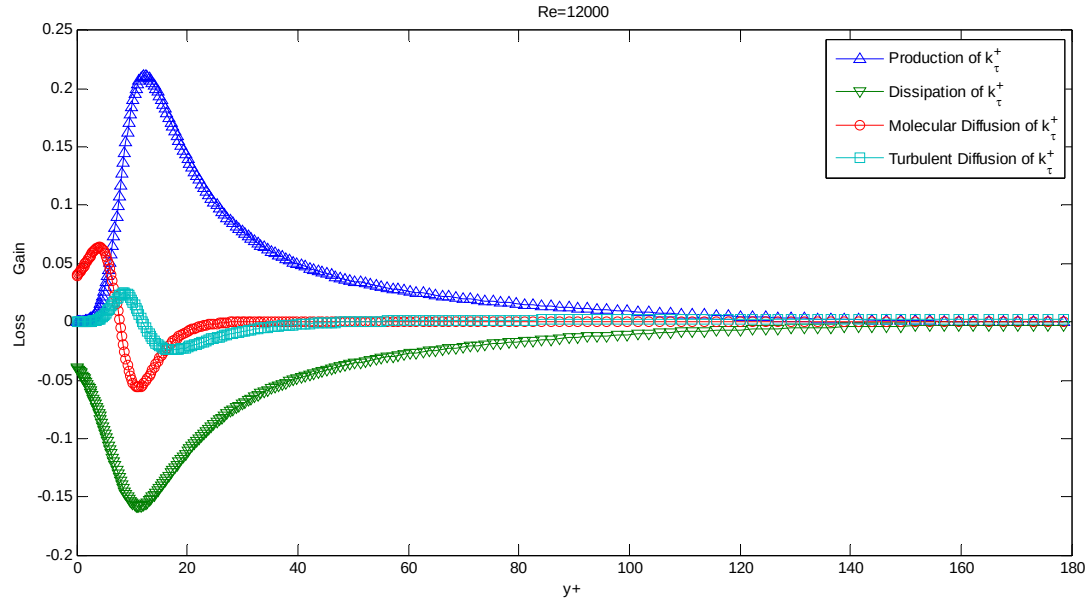

Figure 2.13: Budget of turbulent kinetic energy at Re=12,000.

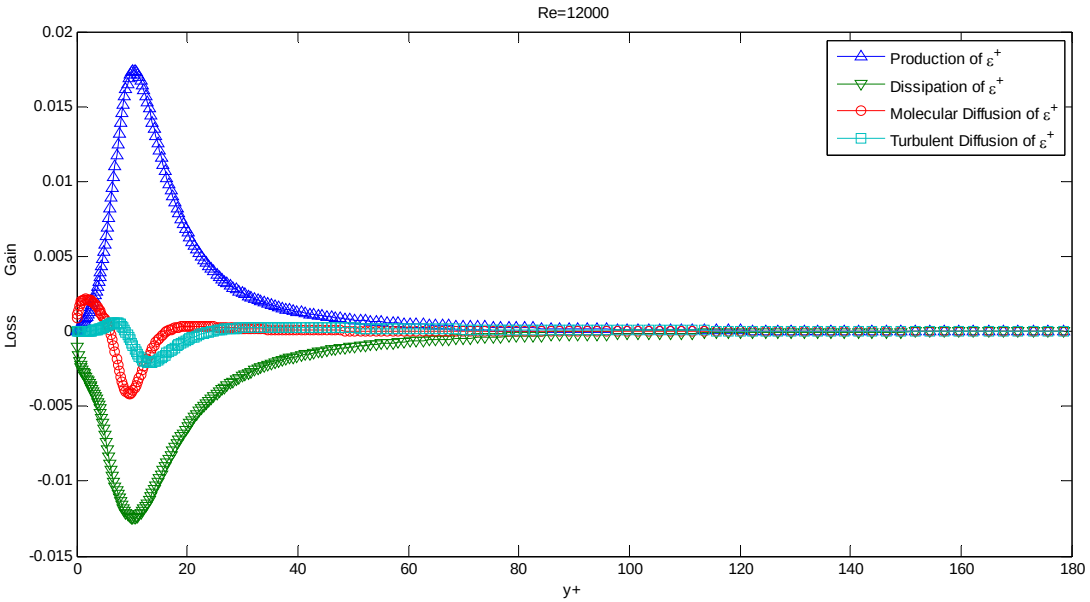

Figure 2.14: Budget of turbulent dissipation rate at Re=12,000.

Below are reported the results of the model at different Reynolds numbers for the same geometrical configuration. It can be seen that results are in accordance with literature.

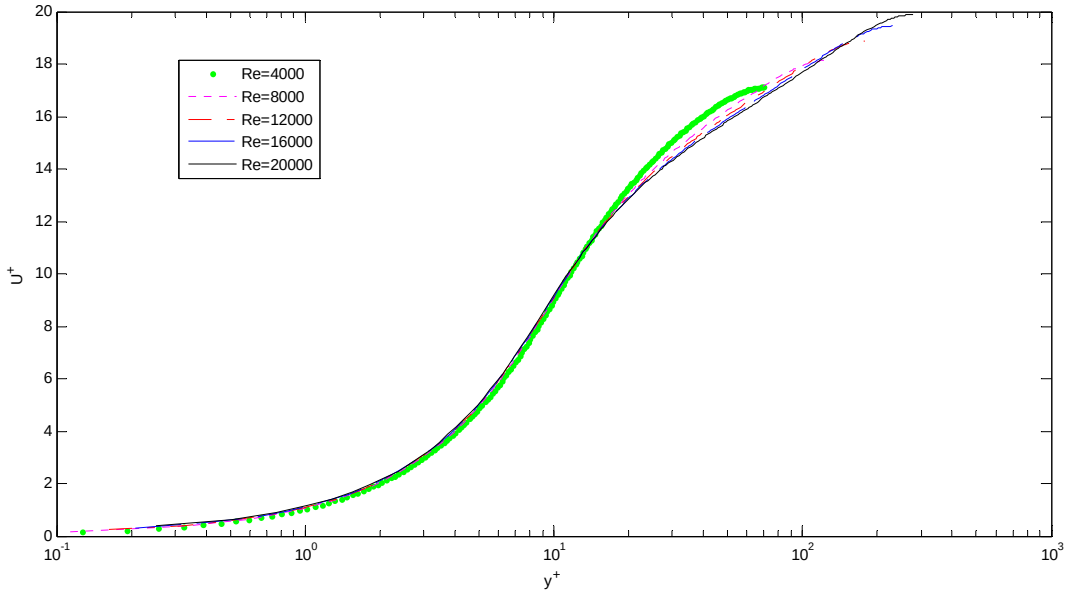

Figure 2.15: Dimensionless Mean Velocity at different Reynolds Numbers

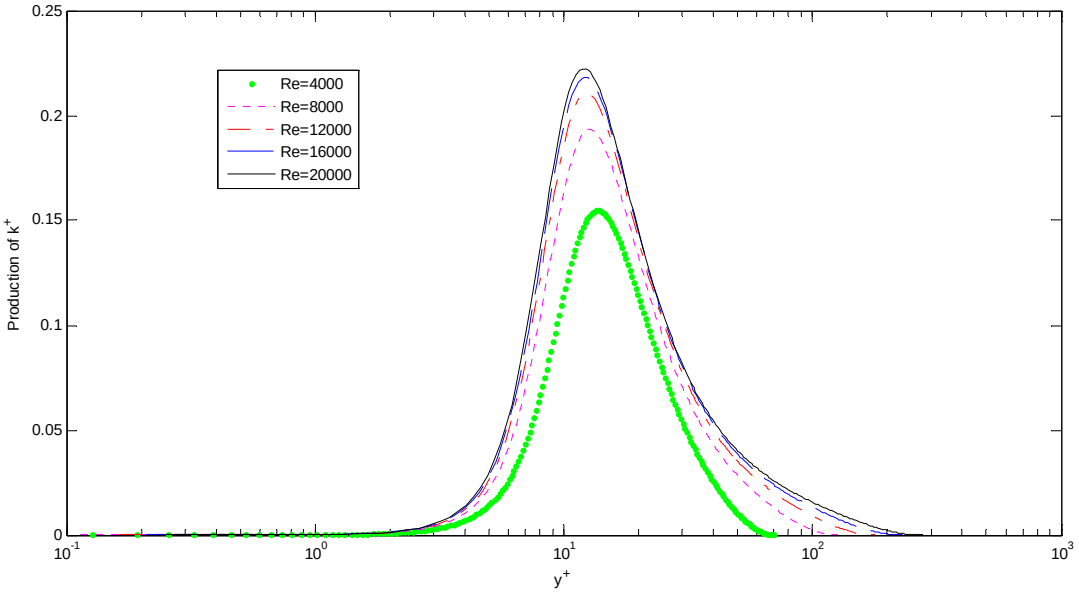

Figure 2.16: Dimensionless Production of Turbulent Kinetic Energy at different Reynolds Numbers

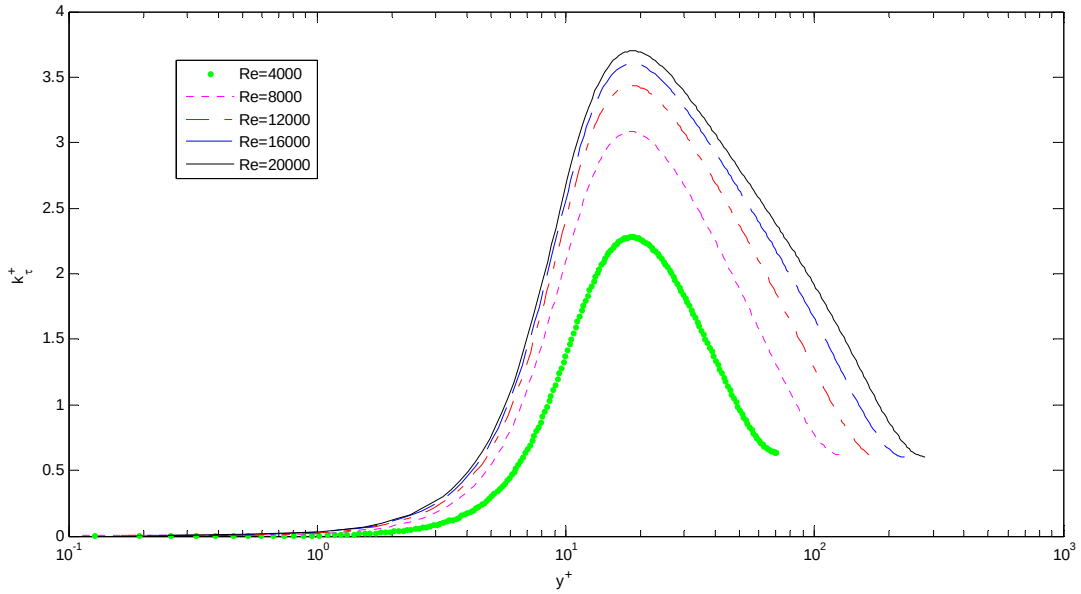

Figure 2.17: Dimensionless Turbulent Kinetic Energy at different Reynolds Numbers

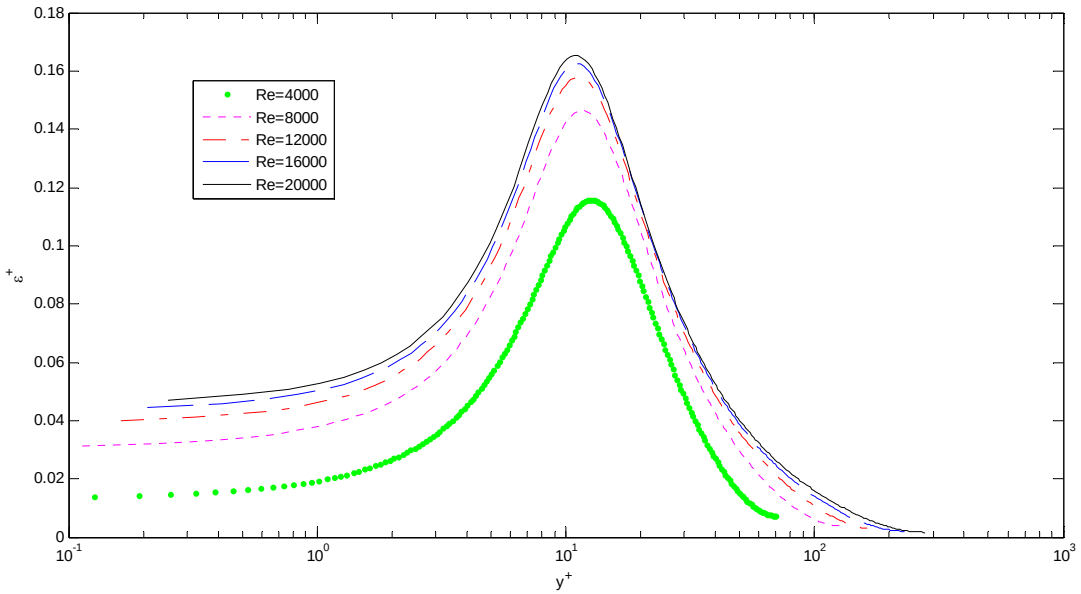

Figure 2.18: Dimensionless Turbulent Dissipation Rate at different Reynolds Numbers

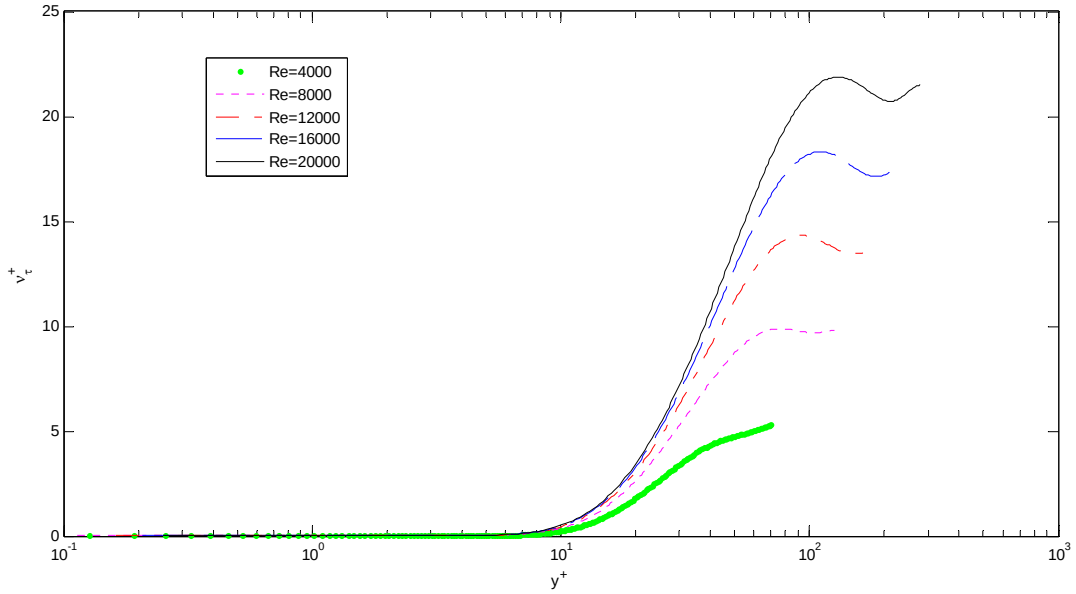

Figure 2.19: Dimensionless Turbulent Viscosity at different Reynolds Numbers

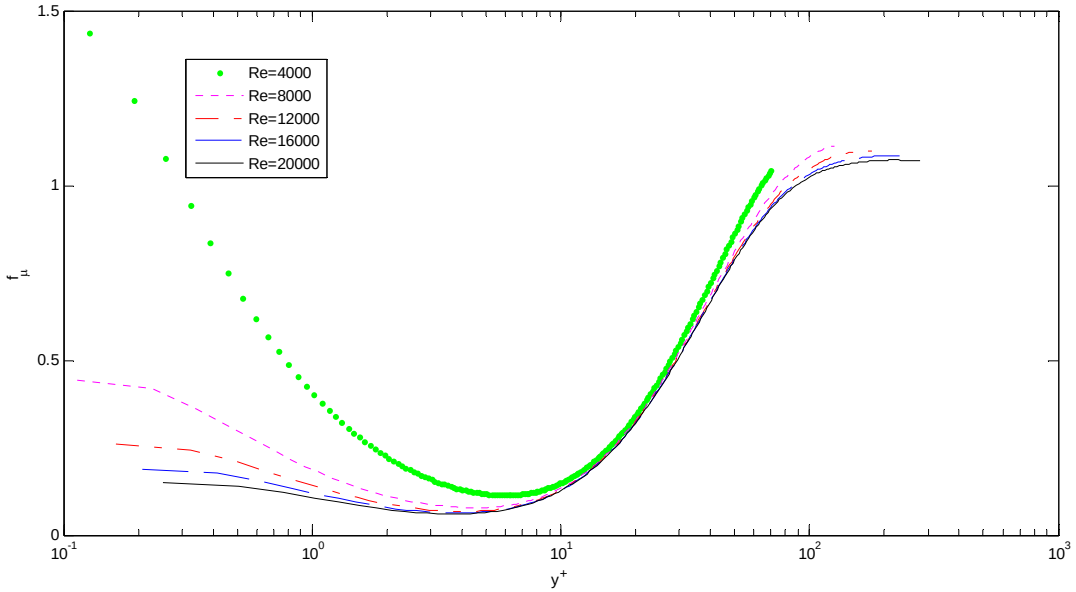

Figure 2.20: Dimensionless Turbulent fmu at different Reynolds Numbers

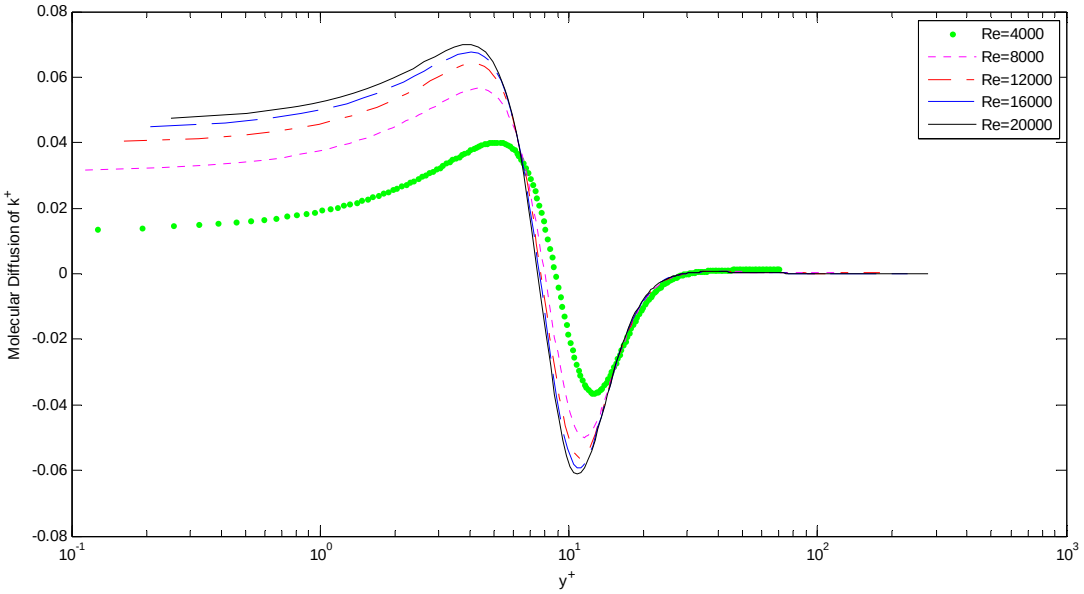

Figure 2.21: Dimensionless Molecular Diffusion of Turbulent Kinetic Energy at different Reynolds Numbers

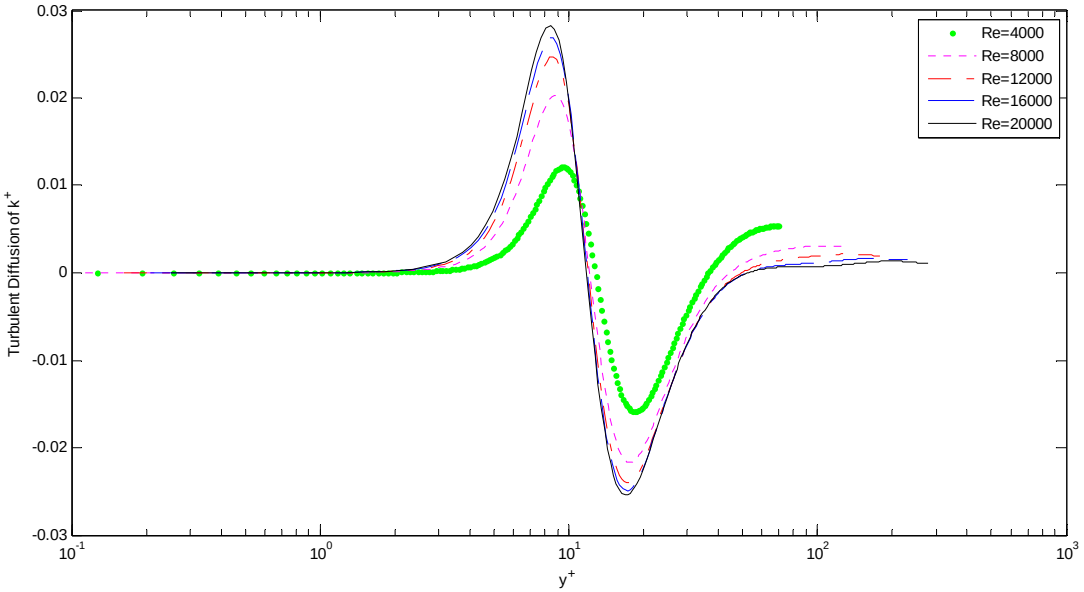

Figure 2.22: Dimensionless Turbulent Diffusion of Turbulent Kinetic Energy at different Reynolds Numbers

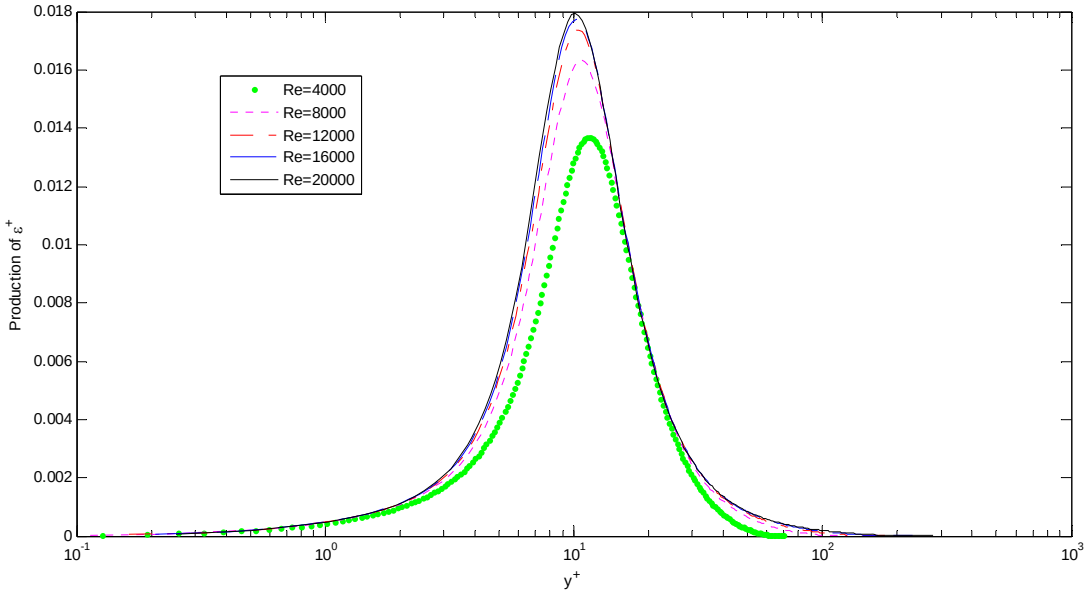

Figure 2.23: Dimensionless Production of Turbulent Dissipation Rate at different Reynolds Numbers

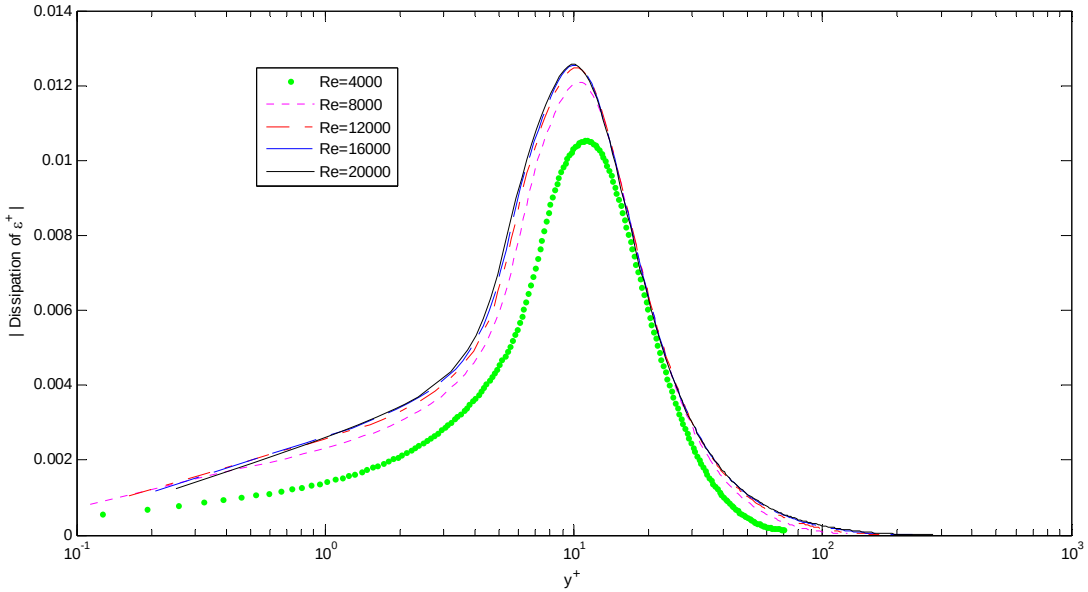

Figure 2.24: Dimensionless Dissipation of Turbulent Dissipation Rate at different Reynolds Numbers

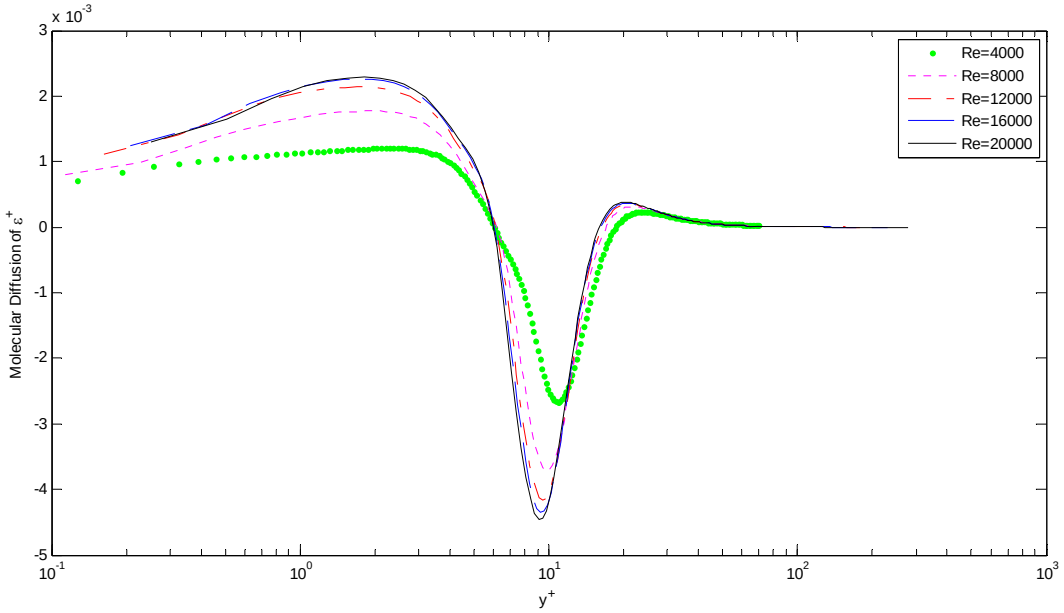

Figure 2.25: Dimensionless Molecular Diffusion of Turbulent Dissipation Rate at different Reynolds Numbers

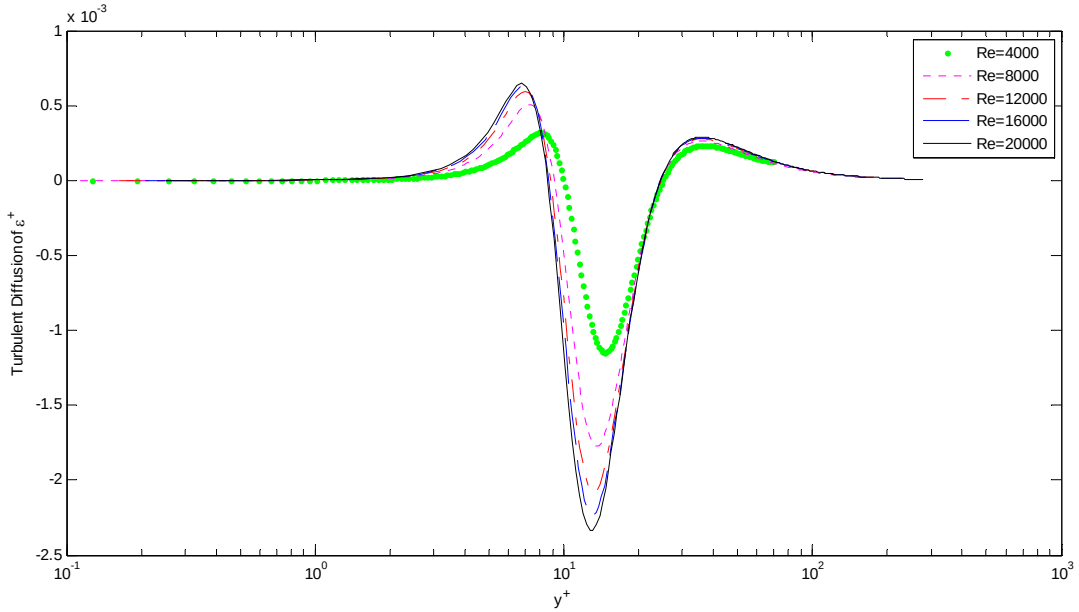

Figure 2.26: Dimensionless Turbulent Diffusion of Turbulent Dissipation Rate at different Reynolds Numbers

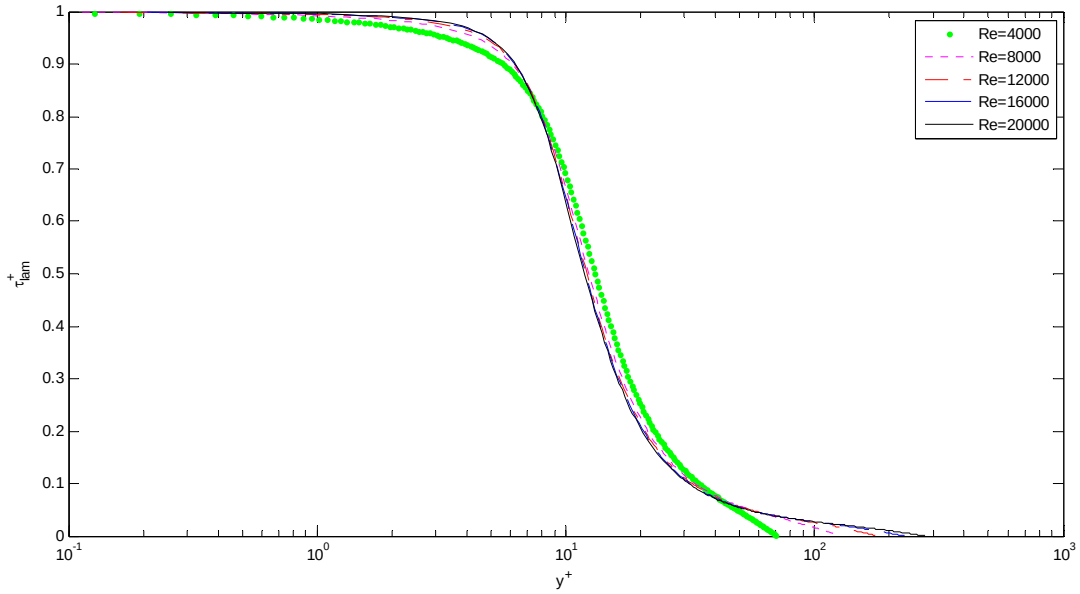

Figure 2.27: Dimensionless Laminar Shear Stress at different Reynolds Numbers

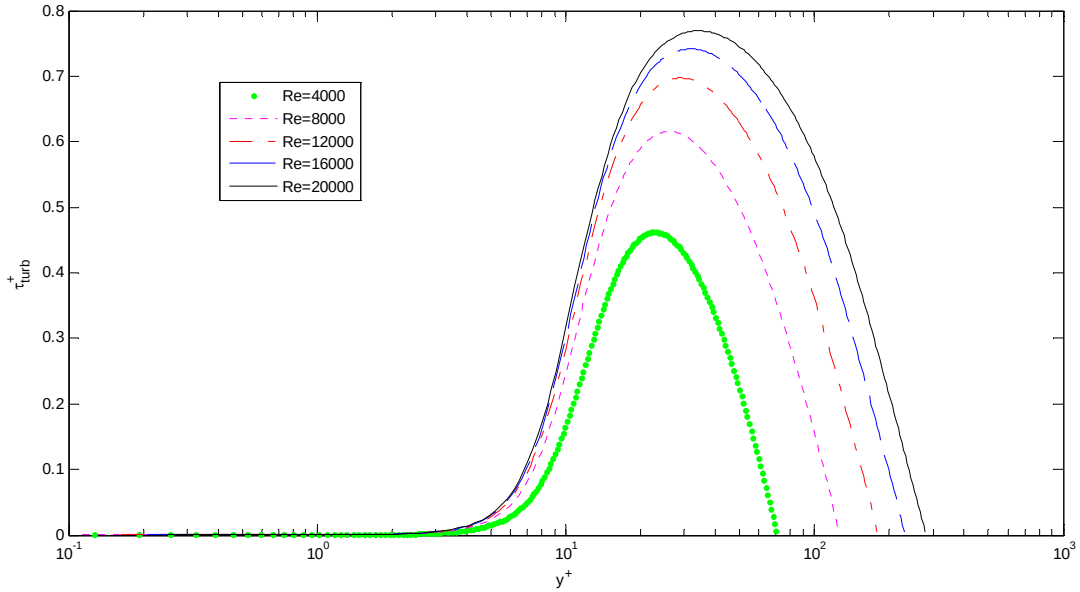

Figure 2.28: Dimensionless Turbulent Shear Stress at different Reynolds Numbers

References of Chapter 2

[2.1] S. V. Patankar. *Numerical Heat Transfer and Fluid Flow*. Hemisphere Publishing Corporation, 1980.

[2.2] H. K. Versteeg, W. Malalasekera. *Introduction to computational fluid dynamics. The finite volume method*. Longman, 1995.

[2.3]W. P. Jones, B. E. Launder. The calculation of low-Reynolds-number phenomena with a two-equation model of turbulence. *International Journal of Heat and Mass Transfer*. 1973 (16-6): 1119-1130.

[2.4] V. C. Patel, W. Rodi, G. Scheuerer. Turbulence Models for Near-Wall and Low Reynolds Number Flows: A Review. *AIAA Journal*. 1985 (23-9): 1308-1319.

[2.5] Y. Nagano, M. Hishida. Improved Form of the k-ε Model for Wall Turbulent Shear Flows. *Journal of Fluids Engineering, Trans. ASME*. 1987 (109-2): 156-160.

[2.6] Y. Nagano, M. Tagawa. An improved k-ε; model for boundary layer flows. *Trans. ASME. Journal of Fluids Engineering*. 1990 (112-1): 33-39.

[2.7] K. M. Hyon, N. Kasagi. A new approach to the improvement of *k-ε* turbulence model for wall-bounded shear flows. *JSME International Journal, Series II (Fluids Engineering, Heat Transfer, Power, Combustion, Thermophysical Properties).* 1990 (33-1): 63-72.

[2.8] C. K. G. Lam, K. A. Bremhorst. A Modified Form of the *k-ε* Model for Predicting Wall Turbulence. *Trans. ASME. Journal of Fluids Engineering*. 1981 (103-3): 456-460.

Chapter 3:

PASSIVE SCALAR EQUATION WITH VARIABLE DIFFUSIVITY IN TURBULENT FLOW

Nomenclature for Passive Scalar equation

Symbol	Definition
Latin	
$\phi_\tau = J_w / u_\tau$	Friction passive scalar
ϕ_w	Wall passive scalar
ϕ	Instantaneous Passive scalar
D_h	Hydraulic diameter
$\langle \Gamma(\phi) \rangle$	mean diffusivity
$\Gamma'(\phi)$	Fluctuating Diffusivity
J_w	Wall mass flux
$J_{R,i}$	Mean i-Reynolds Mass Flux Component
$J'_{R,i}$	Instantaneous i-Reynolds Mass Flux Component

$J_{\Gamma,i}$	Mean i-Fluctuating Diffusivity Mass Flux Component
$J'_{\Gamma,i}$	Instantaneous i- Fluctuating Diffusivity Mass Flux Component

Greek

δ	Boundary Layer Thickness
σ_A	Turbulent Prandtl Number of the A variable

Dimensionless

$\Phi^+ = \left(\langle\phi\rangle - \phi_w\right)/\phi_\tau$	Mean passive scalar
$\varphi^+ = \sqrt{\langle\phi'\phi'\rangle}/\phi_\tau$	Root mean square passive scalar

3.1 Passive scalar equation

Passive scalar equation in turbulent flow of an incompressible fluid with diffusivity dependent on passive scalar is

$$\frac{\partial\phi}{\partial t} + u_i\frac{\partial\phi}{\partial x_i} = \frac{\partial}{\partial x_i}\left(\Gamma(\phi)\frac{\partial\phi}{\partial x_i}\right) \tag{3.1}$$

Assuming each instantaneous variable, as velocity components, diffusivity, Γ, and passive scalar, ϕ, is the sum of an average and a fluctuating term, as, for example, for the passive scalar, ϕ,

$$\phi = \langle\phi\rangle + \phi' \tag{3.2}$$

Introducing each variable into Eq. (3.1) it is obtained

$$\frac{\partial}{\partial t}\left(\langle\phi\rangle+\phi'\right)+\left(U_i+u_i'\right)\frac{\partial}{\partial x_i}\left(\langle\phi\rangle+\phi'\right)=\frac{\partial}{\partial x_i}\left(\left(\langle\Gamma\rangle+\Gamma'\right)\frac{\partial}{\partial x_i}\left(\langle\phi\rangle+\phi'\right)\right) \tag{3.3}$$

Equation (3.3) can be written as two separate equations after time averaging. Time average equation is

$$\frac{\partial\langle\phi\rangle}{\partial t}+U_i\frac{\partial\langle\phi\rangle}{\partial x_i}=\frac{\partial}{\partial x_i}\left(\langle\Gamma\rangle\frac{\partial\langle\phi\rangle}{\partial x_i}-\langle u_i'\phi'\rangle+\left\langle\Gamma'\frac{\partial\phi'}{\partial x_i}\right\rangle\right) \tag{3.4}$$

while fluctuating one is

$$\frac{\partial\phi'}{\partial t}+U_i\frac{\partial\phi'}{\partial x_i}=-u_i'\frac{\partial\langle\phi\rangle}{\partial x_i}+\frac{\partial}{\partial x_i}\left(-u_i'\phi'+\langle u_i'\phi'\rangle+\langle\Gamma\rangle\frac{\partial\phi'}{\partial x_i}+\Gamma'\frac{\partial\langle\phi\rangle}{\partial x_i}+\Gamma'\frac{\partial\phi'}{\partial x_i}-\left\langle\Gamma'\frac{\partial\phi'}{\partial x_i}\right\rangle\right) \tag{3.5}$$

Multiplying Eq. (3.5) for C' and averaging the following equation is obtained

$$\begin{aligned}&\frac{\partial}{\partial t}\left(\frac{\langle\phi'\phi'\rangle}{2}\right)+U_i\frac{\partial}{\partial x_i}\left(\frac{\langle\phi'\phi'\rangle}{2}\right)=-\left(\langle u_i'\phi'\rangle+\left\langle\Gamma'\frac{\partial\phi'}{\partial x_i}\right\rangle\right)\frac{\partial\langle\phi\rangle}{\partial x_i}+\\&\frac{\partial}{\partial x_i}\left(-\left\langle u_i'\frac{\phi'\phi'}{2}\right\rangle+\left\langle\Gamma'\frac{\partial}{\partial x_i}\left(\frac{\phi'\phi'}{2}\right)\right\rangle+\langle\Gamma\rangle\frac{\partial}{\partial x_i}\left(\frac{\langle\phi'\phi'\rangle}{2}\right)+\langle\Gamma'\phi'\rangle\frac{\partial\langle\phi\rangle}{\partial x_i}\right)+\\&-\langle\Gamma\rangle\left\langle\frac{\partial\phi'}{\partial x_i}\frac{\partial\phi'}{\partial x_i}\right\rangle-\left\langle\Gamma'\frac{\partial\phi'}{\partial x_i}\frac{\partial\phi'}{\partial x_i}\right\rangle\end{aligned} \tag{3.6}$$

where is possible to distinguish the different terms.

Time average passive scalar equation, Eq. (3.4), has a form very similar to the instantaneous passive scalar equation. The terms transferring energy from small to large scales are two:

$$\langle u_i'\phi'\rangle-\left\langle\Gamma'\frac{\partial\phi'}{\partial x_i}\right\rangle \tag{3.7}$$

The first one is due to velocity fluctuations while the second one has the traditional form of product of fluctuating diffusivity and gradient of fluctuating passive scalar.

Indicating the two terms as:

$$J_{R,i} = \langle u_i' \phi' \rangle \tag{3.8}$$

$$J_{\Gamma,i} = -\left\langle \Gamma' \frac{\partial \phi'}{\partial x_i} \right\rangle \tag{3.9}$$

Eq. (3.4) can be written as

$$\frac{\partial \langle \phi \rangle}{\partial t} + U_i \frac{\partial \langle \phi \rangle}{\partial x_i} = \frac{\partial}{\partial x_i}\left(\langle \Gamma \rangle \frac{\partial \langle \phi \rangle}{\partial x_i} \right) - \frac{\partial}{\partial x_i}\left(J_{R,i} + J_{\Gamma,i} \right) \tag{3.10}$$

and Eq. (3.6) as:

$$\begin{aligned} &\frac{\partial}{\partial t}\left(\frac{\langle \phi' \phi' \rangle}{2} \right) + U_i \frac{\partial}{\partial x_i}\left(\frac{\langle \phi' \phi' \rangle}{2} \right) = -\left(J_{R,i} - J_{\Gamma,i} \right) \frac{\partial \langle \phi \rangle}{\partial x_i} + \\ &\frac{\partial}{\partial x_i}\left(-\left\langle u_i' \frac{\phi' \phi'}{2} \right\rangle + \left\langle \Gamma' \frac{\partial}{\partial x_i}\left(\frac{\phi' \phi'}{2} \right) \right\rangle + \langle \Gamma \rangle \frac{\partial}{\partial x_i}\left(\frac{\langle \phi' \phi' \rangle}{2} \right) + \langle \Gamma' \phi' \rangle \frac{\partial \langle \phi \rangle}{\partial x_i} \right) + \\ &-\langle \Gamma \rangle \left\langle \frac{\partial \phi'}{\partial x_i} \frac{\partial \phi'}{\partial x_i} \right\rangle + \left\langle J_{D,i}' \frac{\partial \phi'}{\partial x_i} \right\rangle \end{aligned} \tag{3.11}$$

The terms of Eq. (3.11) are then discussed.

The convective term is

$$\frac{\partial}{\partial t}\left(\frac{\langle \phi' \phi' \rangle}{2} \right) + U_i \frac{\partial}{\partial x_i}\left(\frac{\langle \phi' \phi' \rangle}{2} \right) \tag{3.12}$$

while the production term is

$$-\left(J_{R,i} - J_{\Gamma,i} \right) \frac{\partial \langle \phi \rangle}{\partial x_i} \tag{3.13}$$

Energy transfer from average to fluctuating field is enhanced by velocity fluctuations and decreased by fluctuating diffusivity. In other words, velocity fluctuations transport energy from average to fluctuating field while fluctuating diffusivity does the opposite.

The transport term is made of four components

$$\frac{\partial}{\partial x_i}\left(-\left\langle u_i'\frac{\phi'\phi'}{2}\right\rangle+\left\langle\Gamma'\frac{\partial}{\partial x_i}\left(\frac{\phi'\phi'}{2}\right)\right\rangle+\langle\Gamma\rangle\frac{\partial}{\partial x_i}\left(\frac{\langle\phi'\phi'\rangle}{2}\right)+\langle\Gamma'\phi'\rangle\frac{\partial\langle\phi\rangle}{\partial x_i}\right) \tag{3.14}$$

The first one is due to the eddy transport. The second and the third ones are due to molecular diffusion, with a contribution due to fluctuating diffusivity and to average diffusivity. In the last term the fluctuating diffusivity is linked to the fluctuating passive scalar.

The last dissipation term is made of two components:

$$-\langle\Gamma\rangle\left\langle\frac{\partial\phi'}{\partial x_i}\frac{\partial\phi'}{\partial x_i}\right\rangle+\left\langle J_{\Gamma,i}'\frac{\partial\phi'}{\partial x_i}\right\rangle \tag{3.15}$$

The first one is molecular dissipation which is linked to average diffusivity and the second one to fluctuating diffusivity.

3.2 Modelling fluctuating diffusivity

Let model diffusivity taking into account different dependences on passive scalar, which can give an increase or a decrease. If diffusivity is linked to fluctuating passive scalar according to a linear relation

$$\Gamma\left(\langle\phi\rangle+\phi'\right)\approx\Gamma\left(\langle\phi\rangle\right)+\left.\frac{d\Gamma}{d\phi}\right|_{\langle\phi\rangle}\phi' \tag{3.16}$$

and is assumed

$$\langle\Gamma\left(\phi\right)\rangle\approx\Gamma\left(\langle\phi\rangle\right) \tag{3.17}$$

it is obtained

$$\Gamma'\left(\phi\right)\approx\left.\frac{d\Gamma}{d\phi}\right|_{\langle\phi\rangle}\phi' \tag{3.18}$$

The term given by Eq. (3.9) becomes, using Eq. (3.18),

$$J_{\Gamma,i} = -\langle \Gamma' \frac{\partial \phi'}{\partial x_i} \rangle = -\left. \frac{d\Gamma}{d\phi} \right|_{\langle \phi \rangle} \frac{\partial}{\partial x_i} \left(\frac{\langle \phi' \phi' \rangle}{2} \right) \tag{3.19}$$

Substituting Eq. (3.19) into Eq. (3.4) the equation becomes

$$\frac{\partial \langle \phi \rangle}{\partial t} + U_i \frac{\partial \langle \phi \rangle}{\partial x_i} = \frac{\partial}{\partial x_i} \left(-\langle u_i' \phi' \rangle + \left. \frac{d\Gamma}{d\phi} \right|_{\langle \phi \rangle} \frac{\partial}{\partial x_i} \left(\frac{\langle \phi' \phi' \rangle}{2} \right) + \Gamma\left(\langle \phi \rangle \right) \frac{\partial \langle \phi \rangle}{\partial x_i} \right) \tag{3.20}$$

and substituting Eq. (3.19) into Eq. (3.6) it is obtained

$$\begin{aligned} &\frac{\partial}{\partial t} \left(\frac{\langle \phi' \phi' \rangle}{2} \right) + U_i \frac{\partial}{\partial x_i} \left(\frac{\langle \phi' \phi' \rangle}{2} \right) = -\left(\langle u_i' \phi' \rangle + \left. \frac{d\Gamma}{d\phi} \right|_{\langle \phi \rangle} \frac{\partial}{\partial x_i} \left(\frac{\langle \phi' \phi' \rangle}{2} \right) \right) \frac{\partial \langle \phi \rangle}{\partial x_i} + \\ &\frac{\partial}{\partial x_i} \left(-\left\langle u_i' \frac{\phi' \phi'}{2} \right\rangle + \left. \frac{d\Gamma}{d\phi} \right|_{\langle \phi \rangle} \frac{\partial}{\partial x_i} \left(\frac{\langle \phi' \phi' \phi' \rangle}{3} \right) + \Gamma\left(\langle \phi \rangle \right) \frac{\partial}{\partial x_i} \left(\frac{\langle \phi' \phi' \rangle}{2} \right) + 2 \left. \frac{d\Gamma}{d\phi} \right|_{\langle \phi \rangle} \frac{\langle \phi' \phi' \rangle}{2} \frac{\partial \langle \phi \rangle}{\partial x_i} \right) + \\ &-\Gamma\left(\langle \phi \rangle \right) \left\langle \frac{\partial \phi'}{\partial x_i} \frac{\partial \phi'}{\partial x_i} \right\rangle - \left. \frac{d\Gamma}{d\phi} \right|_{\langle \phi \rangle} \left\langle \phi' \frac{\partial \phi'}{\partial x_i} \frac{\partial \phi'}{\partial x_i} \right\rangle \end{aligned} \tag{3.21}$$

The solution of Eq. (3.20) requires the solution of Eq. (3.21), which cannot be solved directly, because it contains the cube of the fluctuating passive scalar, and is necessary to simplify average and fluctuating diffusivity.

Under the assumption

$$\langle \phi \rangle >> \sqrt{\langle \phi' \phi' \rangle} \tag{3.22}$$

it is possible to obtained

$$\left. \frac{d\Gamma}{d\phi} \right|_{\langle \phi \rangle} \left\langle \phi' \frac{\partial}{\partial x_i} \left(\frac{\phi' \phi'}{2} \right) \right\rangle \approx \Gamma\left(\langle \phi \rangle \right) \frac{\phi_{rms}}{\langle \phi \rangle} \frac{\phi_{rms}^2}{\delta} \ll \Gamma\left(\langle \phi \rangle \right) \frac{\partial}{\partial x_i} \left(\frac{\langle \phi' \phi' \rangle}{2} \right) \propto \Gamma\left(\langle \phi \rangle \right) \frac{\phi_{rms}^2}{\delta} \tag{3.23}$$

and

$$\left. \frac{d\Gamma}{d\phi} \right|_{\langle \phi \rangle} \left\langle \phi' \frac{\partial \phi'}{\partial x_i} \frac{\partial \phi'}{\partial x_i} \right\rangle \approx \Gamma\left(\langle \phi \rangle \right) \frac{\phi_{rms}}{\langle \phi \rangle} \frac{\phi_{rms}^2}{\delta^2} \ll \Gamma\left(\langle \phi \rangle \right) \left\langle \frac{\partial \phi'}{\partial x_i} \frac{\partial \phi'}{\partial x_i} \right\rangle \propto \Gamma\left(\langle \phi \rangle \right) \frac{\phi_{rms}^2}{\delta^2} \tag{3.24}$$

Equation (3.21) is finally

$$\frac{\partial}{\partial t}\left(\frac{\langle\phi'\phi'\rangle}{2}\right)+U_i\frac{\partial}{\partial x_i}\left(\frac{\langle\phi'\phi'\rangle}{2}\right)=-\left(\langle u_i'\phi'\rangle+\left.\frac{d\Gamma}{d\phi}\right|_{\langle\phi\rangle}\frac{\partial}{\partial x_i}\left(\frac{\langle\phi'\phi'\rangle}{2}\right)\right)\frac{\partial\langle\phi\rangle}{\partial x_i}+$$
$$\frac{\partial}{\partial x_i}\left(-\left\langle u_i'\frac{\phi'\phi'}{2}\right\rangle+\Gamma\left(\langle\phi\rangle\right)\frac{\partial}{\partial x_i}\left(\frac{\langle\phi'\phi'\rangle}{2}\right)+2\left.\frac{d\Gamma}{d\phi}\right|_{\langle\phi\rangle}\frac{\langle\phi'\phi'\rangle}{2}\frac{\partial\langle\phi\rangle}{\partial x_i}\right)-\Gamma\left(\langle\phi\rangle\right)\left\langle\frac{\partial\phi'}{\partial x_i}\frac{\partial\phi'}{\partial x_i}\right\rangle \tag{3.25}$$

3.3 Turbulence modelling

Equations (3.20) and (3.25) contain terms that can be modelled specifying the approach to solve the turbulent flow. The model chosen in the present work is the *k*-ε turbulence model improved by Nagano and Tagawa [23] (referred to as NT model in the following) which reproduces strictly the limiting behaviour of wall and free turbulence. In the NT model, the eddy viscosity relation $\nu_T \propto k^{1/2}l$ (3.being l large-scale) holds far from the wall where is determined by large scale energy-containing eddies, while the relation is $\nu_T \propto k^{1/2}\eta$ (being η is the Kolmogorov micro-scale) close to the wall where is determined by small-scale eddies, dominating mainly the dissipation process.

Using a Boussinesq type relation Eq. (3.20) becomes

$$\frac{\partial\langle\phi\rangle}{\partial t}+U_i\frac{\partial\langle\phi\rangle}{\partial x_i}=\frac{\partial}{\partial x_i}\left(\left(\Gamma\left(\langle\phi\rangle\right)+\frac{\nu_T}{\sigma_\phi}\right)\frac{\partial\langle\phi\rangle}{\partial x_i}+\left.\frac{d\Gamma}{d\phi}\right|_{\langle\phi\rangle}\frac{\partial}{\partial x_i}\left(\frac{\langle\phi'\phi'\rangle}{2}\right)\right) \tag{3.26}$$

while Eq. (3.25)

$$\frac{\partial}{\partial t}\left(\frac{\langle\phi'\phi'\rangle}{2}\right)+U_i\frac{\partial}{\partial x_i}\left(\frac{\langle\phi'\phi'\rangle}{2}\right)=-\left(\frac{\nu_T}{\sigma_\phi}\frac{\partial\langle\phi\rangle}{\partial x_i}+\left.\frac{d\Gamma}{d\phi}\right|_{\langle\phi\rangle}\frac{\partial}{\partial x_i}\left(\frac{\langle\phi'\phi'\rangle}{2}\right)\right)\frac{\partial\langle\phi\rangle}{\partial x_i}+$$
$$\frac{\partial}{\partial x_i}\left(\left(\Gamma\left(\langle\phi\rangle\right)+\frac{\nu_T}{\sigma_{\langle\phi'\phi'\rangle}}\right)\frac{\partial}{\partial x_i}\left(\frac{\langle\phi'\phi'\rangle}{2}\right)+2\left.\frac{d\Gamma}{d\phi}\right|_{\langle\phi\rangle}\frac{\langle\phi'\phi'\rangle}{2}\frac{\partial\langle\phi\rangle}{\partial x_i}\right)-2C_{2,\langle\phi'\phi'\rangle}f_{2,\langle\phi'\phi'\rangle}\frac{\Gamma\left(\langle\phi\rangle\right)}{\nu}\frac{\langle\phi'\phi'\rangle}{2}\frac{\varepsilon}{k} \tag{3.27}$$

where it has been used the classical closure formula for the dissipation term appearing in the second order turbulence model i.e. the dissipation term is proportional to the second order transported variable multiplied by the frequency $\frac{\varepsilon}{k}$.

Constant $C_{2,\langle\phi'\phi'\rangle}$ of Eq. (3.26) is determined by turbulence near wall behaviour, where velocity components and turbulent kinetic energy must vanish, giving

$$0 = -\left.\frac{d\Gamma}{d\phi}\right|_{\langle\phi\rangle} \frac{\partial\langle\phi\rangle}{\partial x_i}\frac{\partial}{\partial x_i}\left(\frac{\langle\phi'\phi'\rangle}{2}\right) - 2C_{2,\langle\phi'\phi'\rangle} f_{2,\langle\phi'\phi'\rangle} \frac{\Gamma\left(\langle\phi\rangle\right)}{\nu}\frac{\langle\phi'\phi'\rangle}{2}\frac{\varepsilon}{k} + \frac{\partial}{\partial x_i}\left(\left(\Gamma\left(\langle\phi\rangle\right) + \frac{\nu_T}{\sigma_{\langle\phi'\phi'\rangle}}\right)\frac{\partial}{\partial x_i}\left(\frac{\langle\phi'\phi'\rangle}{2}\right) + 2\left.\frac{d\Gamma}{d\phi}\right|_{\langle\phi\rangle}\frac{\langle\phi'\phi'\rangle}{2}\frac{\partial\langle\phi\rangle}{\partial x_i}\right) \tag{3.28}$$

From equation (3.28) it is obtained

$$0 = \Gamma^+\frac{\partial}{\partial y^+}\left(\frac{\partial}{\partial y^+}\left(\frac{\varphi^+\varphi^+}{2}\right)\right) + 2\frac{d\Gamma^+}{d\Phi^+}\frac{\partial\Phi^+}{\partial y^+}\frac{\partial}{\partial y^+}\left(\frac{\varphi^+\varphi^+}{2}\right) - 2C_{2,\varphi^+\varphi^+}D^+\frac{\varphi^+\varphi^+}{2}\frac{\varepsilon^+}{k^+} \Rightarrow$$

$$C_{2,\varphi^+\varphi^+} = \left\{\frac{k^+}{\varepsilon^+}\left(\frac{1}{\sqrt{\varphi^+\varphi^+}}\frac{\partial\sqrt{\varphi^+\varphi^+}}{\partial y^+}\right)^2\left(1 + 2\frac{1}{\Gamma^+}\left.\frac{d\Gamma^+}{d\Phi^+}\right|_w\frac{\partial\Phi^+}{\partial y^+}\left(\frac{1}{\sqrt{\varphi^+\varphi^+}}\frac{\partial\sqrt{\varphi^+\varphi^+}}{\partial y^+}\right)^{-1}\right)\right\}^2_w \tag{3.29}$$

From the asymptotic analysis it is known that

$$k^+ = A^+ y^{+2} + B^+ y^{+3} + O\left(y^{+4}\right) \tag{3.30}$$

$$\varepsilon^+ = 2A^+ + 4B^+ y^+ + O\left(y^{+2}\right) \tag{3.31}$$

$$\varphi^+\varphi^+ = A_\phi^+ y^{+2} + B_\phi^+ y^{+4} + O\left(y^{+5}\right) \tag{3.32}$$

$$\Phi^+ = \mathrm{Sc} y^+ + O\left(y^{+2}\right) \tag{3.33}$$

It is then possible to obtain

$$\frac{k^+}{\varepsilon^+}=\frac{y^{+2}}{2}\frac{\left(1+\frac{B^+}{A^+}y^+ +O\left(y^{+2}\right)\right)}{\left(1+\frac{4B^+}{2A^+}y^+ +O\left(y^{+2}\right)\right)}\approx\frac{y^{+2}}{2} \tag{3.34}$$

also

$$\begin{cases} \dfrac{\partial\sqrt{\varphi^+\varphi^+}}{\partial y^+}=\sqrt{A_\phi^{\ +}}\dfrac{\left(1+2\dfrac{B_\phi^+ y^{+2}}{A_\phi^{\ +}}+O\left(y^{+3}\right)\right)}{\sqrt{\left(1+\dfrac{B_\phi^+ y^{+2}}{A_\phi^{\ +}}+O\left(y^{+3}\right)\right)}}\approx\sqrt{A_\phi^{\ +}} \\ \dfrac{1}{\varphi^+\varphi^+}\left(\dfrac{\partial\sqrt{\varphi^+\varphi^+}}{\partial y^+}\right)^2=\dfrac{1}{y^{+2}}\left(\dfrac{1}{\left(1+\dfrac{B_\phi^+ y^{+2}}{A_\phi^{\ +}}+O\left(y^{+3}\right)\right)}\left(\dfrac{\left(1+2\dfrac{B_\phi^+ y^{+2}}{A_\phi^{\ +}}+O\left(y^{+3}\right)\right)}{\sqrt{\left(1+\dfrac{B_\phi^+ y^{+2}}{A_\phi^{\ +}}+O\left(y^{+3}\right)\right)}}\right)^2\right)\approx\dfrac{1}{y^{+2}} \end{cases} \tag{3.35}$$

Using the relation

$$\frac{k^+}{\varepsilon^+}\left(\frac{1}{\sqrt{\varphi^+\varphi^+}}\frac{\partial\sqrt{\varphi^+\varphi^+}}{\partial y^+}\right)^2\left(1+\frac{2}{\Gamma^+}\frac{d\Gamma^+}{d\Phi^+}\bigg|_w\frac{\partial\Phi^+}{\partial y^+}\left(\frac{1}{\sqrt{\varphi^+\varphi^+}}\frac{\partial\sqrt{\varphi^+\varphi^+}}{\partial y^+}\right)^{-1}\right)\approx\frac{1}{2}\left(1+\frac{2}{\Gamma^+}\frac{d\Gamma^+}{d\Phi^+}\bigg|_w \mathrm{Sc}y^+\right) \tag{3.36}$$

Now, if

$$\lim_{y^+\to 0}\frac{1}{\Gamma^+}\frac{d\Gamma^+}{d\Phi^+}y^+=0 \tag{3.37}$$

it is obtained

$$C_{2,\langle\phi'\phi'\rangle}=0.5 \tag{3.38}$$

Assuming the passive scalar variance dissipation rate, ε_C, [21], at the wall as equal to

$$\varepsilon_\phi=f_{2,\langle\phi'\phi'\rangle}\frac{\Gamma\left(\langle\phi\rangle\right)}{\nu}\frac{\langle\phi'\phi'\rangle}{2}\frac{\varepsilon}{k} \tag{3.39}$$

the time scale ratio, *r,* can be defined as

$$r = \frac{\langle \phi' \phi' \rangle / \varepsilon_\phi}{2k/\varepsilon} = \frac{\nu}{\Gamma\left(\langle \phi' \rangle\right)} = \mathrm{Sc}\frac{1}{\Gamma^+\left(\varphi^+\right)} \tag{3.40}$$

It can be seen that it is proportional to the Schmidt number.

It was shown in [21] that the passive scalar variance dissipation rate, ε_C, approaches 1 at the centre of the duct. In order to take into account the variation of the passive scalar variance dissipation rate from the wall to the centre of the duct it is assumed the following damping function in the present work, [3.1-3.3]

$$f_{2,\varphi^+\varphi^+} = 1 \Bigg/ \left(e^{-y^+/6} + \frac{\Gamma^+\left(\Phi^+\right)}{\mathrm{Sc}}\left(1 - e^{-y^+/6}\right) \right) \tag{3.41}$$

References of Chapter 3

[3.1] F. Gori, A. Boghi. On a New Turbulent Energy Equation with Variable Thermal Conductivity. IMECE2008, October 31-November 6/2008, Boston Massachusset, USA.

[3.2] F. Gori, A. Boghi. On a New Passive Scalar Equation with Variable Mass Diffusivity. IMECE2008, October 31-November 6,2008, Boston Massachusset, USA

[3.3] F. Gori, A. Boghi. On a New Passive Scalar Equation with Variable Mass Diffusivity: Flow between Parallel Plates, submitted paper.

Chapter 4:

ON A NEW PASSIVE SCALAR EQUATION WITH VARIABLE MASS DIFFUSIVITY: FLOW BETWEEN PARALLEL PLATES

4.1 Introduction

In several examples of mass diffusion, as dilute solutions, mass diffusivity is almost constant while in others, as heavy polymers, dyes and macro-molecules, mass diffusivity is strongly dependent on concentration [4.1]. Several experimental works investigated the concentration dependent mass diffusivity for different substances. Rao and Rao [4.2] derived equations for binary liquids showing that concentration dependency of diffusion coefficients can lead to significant errors in estimating liquid-phase mass transfer coefficients. Carlfors and Rymdén [4.3] measured self-diffusion coefficients of small penetrants in aqueous solutions at varying concentrations of poly-vinylpyrrolidone, using NMR, Pulsed Gradient Spin-Echo (PGSE) technique and Classical Gradient Diffusion (CGD) method, modified for ternary systems, showing a linear relationship between mass diffusivity and reciprocal volume fraction of solvent. Kenneth et al. [4.4] measured mutual diffusion coefficients for aqueous solutions of ethanol and propan-1-ol at 25 °C with the Taylor dispersion technique, founding that, for aqueous ethanol system, the diffusion coefficient has a minimum at low ethanol mole fraction. Tanahatoe and Kuil [4.5] performed dynamic light scattering experiments on flexible highly charged polyelectrolyte sodium poly-styrenesulfonate determining the apparent diffusion

coefficient of five molar masses at the fixed ionic strength of 0.1 M of dilute polyelectrolyte concentrations. The dependence of the diffusion second virial coefficient was linearly proportional to the molar mass and could be interpreted with small ion-polyion coupled mode theories. Gao et al. [4.6] used self-diffusion coefficient measurements of NMR to study the properties of polyethylene glycol (23), lauryl ether (Brij-35) with cetyltrimethylammonium bromide (CTAB) in mixed aqueous solutions with different mole fractions of CTAB. The mixed micellar self-diffusion coefficients increase slightly at lower CTAB molar ratios but more rapidly with increasing CTAB mole fraction. Valente et al. [4.7] measured inter-diffusion coefficients of lead (II) nitrate in water and in nitric acid (10y5–10y2 M) mixtures at 298.15 K, and at concentrations from 0.001 to 0.1 M, using a conductimetric cell and an automatic apparatus to follow diffusion. The diffusion of lead (II) nitrate was clearly affected by the presence of HNO_3, as well as by the lead (II) hydrolysis. The experimental inter-diffusion coefficients are discussed with the Onsager–Fuoss model.

Chang and Lin [4.8] studied, with the Taylor dispersion method, the diffusion coefficients of alkanol-amines in water at infinite dilution and the mutual diffusion coefficients of aqueous bi-glycol-amine, tri-ethanol-amine, 2-amino-2-methyl-l-propanol, and 2-piperidineethanol solutions, founding that the diffusion coefficients of alkanol-amines in water vary systematically with the molar mass of alkanol-amines. Grossmann and Winkelmann [4.9] determined the concentration dependence of the mutual diffusion coefficients in the ternary liquid mixture glycerol + acetone + water at 298.15 K, with the Taylor dispersion technique, along two concentration paths of constant water mole fractions. Eigenvalues of Fick diffusion coefficient matrix were found, and the influence of the optical properties of the system on the diffusion coefficient was discussed. Wittko and Köhler [4.10] measured the mutual mass diffusion

coefficient of liquids as acetone, benzene, benzene-d1, benzene-d3, benzene-d5, benzene-d6, benzene-13C6, n-hexane, toluene, 1-, 2-, 3-, 4-tetrahydronaphtalene, isobutylbenzene, and 1-6-dibromohexane in protonated and perdeuterated cyclohexane with a transient holographic grating technique at a temperature of 25 ±C. The mass diffusion coefficient shows pronounced concentration dependence.

Latrous et al. [4.11] determined the self-diffusion coefficients D of the trivalent ions in aqueous solutions of Eu and Gd in electrolyte support $Gd(NO_3)_3$, and of Am, Bk, Cf and Es in electrolyte support $Nd(ClO_4)_3$, in concentrated solutions at (pH=2.5) HNO_3, $HClO_4$ and at 25 °C using the Open End Capillary Method (OECM). The variation of mass diffusivity with the square root of solution concentration was found to be quasi-linear in the studied concentration range ($C \leq 1.5$ M). Results of diffusion for the two couples (Am–Eu) and (Bk–Gd) show that 4f and 5f elements, having similar electronic configuration and-or sub shell half-filled configuration of trivalent ions, have the same behaviour. Ouerfelli et al. [4.12] determined the ionic self-diffusion coefficients of the trivalent ion 152Eu (III) in aqueous $Gd(NO_3)_3$–HNO_3 concentrated solutions (pH=2.50) at 25 °C by OECM as a function of the concentration of supporting electrolytes. The diffusion data allowed to derive information on the validity of the Onsager limiting law and the ionic self-diffusion coefficient as a function of the ionic strength, for asymmetrical 3:1 electrolytes in dilute solutions.

Lin [4.13] extended the Sada model to reacting dyes with the hypothesis of an exponential relation between mass diffusivity and concentration, obtaining better predictions than before. Tsunashima, Hashimoto, and Nakano [4.14] performed sedimentation measurements and dynamic light scattering determining the coefficient of mutual diffusion of a linear flexible polymer with the conclusion that the sedimentation coefficients are function of the concentration

according to a polynomial law. Kuntz and Lavallee [4.15] showed that simple compounds, like copper sulphate in water environment, exhibited a mass diffusivity decreasing hyperbolically with the concentration.

Among the substances that exhibit concentration-dependent diffusion coefficient are also biological molecules like proteins. Gaigalas et al. [4.16] proposed a non-perturbative relation between mutual diffusion coefficient and viscosity in suspensions of binary fluid mixtures near a critical mixing point. They applied this theory to protein solutions, measuring mutual diffusion coefficients of several globular proteins in aqueous solutions and concluding that a non-perturbative relation provides a convenient estimate of protein diffusion coefficients as a function of protein concentration. Bowen [4.17] investigated the physicochemical conditions on the permeation rate in cross-flow ultra-filtration of a colloidal suspension. A numerical solution of the relative equations was performed to model the concentration polarisation and to predict the rate of cross-flow ultra-filtration, taking into account variation of physical properties with mass diffusivity. Results were compared to experimental data for the proteins bovine serum albumin and recombinant human lacto-ferrin with a good agreement between numerical predictions and experimental cross-flow ultra-filtration data. In conclusion the effects of variable diffusivity were both significant and comparable in magnitude. The insight of diffusion process of specific proteins, like fibrin and selectines in blood flow, has a critical relevance in the thrombus formation. Further on, blood flow sets the transport of cells and proteins on the surface of implantable devices, like stent. Many researches focus the attention on platelet deposition, even if literature about turbulence and thrombus formation is scanty. The effort is to design new devices with a smaller recirculation zone where thrombi are deposited. These aspects are resumed in Gorbedt and Sefton [4.18].

Among the macromolecules that diffuse in human body, like drugs, are aerosolized medications which include bronchodilators and corticosteroids to treat asthma, realised by biomedical devices. Deposition on lung surfaces is attractive for many reasons. For pulmonary disorders it is useful to apply medication directly to the lung surfaces, in order to increase drug concentration in the affected area without increasing total dosage. Using current aerosol drug delivery equipment, less than 10% of the aerosolized medication for jet-nebulizers and less than 20% for metered dose inhalers is deposited on the alveolar surfaces of the lungs. Gemci et al. [4.19] have analyzed deposition of a series of mono-disperse aerosol injections in 70/30 helium/oxygen (Heliox) and air for the larynx and trachea with Computational Fluid Dynamics (CFD) software. Flow measurements such as turbulent kinetic energy and velocity magnitude typically are different by less than 5%. The authors have implemented a k-ε turbulence model to perform the simulation for mass, momentum and energy conservation equations and stochastic particle technique to solve the spray equation. Tennekes and Lumley [4.20] showed that scale of fluctuations reduces increasing Schmidt number, as in dyes and macro-molecules, with the consequent increase of fluctuations of passive scalar. This behaviour has been confirmed by other papers of DNS simulations, as Schwertfirm and Manhart [4.21], who investigated low Reynolds numbers flow with a Schmidt number ranging from 3 to 49. The numerical modelling of a passive scalar in turbulent flow is usually done using the Reynolds analogy; despite some researchers argue it is no more valid at high Schmidt numbers. Hasegawa and Kasagi [4.22] modelled numerically, with DNS, a fluid with high Schmidt number flowing onto a free or a solid surface. The mass transfer is shown to be dominated by velocity fluctuations at low frequency, implying the analogy between mass and momentum transfer is no more valid. Indeed,

at high Schmidt numbers the eddy diffusivity of mass is different from the momentum eddy diffusivity, or, in other words, the turbulent Schmidt number is not unity.

The present work is aimed to investigate theoretically the turbulent flow taking into account a mass diffusivity variable with the concentration.

Nomenclature for Mass Transfer Model

Symbol	Definition	SI Unit
Latin		
$C_\tau = J_w / u_\tau$	Friction concentration	mol
C_w	Wall concentration	mol
C	Instantaneous Concentration	
$\langle C \rangle$	Mean concentration	mol
C'	Fluctuating concentration	mol
$\sqrt{\langle C'C' \rangle}$	Root mean square concentration	mol
D	Mass Diffusivity	$m^2 \cdot s^{-1}$
$\langle D(C) \rangle$	mean mass diffusivity	
$D'(C)$	Fluctuating Mass Diffusivity	
J_w	Wall mass flux	$mol \cdot m \cdot s^{-1}$
$J_{R,i}$	Mean i-Reynolds Mass Flux Component	
$J'_{R,i}$	Instantaneous i-Reynolds Mass Flux	

	Component
$J_{D,i}$	Mean i-Fluctuating Diffusivity Mass Flux
	Component
$J'_{D,i}$	Instantaneous i- Fluctuating Diffusivity Mass
	Flux Component

Greek

σ_A	Turbulent Prandtl Number of the *A* variable

Dimensionless

$f(C)$	Variable concentration function
Sc	Molecular Prandtl number
$C^+ = \left(\langle C\rangle - C_w\right)/C_\tau$	Mean concentration
$c^+ = \sqrt{\langle C'C'\rangle}/C_\tau$	Root mean square concentration
$D^+ = \mathrm{Sc}D/\nu$	Mass Diffusivity
J_D^+	Mass flux due to variation of mass
	Diffusivity
J_{Re}^+	Reynolds Mass Flux
J_{lam}^+	Laminar Mass Flux
J_{tot}^+	Total Mass Flux

4.2 Mass diffusion equation

Mass diffusion equation for turbulent flow between parallel plates of an incompressible fluid, without chemical reactions, following Fick law and with mass diffusivity dependent on concentration is

$$\frac{\partial C}{\partial t}+u_i\frac{\partial C}{\partial x_i}=\frac{\partial}{\partial x_i}\left(D(C)\frac{\partial C}{\partial x_i}\right) \tag{4.1}$$

Assuming each instantaneous variable, as velocity components, mass diffusivity, *D,* and concentration, *C,* is the sum of an average and a fluctuating term, as, for example, for the concentration, *C*,

$$C=\langle C\rangle+C' \tag{4.2}$$

Introducing each variable into Eq. (4.1) it is obtained

$$\frac{\partial}{\partial t}\left(\langle C\rangle+C'\right)+\left(U_i+u_i'\right)\frac{\partial}{\partial x_i}\left(\langle C\rangle+C'\right)=\frac{\partial}{\partial x_i}\left(\left(\langle D\rangle+D'\right)\frac{\partial}{\partial x_i}\left(\langle C\rangle+C'\right)\right) \tag{4.3}$$

Equation (4.3) can be written as two separate equations after time averaging. Time average equation is

$$\frac{\partial\langle C\rangle}{\partial t}+U_i\frac{\partial\langle C\rangle}{\partial x_i}=\frac{\partial}{\partial x_i}\left(\langle D(C)\rangle\frac{\partial\langle C\rangle}{\partial x_i}-\langle u_i'C'\rangle+\langle D'(C)\frac{\partial C'}{\partial x_i}\rangle\right) \tag{4.4}$$

While concentration variance is

$$\begin{aligned}&\frac{\partial}{\partial t}\left(\frac{\langle C'C'\rangle}{2}\right)+U_i\frac{\partial}{\partial x_i}\left(\frac{\langle C'C'\rangle}{2}\right)=-\left(\langle u_i'C'\rangle+\langle D'(C)\frac{\partial C'}{\partial x_i}\rangle\right)\frac{\partial\langle C\rangle}{\partial x_i}+\\&\frac{\partial}{\partial x_i}\left(-\langle u_i'\frac{C'C'}{2}\rangle+\langle D'(C)\frac{\partial}{\partial x_i}\left(\frac{C'C'}{2}\right)\rangle+\langle D(C)\rangle\frac{\partial}{\partial x_i}\left(\frac{\langle C'C'\rangle}{2}\right)+\langle D'(C)C'\rangle\frac{\partial\langle C\rangle}{\partial x_i}\right)+\\&-\langle D(C)\rangle\langle\frac{\partial C'}{\partial x_i}\frac{\partial C'}{\partial x_i}\rangle-\langle D'(C)\frac{\partial C'}{\partial x_i}\frac{\partial C'}{\partial x_i}\rangle\end{aligned} \tag{4.5}$$

where is possible to distinguish the different terms.

Time average concentration equation, Eq. (4.4), has a form very similar to the instantaneous concentration equation. The terms transferring energy from small to large scales are two:

$$\langle u_i' C' \rangle - \langle D'(C) \frac{\partial C'}{\partial x_i} \rangle \tag{4.6}$$

The first one is due to velocity fluctuations while the second one has the traditional form of product of fluctuating mass diffusivity and gradient of fluctuating concentration.

Indicating the two terms as:

$$J_{R,i} = \langle C' u_i' \rangle \tag{4.7}$$

$$J_{D,i} = -\langle D'(C) \frac{\partial C'}{\partial x_i} \rangle \tag{4.8}$$

4.3 Modelling fluctuating mass diffusivity

Let model mass diffusivity taking into account different dependences on concentration, which can give an increase or a decrease. If mass diffusivity is linked to fluctuating concentration according to a linear relation

$$D(\langle C \rangle + C') \approx D(\langle C \rangle) + \left. \frac{dD}{dC} \right|_{\langle C \rangle} C' \tag{4.9}$$

and is assumed

$$\langle D(C) \rangle \approx D(\langle C \rangle) \tag{4.10}$$

it is obtained

$$D'(C) \approx \left. \frac{dD}{dC} \right|_{\langle C \rangle} C' \tag{4.11}$$

Considering the following two different relations between diffusivity and concentration

$$D_1(C) = A e^{BC} \tag{4.12}$$

and

$$D_2(C) = \frac{E}{F + C} \tag{4.13}$$

it is found, for Eq. (4.12)

$$D_1(C) \approx Ae^{B\langle C\rangle} + ABe^{B\langle C\rangle}C' = Ae^{B\langle C\rangle}(1 + BC'), \tag{4.14}$$

and, for Eq. (4.13)

$$D_2(C) \approx \frac{E}{F + \langle C\rangle} - \frac{E}{(F + \langle C\rangle)^2}C' = \frac{E}{F + \langle C\rangle}\left(1 - \frac{C'}{F + \langle C\rangle}\right) \tag{4.15}$$

The relative error can be defined as:

$$err = \frac{D_{exact} - D_{approx}}{D_{exact}} \tag{4.16}$$

For the expression given by Eq. (4.12), after substituting *C'* with C_{rms}, the error is then

$$err_1 = \left|1 - e^{-BC_{rms}}(1 + BC_{rms})\right| = \left|1 - e^{-\frac{C_{rms}}{\langle C\rangle}B\langle C\rangle}\left(1 + \frac{C_{rms}}{\langle C\rangle}B\langle C\rangle\right)\right| \tag{4.17}$$

which, under the hypothesis of 25% of turbulence, becomes

$$err_1 = \left|1 - e^{-\frac{1}{4}B\langle C\rangle}\left(1 + \frac{1}{4}B\langle C\rangle\right)\right| \tag{4.18}$$

and, under the typical values of B and $\langle C\rangle$ of [4.1], becomes lower than 10%.

For the expression given by Eq. (4.13) the error is

$$err_2 = \left|1 - \left(\frac{F + \langle C\rangle + C_{rms}}{F + \langle C\rangle}\right)\left(1 - \frac{C_{rms}}{F + \langle C\rangle}\right)\right| = \left|1 - \left(1 + \frac{C_{rms}}{F + \langle C\rangle}\right)\left(1 - \frac{C_{rms}}{F + \langle C\rangle}\right)\right| = \left|\frac{C_{rms}}{F + \langle C\rangle}\right|^2 = \left|\frac{\langle C\rangle}{F + \langle C\rangle}\frac{C_{rms}}{\langle C\rangle}\right|^2 \tag{4.19}$$

which is lower than 6% for a turbulence of 25%

$$err_2 = \frac{1}{16}\left|\frac{\langle C\rangle}{F+\langle C\rangle}\right|^2 \tag{4.20}$$

The term given by Eq. (4.8) becomes, using Eq. (4.11),

$$J_{D,i} = -\langle D'(C)\frac{\partial C'}{\partial x_i}\rangle = -\left.\frac{dD}{dC}\right|_{\langle C\rangle}\frac{\partial}{\partial x_i}\left(\frac{\langle C'C'\rangle}{2}\right) \tag{4.21}$$

4.4 Turbulence modelling

Equations (4.29) and (4.34) contain terms that can be modelled specifying the approach to solve the turbulent flow. The model chosen in the present work is the *k*-*ε* turbulence model improved by Nagano and Tagawa [4.23] (referred to as NT model in the following) which reproduces strictly the limiting behaviour of wall and free turbulence. In the NT model, the eddy viscosity relation $\nu_T \propto k^{1/2} l$ (being l large-scale) holds far from the wall where is determined by large scale energy-containing eddies, while the relation is $\nu_T \propto k^{1/2}\eta$ (4.being η is the Kolmogorov micro-scale) close to the wall where is determined by small-scale eddies, dominating mainly the dissipation process.

Using a Boussinesq type relation Eq. (4.4) becomes

$$\frac{\partial\langle C\rangle}{\partial t} + U_i\frac{\partial\langle C\rangle}{\partial x_i} = \frac{\partial}{\partial x_i}\left(\left(D(\langle C\rangle) + \frac{\nu_T}{\sigma_C}\right)\frac{\partial\langle C\rangle}{\partial x_i} + \left.\frac{dD}{dC}\right|_{\langle C\rangle}\frac{\partial}{\partial x_i}\left(\frac{\langle C'C'\rangle}{2}\right)\right) \tag{4.22}$$

while Eq. (4.5)

$$\begin{aligned}&\frac{\partial}{\partial t}\left(\frac{\langle C'C'\rangle}{2}\right) + U_i\frac{\partial}{\partial x_i}\left(\frac{\langle C'C'\rangle}{2}\right) = \left(\frac{\nu_T}{\sigma_C}\frac{\partial\langle C\rangle}{\partial x_i} - \left.\frac{dD}{dC}\right|_{\langle C\rangle}\frac{\partial}{\partial x_i}\left(\frac{\langle C'C'\rangle}{2}\right)\right)\frac{\partial\langle C\rangle}{\partial x_i} + \\ &\frac{\partial}{\partial x_i}\left(\left(D(\langle C\rangle) + \frac{\nu_T}{\sigma_{C'}}\right)\frac{\partial}{\partial x_i}\left(\frac{\langle C'C'\rangle}{2}\right) + 2\left.\frac{dD}{dC}\right|_{\langle C\rangle}\frac{\langle C'C'\rangle}{2}\frac{\partial\langle C\rangle}{\partial x_i}\right) - f_{2,\langle C'C'\rangle}\frac{D(\langle C\rangle)}{\nu}\frac{\langle C'C'\rangle}{2}\frac{\varepsilon}{k}\end{aligned} \tag{4.23}$$

Equations are rewritten in non-dimensional form before to be solved numerically.

Mean concentration equation is

$$\frac{\partial C^+}{\partial t^+} + U_i^+ \frac{\partial C^+}{\partial x_i^+} = \frac{\partial}{\partial x_i^+}\left(\left(\frac{1}{\mathrm{Sc}} D^+ + \frac{\nu_\tau^+}{\sigma_T}\right)\frac{\partial C^+}{\partial x_i^+} + \frac{1}{\mathrm{Sc}}\frac{dD^+}{dC^+}\frac{\partial}{\partial x_i^+}\left(\frac{c^+c^+}{2}\right)\right) \tag{4.24}$$

Concentration variance equation is

$$\begin{aligned}\frac{\partial}{\partial t^+}\left(\frac{c^+c^+}{2}\right) + U_i^+ \frac{\partial}{\partial x_i^+}\left(\frac{c^+c^+}{2}\right) &= \left(\frac{\nu_\tau^+}{\sigma_T}\frac{\partial C^+}{\partial x_i^+} - \frac{1}{\mathrm{Sc}}\frac{dD^+}{dC^+}\frac{\partial}{\partial x_i^+}\left(\frac{c^+c^+}{2}\right)\right)\frac{\partial C^+}{\partial x_i^+} + \\ \frac{\partial}{\partial \tilde{x}_i}\left(\left(\frac{1}{\mathrm{Sc}} D^+ + \frac{\nu_\tau^+}{\sigma_T}\right)\frac{\partial}{\partial \tilde{x}_i}\left(\frac{c^+c^+}{2}\right) + \frac{1}{\mathrm{Sc}} 2\frac{dD^+}{dC^+}\frac{c^+c^+}{2}\frac{\partial C^+}{\partial x_i^+}\right) &- \frac{1}{\mathrm{Sc}} f_{2,\langle C'C'\rangle} D^+ \frac{c^+c^+}{2}\frac{\varepsilon^+}{k^+}\end{aligned} \tag{4.25}$$

Details of non-dimensional process are in Appendix A2.

4.5 Numerical solution and boundary conditions

Conservation equations are solved using the finite volume method (FVM), with a HYBRID differential scheme for velocity, temperature and turbulent variables, in a uniform staggered Cartesian grid system, employing iterative SIMPLER algorithm. Non-linear algebraic equations over the flow domain are solved iteratively with the Thomas algorithm (TDMA) method. Details of the numerical scheme can be found in [4.24-4.25]. The numerical approach adopted here is the classical one.

The problem is more complicated with a mixture of two species interacting. One method of the literature to face this problem is that of Shapiro and Drikakis [4.26] where are presented several formulations of the characteristics-based schemes, in the framework of an artificial compressibility method, for variable-density incompressible flow employing the Godunov-type discretization. The same authors presented in [4.27] a multigrid implementation and numerical studies for variable density flow. Others examples of numerical methods can be found in [4.28-29]. Thornber et al. proposed in [4.28] a simple modification of the variable reconstruction

process within finite volume schemes to allow improved solution of low Mach number perturbations for use in mixed compressible/incompressible flows. Allaire et al. [4.29] proposed in [4.29] a diffuse-interface method for the simulation of interfaces between compressible fluids with general equations of state. A mixture model is given for the transition region. The conservation equations are written for the mass of each fluid and for the total momentum and energy of the mixture and an advection equation for the volume fraction of one of the two fluids. A Roe-type numerical scheme for the simulation of the model was proposed.

Several theoretical expressions have been proposed for the mass diffusivity dependent on concentration, as shown in [4.1] and [4.30]. Most of them have been proposed by Barrer [4.30] for flow across membranes but also for solutions. In the present work the law employed is

$$\begin{cases} D(C) = D_0\left(1 + f(C)\right) \\ f(C) = \dfrac{A_D + B_D e^{-\frac{C}{C_0}}}{D_0} - 1 \\ D_0 = A_D + B_D \end{cases} \tag{4.26}$$

Some example of solutions following this law can be found in [4.9]. The Schmidt number employed to perform the simulations is referred to as mass diffusivity D_0.

The case studied in the present paper is relative to a solute, considered as a passive scalar and obeying to Eq. (4.26), spreading in a fully developed turbulent flow between parallel plates at $\mathrm{Re}_\tau = 190$, based on friction velocity u_τ, channel half width $D_h/2$ and kinematic viscosity ν. In order to investigate the dependence of the solutions on the Schmidt number the simulations have been performed at five different Schmidt numbers: 1, 3, 10, 25 and 49. It can be remarked that these values, although smaller than those of the literature [4.2-4.16], have been used in order to make qualitative comparisons with the results presented in [4.21].

The simulations are performed on a rectangular grid of uniform spacing, $dy^+ = 0.4; dx^+ = 4.0$, with 800 cells in the direction normal to the wall and 400 cells in the longitudinal direction. On the inlet the solute has uniform mean concentration and concentration variance. The solute spreads due to turbulent, molecular and fluctuating mass diffusivity. The magnitudes of the mass fluxes are evaluated to show the importance of the new mass flux introduced in the model.

Boundary conditions at the wall ($y = 0$) for velocity field and k-ε are:

$$\begin{cases} U_i^+ = 0, \forall i \\ k^+ = 0 \\ \varepsilon^+\big|_w = 2\left(\partial\sqrt{k^+}/\partial x_i^+\right)^2\Big|_w \end{cases} . \tag{4.27}$$

Wall boundary conditions for concentration are:

$$\begin{cases} C^+\big|_w = 0 \\ c^+c^+\big|_w = 0 \end{cases} \tag{4.28}$$

which are slightly different than in [4.21]. The plates are permeable walls with constant concentration and the simulations are carried out until fully developed profiles are obtained.

4.6 Results

Figures 4.1-4.2 present the mean concentration and the root mean square of concentration fluctuations for Sc = 1–49. The shape and the trend of the curves are in qualitative agreement to [4.21]. The different values are due to the different boundary conditions and the slightly higher turbulent Reynolds number.

Figure 4.2 shows that the maximum of the concentration fluctuation is higher and closer to the wall for a bigger Sc number. Similar trends are reported by Kawamura et al. [4.31] for a channel flow at $\mathrm{Re}_\tau = 180$, a uniform heating from both walls and for Sc number ranging from Sc = 0.025 to Sc = 5.

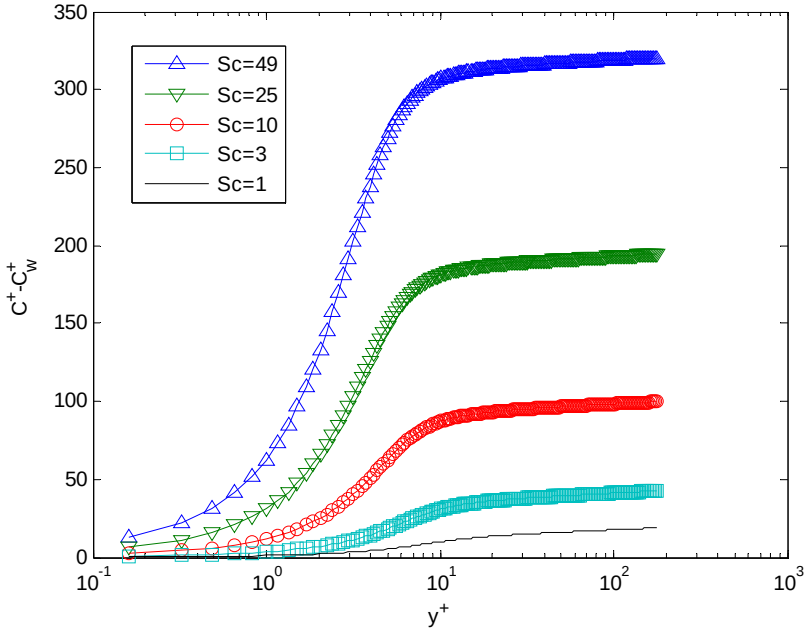

Figure 4.1: Mean concentration

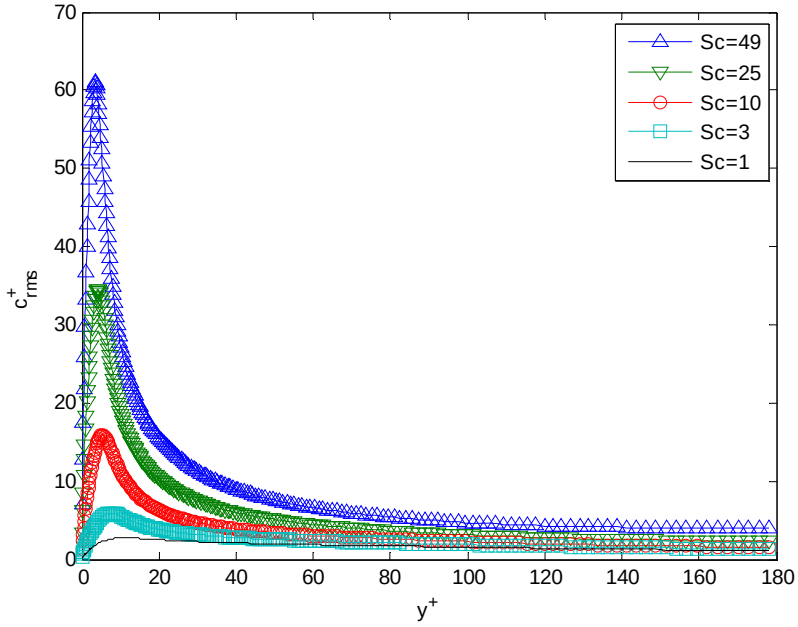

Figure 4.2: Root mean square of concentration fluctuation

Figures 4.3-4.6 show the terms of the transport equation for the scalar variance at different Schmidt numbers. The maximum of each transport term moves closer to the wall with the increase of the Schmidt number, differently from what reported in [4.21] where the maximum of the production term is present at $y^+ = 2$ for all the Schmidt numbers. Turbulent and molecular diffusion at small Sc numbers are important only close to the wall, in agreement to [4.21]. For higher Sc numbers (Sc = 10–49) turbulent and molecular diffusion terms are more important and even comparable to the dissipation term close to the wall, as observed in [4.31] for Sc =5. The turbulent diffusion term becomes more important at higher Sc numbers and is of the same order of magnitude (or even larger) than the production term between $20 < y^+ < 80$ for Sc =25 and Sc =49. This is an indication that within this distance from the wall the main part of the scalar variance stems from turbulent transport.

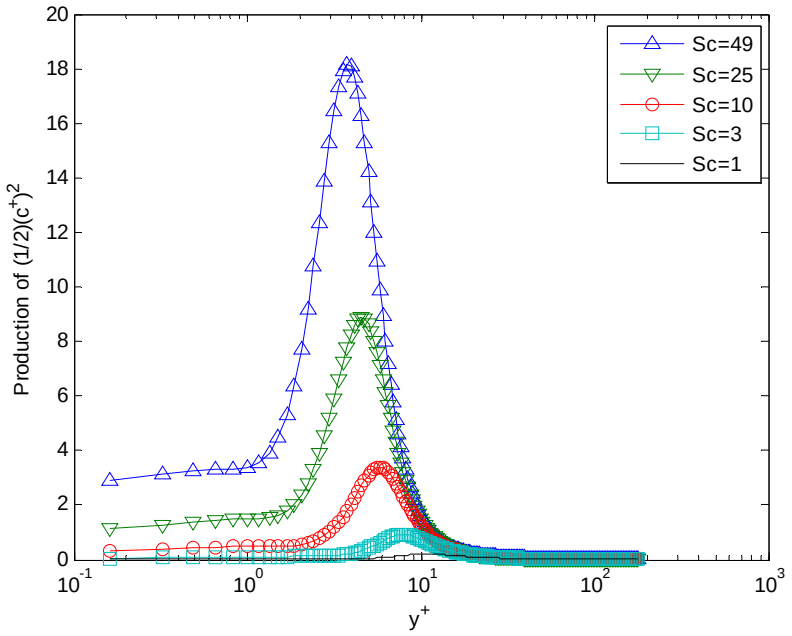

Figure 4.3: Production of concentration variance

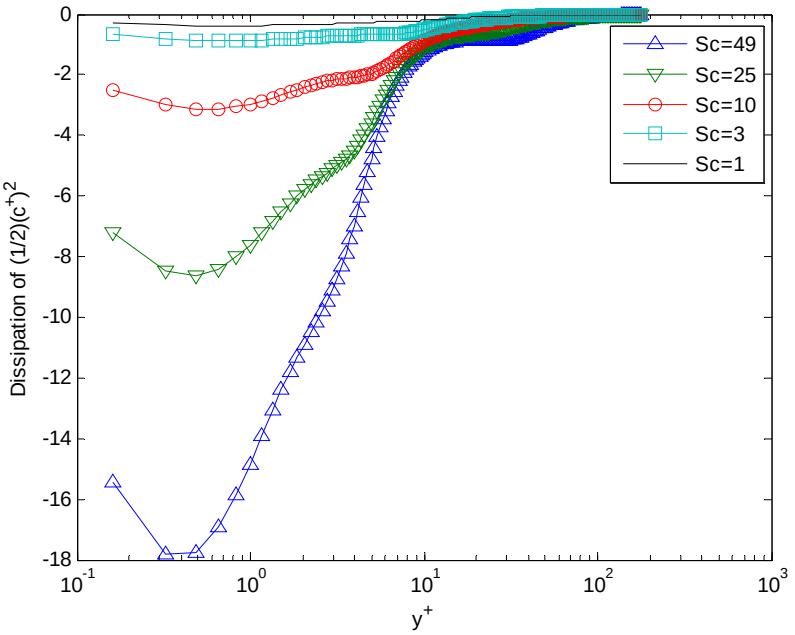

Figure 4.4: Dissipation of concentration variance

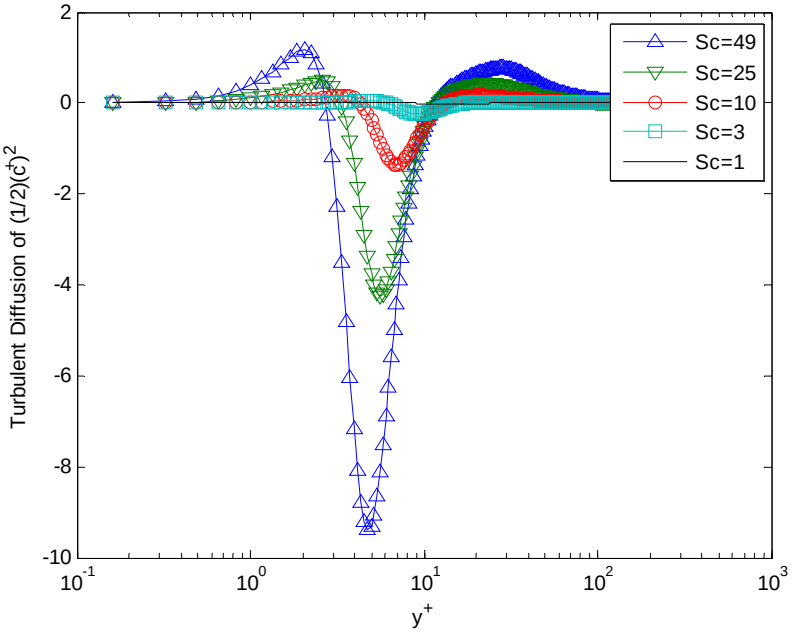

Figure 4.5: Turbulent diffusion of concentration variance

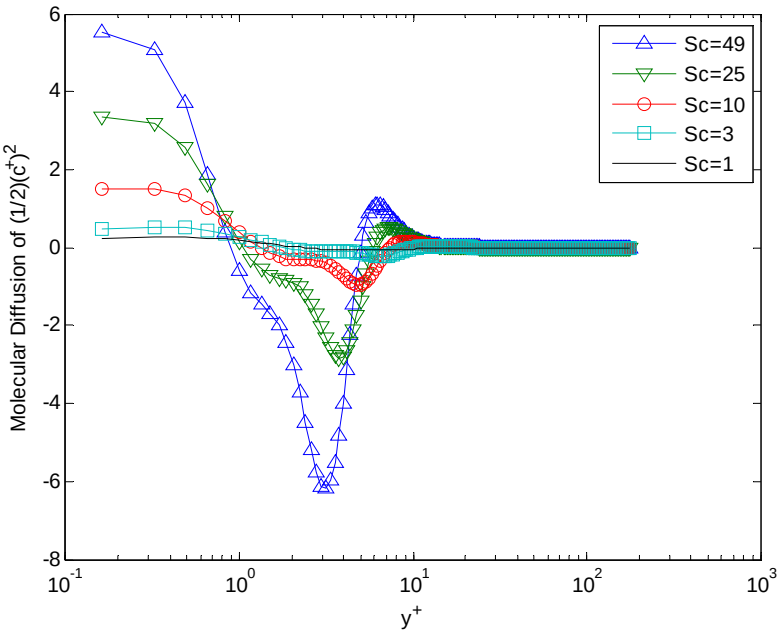

Figure 4.6: Molecular diffusion of concentration variance.

Figure 4.7 reports the trend of the new term for the concentration variance diffusion, which is important close to the wall, between $0 < y^+ < 10$, also if it is slightly lower than the other two diffusion terms.

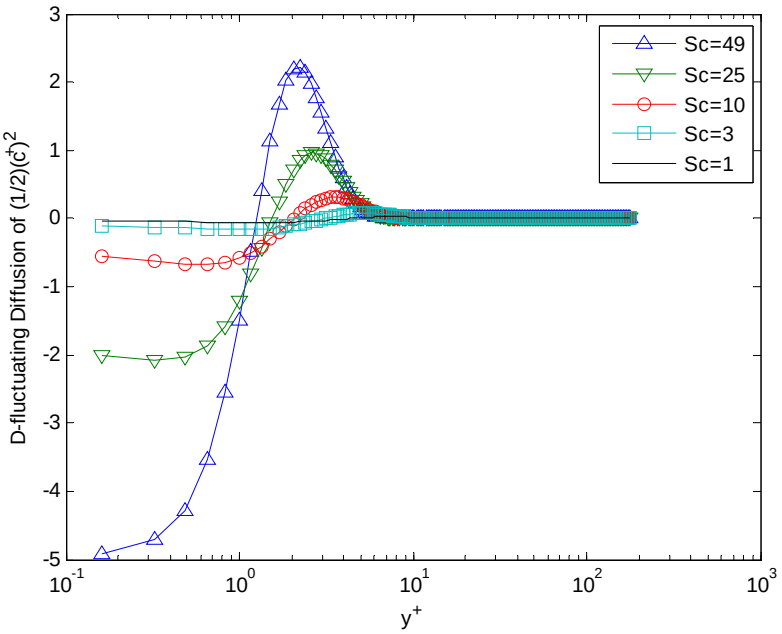

Figure 4.7: D-fluctuating diffusion of concentration variance

Figure 4.8 presents the budget of concentration variance at Sc=49, which is in agreement to [4.29]. Moreover it can be seen that for $y^+ > 20$ the contribution of all terms is negligible, with an approximate balance between production and dissipation.

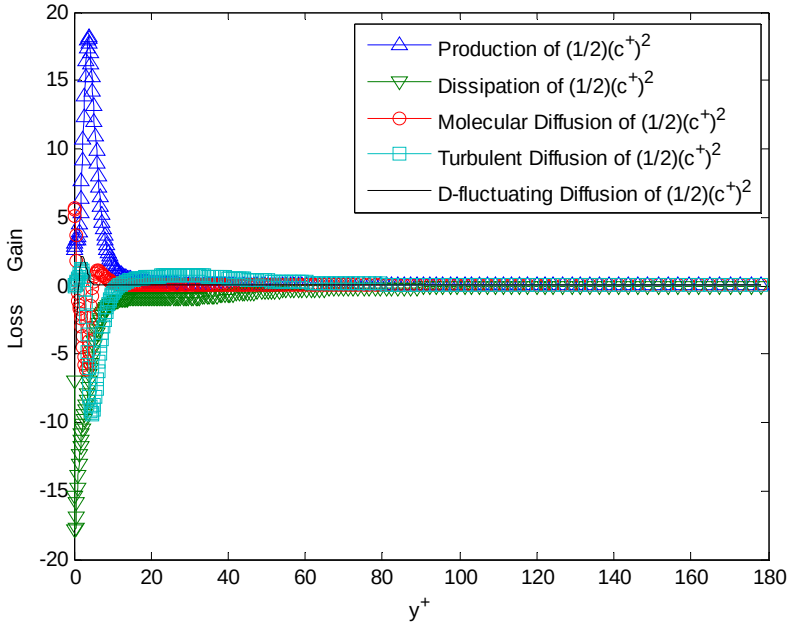

Figure 4.8: Budget of concentration variance for Sc=49.

The time scale ratio and the concentration variance time scale are reported in Fig. 4.9-4.10 with a double logarithmic scale in order to evidence the detailed structure close to the wall. The timescale ratio *r* approaches the Sc number at the wall, as pointed out in [4.31] and [4.21]. In the centre of the channel the timescale ratio is equal to 1, differently from the results of [4.21] where its value is slightly higher. This difference can be attributed to the RANS modelling simulation which must be simple to produce enough accurate results with a smaller computational effort. The time scale ratio and the concentration variance time scale are predicted with a trend similar to that found in [4.21] with DNS until $y^+=20$. At higher distances the differences are bigger.

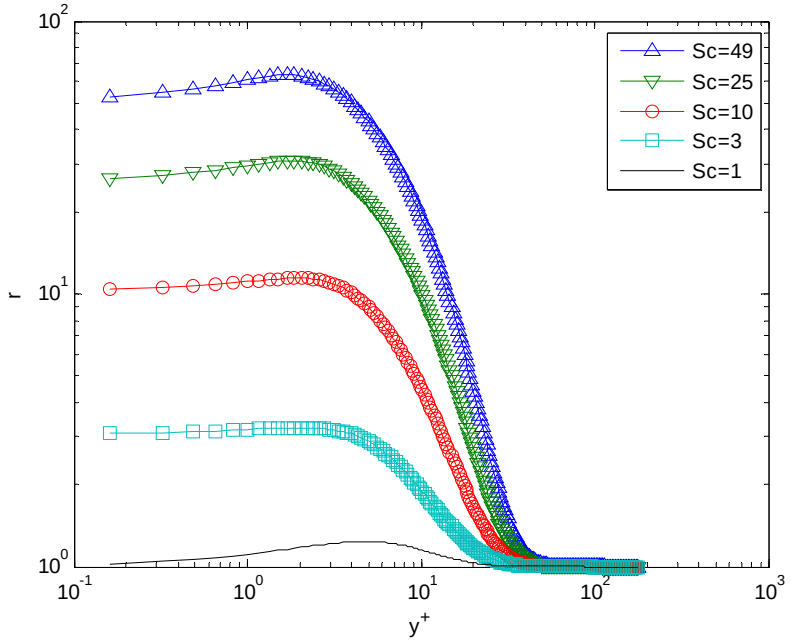

Figure 4.9: Time scale ratio

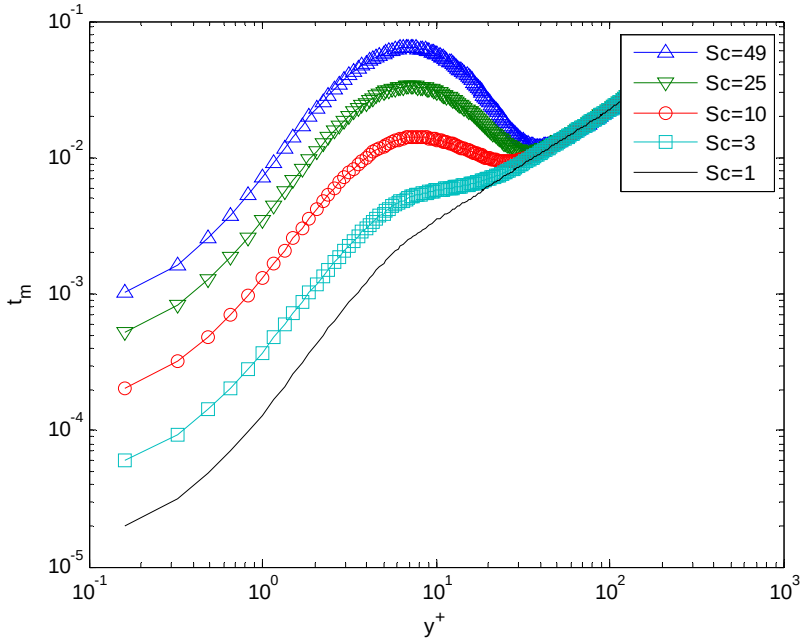

Figure 4.10: Concentration variance time scale

Diffusive mass fluxes are reported in Figures 4.11-4.14 versus the wall distance. The contribution of the diffusive mass fluxes to the total one becomes negligible in the core of the

flow, while the diffusive sub-layer, where the contribution to the total mass flux is important becomes thinner for bigger Sc numbers. For greater Sc numbers the maximum of the turbulent mass fluxes is higher and closer to the wall, while in the core of the duct the influence of the Schmidt number is negligible. A similar behaviour of the D-fluctuating mass flux is shown in Figure 4. 13. For $y^+ > 10$ the contribution of the new mass flux is negligible, also if very close to the wall, i.e. $y^+ < 3$, it is greater than the turbulent one.

It is necessary to remark that the Schmidt numbers employed in the present work are smaller than those reported in [4.2-4.16], with the conclusion that at greater Schmidt numbers the maximum could be higher.

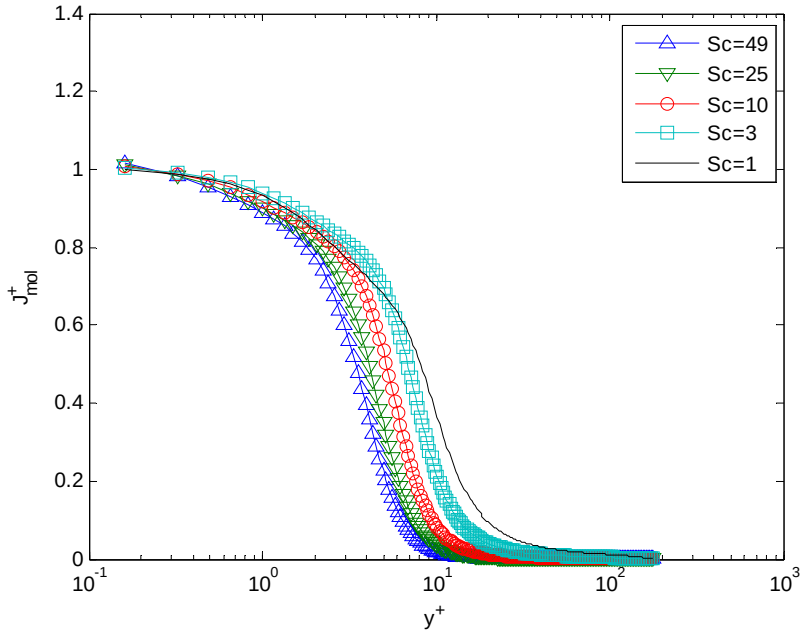

Figure 4.11: Molecular mass flux

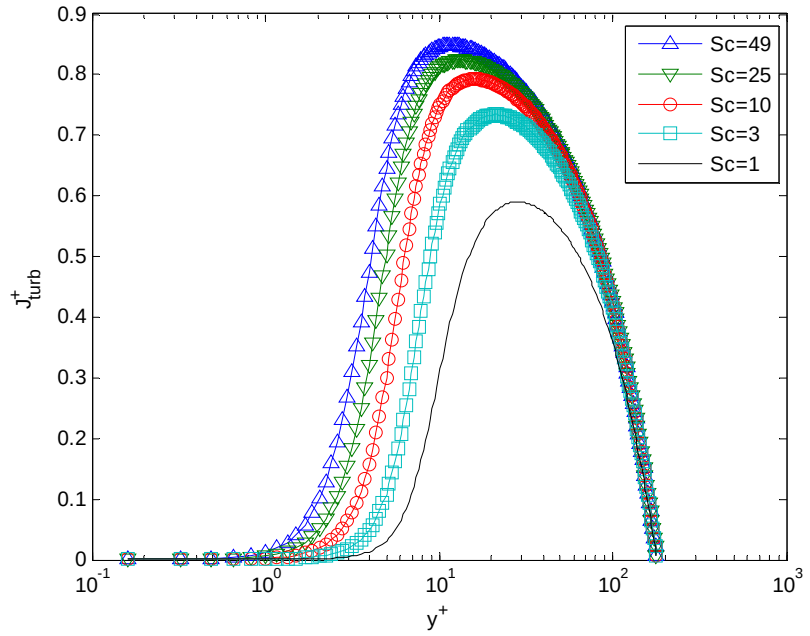

Figure 4.12: Turbulent mass flux

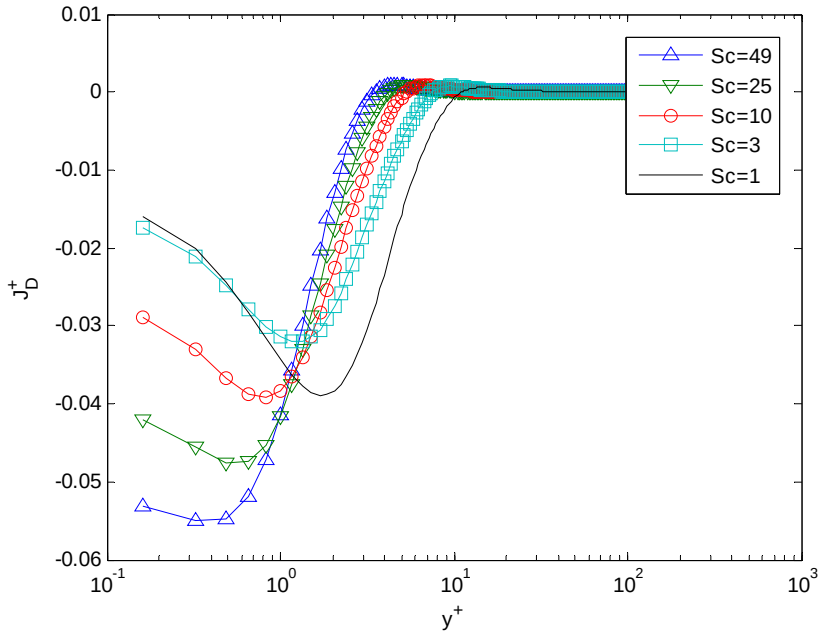

Figure 4.13: D-fluctuating mass flux

Figure 4.14 presents the mass fluxes for Sc=49 which shows the relative importance of each term.

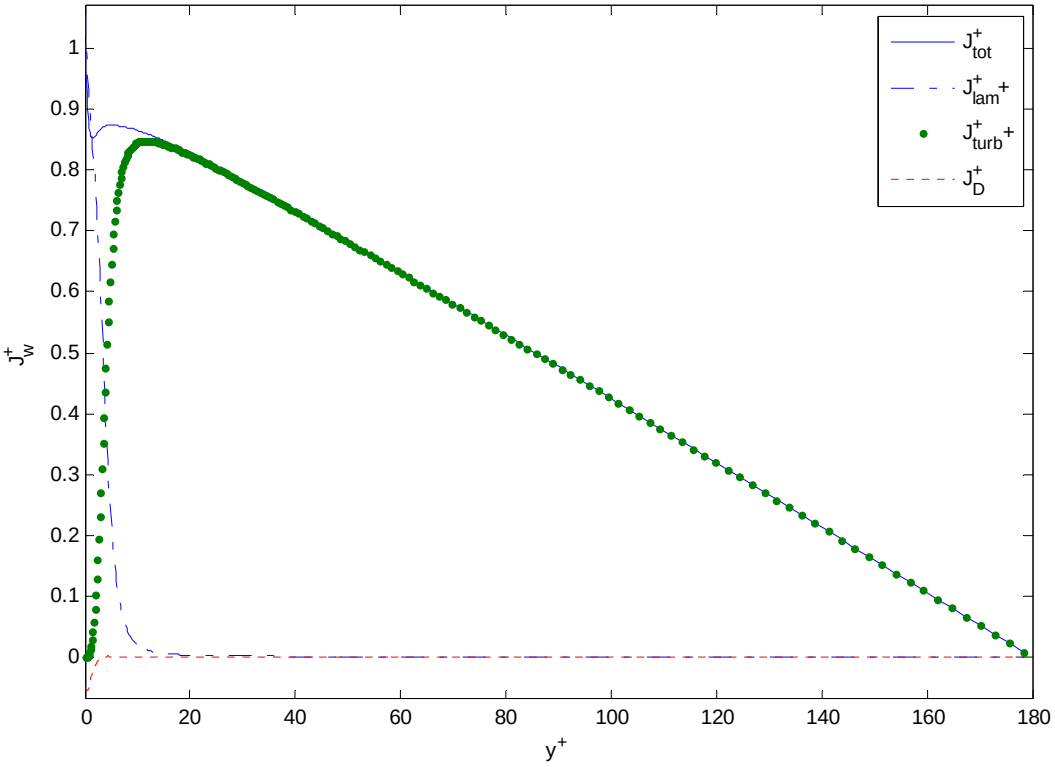

Figure 4.14: Mass fluxes for Sc=49.

4.7 Discussion on the model

It is important to remind that the contribution of the new mass flux on the mass diffusion process is dependent on the relation linking mass diffusivity and concentration. Higher is the variation of the mass diffusivity with the concentration and higher is the contribution of the new mass flux on the diffusion process. In other words the new term, given by Eq. (28), can allow a decrease or an increase of mass transfer according to the relation between mass diffusivity and concentration.

The present work investigated numerically the equations developed in order to evaluate the effect of the new terms on the concentration distribution for turbulent flow between parallel plates at five different Schmidt numbers, which are quite smaller than those governing a solute

diffusion process. For a greater Schmidt number process it is present a thinner boundary layer and a bigger gradient of concentration at the wall. The production of concentration variance is proportional to the mean concentration gradient, so that for a greater mean concentration the concentration variance is greater as well as the new mass flux, as shown theoretically by Tennekes and Lumley [4.20] and numerically by the DNS results of Hasegawa [4.22].

The new production term appearing in the transport equation of concentration variance, Eq. (4.37), has different influence from the energy point of view. Indeed, is difficult to say whether the new production term is a productive or dissipative because production term is always positive while dissipation term is always negative and its behaviour is dependent whether the mass diffusivity decreases or increases with the concentration. For this reason the term is treated as an increase or decrease of production. Since this new production term is proportional to the mean concentration gradient and the Schmidt number is high, it increases the new mass flux if the mass diffusivity increases with concentration or reduces if the mass diffusivity decreases with concentration.

The numerical results of the present paper for five different Schmidt numbers show that the contribution of the new mass flux term increases with the Schmidt number. It is then expected that in the diffusion of real substances with a higher Schmidt number the importance of the new term will have a greater influence on the final concentration distribution. Also the type of boundary condition and the Reynolds number assumed in this paper have a relative importance for the new turbulent mass flux.

4.8 Conclusions

The present theoretical model investigates the influence of the variable mass diffusivity with concentration on the concentration distribution in a fluid in turbulent flow between parallel plates. The application of a Reynolds-type average with variable mass diffusivity in the equation of instantaneous mass concentration allow to show the presence of a new term in the average concentration equation and two new terms in the concentration variance equation.

The mass flux due to variable mass diffusivity is related to the concentration variance. The equation of concentration variance and the equation of average mass concentration can be solved coupled with the turbulent kinetic energy and the dissipation of kinetic energy. The numerical solution of the above mentioned equations requires the solution of an additional equation compared to the case of constant mass diffusivity.

RANS numerical simulation of passive scalar transport in fully developed turbulent channel flow at $\mathrm{Re}_\tau = 190$ and $1 \le \mathrm{Sc} \le 49$ are performed with a Finite Volume HYBRID differential scheme on an uniform grid. The maximum moves closer to the wall and the sub-layer becomes thinner with the increase of the Sc number, due to the growth of mean and concentration variance gradient which leads to an increase of the new mass flux. Detailed analysis of the transport equation for the scalar variance reveals that all terms are important in the range $0 < y^+ < 10$, except turbulent diffusion and dissipation terms which are important also in the range of $10 < y^+ < 100$, [4.32-4.33].

References of Chapter 4

[4.1] J. Crank. 1990. The Mathematics of Diffusion. Oxford University Press, London.

[4.2] D.P. Rao and G.H. Rao. The Effect of Concentration Dependent Diffusivities on Mass Transfer Coefficients. *Letters in Heat and Mass Transfer.* 1980: 7 (4.93-170).

[4.3] J. Carlfors and R. Rymdén. Self diffusion of small molecules in aqueous solution of poly(4.vinylpyrrolidone). *Polymer*. 1985: 26 (4.840-944).

[4.4] K. R. Harris, T. Goscinska and H. N. Lam. Mutual Diffusion Coefficients for the Systems Water-Ethanol and Water-Propan-1-ol at 25 °C. *J. Chem. Soc. Faraday Trans*. 1993: 89(4.12), (4.1269-1974).

[4.5] J. J. Tanahatoe and M. E. Kuil. Molar Mass Dependence of the Apparent Diffusion Coefficient of Flexible Highly Charged Polyelectrolytes in the Dilute Concentration Regime. *J. Phys. Chem. A* 1997:101(4.7389-8394).

[4.6] H. C. Gao, R. X. Zhu, X. Y. Yang, S. Z. Mao, S. Zhao, J. Y. Yu, and Y. R. Du. Properties of polyethylene glycol (4.16) lauryl ether with cetyltrimethylammonium bromide in mixed aqueous solutions studied by self-diffusion coefficient NMR. *Journal of Colloid and Interface Science* 2004:273 (4.526–631).

[4.7] A. J.M. Valente, A. C. F. Ribeiro, V. M. M. Lobo, and A. Jiménez. Diffusion coefficients of lead (4.II) nitrate in nitric acid aqueous solutions at 298 K. *Journal of Molecular Liquids*. 2004:111 (4.33–38).

[4.8] L. C. Chang, T. I. Lin and M. H. Li. Mutual Diffusion Coefficients of Some Aqueous Alkanolamines Solutions. *J. Chem. Eng. Data.* 2005: 50 (4.67-84).

[4.9] T. Grossmann and J. Winkelmann. Ternary Diffusion Coefficients of Glycerol + Acetone + Water by Taylor Dispersion Measurements at 298.15 K. *J. Chem. Eng. Data.* 2005:50 (4.1396-1403).

[4.10] G. Wittko and W. Köhler. Influence of isotopic substitution on the diffusion and thermal diffusion coefficient of binary liquids. *Eur. Phys. J.* 2006: E 21 (4.213-291).

[4.11] H. Latrous, R. Besbes and N. Ouerfelli. Self-diffusion coefficients and structure of the trivalent f-element ions, Eu, Gd, Am, Bk, Cf and Es in aqueous diluted and concentrated solutions. *Journal of Molecular Liquids*. 2008: 138 (4.27–54).

[4.12] N. Ouerfelli, H. Latrous, M. Ammar. An equation for self-diffusion coefficients of the trivalent lanthanide ion 152Eu (4.III) in concentrated asymmetrical 3:1 electrolyte aqueous solutions at pH 2.50 and at 298.15 K. *Journal of Molecular Liquids*. 2009: 146 (4.52–59).

[4.13] S. H. Lin. Concentration-dependent diffusion of dye in reactive dyeing systems. *Journal of Applied Polymer Science*. 1992: 44-10 (4.1743–1749).

[4.14] Y. Tsunashima, T. Hashimoto and T. Nakano. First and Second Concentration-Dependent Coefficients of Translational Diffusion and Sedimentation for Poly(4.R-methylstyrene) in a Good Solvent. *Macromolecules*. 1996: 29 (4.3475-3484).

[4.15] M. Kuntz and P. Lavall´ee. Anomalous diffusion is the rule in concentration-dependent diffusion processes. *J. Phys. D: Appl. Phys.* 2004:37 (4.L5–L8).

[4.16] A. K. Gaigalas, V. Reipa, J. B. Hubbard, J. Edwards and J. Douglas. A non-Perturbative Relation between the Mutual Diffusion Coefficient, Suspension Viscosity, and Osmotic Compressibility: Application to Concentrated Protein Solutions. *Chemical Engineering Science.* 1995: 50-7 (4.1107-1114).

[4.17] W. R. Bowen, P. M. Williams. Prediction of the rate of cross-flow ultra filtration of colloids with concentration-dependent diffusion coefficient and viscosity theory and experiment. *Chemical Engineering Science*. 2001: 56 (4.3083-3099).

[4.18] M. B. Gorbet, M. V. Sefton. Biomaterial-associated thrombosis: roles of coagulation factors, complement, platelets and leukocytes. *Biomaterials*. 2004: 25 (4.5681–5703).

[4.19] T. Gemci, B. Shortall, G. M. Allen, T. E. Corcoran and N. A. Chigier. A CFD study of the throat during aerosol drug delivery using heliox and air. *Aerosol Science*. 2003: 34 (4.1175–1192).

[4.20] H. Tennekes and J. L. Lumley. 1972. A First Course in Turbulence, MIT Press, Cambridge.

[4.21] F. Schwertfirm and M. Manhart. DNS of passive scalar transport in turbulent channel flow at high Schmidt numbers. *International Journal of Heat and Fluid Flow*. 2007: 28 (4.1204–1214).

[4.22] Y. Hasegawa and N. Kasagi. Effects of interfacial velocity boundary condition on turbulent mass transfer at high Schmidt numbers. *International Journal of Heat and Fluid Flow*. 2007: 28 (4.1192–1203).

[4.23] Y. Nagano and M. Tagawa.. An improved k-ε model for boundary layer flows, *J. Fluids Eng.* 1990: 112 (4.33—39).

[4.24] S. V. Patankar. *Numerical Heat Transfer and Fluid Flow.* 1st Edition. Hemisphere Publishing Corporation, 1980.

[4.25] H. K. Versteeg and W. Malalasekera. *Introduction to computational fluid dynamics. The finite volume method*, 1st Edition, Longman, 1995.

[4.26] E. Shapiro and D. Drikakis. Artificial compressibility, characteristics-based schemes for variable density, incompressible, multi-species flows. Part I. Derivation of different formulations and constant density limit *Journal of Computational Physics* 210 (4.1305) 584–607.

[4.27] E. Shapiro and D. Drikakis. Artificial compressibility, characteristics-based schemes for variable-density, incompressible, multispecies flows: Part II. Multigrid implementation and numerical tests *Journal of Computational Physics* 210 (4.1305) 608–631.

[4.28] B. Thornber, A. Mosedale, D. Drikakis, D. Youngs and R. J. R. Williams. An improved reconstruction method for compressible flows with low Mach number features. *Journal of Computational Physics* 227 (4.1308) 4873–4894

[4.29] G. Allaire, S. Clerc, and S. Kokh. A Five-Equation Model for the Simulation of Interfaces between Compressible Fluids. *Journal of Computational Physics* 181, 577–616 (4.1302).

[4.30] R. M. Barrer. *Proc. Phys. Soc. London.* 1946: 58 (4.321).

[4.31] Kawamura, H., Ohsaka, K., Abe, H., Yamamoto, K., 1998. DNS of turbulent heat transfer in channel flow with low to medium-high Prandtl number fluid. Int. J. Heat Fluid Flow 19, 482–491.

[4.32] F. Gori, A. Boghi. On a New Passive Scalar Equation with Variable Mass Diffusivity. IMECE2008, October 31-November 6,2008, Boston Massachusset, USA

[4.33] F. Gori, A. Boghi. On a New Passive Scalar Equation with Variable Mass Diffusivity: Flow between Parallel Plates, submitted paper.

Chapter 5:

ON A NEW TURBULENT ENERGY EQUATION WITH VARIABLE THERMAL CONDUCTIVITY

5.1 Introduction

The fluids used as cooler in thermal plants with very high heat fluxes range in a wide spectrum of Prandtl numbers. Liquid metals have been widely used after World War II as coolers in nuclear power plants. These fluids have a very low Prandtl number because their thermal conductivity is very high. One of the first approaches to the liquid metals heat transfer has been the analogy between momentum transport and heat transfer with some modifications of the Reynolds analogy [5.1]. The classical approach to solve the problem of predicting heat transfer in liquid metals has been the use of empirical expressions, as reported in [5.2].

Because of the large scatter between experimental data and empirical predictions, due to the scale separation between momentum and heat transfer [5.3], it has been suggested to modify the turbulent Prandtl number on empirical basis [5.4], while several models have been reviewed in [5.5]. With the use of modern type computers the approach to the prediction of heat transfer to liquid metals has incorporated the use of the turbulent Prandtl number in the turbulent models. One of the approach of this kind [5.6] has been followed by [5.7-8] as reviewed recently [5.9].

The cooling of nuclear reactors with molten salts with high Prandtl numbers has been the subject of several papers, as reviewed in [5.10], due to the importance of the convective and turbulent heat transfer. The use of these molten salts is also related to the radioactive and toxic properties [5.11]. The enhancement of heat transfer with molten salts has been proposed in [5.12]. A special kind of molten salts, called Flibe, has been investigated with the DNS approach [5.13]. Fluids with high Prandtl number have been used in MHD, i.e. subject to magnetic fields, in order to optimize the design of MHD instruments [5.14]. The investigation pointed out an increase of the turbulent diffusivity close to the free surface and the increase of heat flux and temperature fluctuations with the increase of the Prandtl number.

Molten salts are actually used also in solar plants because of the economical evaluation of hybrid solar plants [5.15]. Molten salts are used in a Japanese project named "Solar Hybrid Fuel Project" with the solar concentration [5.16]. Molten salts like sodium and potassium nitrates are proposed in parabolic solar concentrators and power towers [5.17].

In fluids with high Prandtl number the smallest scale of the temperature fluctuation is inversely proportional to the square root of the molecular Prandtl number, which means the temperature fluctuations increase with the Prandtl number [5.3]. The description of turbulence in liquid metals needs the knowledge of the temperature fluctuations which have a temporal scale different from the velocity one. The temperature fluctuations are high in fluids with high Prandtl numbers, as shown by a DNS study with different Prandtl number fluids [5.18]. Among the fluids with high Prandtl number, a special importance is given to non-Newtonian fluids which present a reduction in heat transfer. A recent DNS study [5.19] showed an increase of the temperature fluctuations and a reduction of the velocity fluctuations perpendicular to the wall.

Besides the temperature fluctuations, it is important to recall the importance of the variation of the fluid properties with the temperature, which has been usually considered in laminar flow. Only few works have dealt with this variability in turbulent flow [5.20-5.21] which has been recently investigated with a model based on the Reynolds stresses [5.22-5.25].

One of the main criticisms to the previous models is that the equations are previously deduced with the assumption of constant physical properties and later on the dependence on the temperature is introduced. The present work is aimed to study the energy equation with temperature dependent thermal conductivity.

Nomenclature for Heat Transfer Model

Symbol	**Definition**	**SI Unit**
Latin		
c_p	Specific heat at constant pressure	$J\,kg^{-1}K^{-1}$
q_w	Wall heat flux	$W\cdot m^{-2}$
$\vec{\dot{q}}_R$	Mean Reynolds heat flux	$W\cdot m^{-2}$
$\vec{\dot{q}}'_R$	Instantaneous Reynolds heat flux	$W\cdot m^{-2}$
$\vec{\dot{q}}_\lambda$	Mean Heat flux due to variation of thermal conductivity	$W\cdot m^{-2}$
$\vec{\dot{q}}'_\lambda$	fluctuating Heat flux due to variation of thermal conductivity	$W\cdot m^{-2}$
T	Instantaneous temperature	K
$T_\tau = q_w \big/ \left(\rho c_p u_\tau\right)$	Friction temperature	K

T_w	Wall temperature	K
$\langle T \rangle$	Mean temperature	K
T'	Fluctuating temperature	K
$\sqrt{\langle T'T' \rangle}$	Root mean square temperature	K

Greek

λ	Instantaneous Thermal Conductivity	$W \cdot m^{-1} \cdot K^{-1}$
$\langle \lambda \rangle$	Mean Thermal Conductivity	
λ'	fluctuating Thermal Conductivity	

Dimensionless

Pr	Molecular Prandtl number
$\dot{q}_\lambda^+$	Heat flux due to variation of thermal conductivity
$\Theta^+ = \left(\langle T \rangle - T_w\right) / T_\tau$	Mean temperature
$\theta^+ = \sqrt{\langle T'T' \rangle} / T_\tau$	Root mean square temperature
$\lambda^+ = \mathrm{Pr}\, \lambda / \left(\rho c_p \nu\right)$	Thermal conductivity

5.2 Energy conservation equations

Let consider a fluid in turbulent flow in a two dimensional domain with the thermal conductivity dependent on the temperature

$$\rho c\frac{\partial T}{\partial t}+\rho cu_i\frac{\partial T}{\partial x_i}=\frac{\partial}{\partial x_i}\left(\lambda(T)\frac{\partial T}{\partial x_i}\right) \tag{5.1}$$

Assuming the temperature is made of a time average and a fluctuating component

$$T=\langle T\rangle+T' \tag{5.2}$$

Eq. (5.1) becomes

$$\rho c\frac{\partial}{\partial t}\left(\langle T\rangle+T'\right)+\rho c\left(U_i+u_i'\right)\frac{\partial}{\partial x_i}\left(\langle T\rangle+T'\right)=\frac{\partial}{\partial x_i}\left(\left(\langle\lambda\rangle+\lambda'\right)\frac{\partial}{\partial x_i}\left(\langle T\rangle+T'\right)\right) \tag{5.3}$$

Equation (5.3) can be split in two equations: the first one contains the time average temperature

$$\rho c\frac{\partial\langle T\rangle}{\partial t}+\rho cU_i\frac{\partial\langle T\rangle}{\partial x_i}=\frac{\partial}{\partial x_i}\left(\langle\lambda(T)\rangle\frac{\partial\langle T\rangle}{\partial x_i}-\rho c\langle u_i'T'\rangle+\langle\lambda'(T)\frac{\partial T'}{\partial x_i}\rangle\right) \tag{5.4}$$

While temperature variance is

$$\begin{aligned}&\rho c\frac{\partial}{\partial t}\left(\frac{\langle T'T'\rangle}{2}\right)+\rho cU_i\frac{\partial}{\partial x_i}\left(\frac{\langle T'T'\rangle}{2}\right)=-\left(\langle\rho cu_i'T'\rangle+\langle\lambda'(T)\frac{\partial T'}{\partial x_i}\rangle\right)\frac{\partial\langle T\rangle}{\partial x_i}\\&\frac{\partial}{\partial x_i}\left(-\langle\rho cu_i'\frac{T'T'}{2}\rangle+\langle\lambda'(T)\frac{\partial}{\partial x_i}\left(\frac{T'T'}{2}\right)\rangle+\langle\lambda(T)\rangle\frac{\partial}{\partial x_i}\left(\frac{\langle T'T'\rangle}{2}\right)+\langle\lambda'(T)T'\rangle\frac{\partial\langle T\rangle}{\partial x_i}\right)+\\&-\langle\lambda(T)\rangle\langle\frac{\partial T'}{\partial x_i}\frac{\partial T'}{\partial x_i}\rangle-\langle\lambda'(T)\frac{\partial T'}{\partial x_i}\frac{\partial T'}{\partial x_i}\rangle\end{aligned} \tag{5.5}$$

The equation for the time average temperature, i.e. Eq. (5.7), has two terms which transfer energy from small to large scales. The first one is the classical term which couples the temperature fluctuation to the velocity fluctuation. The second one is a new term which couples the thermal conductivity fluctuation to the fluctuation of the temperature gradient.

The two terms can also be written as

$$\vec{q}_R=\langle\rho cT'\vec{v}'\rangle \tag{5.6}$$

and

$$\vec{q}_\lambda=-\langle\lambda'(T)\nabla T'\rangle \tag{5.7}$$

5.3 Modelling the fluctuating Thermal Conductivity

The thermal conductivity can be approximated by a polynomial expression as

$$\lambda(T) = \sum_{i=0}^{N} a_i T^i = a_0 + a_1 T + a_2 T^2 + ... + a_N T^N \tag{5.8}$$

Some cases are examined. The first one is the linear variation

$$\lambda(T) = a_0 + a_1 T \tag{5.9}$$

Introducing the fluctuating temperature, Eq. (5.2), it is obtained for the average thermal conductivity

$$\langle \lambda(T) \rangle = a_0 + a_1 \langle T \rangle \tag{5.10}$$

and for the fluctuating thermal conductivity

$$\lambda'(T) = a_1 T' . \tag{5.11}$$

The average thermal conductivity depends only on the average temperature and the fluctuating thermal conductivity on the fluctuating temperature.

If the relation is a quadratic one

$$\lambda(T) = a_0 + a_1 T + a_2 T^2 , \tag{5.12}$$

the application of Eq. (5.2) gives for the average term

$$\langle \lambda(T) \rangle = a_0 + a_1 \langle T \rangle + a_2 \left(\langle T \rangle \langle T \rangle + \langle T'T' \rangle \right) \tag{5.13}$$

and for the fluctuating one

$$\lambda'(T) = a_1 T' + a_2 \left(2\langle T \rangle T' + T'T' - \langle T'T' \rangle \right) \tag{5.14}$$

Equation (5.14) shows the interaction between average and fluctuating temperature in the quadratic case.

If the relation is a cubic one

$$\lambda(T) = a_0 + a_1 T + a_2 T^2 + a_3 T^3, \tag{5.15}$$

the average thermal conductivity is

$$\langle \lambda(T) \rangle = a_0 + a_1 \langle T \rangle + a_2 \left(\langle T \rangle \langle T \rangle + \langle T'T' \rangle \right) + a_3 \left(\langle T \rangle \langle T \rangle \langle T \rangle + 3 \langle T \rangle \langle T'T' \rangle + \langle T'T'T' \rangle \right) \tag{5.16}$$

and the fluctuating one

$$\lambda'(T) = a_1 T' + a_2 \left(2 \langle T \rangle T' + T'T' - \langle T'T' \rangle \right) + a_3 \left(3 \langle T \rangle \langle T \rangle T' + 3 \langle T \rangle T'T' - 3 \langle T \rangle \langle T'T' \rangle + T'T'T' - \langle T'T'T' \rangle \right) \tag{5.17}$$

If the relation is a forth power one

$$\lambda(T) = a_0 + a_1 T + a_2 T^2 + a_3 T^3 + a_4 T^4, \tag{5.18}$$

the average thermal conductivity is

$$\begin{aligned} \langle \lambda(T) \rangle = {} & a_0 + a_1 \langle T \rangle + a_2 \left(\langle T \rangle \langle T \rangle + \langle T'T' \rangle \right) + a_3 \left(\langle T \rangle \langle T \rangle \langle T \rangle + 3 \langle T \rangle \langle T'T' \rangle + \langle T'T'T' \rangle \right) + \\ & a_4 \left(\langle T \rangle \langle T \rangle \langle T \rangle \langle T \rangle + 6 \langle T \rangle \langle T \rangle \langle T'T' \rangle + 4 \langle T \rangle \langle T'T'T' \rangle + \langle T'T'T'T' \rangle \right) \end{aligned} \tag{5.19}$$

and the fluctuating one

$$\begin{aligned} \lambda'(T) = {} & a_1 T' + a_2 \left(2 \langle T \rangle T' + T'T' - \langle T'T' \rangle \right) + a_3 \left(3 \langle T \rangle \langle T \rangle T' + 3 \langle T \rangle T'T' - 3 \langle T \rangle \langle T'T' \rangle + T'T'T' - \langle T'T'T' \rangle \right) + \\ & a_4 \left(4 \langle T \rangle \langle T \rangle \langle T \rangle T' + 6 \langle T \rangle \langle T \rangle T'T' + 4 \langle T \rangle T'T' + T'T'T'T' \right) - a_4 \left(6 \langle T \rangle \langle T \rangle \langle T'T' \rangle + 4 \langle T \rangle \langle T'T' \rangle + \langle T'T'T'T' \rangle \right) \end{aligned} \tag{5.20}$$

The average and fluctuating thermal conductivity are then resumed in the following. For the constant case:

$$\begin{aligned} & \langle \lambda(T) \rangle = a_0; \\ & \lambda'(T) = 0; \end{aligned}, \tag{5.21}$$

for the linear one

$$\begin{aligned} & \langle \lambda(T) \rangle = a_0 + a_1 \langle T \rangle; \\ & \lambda'(T) = a_1 T'; \end{aligned}, \tag{5.22}$$

for the quadratic one

$$\begin{aligned}&\langle\lambda(T)\rangle=\left(a_0+a_1\langle T\rangle+a_2\langle T\rangle\langle T\rangle\right)+\left(a_2\langle T'T'\rangle\right);\\&\lambda'(T)=\left(a_1+2a_2\langle T\rangle\right)T'+a_2\left(T'T'-\langle T'T'\rangle\right);\end{aligned}\tag{5.23}$$

for the cubic one

$$\begin{aligned}&\langle\lambda(T)\rangle=\left(a_0+a_1\langle T\rangle+a_2\langle T\rangle\langle T\rangle+a_3\langle T\rangle\langle T\rangle\langle T\rangle\right)+\left(a_2+3a_3\langle T\rangle\right)\langle T'T'\rangle+\left(a_3\langle T'T'T'\rangle\right);\\&\lambda'(T)=\left(a_1+2a_2\langle T\rangle+3a_3\langle T\rangle\langle T\rangle\right)T'+\left(a_2+3a_3\langle T\rangle\right)\left(T'T'-\langle T'T'\rangle\right)+a_3\left(T'T'T'-\langle T'T'T'\rangle\right);\end{aligned}\tag{5.24}$$

and for the forth power case

$$\begin{aligned}&\langle\lambda(T)\rangle=\left(a_0+a_1\langle T\rangle+a_2\langle T\rangle\langle T\rangle+a_3\langle T\rangle\langle T\rangle\langle T\rangle+a_4\langle T\rangle\langle T\rangle\langle T\rangle\langle T\rangle\right)+\\&\left(a_2+3a_3\langle T\rangle+6a_4\langle T\rangle\langle T\rangle\right)\langle T'T'\rangle+\left(a_3+4a_4\langle T\rangle\right)\langle T'T'T'\rangle+a_4\langle T'T'T'T'\rangle;\\&\lambda'(T)=\left(a_1+2a_2\langle T\rangle+3a_3\langle T\rangle\langle T\rangle+4a_4\langle T\rangle\langle T\rangle\langle T\rangle\right)T'+\\&\left(a_2+\left(3a_3+4a_4\right)\langle T\rangle+6a_4\langle T\rangle\langle T\rangle\right)\left(T'T'-\langle T'T'\rangle\right)+\\&a_3\left(T'T'T'-\langle T'T'T'\rangle\right)+a_4\left(T'T'T'T'-\langle T'T'T'T'\rangle\right);\end{aligned}\tag{5.25}$$

In conclusion, the following general expression can be assumed for the average thermal conductivity

$$\langle\lambda(T)\rangle=\lambda\left(\langle T\rangle\right)+\sum_{k=2}^{N}P_k\left(\langle T\rangle\right)\langle T'^k\rangle\tag{5.26}$$

and for the fluctuating thermal conductivity

$$\lambda'(T)=\left.\frac{d\lambda}{dT}\right|_{T=\langle T\rangle}\cdot T'+\sum_{k=2}^{N}Q_k\left(\langle T\rangle\right)\cdot\left(T'^k-\langle T'^k\rangle\right)\tag{5.27}$$

The average thermal conductivity is due to the thermal conductivity at the average temperature and of polynomials where the temperature fluctuations are present at several powers. The fluctuating thermal conductivity is due to the product of the first derivative and the fluctuating thermal conductivity and several polynomials.

The structure of the thermal conductivity can be simplified with the following expression

$$\lambda(T)=\lambda\left(\langle T\rangle\right)+\left.\frac{d\lambda}{dT}\right|_{T=\langle T\rangle}\cdot\left(T-\langle T\rangle\right)+o\left(T-\langle T\rangle\right)\tag{5.28}$$

or

$$\lambda(T) = \lambda(\langle T\rangle) + \left.\frac{d\lambda}{dT}\right|_{T=\langle T\rangle} \cdot T' + o(T') \tag{5.29}$$

It is then possible to obtain for the average thermal conductivity

$$\langle \lambda(T)\rangle \approx \lambda(\langle T\rangle) \tag{5.30}$$

and for the fluctuating thermal conductivity

$$\lambda'(T) \approx \left.\frac{d\lambda}{dT}\right|_{T=\langle T\rangle} T' \tag{5.31}$$

From Eq.(5.26) and Eq. (5.30) it is possible to conclude

$$\left\|\lambda(\langle T\rangle)\right\| >> \left\|\sum_{k=2}^{N} P_k(\langle T\rangle)\langle T'^k\rangle\right\| \tag{5.32}$$

and from Eq. (5.27) and (5.31)

$$\left\|\left.\frac{d\lambda}{dT}\right|_{T=\langle T\rangle} \cdot T'\right\| >> \left\|\sum_{k=2}^{N} Q_k(\langle T\rangle)\cdot\left(T'^k - \langle T'^k\rangle\right)\right\|. \tag{5.33}$$

Equations (5.32) and (5.33) are confirmed by the assumption

$$\left\|\langle T\rangle\right\| >> \left\|T'\right\|. \tag{5.34}$$

From the physical point of view the coefficients of the polynomial expressions follow the rule

$$\left\|a_{n+1}\right\| << \left\|a_n\right\|; n > 1, \tag{5.35}$$

i.e. the contribution of the coefficients of higher order are less influencing the variation of the thermal conductivity. The polynomials $P_k(\langle T\rangle)$, $Q_k(\langle T\rangle)$ contain the coefficients a_n of higher order and are smaller than the thermal conductivity at the average temperature and of its derivative. On the basis of the experimental evidence that the coefficients a_n decrease of some

orders of magnitude with the increase of n it is possible to conclude that Eqs. (5.30) and (5.31) are valid.

Using Eqs. (5.30) and (5.31) it is possible to obtain

$$\vec{q}_\lambda = -\left.\frac{d\lambda}{dT}\right|_{T=\langle T\rangle} \nabla\frac{\langle T'T'\rangle}{2} \tag{5.36}$$

5.4 Turbulence modelling

Equations (5.19) and (5.24) contain terms that can be modelled specifying the approach to solve the turbulent flow. The model chosen in the present work is the *k-ε* turbulence model improved by Nagano and Tagawa [5.23]. Using a Boussinesq type relation Eq. (5.4) becomes

$$\rho c\frac{\partial\langle T\rangle}{\partial t}+\rho cU_i\frac{\partial\langle T\rangle}{\partial x_i}=\frac{\partial}{\partial x_i}\left(\left(\lambda\left(\langle T\rangle\right)+\rho c\frac{\nu_T}{\sigma_T}\right)\frac{\partial\langle T\rangle}{\partial x_i}+\left.\frac{d\lambda}{dT}\right|_{\langle T\rangle}\frac{\partial}{\partial x_i}\left(\frac{\langle T'T'\rangle}{2}\right)\right) \tag{5.37}$$

while Eq. (5.5)

$$\begin{aligned}&\rho c\frac{\partial}{\partial t}\left(\frac{\langle T'T'\rangle}{2}\right)+\rho cU_i\frac{\partial}{\partial x_i}\left(\frac{\langle T'T'\rangle}{2}\right)=\left(\rho c\frac{\nu_T}{\sigma_T}\frac{\partial\langle T\rangle}{\partial x_i}-\left.\frac{d\lambda}{dT}\right|_{\langle T\rangle}\frac{\partial}{\partial x_i}\left(\frac{\langle T'T'\rangle}{2}\right)\right)\frac{\partial\langle T\rangle}{\partial x_i}+\\&\frac{\partial}{\partial x_i}\left(\left(\lambda\left(\langle T\rangle\right)+\rho c\frac{\nu_T}{\sigma_T}\right)\frac{\partial}{\partial x_i}\left(\frac{\langle T'T'\rangle}{2}\right)+2\left.\frac{d\lambda}{dT}\right|_{\langle T\rangle}\frac{\langle T'T'\rangle}{2}\frac{\partial\langle T\rangle}{\partial x_i}\right)-\frac{\lambda\left(\langle T\rangle\right)}{\nu}\frac{\langle T'T'\rangle}{2}\frac{\varepsilon}{k}\end{aligned} \tag{5.38}$$

Equations are rewritten in non-dimensional form before to be solved numerically.

The equation for energy conservation (or mean temperature equation)

$$\frac{\partial\Theta^+}{\partial t^+}+U_i^+\frac{\partial\Theta^+}{\partial x_i^+}=\frac{\partial}{\partial x_i^+}\left(\left(\frac{1}{\mathrm{Pr}}\lambda^+\left(\Theta^+\right)+\frac{\nu_T^+}{\sigma_T}\right)\frac{\partial\Theta^+}{\partial x_i^+}\right)+\frac{\partial}{\partial x_i^+}\left(\frac{1}{\mathrm{Pr}}\frac{d\lambda^+}{d\Theta^+}\frac{\partial}{\partial x_i^+}\left(\frac{\theta^+\theta^+}{2}\right)\right) \tag{5.39}$$

where is present the new term for heat flux, q_λ^+, due to the variation of thermal conductivity,

$$q_\lambda^+ = -\frac{1}{\mathrm{Pr}}\frac{d\lambda^+}{d\Theta^+}\frac{\partial}{\partial x_i^+}\left(\frac{\theta^+\theta^+}{2}\right) \tag{5.40}$$

The equation for temperature variance

$$\begin{aligned}&\frac{\partial}{\partial t^+}\left(\frac{\theta^+\theta^+}{2}\right)+U_i^+\frac{\partial}{\partial x_i^+}\left(\frac{\theta^+\theta^+}{2}\right)=\left(\frac{\nu_T^+}{\sigma_T}\frac{\partial\Theta^+}{\partial x_i^+}-\frac{1}{\mathrm{Pr}}\frac{d\lambda^+}{d\Theta^+}\frac{\partial}{\partial x_i^+}\left(\frac{\theta^+\theta^+}{2}\right)\right)\frac{\partial\Theta^+}{\partial x_i^+}+\\&\frac{\partial}{\partial x_i^+}\left(\left(\frac{1}{\mathrm{Pr}}\lambda^+ +\frac{\nu_T^+}{\sigma_T}\right)\frac{\partial}{\partial x_i^+}\left(\frac{\theta^+\theta^+}{2}\right)\right)+\frac{\partial}{\partial x_i^+}\left(2\frac{1}{\mathrm{Pr}}\frac{d\lambda^+}{d\Theta^+}\frac{\theta^+\theta^+}{2}\frac{\partial\Theta^+}{\partial x_i^+}\right)-\frac{1}{\mathrm{Pr}}\lambda^+\frac{\theta^+\theta^+}{2}\frac{\varepsilon^+}{k^+}\end{aligned} \tag{5.41}$$

where is present also the new heat flux term.

The thermal conductivity is supposed to be dependent on temperature according to the following expression, [5.1],

$$\lambda^+\left(\Theta^+\right) = A_\Theta^+ + B_\Theta^+\Theta^+ \tag{5.42}$$

The aim of the present work is to solve numerically the system of equations, derived in [5.1], with a RANS model. The system of equations is comprehensive of the classical equations for the mean motion, i.e. turbulent kinetic energy and dissipation rate, mass and energy conservation, including the new terms of fluctuating thermal conductivity.

The new equation, derived for the transport of temperature variance, has never been used before in the classical RANS modelling but is necessary to calculate the new fluctuating thermal conductivity terms of the present model. The presence of the equation of temperature variance makes this model a three-equation-RANS model. Thermal conductivity is relative to fluids with Prandtl number spanning from low to high values because, as remarked in [5.1], great differences are expected for the extreme Prandtl number fluids.

The case investigated in the present paper is relative to fully developed turbulent flow between parallel plates, with constant heat flux from both walls, and thermal conductivity variable according to Eq. (5.42). On the inlet of the parallel plates the fluid has uniform mean

temperature and temperature variance. One goal of the present numerical simulations is to investigate the influence of Prandtl number on the amplitude of the new heat flux term, q_λ^+ , Eq. (5.40).

Thermal boundary conditions at the wall are:

$$\begin{cases} \left.\dfrac{\partial \Theta^+}{\partial x_i^+}\right|_w = \dfrac{\mathrm{Pr}}{\lambda^+(0)} \\ \left.\theta^+\theta^+\right|_w = 0 \end{cases} \tag{5.43}$$

5.5 Numerical Model

The turbulence model is the *k-ε* proposed by Nagano and Tagawa [5.20]. The equations are solved using the finite volume method (FVM) with a HYBRID differential scheme for velocities, temperature and turbulent variables. A uniform staggered Cartesian grid system is used. The iterative SIMPLER algorithm is employed to relax the coupled equations. The non-linear algebraic equations over the flow domain are solved iteratively with the Thomas algorithm (TDMA) method [5.21-5.22]. Numerical simulations are carried on until fully developed temperature profiles are obtained.

5.6 Results

Numerical simulations are carried on for fully developed turbulent flow between parallel plates, at Reynolds number equal to 8,000 and three Prandtl numbers, which corresponds to liquid metal (Pr=0.44), water (Pr=4.4) and oil (Pr=44).

The numerical results for the new heat flux term, are presented in Figure 5.6, which shows that the contribution of the new term is important close to the wall and its importance is increasing with the increase of Prandtl number.

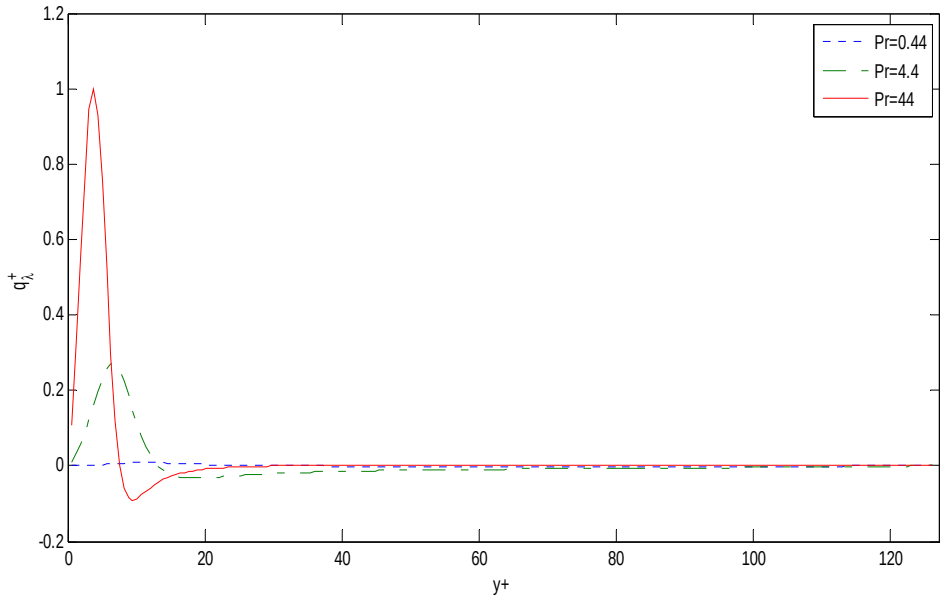

Figure 5.1: New heat flux term due to variation of thermal conductivity.

Figure 5.7 presents numerical results for heat flux contributions, i.e. total, turbulent, laminar and $\dot{q}^+_\lambda$, for a fluid with Prandtl number equal to 44. The contribution of $\dot{q}^+_\lambda$ is important mainly at the wall where is not negligible.

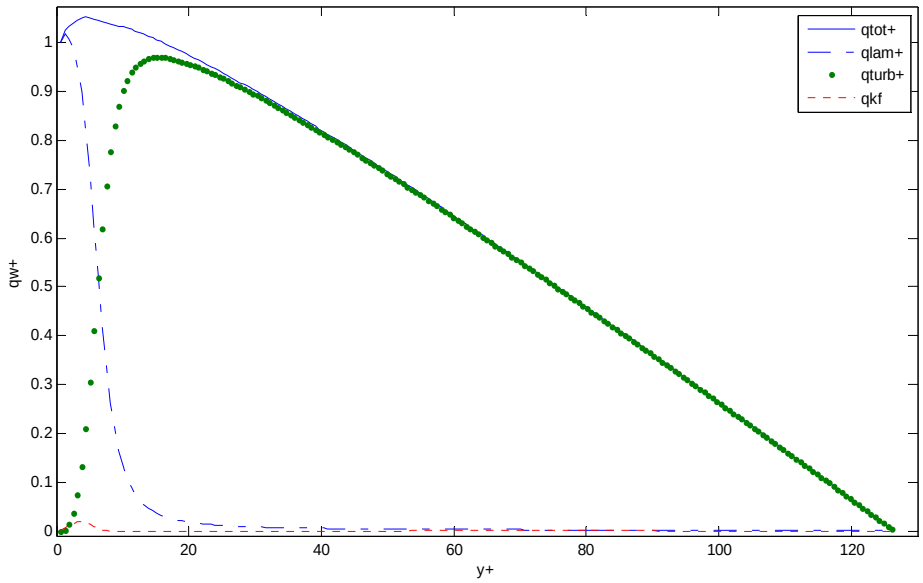

Figure 5.2: Heat fluxes for Pr=44.

The temperature variance profile for Pr=44 is reported in Figure 5. 8, using the friction temperature to normalize the root-mean-square temperature variance. Temperature variance undergoes a sharp rise nearby y^+=10 in the near-wall region.

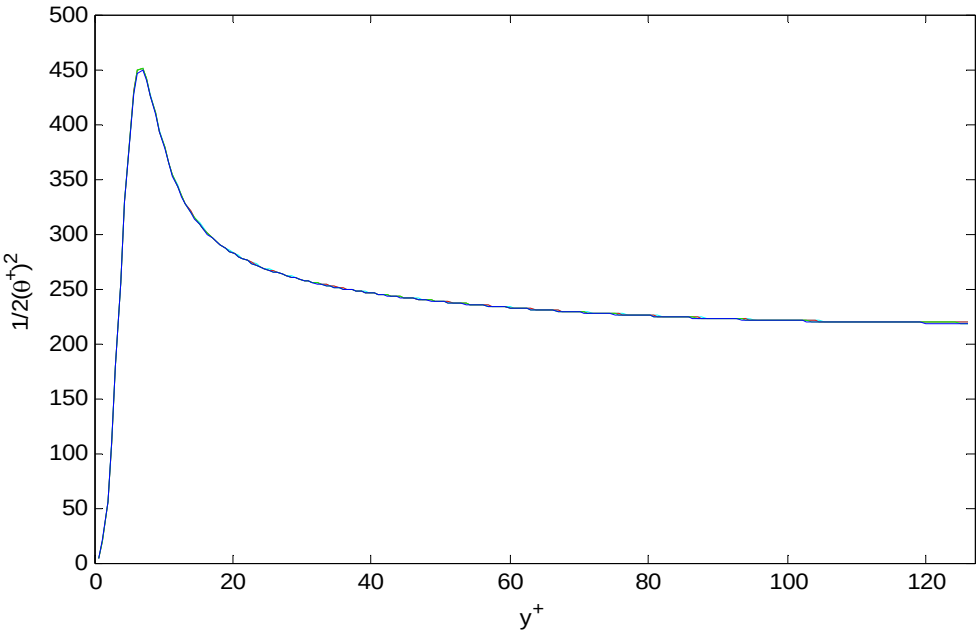

Figure 5.3: Temperature Variance for Pr=44.

The budget of temperature variance for Pr=44 is reported in Figure 5. 9. The results show the influence of the new transport term, which has a similar pattern to molecular and turbulent ones, also if the amplitude is slightly smaller but with the same order of magnitude.

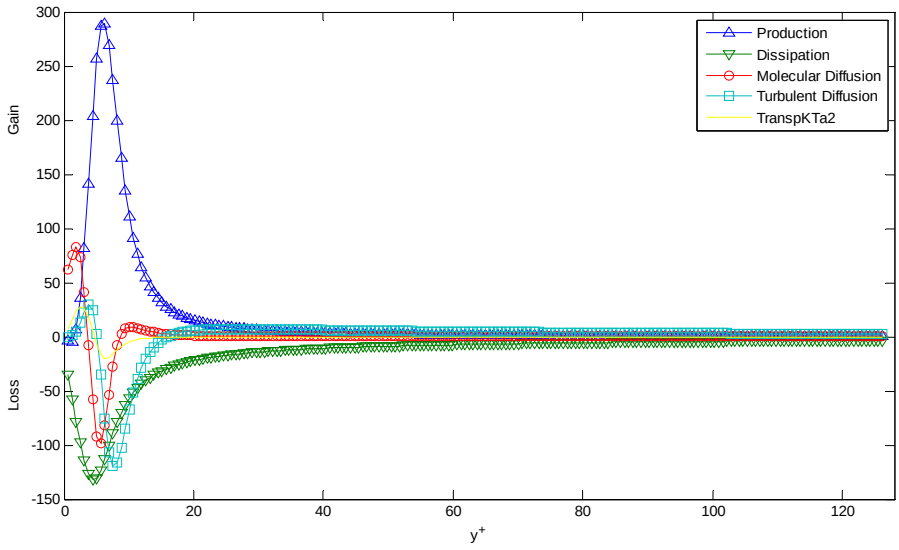

Figure 5.4: Budget of Temperature Variance for Pr=44.

Mean-temperature in the turbulent boundary layer for Pr=44 is reported in Figure 5. 10. The profile is in fair agreement with the theoretical distribution, $\Theta^+ = \Pr y^+$, in the viscous sub-layer, because thermal conductivity is not constant. Moreover, it is in agreement with the law of the wall in the logarithmic region.

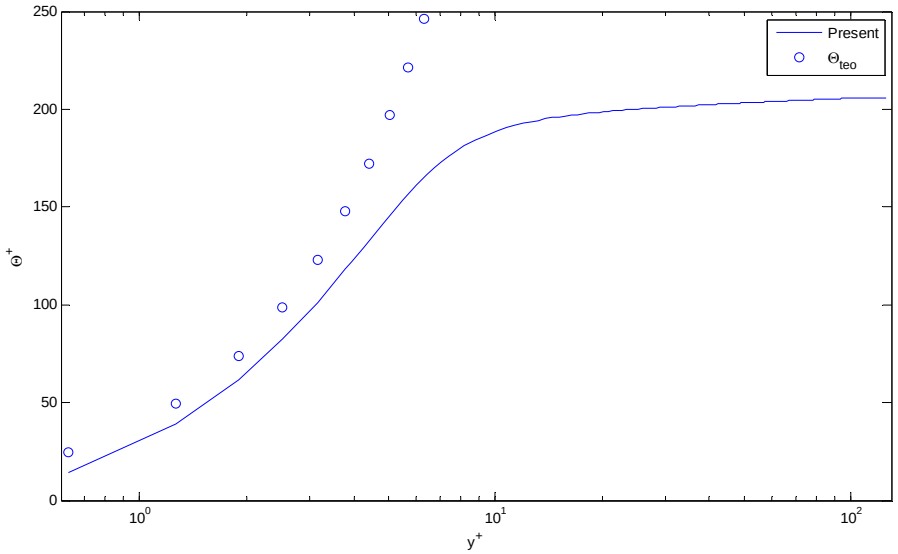

Figure 5.5: Mean Temperature for Pr=44.

The results presented in this work are limited to fluids with Prandtl number lower or equal than 44 because the computational time increases at large extent with the increase of Prandtl number. It can be pointed out that Prandtl number of some oil can span between $10^3 \div 4 \cdot 10^4$, when is expected a greater influence of the new term, $\dot{q}_\lambda^+$ on heat transfer.

5.7 Discussion

The equation for the conservation of energy with the average temperature, i.e. Eq. (5.54) for a two dimensional case, presents two terms with a variation of the thermal conductivity. The new result of Eq. (5.54) is the link between the variation of the thermal conductivity and the square of the temperature fluctuation in turbulent flow, which makes the present equation a new kind of energy conservation equation. As an example the energy equation for the time average temperature, solved in [5.7] for turbulent steady flow, is a particular case of Eq. (5.54).

Also Eq. (5.55) is a new kind of energy equation for the square of the fluctuating temperature where two kinds of new terms are present representing the variation of the thermal conductivity with the temperature.

The solution of Eq. (5.54) is possible with the solution of Eq. (5.55), which on the other hand, requires the solution of Eqs. (5.56) and (5.57).

The contribution of the new heat flux term on heat transfer is dependent on the relation linking thermal conductivity and temperature. Greater is the variation of thermal conductivity with temperature and greater is the contribution of the new term, which can allow a decrease or an increase of heat transfer according to the relation between thermal conductivity and temperature.

The present work investigates numerically fluids with Prandtl number much smaller than, for example, a lubricant or heavy oil. A greater Prandtl number fluid implies a much thinner boundary layer and a bigger temperature gradient near the wall. The term for the production of temperature variance is proportional to the mean temperature gradient, which means that with a greater mean temperature the temperature variance is greater, as well as the new heat flux term, as shown theoretically in [5.3].

The new heat flux term, appearing in the transport equation for temperature variance, Eq. (5.41), has different influence from the energy point of view and is difficult to say whether it is a production or a dissipation term. Indeed, a productive term is always positive while a dissipative one is always negative. Since the behaviour of the new heat flux term is dependent whether the thermal conductivity decreases or increases with temperature and is proportional to the mean temperature gradient, the new term increases if the thermal conductivity increases with

temperature or decreases if the thermal conductivity decreases with temperature. In conclusion, the new term is treated as increase or decrease of production.

5.8 Conclusions

The present theoretical work is aimed to take into account the variation of the thermal conductivity of a fluid flowing in turbulent flow. The equations of the energy conservation have been studied in the form of the average temperature and the square of the fluctuating temperature. The variation of the thermal conductivity has been modelled mathematically with physical hypothesis, making possible to correlate the derivative of the thermal conductivity, with respect to the average temperature, multiplied to the space gradient of the square of the fluctuating temperature. The final equations of the average and the fluctuating temperature need to be solved together to the turbulent kinetic energy and the energy dissipation in order to take into account the variation of the thermal conductivity.

The present numerical results, carried on for a two dimensional fully developed turbulent flow between two parallel plates, at Re=8,000 and Prandtl number equal to Pr=0.44, 4.4, 44, show the relative importance of the new heat flux term, due to the variation of thermal conductivity. Numerical simulations are limited to a relatively small Reynolds number and to a maximum value of Prandtl number equal to 44, because of the present limited computational resources.

References of Chapter 5

[5.1] Martinelli, R.C. 1947. Heat transfer to molten metals. Trans. ASME, 69, 47–59.

[5.2] Lyon, R.N. 1951. Liquid metal heat transfer coefficients. Chem. Eng. Progr., 47, 75–79.

[5.3] Tennekes, H., Lumley, J.L. 1972. A First Course in Turbulence. MIT Press, Cambridge, MA.

[5.4] Aoki, S. 1963. A consideration on the heat transfer in liquid metal. Bull. Tokyo Inst. Tech., 54, 63–73.

[5.5] Reynolds, A.J. 1975. The prediction of turbulent Prandtl and Schmidt numbers. Int. J. Heat Mass Transfer, 18, 1055–1069.

[5.6] F. Gori, M.A. El Hadidy, and D.B. Spalding. Numerical Prediction of the Heat Transfer to Low-Prandtl Number Fluids. Numerical Heat Transfer, 2, 441-454, 1979.

[5.7] S. Faggiani and F. Gori. Influence of Streamwise Molecular Heat Conduction on the Heat Transfer Coefficient for Liquid Metals in Turbulent Flow between Parallel Plates. Journal of Heat Transfer, ASME, 102, 2, 292-296, 1980.

[5.8] M.A. El Hadidy, F. Gori and D.B. Spalding. Further Results on the Heat Transfer to Low-Prandtl Number Fluids in Pipes. Numerical Heat Transfer, 5, 107-117, 1982.

[5.9] Cheng X., Tak N. Investigation on turbulent heat transfer to lead–bismuth eutectic flows in circular tubes for nuclear applications. Nuclear Engineering and Design, 236 (5.2006) 385–393.

[5.10] M. Satake, K. Yuki, S. Chiba, H. Hashizume. Numerical analysis of MHD flow structure behind a square rod. Fusion Engineering and Design, 81 (5.2006) 525–532.

[5.11] L. C. Cadwallader G. R. Longhurst. FLIBE use in fusion reactors: an initial safety assessment. Idaho National Engineering and Environmental Laboratory Idaho Falls, Idaho, 83415 INEEL/EXT-99-00331, March 1999.

[5.12] Shin-Ya Chiba, Kazuhisa Yuki Hidetoshi Hashizume, Saburo Toda, Akio Sagara. Numerical research on heat transfer enhancement for high Prandtl-number fluid. Fusion Engineering and Design, 81 (5.2006) 513–517.

[5.13] T. Kunugi, S. Satake, A. Sagara. Direct numerical simulation of turbulent free-surface high Prandtl number fluid flows in fusion reactors. Nuclear Instruments and Methods in Physics Research A, 464 (5.2001) 165–171.

[5.14] H. Nakaharai, J. Takeuchi, T. Yokomine, T. Kunugi, S. Satake, N.B. Morley, M.A. Abdou. The influence of a magnetic field on turbulent heat transfer of a high Prandtl number fluid. Experimental Thermal and Fluid Science, 32 (5.2007) 23–28.

[5.15] Gregory J. Kolbov. Economic Evaluation of Solar-Only and Hybrid Power Towers Using Molten-Salt Technology. Solar Energy, 62, 1, 51-61, 1998.

[5.16] Hiroshi Hasuike, Yoshio Yoshizawa, Akio Suzuki, Yutaka Tamaura. Study on design of molten salt solar receivers for beam-down solar concentrator. Solar Energy, 80 (5.2006) 1255–1262.

[5.17] F. Donatini, C. Zamparelli, A. Maccari and M. Vignolini. High efficency integration of thermodynamic solar plant with natural gas combined cycle. 2007 International Conference on Clean Electrical Power, ICCEP '07, 2007, 770-776.

[5.18] Hiroshi Kawamura, Kouichi Ohsaka, Hiroyuki Abe, Kiyoshi Yamamoto. DNS of turbulent heat transfer in channel flow with low to medium-high Prandtl number fluid. International Journal of Heat and Fluid Flow, 19 (5.1998) 482-491.

[5.19] Bo Yu, Yasuo Kawaguchi. DNS of fully developed turbulent heat transfer of a viscoelastic drag-reducing flow. International Journal of Heat and Mass Transfer, 48 (5.2005) 4569–4578.

[5.20] Petukhov, B.S. Heat Transfer and Friction in Turbulent Pipe Flow with Variable Physical Properties. Advances in Heat Transfer, 6, 503-565, 1970.

[5.21] S. Faggiani and F. Gori. Remarks on the Heat Transfer to Gases in Turbulent Flow between Parallel Plates. The 7th International Heat Transfer Conference, Munchen, Germany , 3, 33-38 1982.

[5.22] E. P. Valueva. Hydrodynamics and Heat Transfer in Pulsating Turbulent Pipe Flow of a Liquid of Variable Properties. High Temperature, 43, 6, 2005, 890–899.

[5.23] E. P. Valueva. Hydrodynamics and Heat Transfer in Pulsating Turbulent Flow of Gas in a Heated Pipe. High Temperature, 44, 1, 2006, 120–128.

[5.24] E. P. Valueva. Integral Methods of Calculation of Heat Transfer and Drag under Conditions of Turbulent Pipe Flow of Liquid of Variable Properties: Steady-State and Quasi-Steady-State Flows in a Round Pipe with Constant Density of Heat Flux to the Wall. High Temperature, 2007, 45, 1, 49–57.

[5.25] E. P. Valueva. Integral Methods of Calculation of Heat Transfer and Drag under Conditions of Turbulent Pipe Flow of Liquid of Variable Properties: Pulsating High-Frequency Flow. High Temperature, 2007, 45, 4, 502–508.

[5.26] F. Gori, A. Boghi. On a New Turbulent Energy Equation with Variable Thermal Conductivity. IMECE2008, October 31-November 6/2008, Boston Massachusset, USA.

[5.27] F. Gori, A. Boghi. RANS modelling of a New Turbulent Energy Equation with Variable Thermal Conductivity: ASME-ATI-UIT 2010 May, 16-19, 2010, Sorrento, Italy

Chapter 6:

TWO NEW DIFFERENTIAL EQUATIONS OF TURBULENT DISSIPATION RATE AND APPARENT VISCOSITY FOR NON-NEWTONIAN FLUIDS

6.1 Introduction

Non-Newtonian fluids are present in several industrial applications and biological problems, like blood flow. Literature presents many theoretical solutions and numerical simulations in laminar flow, including two papers published by the first author more than thirty years ago [6.1-6.2].

Few numerical investigations dealt with turbulent flow of pseudo-plastic fluids (shear-thinning fluid) because of the lack of models with one or two point closure and, for this reason, some investigators performed DNS (Direct Numerical Simulation). Rudman and Blackburn used the Spectral Element-Fourier Method (SEM) in a duct flow, [6.3], and compared the DNS results of a power law fluid with small consistency index and a Herschel-Bulkley fluid with experimental data [6.4]. Dimitropoulos [6.5-6.6] carried out DNS of a polymeric solution using FENE-P and *Giesekus* models, employing spectral approximation and semi-implicit algorithm to predict the drag reduction. New results on Reynolds stresses and pressure are presented in [6.6], where the convergence of the pseudo-spectral algorithm is discussed. A non-refined mesh and a high artificial viscosity are introduced to stabilize the algorithm. The FENE-P model is used in [6.7] for a DNS one-dimensional approach to explain the phenomenon of drag reduction. A

turbulent model for a non-Newtonian power law fluid is developed in [6.8], in analogy to the turbulent viscosity, determining the temperature distribution for soybean milk flowing inside a tubular heat exchanger.

Turbulent flow of a non-Newtonian fluid is important also in the medical field. A model to predict the turbulent flow of a power-law fluid in a bio-reactor for anaerobic digestion is developed in [6.9] with the classical k-ε model and the power-law viscosity.

The *k-ε* equations are derived in [6.10-6.11] for power-law and Herschel-Bulkley fluid using the apparent viscosity of a non-Newtonian fluid in the RANS equations for a Newtonian fluid, but the agreement is not good enough. The introduction of the third invariant of the rate of deformation tensor in the viscosity contributes to an increase of viscous diffusion and dissipation rate in the turbulent kinetic energy confirming the dependence of the viscosity on the second invariant of rate of deformation tensor in a 2D flow [6.12].

The Generalized Newtonian Fluid (GNF) constitutive equation is applied to a *Bird-Carreau* fluid in order to derive a *k-ε* model for the equations of Reynolds stresses tensor, turbulent kinetic energy and dissipation rate [6.13]. The viscosity is dependent on the invariants of the rate of deformation tensor, shear-rate and strain-rate. An algebraic equation is proposed to correlate the instantaneous viscosity to the dissipation rate while average viscosity and dissipation rate are correlated with a normal logarithmic probability distribution of the dissipation rate. The final equation of dissipation rate is written in non conservative form because two derivatives are present, one for the dissipation rate itself and one for the average dynamic viscosity.

Direct Numerical Simulation of viscoelastic fluids in turbulent channel flow is carried out using the FENE-P model to find relationships between flow and fluid rheological parameters

[6.14]. Three different regimes of drag reduction, namely low, high and medium are identified proposing mathematical expressions for the eddy viscosity in the three regimes. A procedure based on the DNS predictions of the budgets of momentum and viscoelastic shear stress is developed to evaluate the mean velocity profile. A RANS model is employed using the FENE-P constitutive relationship to describe the rheology of polymer-induced turbulent drag reduction [6.15]. Correlations among flow and polymer conformation variables are identified by analyzing recent DNS results of dilute polymer solutions. Closures are obtained for turbulent correlations and incorporated into a single-point k−ε model.

The present work is aimed to derive the equation of the dissipation rate in a conservative form for an incompressible GNF in 2D (two-dimensional) flow. Viscosity is on the shear-rate, as shown in [6.12] in a 2D flow, and done in all the papers found in the literature, without an explicit statement of the relation with the shear-rate. A 2D theory of turbulence has been developed since the 70's in [6.16-6.20] despite the differences with the real 3D flow and the absence of vortex-stretching terms. It is also affirmed in [6.21] that it seems natural to investigate the behavior of a 2D flow, in the hope that it sheds some light on "almost" 2D turbulence. Due to the difficulty of deriving the governing equations directly in a 3D flow, it is considered a guide to develop first a 2D turbulent model. The importance of studying a 2D model, which can be generalized in 3D, is also remarked in [6.12], where the authors developed an order of magnitude analysis for a 2D turbulent flow, without loss of generality.

The transport equation of ε is deduced in this work by the use of a completely new transport equation for the apparent viscosity and is not necessary a constitutive link between apparent viscosity and shear rate. No hypotheses are necessary on the dependence of the turbulent dissipation rate on the fluctuating part of the rate of deformation tensor, as required in

[6.15], neither a particular statistical distribution for the average viscosity, as required in [6.16]. The present procedure allows obtaining a new transport equation of ε in a conservative form, which is more general than that obtained previously in the literature. Moreover, the conservative form of the ε equation allows avoiding the calculation of the temporal derivative of the apparent viscosity, due to the presence of a transport equation for the apparent viscosity.

The chapter has the following structure. The transport equations for the average variables and the turbulent kinetic energy are derived first and then the transport equation for the shear-rate. The new differential equation for the apparent viscosity is deduced using the scalar product of the instantaneous rate of deformation tensor by itself. From this equation it is possible to derive the equation of dissipation rate in conservative form and to give a physical interpretation to the new terms. The method used in this work allows explaining each term and classifying it as transport, production and dissipation one. Finally, an order of magnitude analysis is carried out.

Nomenclature for Non-Newtonian Model

Symbol	Definition	SI Unit
Latin		
p	Instantaneous pressure	Pa
S_{ij}	ij-component of Instantaneous rate of deformation tensor	s^{-1}
$	Variable defined in Eq. (6.23)	s^{-1}
$T_{\mu,ij}$	ij-component of mean polymeric stress tensor	Pa
$T'_{\mu,ij}$	ij-component of instantaneous polymeric stress tensor	Pa
Greek		
$\dot{\gamma}$	Shear rate	s^{-1}
δ_{ij}	Kronecher delta	
μ_{app}	Instantaneous Apparent dynamic viscosity	Pa·s
$\langle \mu_{app} \rangle$	mean Apparent dynamic viscosity	Pa·s
μ'_{app}	fluctuating Apparent dynamic viscosity	Pa·s

τ_c	Yield stress	Pa
Ω_{ij}	ij-component of Instantaneous rotation rate tensor	s^{-1}

6.2 Constitutive equation

The present 2D analysis is carried on for a Generalized Newtonian Fluid, GNF. The constitutive equation for the incompressible non-Newtonian fluid is written similarly to a Newtonian one with the apparent viscosity function of the shear-rate

$$T_{ij} = -p\delta_{ij} + 2\mu_{app}S_{ij}, \tag{6.1}$$

where T_{ij} is the stress tensor and p the static pressure.

The rate of deformation tensor S_{ij} is

$$S_{ij} = \frac{1}{2}\left(\frac{\partial u_i}{\partial x_j} + \frac{\partial u_j}{\partial x_i}\right), \tag{6.2}$$

and the shear-rate $\dot{\gamma}$ is

$$\dot{\gamma} = \sqrt{2S_{ij}^2}\,. \tag{6.3}$$

Defining S as

$$S = \frac{\dot{\gamma}}{\sqrt{2}}, \tag{6.4}$$

the shear-rate will be treated as S from now on.

6.3 Conservation equations of mass, momentum and turbulent kinetic energy

The conservation equations for the instantaneous variables are the followings, in a 2D flow,

$$\frac{\partial u_i}{\partial x_i} = 0\,, \tag{6.5}$$

for the mass, and

$$\rho \frac{\partial u_i}{\partial t} + \rho u_k \frac{\partial u_i}{\partial x_k} = -\frac{\partial p}{\partial x_i} + \frac{\partial}{\partial x_k}\left(2\mu_{app} S_{ik}\right), \tag{6.6}$$

for the momentum.

Each instantaneous variable is decomposed in mean and fluctuating components,

$$u_i = U_i + u_i'\,, \tag{6.7}$$

$$p = P + p'\,, \tag{6.8}$$

$$\mu_{app} = \langle \mu_{app} \rangle + \mu'_{app}\,. \tag{6.9}$$

The mean component of the stress tensor, Eq. (6.1), becomes

$$\langle T_{ij} \rangle = -P\delta_{ij} + 2\langle \mu_{app} \rangle \langle S_{ij} \rangle + 2\langle \mu'_{app} S'_{ij} \rangle\,, \tag{6.10}$$

and the fluctuating one

$$T'_{ij} = -p'\delta_{ij} + 2\mu'_{app}\langle S_{ij} \rangle + 2\langle \mu_{app} \rangle S'_{ij} + 2\mu'_{app} S'_{ij} - 2\langle \mu'_{app} S'_{ij} \rangle\,. \tag{6.11}$$

The third term of the mean component, Eq. (6.10), is due to the viscosity fluctuations while different combinations of mean and fluctuating components are present in the fluctuating tensor, Eq. (6.11).

The conservation equations of the mean variables are

$$\frac{\partial U_i}{\partial x_i} = 0\,, \tag{6.12}$$

for the mass, and

$$\rho \frac{\partial U_i}{\partial t} + \rho U_k \frac{\partial U_i}{\partial x_k} = -\frac{\partial P}{\partial x_i} + \frac{\partial}{\partial x_k}\left(2\langle \mu_{app} \rangle \langle S_{ik} \rangle + T_{R,ij} + T_{\mu,ij}\right), \tag{6.13}$$

for the momentum.

In the mean flow, the Reynolds stress tensor is given by

$$T_{R,ij} = -\langle \rho u_i' u_j' \rangle \,, \tag{6.14}$$

while the polymeric stress tensor, so-called also for a non-polymer fluid, is, according to [6.13],

$$T_{\mu,ij} = 2\langle \mu_{app}' S_{ij}' \rangle \,. \tag{6.15}$$

For constant viscosity the Reynolds stresses, due to convection, are the only terms responsible for the energy transfer from mean to fluctuating scale, while, for variable viscosity, the polymeric stresses are active in conjunction to the Reynolds stresses in the energy transfer from mean to fluctuating scale.

The conservation equations for the fluctuating components and the turbulent kinetic energy are derived in Appendix A and the final equation is

$$\begin{aligned} &\frac{\partial}{\partial t}(\rho k) + U_j \frac{\partial}{\partial x_j}(\rho k) = \left(T_{R,ij} - T_{\mu,ij}\right)\langle S_{ij} \rangle + \\ &-\frac{\partial}{\partial x_j}\left(\langle \rho k' u_j' \rangle + \langle p' u_j' \rangle - \langle \mu_{app}' \frac{\partial k'}{\partial x_j} \rangle - \langle \mu_{app} \rangle \frac{\partial k}{\partial x_j} - 2\langle u_i' \mu_{app}' \rangle \langle S_{ij} \rangle - \frac{\langle \mu_{app} \rangle}{\rho} \frac{\partial T_{R,ij}}{\partial x_i} - \langle \frac{\mu_{app}'}{\rho} \frac{\partial T_{R,ij}'}{\partial x_i} \rangle \right) + \cdot \\ &-2\langle \mu_{app} \rangle \langle S_{ij}' S_{ij}' \rangle - 2\langle \mu_{app}' S_{ij}' S_{ij}' \rangle \end{aligned} \tag{6.16}$$

6.4 Discussion on the turbulent kinetic energy

Three groups of terms are present in Eq. (6.16), as in a Newtonian fluid, but with some differences.

The first group is a production one

$$\left(T_{R,ij} - T_{\mu,ij}\right)\langle S_{ij} \rangle \,. \tag{6.17}$$

In a Newtonian fluid only the term due to the product of Reynolds stresses and mean strain rates is present while in a GNF flow is present also a term which takes into account the polymeric stresses, with an opposite sign. In the mean equation, Eq. (6.10), the Reynolds stresses

component is added to the polymeric stresses while in Eq. (6.17) they subtract because they have a different influence on the fluid motion. If the Reynolds stresses transfer energy from the mean flow to increase the fluctuating component, the polymeric stresses will reduce these effects. In conclusion, the Reynolds stresses transfer energy from the mean flow to increase the fluctuating component while the polymeric stresses reduce the effects of the Reynolds stresses.

The second group, in extensive form, is a transport one

$$-\frac{\partial}{\partial x_j}\left(\langle\rho k' u_j'\rangle+\langle p' u_j'\rangle-\langle\mu_{app}\rangle\frac{\partial k}{\partial x_j}-\frac{\langle\mu_{app}\rangle}{\rho}\frac{\partial T_{R,ij}}{\partial x_i}-\langle\mu_{app}'\frac{\partial k'}{\partial x_j}\rangle-\langle\frac{\mu_{app}'}{\rho}\frac{\partial T_{R,ij}'}{\partial x_i}\rangle-2\langle u_i'\mu_{app}'\rangle\langle S_{ij}\rangle\right). \qquad (6.18)$$

The first four terms are present also in a Newtonian fluid while the remaining three terms, which are the mean product of instantaneous viscosity and each instantaneous variable, are present only in a GNF flow. The new term, appearing as the product of the mean rate of deformation tensor, the mean product of the velocity fluctuation and the apparent viscosity fluctuation, has a diffusive form, as the others present in the divergence operator, and is directly connected to the mean flow because is dependent on the mean rate of deformation tensor.

The third group, in extensive form, is the dissipation one

$$-2\langle\mu_{app}\rangle\langle S_{ij}'S_{ij}'\rangle-2\langle\mu_{app}'S_{ij}'S_{ij}'\rangle. \qquad (6.19)$$

Two terms are present because viscosity is split into mean and fluctuating component. The first one is the product of the mean viscosity and the mean square of the fluctuating shear rate while the second one is the mean of the product of the fluctuating viscosity and the square of the fluctuating shear rate. A term can be classified productive if positive, or if contributes to the increase of a certain variable, while is dissipative in the opposite case. In the second term, the viscosity fluctuations are unknown, a priori, as concurrent or not to the velocity fluctuations gradient and cannot be stated if these terms are productive or dissipative from a theoretical point

of view. The square of the fluctuating strain rates is positive but cannot be said a priori if it is a dissipative term when is multiplied for the viscosity fluctuations and averaged. The choice to call this term productive or dissipative depends on the similarity with the classical production or dissipation term. In conclusion, it is possible to consider the term with the fluctuating viscosity as an "increase" or a "decrease" of the production or an "increase" or a "decrease" of the dissipation.

6.5 Transport equations for mean and fluctuating shear rate

The equation for the dissipation rate, ε, of the turbulent kinetic energy is written in conservative form as

$$\rho \frac{D\varepsilon}{Dt} = f\left(x_j, t\right), \tag{6.20}$$

being defined, in analogy to [6.13], as

$$\varepsilon = \frac{2}{\rho}\langle \mu_{app} \rangle \langle \$^2 \rangle + \frac{2}{\rho}\langle \mu'_{app} \$^2 \rangle, \tag{6.21}$$

where

$$\$^2 = S'_{ij} S'_{ij}. \tag{6.22}$$

The transport equation for the rate of deformation tensor, S_{ij}, is obtained considering the symmetrical part of the gradient of Eq. (6.6). Using the definition of Ω_{ij}

$$\Omega_{ij} = \frac{1}{2}\left(\frac{\partial u_i}{\partial x_j} - \frac{\partial u_j}{\partial x_i} \right), \tag{6.23}$$

the transport equations for the S_{ij} components are

$$\rho\frac{\partial S_{ij}}{\partial t}+\rho u_k\frac{\partial S_{ij}}{\partial x_k}=-\frac{1}{2}\frac{\partial}{\partial x_i}\left(\frac{\partial p}{\partial x_j}\right)-\frac{1}{2}\frac{\partial}{\partial x_j}\left(\frac{\partial p}{\partial x_i}\right)+\frac{\partial}{\partial x_k}\left(\mu_{app}\frac{\partial S_{ij}}{\partial x_k}+S_{ij}\frac{\partial \mu_{app}}{\partial x_k}\right)+ \\ \left(-\rho S_{jk}^2+\rho\Omega_{jk}^2+\frac{\partial}{\partial x_k}\left(\left(S_{kj}-\Omega_{kj}\right)\frac{\partial \mu_{app}}{\partial x_j}\right)\right)\delta_{ij} \tag{6.24}$$

The details of the algebra are reported in Appendix B.

The transport equation for the square of the shear rate, S^2, is obtained multiplying Eq. (6.24) for each term of the rate of deformation tensor by itself and summing all of them.

$$\rho\frac{\partial}{\partial t}\left(\frac{S^2}{2}\right)+\rho u_k\frac{\partial}{\partial x_k}\left(\frac{S^2}{2}\right)=\frac{\partial}{\partial x_k}\left(\mu_{app}\frac{\partial}{\partial x_k}\left(\frac{S^2}{2}\right)+S^2\frac{\partial \mu_{app}}{\partial x_k}-S_{kj}\frac{\partial p}{\partial x_j}\right)+ \\ -\left(\frac{\partial}{\partial x_k}\left(\mu_{app}S_{ij}\right)\right)\frac{\partial S_{ij}}{\partial x_k}+\frac{\partial S_{kj}}{\partial x_k}\frac{\partial p}{\partial x_k} \tag{6.25}$$

A transport equation for the fluctuating components of the rate of deformation tensor is obtained by subtracting the mean equation from the instantaneous one

$$\rho\frac{\partial S'_{ij}}{\partial t}+\rho U_k\frac{\partial S'_{ij}}{\partial x_k}=-\rho u'_k\frac{\partial\langle S_{ij}\rangle}{\partial x_k}-\frac{1}{2}\frac{\partial}{\partial x_i}\left(\frac{\partial p'}{\partial x_j}\right)-\frac{1}{2}\frac{\partial}{\partial x_j}\left(\frac{\partial p'}{\partial x_i}\right)+ \\ \frac{\partial}{\partial x_k}\left(-\rho u'_k S'_{ij}+\langle\rho u'_k S'_{ij}\rangle-\frac{\partial}{\partial x_k}\left(\langle\mu'_{app}S'_{ij}\rangle\right)+\frac{\partial}{\partial x_k}\left(\mu_{app}S'_{ij}\right)+\frac{\partial}{\partial x_k}\left(\mu'_{app}\langle S_{ij}\rangle\right)\right)+ \\ \left(-2\rho S'_{jk}\langle S_{jk}\rangle+2\rho\Omega'_{jk}\langle\Omega_{jk}\rangle-\rho S'_{jk}S'_{jk}+\rho\Omega'_{jk}\Omega'_{jk}\right)\delta_{ij}+ \\ \left(\frac{\partial}{\partial x_k}\left(-\langle\left(S'_{kj}-\Omega'_{kj}\right)\frac{\partial\mu'_{app}}{\partial x_j}\rangle+\left(S'_{kj}-\Omega'_{kj}\right)\frac{\partial\mu_{app}}{\partial x_j}+\left(\langle S_{kj}\rangle-\langle\Omega_{kj}\rangle\right)\frac{\partial\mu'_{app}}{\partial x_j}\right)\right)\delta_{ij} \tag{6.26}$$

The conservation equation for the dissipative terms of the turbulent kinetic energy is written using the conservation equation for the variable $\$^2$, obtained multiplying the transport equation of each term for the rate of deformation tensor, Eq. (6.26), by itself and summing all of them. The details of the procedure are reported in Appendix C and the following expression is finally obtained

$$\rho\frac{D}{Dt}\left(\frac{\$^2}{2}\right)=\frac{1}{2}\nabla\left[T'_R\right]\vdots\nabla\langle[S]\rangle-\rho\nabla k'\cdot\left(\nabla\cdot\langle[S]\rangle\right)-\nabla\left(\mu'_{app}\langle[S]\rangle\right)\vdots\nabla[S']+$$
$$\nabla\cdot\left(-[S']\nabla p'-\rho\vec{u}'\frac{\$^2}{2}+\mu_{app}\nabla\left(\frac{\$^2}{2}\right)+\$^2\nabla\mu_{app}+[S']:\nabla\left(\mu'_{app}\langle[S]\rangle\right)+[S']\rho\nabla k-\frac{1}{2}[S']:\nabla\left(\left[T_R\right]+\left[T_\mu\right]\right)\right)+ \quad (6.27)$$
$$\nabla p'\cdot\left(\nabla\cdot[S']\right)-\nabla\left(\mu_{app}[S']\right)\vdots\nabla[S']+\frac{1}{2}\nabla\left(\left[T_R\right]+\left[T_\mu\right]\right)\vdots\nabla[S']-\rho\nabla k\cdot\left(\nabla\cdot[S']\right)$$

The conservation equation for the dissipation rate can be obtained by Eq. (6.21), using Eq. (6.27), and applying the principle of conservation. This operation is not trivial because viscosity is variable. For a Newtonian fluid the conservation equations can be obtained easily because each one has the same structure. Multiplication of each variable for the relative transport equation of the other and summation are necessary to derive the transport equation for the product of the two terms.

6.6 Transport equation for the apparent viscosity

In order to obtain the conservation equations for the turbulent dissipation rate the following equations are necessary:

- Transport equation of the apparent viscosity.
- Transport equation of the apparent viscosity, written to recognize terms similar to $\$^2$.
- Transport equation of the apparent viscosity multiplied for the transported term and summed to the product of the transport equation with the viscosity.

The apparent viscosity of a Newtonian fluid is a physical property while in a non–Newtonian *Reiner-Rivlin* fluid is function of the shear rate and can be generally written as function of S, on his side function of space and time, as

$$\mu_{app}=f\left(S\left(x_j,t\right)\right). \quad (6.28)$$

Taking into account the following relations

$$\frac{\partial \mu_{app}}{\partial t} = \frac{df}{dS}\frac{\partial S}{\partial t},\ \frac{\partial \mu_{app}}{\partial x_j} = \frac{df}{dS}\frac{\partial S}{\partial x_j}, \tag{6.29}$$

and deriving, the transport equation for the apparent viscosity can be finally obtained

$$\frac{\partial \mu_{app}}{\partial t} + u_j \frac{\partial \mu_{app}}{\partial x_j} = \frac{df}{dS}\frac{\partial S}{\partial t} + \frac{df}{dS} u_j \frac{\partial S}{\partial x_j} = \frac{df}{dS}\left(\frac{\partial S}{\partial t} + u_j \frac{\partial S}{\partial x_j}\right). \tag{6.30}$$

The apparent viscosity must be multiplied for the transport equation, Eq. (6.27), in order to have a structure similar to the transport equation of $\$^2$. Let assume the apparent viscosity is function of the square of the shear rate, S^2. To avoid confusion between the second and the first derivatives with respect the square of a variable let assume

$$S^2 = A. \tag{6.31}$$

The apparent viscosity is then

$$\mu_{app} = f\left(A\left(x_j, t\right)\right), \tag{6.32}$$

and, using the following relations

$$\frac{\partial \mu_{app}}{\partial t} = \frac{df}{dA}\frac{\partial S^2}{\partial t},\ \frac{\partial \mu_{app}}{\partial x_j} = \frac{df}{dA}\frac{\partial S^2}{\partial x_j}, \tag{6.33}$$

the transport equation for apparent viscosity can be finally written as

$$\frac{\partial \mu_{app}}{\partial t} + u_j \frac{\partial \mu_{app}}{\partial x_j} = \frac{df}{dA}\frac{\partial S^2}{\partial t} + \frac{df}{dA} u_j \frac{\partial S^2}{\partial x_j} = \frac{df}{dA}\left(\frac{\partial S^2}{\partial t} + u_j \frac{\partial S^2}{\partial x_j}\right). \tag{6.34}$$

Defining

$$C = \frac{df}{dA}, \tag{6.35}$$

and multiplying Eq. (6.25) by $2C$, Eq. (6.34) can be written as

$$\rho\frac{\partial\mu_{app}}{\partial t}+\rho u_k\frac{\partial\mu_{app}}{\partial x_k}=\frac{\partial}{\partial x_k}\left(\left(\mu_{app}+2CS^2\right)\frac{\partial\mu_{app}}{\partial x_k}-2CS_{kj}\frac{\partial p}{\partial x_j}\right)+ \left(\frac{\partial p}{\partial x_j}-\frac{\partial}{\partial x_k}\left(\mu_{app}S_{ij}\right)\right)\frac{\partial}{\partial x_k}\left(2CS_{ij}\right) \tag{6.36}$$

In conclusion, Eq. (6.36) is the transport equation of the apparent viscosity, which is a differential equation rather than an algebraic expression. The form of Eq. (6.36) is similar to the $\$^2$ transport equation.

6.7 Transport equation for turbulent dissipation rate

The turbulent dissipation rate is defined as

$$\varepsilon=\frac{2}{\rho}\langle\mu_{app}\rangle\langle\$^2\rangle+\frac{2}{\rho}\langle\mu'_{app}\$^2\rangle, \tag{6.37}$$

while its instantaneous component is

$$\varepsilon'=\frac{2}{\rho}\mu_{app}\$^2. \tag{6.38}$$

and its transport equation can be obtained by the sum of Eq. (6.27), multiplied by $4\frac{\mu_{app}}{\rho}$, and Eq. (6.36), multiplied by $\frac{2}{\rho}\$^2$. The instantaneous dissipation rate is finally averaged to give the detailed form of the transport equation

$$\rho\frac{\partial\varepsilon}{\partial t}+\rho U_k\frac{\partial\varepsilon}{\partial x_k}=\frac{2}{\rho}\left(\langle\mu_{app}\frac{\partial T'_{R,ij}}{\partial x_k}\rangle\frac{\partial\langle S_{ij}\rangle}{\partial x_k}\right)-4\langle\mu_{app}\frac{\partial k'}{\partial x_k}\rangle\frac{\partial\langle S_{kj}\rangle}{\partial x_j}+$$
$$\frac{1}{\rho}\frac{\partial T_{\mu,ij}}{\partial x_k}\frac{\partial}{\partial x_k}\left(T_{R,ij}+T_{\mu,ij}+2\langle\mu_{app}\rangle\langle S_{ij}\rangle\right)-2\frac{\partial T_{\mu,ij}}{\partial x_k}\frac{\partial k}{\partial x_j}+$$
$$\frac{\partial}{\partial x_k}\left(-\frac{4}{\rho}\langle\mu_{app}S'_{kj}\frac{\partial p'}{\partial x_j}\rangle-\frac{4}{\rho}\langle C\$^2S_{kj}\frac{\partial p}{\partial x_j}\rangle-\langle\rho u'_k\varepsilon'\rangle+\langle\mu_{app}\frac{\partial\varepsilon'}{\partial x_k}\rangle+2\langle\varepsilon'\left(1+\frac{CS^2}{\mu_{app}}\right)\frac{\partial\mu_{app}}{\partial x_k}\rangle\right)+, \quad (6.39)$$
$$\frac{\partial}{\partial x_k}\left(\frac{4}{\rho}\langle\mu_{app}S'_{ij}\frac{\partial}{\partial x_k}\left(\mu_{app}\langle S_{ij}\rangle\right)\rangle-\frac{1}{\rho}T_{\mu,ij}\frac{\partial}{\partial x_k}\left(T_{R,ij}+T_{\mu,ij}+2\langle\mu_{app}\rangle\langle S_{ij}\rangle\right)+2T_{\mu,ij}\frac{\partial k}{\partial x_j}\right)+$$
$$\frac{4}{\rho}\langle\frac{\partial}{\partial x_k}\left(\mu_{app}S'_{kj}\right)\frac{\partial p'}{\partial x_j}\rangle+\frac{4}{\rho}\langle\frac{\partial}{\partial x_k}\left(C\$^2S_{kj}\right)\frac{\partial p}{\partial x_j}\rangle-\frac{4}{\rho}\langle\frac{\partial}{\partial x_k}\left(\mu_{app}S_{ij}\right)\frac{\partial}{\partial x_k}\left(\mu_{app}S'_{ij}+C\$^2S_{ij}\right)\rangle$$

or, in compact form, as

$$\rho\frac{D\varepsilon}{Dt}=\frac{2}{\rho}\langle\mu_{app}\nabla\left[T'_R\right]\rangle:\nabla\langle\left[S\right]\rangle-4\langle\mu_{app}\nabla k'\rangle\cdot\left(\nabla\cdot\langle\left[S\right]\rangle\right)+$$
$$\frac{1}{\rho}\nabla\left[T_\mu\right]:\nabla\left(\left[T_R\right]+\left[T_\mu\right]+2\langle\mu_{app}\rangle\langle\left[S\right]\rangle\right)-2\nabla k\cdot\left(\nabla\cdot\left[T_\mu\right]\right)+$$
$$\nabla\cdot\left(-\frac{4}{\rho}\langle\mu_{app}\left[S'\right]\nabla p'\rangle-\frac{4}{\rho}\langle C\$^2\left[S\right]\nabla p\rangle-\langle\rho\vec{u}'\varepsilon'\rangle+\langle\mu_{app}\nabla\varepsilon'\rangle+2\langle\varepsilon'\left(1+\frac{CS^2}{\mu_{app}}\right)\nabla\mu_{app}\rangle\right)+. \quad (6.40)$$
$$\nabla\cdot\left(\frac{4}{\rho}\langle\mu_{app}\left[S'\right]:\nabla\left(\mu_{app}\langle\left[S\right]\rangle\right)\rangle+2\left[T_\mu\right]\nabla k-\frac{1}{\rho}\left[T_\mu\right]:\nabla\left(\left[T_R\right]+\left[T_\mu\right]+2\langle\mu_{app}\rangle\langle\left[S\right]\rangle\right)\right)+$$
$$\frac{4}{\rho}\langle\nabla p'\cdot\left(\nabla\cdot\mu_{app}\left[S'\right]\right)\rangle+\frac{4}{\rho}\langle\nabla\cdot\left(C\$^2\left[S\right]\right)\cdot\nabla p\rangle-\frac{4}{\rho}\langle\nabla\left(\mu_{app}\left[S\right]\right):\nabla\left(\mu_{app}\left[S'\right]+C\$^2\left[S\right]\right)\rangle$$

The details are reported in Appendix D.

6.8 Discussion on the conservation equation for the dissipation rate

Each group of terms of Eq. (6.40) is discussed in the following.

The group of four terms, in explicit form,

$$\frac{2}{\rho}\left(\langle\mu_{app}\frac{\partial T'_{R,ij}}{\partial x_k}\rangle\frac{\partial\langle S_{ij}\rangle}{\partial x_k}\right)-4\langle\mu_{app}\frac{\partial k'}{\partial x_k}\rangle\frac{\partial\langle S_{kj}\rangle}{\partial x_j}+$$
$$\frac{1}{\rho}\frac{\partial T_{\mu,ij}}{\partial x_k}\frac{\partial}{\partial x_k}\left(T_{R,ij}+T_{\mu,ij}+2\langle\mu_{app}\rangle\langle S_{ij}\rangle\right)-2\frac{\partial T_{\mu,ij}}{\partial x_k}\frac{\partial k}{\partial x_j}\quad,\tag{6.43}$$

represents the production of dissipation rate which involves the instantaneous apparent viscosity, the instantaneous Reynolds stresses tensor, the mean rate of deformation tensor, the instantaneous turbulent kinetic energy, the gradient of the polymeric stresses tensor and the gradient of the total stresses tensor acting on the mean flow. In a Newtonian fluid the similar term is the product of the gradients of the Reynolds stresses tensor and the mean rate of deformation tensor multiplied the viscosity.

The group of eight terms, in explicit form,

$$\frac{\partial}{\partial x_k}\left(-\frac{4}{\rho}\langle\mu_{app}S'_{kj}\frac{\partial p'}{\partial x_j}\rangle-\frac{4}{\rho}\langle C\$^2\,S_{kj}\frac{\partial p}{\partial x_j}\rangle-\langle\rho u'_k\varepsilon'\rangle+\langle\mu_{app}\frac{\partial\varepsilon'}{\partial x_k}\rangle+2\langle\varepsilon'\left(1+\frac{CS^2}{\mu_{app}}\right)\frac{\partial\mu_{app}}{\partial x_k}\rangle\right)+$$
$$\frac{\partial}{\partial x_k}\left(\frac{4}{\rho}\langle\mu_{app}S'_{ij}\frac{\partial}{\partial x_k}\left(\mu_{app}\langle S_{ij}\rangle\right)\rangle-\frac{1}{\rho}T_{\mu,ij}\frac{\partial}{\partial x_k}\left(T_{R,ij}+T_{\mu,ij}+2\langle\mu_{app}\rangle\langle S_{ij}\rangle\right)+2T_{\mu,ij}\frac{\partial k}{\partial x_j}\right)\tag{6.44}$$

represents the transport of dissipation rate. The first and the second terms are connected to the static pressure, respectively fluctuating and instantaneous, with the first one similar to a Newtonian fluid. The following three terms represent the turbulent transport due to vortices, apparent viscosity fluctuations and molecular transport or average apparent viscosity. The fifth term involves molecular and turbulent transport due to viscosity fluctuations and is present because of the viscosity variation with the position. The remaining three terms are completely new. The sixth term, which involves the mean rate of deformation tensor and the apparent viscosity, is similar to the transport of the turbulent kinetic energy term, where is present the product of the fluctuating viscosity, the tensors of the mean strain rate and the fluctuating velocity. The seven term is made with the product of the polymeric stresses by the gradient of the

total stresses acting on the mean flow. The eighth term is made with the product of the polymeric stresses by the gradient of the turbulent kinetic energy.

The group of three terms, in explicit form,

$$\frac{4}{\rho}\langle\frac{\partial}{\partial x_k}\left(\mu_{app}S'_{kj}\right)\frac{\partial p'}{\partial x_j}\rangle+\frac{4}{\rho}\langle\frac{\partial}{\partial x_k}\left(C\$^2\,S_{kj}\right)\frac{\partial p}{\partial x_j}\rangle-\frac{4}{\rho}\langle\frac{\partial}{\partial x_k}\left(\mu_{app}S_{ij}\right)\frac{\partial}{\partial x_k}\left(\mu_{app}S'_{ij}+C\$^2\,S_{ij}\right)\rangle\,, \qquad (6.45)$$

represents the dissipation contribution. The first two terms are related to the pressure, where the first one is similar to a Newtonian fluid while the second one is due to the transport equation of the apparent viscosity and is new. The last term is a typical dissipation one made by the sum of a term similar to a Newtonian fluid and the last one due to the equation for the transport of viscosity.

6.9 Order of Magnitude Analysis

The previous equations for the kinetic energy, the apparent viscosity and the rate of dissipation are examined with an order of magnitude analysis, according to [6.22]. The following characteristics scales are introduced for a Newtonian fluid,

- l, viscous length scale,
- L, geometric length scale,
- u, velocity fluctuation scale,
- λ, Taylor length scale,
- U, Mean velocity scale.

A space derivative is assumed inversely proportional, in the order of magnitude analysis, to an appropriate length which depends on the origin of the term, e.g. the component of the mean

deformation rate tensor is of the order of $\frac{U}{l}$ in a viscous term while is of the order of $\frac{U}{L}$ in a convective term.

Dealing with a non-Newtonian fluid and assuming a variable viscosity it is necessary to introduce also the scales for the average viscosity and its fluctuation. Under the hypothesis of investigating boundary layers it is assumed that the average viscosity is proportional to the wall value

$$\langle \mu_{app} \rangle \sim \mu_w , \tag{6.46}$$

while, as far as the viscosity fluctuation μ' is concerned, it is introduced a new length scale, called shear-viscous λ_μ, related to the polymeric stress tensor, Eq. (6.15),

$$T_{\mu,ij} = 2\langle \mu'_{app} S'_{ij} \rangle \sim \mu' \frac{u}{\lambda_\mu} . \tag{6.47}$$

The order of magnitude of the derivative of a fluctuating variable is proportional to $\frac{1}{\lambda_\mu}$ when is relative to the fluctuating viscosity while is proportional to $\frac{1}{\lambda}$ when is relative to the mean viscosity

The order of magnitude of the rate of dissipation is assumed valid also for a non-Newtonian fluid, i.e. the first term on the right hand side of Eq. (6.37) is

$$\varepsilon \sim \frac{u^3}{l} \sim \frac{\mu_w}{\rho} \frac{u^2}{\lambda^2} \tag{6.48}$$

From Eq. (6.48) it is possible to conclude that

$$\frac{\rho u \lambda}{\mu_w} = \mathrm{Re}_\lambda \sim \frac{l}{\lambda} , \tag{6.49}$$

Equation (6.49) can be used to evaluate the order of magnitude of the shear-viscous length scale. The assumption that each term of the dissipation rate equation has the same order of magnitude implies that the second term on the right hand side of Eq. (6.37) has the order of magnitude $\frac{\mu'}{\rho}\frac{u^2}{\lambda_\mu \lambda}$, or, in other words, that the product of $S'_{ij}S'_{ij}$ for the fluctuating viscosity is of the order $\frac{u}{\lambda_\mu}\frac{u}{\lambda}$. Since the viscosity fluctuation is smaller than the average one, it is possible to conclude that the shear-viscous length scale is smaller than the Taylor one

$$\frac{u^3}{l} \sim \frac{\mu_w}{\rho}\frac{u^2}{\lambda^2} \sim \frac{\mu'}{\rho}\frac{u^2}{\lambda_\mu \lambda} \Rightarrow \frac{\lambda_\mu}{\lambda} \sim \frac{\mu'}{\mu_w} \Rightarrow \frac{\lambda_\mu}{\lambda} \ll 1, \tag{6.50}$$

In the boundary layer, in analogy to [6.22], it is obtained

$$\rho u^2 \frac{U}{L} \sim \rho \frac{u^3}{l} \Rightarrow \frac{l}{L} \sim \frac{u}{U}. \tag{6.51}$$

The order of magnitude analysis of the stress terms has given the following conclusions:

- for the Reynolds stresses

$$T_{R,ij} = -\langle \rho u'_i u'_j \rangle \sim \rho u^2 \sim \mu_w \frac{u}{\lambda} \mathrm{Re}_\lambda, \tag{6.52}$$

- for the polymeric stresses

$$T_{\mu,ij} = 2\langle \mu'_{app} S'_{ij} \rangle \sim \mu' \frac{u}{\lambda_\mu} \sim \mu_w \frac{u}{\lambda}, \tag{6.53}$$

- for the apparent viscosity stresses

$$2\langle \mu_{app} \rangle \langle S_{ij} \rangle \sim \mu_w \frac{U}{l} \sim \mu_w \frac{u}{\lambda} \frac{1}{\mathrm{Re}_\lambda} \left(\frac{U}{u} \right). \tag{6.54}$$

The order of magnitude analysis for the turbulent kinetic energy, Eq. (6.16), presented with details in Appendix E, has given the following conclusions:

If $\mathrm{Re}_\lambda = O(1)$ it is possible to neglect the term containing $\frac{\lambda_\mu}{\lambda}$, i.e. the shear-viscous length scale, which is smaller than the Taylor length scale, and the equation of kinetic energy becomes

$$\begin{aligned}&\frac{\partial}{\partial t}(\rho k)+U_j\frac{\partial}{\partial x_j}(\rho k)=\left(T_{R,ij}-T_{\mu,ij}\right)\langle S_{ij}\rangle+\\&-\frac{\partial}{\partial x_j}\left(\langle\rho k'u_j'\rangle+\langle p'u_j'\rangle-\langle\mu_{app}'\frac{\partial k'}{\partial x_j}\rangle-\langle\mu_{app}\rangle\frac{\partial k}{\partial x_j}-\frac{\langle\mu_{app}\rangle}{\rho}\frac{\partial T_{R,ij}}{\partial x_i}-\langle\frac{\mu_{app}'}{\rho}\frac{\partial T_{R,ij}'}{\partial x_i}\rangle\right)-\rho\varepsilon\end{aligned}, \tag{6.55}$$

- if $\mathrm{Re}_\lambda = O(10)$ it is possible to neglect also the terms proportional to $\frac{1}{\mathrm{Re}_\lambda^2}$ and the equation of kinetic energy becomes

$$\frac{\partial}{\partial t}(\rho k)+U_j\frac{\partial}{\partial x_j}(\rho k)=\left(T_{R,ij}-T_{\mu,ij}\right)\langle S_{ij}\rangle-\frac{\partial}{\partial x_j}\left(\langle\rho k'u_j'\rangle+\langle p'u_j'\rangle-\langle\mu_{app}'\frac{\partial k'}{\partial x_j}\rangle-\langle\frac{\mu_{app}'}{\rho}\frac{\partial T_{R,ij}'}{\partial x_i}\rangle\right)-\rho\varepsilon, \tag{6.56}$$

- if $\mathrm{Re}_\lambda = O(100)$ it is possible to neglect also the terms proportional to $\frac{1}{\mathrm{Re}_\lambda}$. Further on, the polymeric stresses can be neglected versus the Reynolds stresses, in the production group of terms, and the kinetic energy equation becomes.

$$\frac{\partial}{\partial t}(\rho k)+U_j\frac{\partial}{\partial x_j}(\rho k)=T_{R,ij}\langle S_{ij}\rangle-\frac{\partial}{\partial x_j}\left(\langle\rho k'u_j'\rangle+\langle p'u_j'\rangle\right)-\rho\varepsilon. \tag{6.57}$$

Several terms of the dissipation rate equation involve the derivatives of the product of the viscosity and the rate of strain tensor. Assuming that the fluctuations of strain rate tensor are bigger than the mean value it is possible to conclude that

$$\frac{S_{ij}'}{\langle S_{ij}\rangle}=\frac{\frac{u}{\lambda}}{\frac{U}{l}}>1\Rightarrow \mathrm{Re}_\lambda\frac{u}{U}<1, \tag{6.58}$$

Moreover, the derivatives of a mean variable in the transport term are of order $\frac{1}{l}$, while the mean of the product of the derivative of a fluctuating variable is of the order $\frac{1}{\lambda}$, regardless of the viscosity component. The order of magnitude of the derivative of the fluctuating viscosity is $\frac{1}{\lambda}$ in the terms with the mean product of a fluctuating variable and the derivative of the fluctuating viscosity.

The turbulent dissipation rate, Eq. (6.39), is examined with an order of magnitude analysis and the details are presented in Appendix F. The conclusions of the order of magnitude analysis for the turbulent dissipation rate are the followings.

If $\mathrm{Re}_\lambda = O(1)$ it is possible to neglect the terms containing the ratio $\frac{\lambda_\mu}{\lambda}$ because the shear-viscous length scale is smaller than the Taylor length scale, and the energy dissipation rate reduces to

$$\begin{aligned}
&\rho\frac{\partial\varepsilon}{\partial t}+\rho U_k\frac{\partial\varepsilon}{\partial x_k}=\frac{2}{\rho}\left(\langle\mu_{app}\frac{\partial T'_{R,ij}}{\partial x_k}\rangle\frac{\partial\langle S_{ij}\rangle}{\partial x_k}\right)-4\langle\mu_{app}\frac{\partial k'}{\partial x_k}\rangle\frac{\partial\langle S_{kj}\rangle}{\partial x_j}+\frac{1}{\rho}\frac{\partial T_{\mu,ij}}{\partial x_k}\frac{\partial}{\partial x_k}\left(T_{R,ij}+T_{\mu,ij}\right)-2\frac{\partial T_{\mu,ij}}{\partial x_k}\frac{\partial k}{\partial x_j}+\\
&\frac{\partial}{\partial x_k}\left(-\frac{4}{\rho}\langle\mu_{app}S'_{kj}\frac{\partial p'}{\partial x_j}\rangle-\frac{4}{\rho}\frac{CS^2}{\mu_{app}}\langle\mu_{app}S_{kj}\frac{\partial p}{\partial x_j}\rangle-\langle\rho u'_k\varepsilon'\rangle+\langle\mu_{app}\frac{\partial\varepsilon'}{\partial x_k}\rangle+2\left(1+\frac{CS^2}{\mu_{app}}\right)\varepsilon\frac{\partial\langle\mu_{app}\rangle}{\partial x_k}\right)+\\
&\frac{\partial}{\partial x_k}\left(-\frac{1}{\rho}T_{\mu,ij}\frac{\partial}{\partial x_k}\left(T_{R,ij}+T_{\mu,ij}\right)+2T_{\mu,ij}\frac{\partial k}{\partial x_j}\right)+\frac{4}{\rho}\langle\frac{\partial}{\partial x_k}\left(\mu_{app}S'_{kj}\right)\frac{\partial p'}{\partial x_j}\rangle+\frac{4}{\rho}\frac{CS^2}{\mu_{app}}\langle\frac{\partial}{\partial x_k}\left(\mu_{app}S_{kj}\right)\frac{\partial p}{\partial x_j}\rangle+\\
&-\frac{CS^2}{\mu_{app}}\frac{1}{\rho}\frac{\partial}{\partial x_k}\left(2\langle\mu_{app}\rangle\langle S_{ij}\rangle\right)\frac{\partial T_{\mu,ij}}{\partial x_k}-\frac{CS^2}{\mu_{app}}\frac{1}{\rho}\frac{\partial}{\partial x_k}\left(2\langle\mu_{app}\rangle\langle S_{ij}\rangle\right)\frac{\partial}{\partial x_k}\left(2\langle\mu_{app}\rangle\langle S_{ij}\rangle+T_{\mu,ij}\right)+\\
&-\left(1+\frac{CS^2}{\mu_{app}}\right)\frac{1}{\rho}\langle\frac{\partial}{\partial x_k}\left(2\mu_{app}S'_{ij}\right)\frac{\partial}{\partial x_k}\left(2\mu_{app}S'_{ij}\right)\rangle
\end{aligned}\tag{6.59}$$

if $\mathrm{Re}_\lambda = O(10)$ it is possible to neglect also the terms proportional to $\frac{1}{\mathrm{Re}_\lambda^2}$ or proportional to $\frac{1}{\mathrm{Re}_\lambda^3}\left(\frac{U}{u}\right)$, or proportional to $\frac{1}{\mathrm{Re}_\lambda^4}\left(\frac{U}{u}\right)^2$, and the energy dissipation rate reduces to

$$\begin{aligned}
&\rho\frac{\partial\varepsilon}{\partial t}+\rho U_k\frac{\partial\varepsilon}{\partial x_k}=\frac{2}{\rho}\left(\langle\mu_{app}\frac{\partial T'_{R,ij}}{\partial x_k}\rangle\frac{\partial\langle S_{ij}\rangle}{\partial x_k}\right)-4\langle\mu_{app}\frac{\partial k'}{\partial x_k}\rangle\frac{\partial\langle S_{kj}\rangle}{\partial x_j}+\frac{1}{\rho}\frac{\partial T_{\mu,ij}}{\partial x_k}\frac{\partial T_{R,ij}}{\partial x_k}-2\frac{\partial T_{\mu,ij}}{\partial x_k}\frac{\partial k}{\partial x_j}+\\
&\frac{\partial}{\partial x_k}\left(-\frac{4}{\rho}\langle\mu_{app}S'_{kj}\frac{\partial p'}{\partial x_j}\rangle-\frac{4}{\rho}\frac{CS^2}{\mu_{app}}\langle\mu_{app}S_{kj}\frac{\partial p}{\partial x_j}\rangle-\langle\rho u'_k\varepsilon'\rangle+\langle\mu'_{app}\frac{\partial\varepsilon'}{\partial x_k}\rangle\right)+\\
&\frac{\partial}{\partial x_k}\left(-\frac{1}{\rho}T_{\mu,ij}\frac{\partial T_{R,ij}}{\partial x_k}+2T_{\mu,ij}\frac{\partial k}{\partial x_j}\right)+\frac{4}{\rho}\langle\frac{\partial}{\partial x_k}\left(\mu_{app}S'_{kj}\right)\frac{\partial p'}{\partial x_j}\rangle+\frac{4}{\rho}\frac{CS^2}{\mu_{app}}\langle\frac{\partial}{\partial x_k}\left(\mu_{app}S_{kj}\right)\frac{\partial p}{\partial x_j}\rangle\\
&-\left(1+\frac{CS^2}{\mu_{app}}\right)\frac{1}{\rho}\langle\frac{\partial}{\partial x_k}\left(2\mu_{app}S'_{ij}\right)\frac{\partial}{\partial x_k}\left(2\mu_{app}S'_{ij}\right)\rangle
\end{aligned}\tag{6.60}$$

if $\mathrm{Re}_\lambda = O(100)$ it is possible to neglect also the terms proportional to $\frac{1}{\mathrm{Re}_\lambda}$, and the energy dissipation rate reduces to

$$\begin{aligned}
&\rho\frac{\partial\varepsilon}{\partial t}+\rho U_k\frac{\partial\varepsilon}{\partial x_k}=\frac{\partial}{\partial x_k}\left(-\left(1+\frac{CS^2}{\mu_{app}}\right)\frac{4}{\rho}\langle\mu_{app}S'_{kj}\frac{\partial p'}{\partial x_j}\rangle-\langle\rho u'_k\varepsilon'\rangle\right)\\
&+\left(1+\frac{CS^2}{\mu_{app}}\right)\frac{4}{\rho}\langle\frac{\partial}{\partial x_k}\left(\mu_{app}S'_{kj}\right)\frac{\partial p'}{\partial x_j}\rangle-\left(1+\frac{CS^2}{\mu_{app}}\right)\frac{1}{\rho}\langle\frac{\partial}{\partial x_k}\left(2\mu_{app}S'_{ij}\right)\frac{\partial}{\partial x_k}\left(2\mu_{app}S'_{ij}\right)\rangle;
\end{aligned}\tag{6.61}$$

6.10 Discussion on the equations simplified with the order of magnitude analysis

The results of the order of magnitude analysis can be expressed in terms of three non-dimensional groups: Reynolds number, turbulence intensity (ratio between fluctuating and mean velocity) and ratio between shear-viscous and Taylor length scales, for the first time introduced in the present work.

As far as the momentum equation is concerned, if $\mathrm{Re}_\lambda = O(1)$ viscous stresses are dominant in the boundary layer if the turbulence intensity is very low but also if the turbulence intensity is higher, say around 10%, when the contribution of the turbulent stresses is higher. The polymeric stresses are smaller than the Reynolds ones, which have intermediate values and are confirmed by the results of [6.23]. At higher Reynolds numbers the Reynolds stresses become dominant and the polymeric ones are greater.

As far as the turbulent kinetic energy is concerned, only one term is proportional to the ratio between shear-viscous and Taylor length scales, ratio which can be neglected for every turbulence intensity, while all others terms proportional to $1/\mathrm{Re}_\lambda$. If $\mathrm{Re}_\lambda = O(1)$ all terms have the same importance in describing the conservation of turbulent kinetic energy, differently from what happens in the momentum equation where the viscous stresses have a dominant importance. If $\mathrm{Re}_\lambda = O(10)$ the molecular viscous terms are negligible, compared to fluctuating and eddy viscosity ones, and the Reynolds stresses are dominant with respect to the polymeric ones in the production term. Finally, if $\mathrm{Re}_\lambda = O(100)$ also the fluctuating viscosity terms are negligible and the equation is formally the same as for a Newtonian fluid, because only the convective terms are important, since all terms related to the nature of the material are negligible.

As far as the turbulent dissipation rate equation is concerned the terms proportional to the ratio of the polymeric to the Taylor length scales can be neglected in analogy to the others equations. Other terms are inversely proportional to the turbulence intensity and the Reynolds number Re_λ and, if $\mathrm{Re}_\lambda = O(1)$, the dominant terms are those inversely proportional to the turbulent intensity.

The parameter $\frac{n-1}{2}$, which appears in the order of magnitude analysis is null for a Newtonian fluid and depends on the constitutive equation, but in many cases of technical interest is lower than one, and the turbulence intensity is always multiplied for it. If $\mathrm{Re}_\lambda = O(10)$ the terms proportional to the average viscosity are negligible but those proportional to the viscosity fluctuation are not, in analogy to the turbulent kinetic energy equation. Finally, if $\mathrm{Re}_\lambda = O(100)$ also the terms proportional to the viscosity fluctuation are negligible but the non-Newtonian features are still present because some terms are proportional to the parameter $\left(1+\frac{CS^2}{\mu_{app}}\right)$, which contain information relative to the constitutive equation of the fluid. In conclusion, the turbulent dissipation rate equation takes into account the non-Newtonian features of the fluid.

6.11 Conclusions

The mass conservation equation is the same as for a Newtonian fluid because is not dependent on the fluid, while the momentum conservation equation is different because of the presence of the polymeric stresses.

The turbulent kinetic energy and dissipation rate equations contain terms proportional to the viscosity of a Newtonian fluid while, for a GNF, they are proportional to the mean product of the instantaneous variables. Further on, the equations for a non-Newtonian fluid contain terms with viscosity fluctuations and derivatives of the viscosity.

In conclusion, the exact equations derived for a GNF can reduce to those for a Newtonian fluid if the apparent viscosity fluctuations and the C coefficient disappear and the mean apparent

viscosity is constant. An important conclusion of the present paper is the derivation of the dissipation rate in the conservative form of Eq. (6.20), [6.24].

Appendix

The transport equations for a GNF are derived similarly to a Newtonian fluid with a variable apparent viscosity.

A. Transport equation for turbulent kinetic energy

The following equations for the fluctuating components are derived by subtraction of the mean equations from the instantaneous ones.

The mass conservation equation is

$$\frac{\partial u_k'}{\partial x_k} = 0 . \qquad (6.A.1)$$

The momentum conservation equation is

$$\rho \frac{\partial u_i'}{\partial t} + \rho U_k \frac{\partial u_i'}{\partial x_k} = -\frac{\partial p'}{\partial x_i} + \frac{\partial}{\partial x_k}\left(\langle \mu_{app} \rangle \left(\frac{\partial u_i'}{\partial x_k} + \frac{\partial u_k'}{\partial x_i} \right) + \mu_{app}' \left(\frac{\partial U_i}{\partial x_k} + \frac{\partial U_k}{\partial x_i} \right) - \rho u_k' U_i \right) + \frac{\partial}{\partial x_k}\left(\mu_{app}' \left(\frac{\partial u_i'}{\partial x_k} + \frac{\partial u_k'}{\partial x_i} \right) - \langle \mu_{app}' \left(\frac{\partial u_i'}{\partial x_k} + \frac{\partial u_k'}{\partial x_i} \right) \rangle - \rho u_k' u_i' + \langle \rho u_k' u_i' \rangle \right) . \qquad (6.A.2)$$

The turbulent kinetic energy is obtained multiplying Eq. (6.A.2) by u_i', summing up all components and averaging. The same process than in a Newtonian fluid is used for the viscous terms with the derivation by part

$$u_i' \frac{\partial}{\partial x_k}\left(\langle\mu_{app}\rangle\left(\frac{\partial u_i'}{\partial x_k}+\frac{\partial u_k'}{\partial x_i}\right)\right)=\frac{\partial}{\partial x_k}\left(\langle\mu_{app}\rangle u_i'\frac{\partial u_i'}{\partial x_k}+\langle\mu_{app}\rangle u_i'\frac{\partial u_k'}{\partial x_i}\right)-\frac{\partial u_i'}{\partial x_k}\left(\langle\mu_{app}\rangle\left(\frac{\partial u_i'}{\partial x_k}+\frac{\partial u_k'}{\partial x_i}\right)\right)= \\ \frac{\partial}{\partial x_k}\left(\langle\mu_{app}\rangle\frac{\partial}{\partial x_k}\left(\frac{u_i'u_i'}{2}\right)+\langle\mu_{app}\rangle\frac{\partial u_i'u_k'}{\partial x_i}-\langle\mu_{app}\rangle u_k'\frac{\partial u_i'}{\partial x_i}\right)-\frac{\partial u_i'}{\partial x_k}\left(\langle\mu_{app}\rangle\left(\frac{\partial u_i'}{\partial x_k}+\frac{\partial u_k'}{\partial x_i}\right)\right) \quad ,(6.A.3)$$

$$u_i' \frac{\partial}{\partial x_k}\left(\mu_{app}'\left(\frac{\partial U_i}{\partial x_k}+\frac{\partial U_k}{\partial x_i}\right)\right)=\frac{\partial}{\partial x_k}\left(\mu_{app}'u_i'\left(\frac{\partial U_i}{\partial x_k}+\frac{\partial U_k}{\partial x_i}\right)\right)-\left(\frac{\partial U_i}{\partial x_k}+\frac{\partial U_k}{\partial x_i}\right)\mu_{app}'\frac{\partial u_i'}{\partial x_k}. \qquad (6.A.4)$$

Summing up it is obtained the equation for the turbulent kinetic energy (6.16); where the terms with similar physical meaning are close each other, while the Reynolds stresses are closer to those with the fluctuating viscosity components.

B. Transport equation for the shear rate

The exact form of the variable apparent viscosity is obtained by using the fundamental expressions of the rate of deformation tensor and the terms of the rotation rate tensor, $\Omega_{i,j}$, based on mass conservation and relative definitions.

The following basic equations are employed

$$S_{ii}=0, \qquad (6.B.1)$$

$$-\frac{\partial S_{ij}}{\partial x_k}+\frac{1}{2}\left(\frac{\partial S_{ik}}{\partial x_j}+\frac{\partial S_{jk}}{\partial x_i}\right)+\frac{1}{2}\left(\frac{\partial \Omega_{ik}}{\partial x_j}+\frac{\partial \Omega_{jk}}{\partial x_i}\right)=0, \qquad (6.B.2)$$

which allow to derive the conservation equations for the instantaneous variables in a form similar to those for a Newtonian fluid.

The non-Newtonian terms are obtained by changing the order of derivation, summing and subtracting the different terms. Applying the $\frac{\partial}{\partial x_j}$ operator to u_i component and the $\frac{\partial}{\partial x_i}$ operator

to u_j component and dividing by 2 the transport equation for the rate of deformation tensor components can be obtained. Using (6.B.1), (6.B.2) and the following relation

$$\begin{aligned} &-\rho\frac{1}{2}\frac{\partial u_k}{\partial x_j}\frac{\partial u_i}{\partial x_k}-\rho\frac{1}{2}\frac{\partial u_k}{\partial x_i}\frac{\partial u_j}{\partial x_k}= \\ &-\rho\frac{1}{2}\left(S_{kj}+\Omega_{kj}\right)\left(S_{ik}+\Omega_{ik}\right)-\rho\frac{1}{2}\left(S_{ki}+\Omega_{ki}\right)\left(S_{jk}+\Omega_{jk}\right)=-\rho S_{ik}S_{jk}+\rho\Omega_{ik}\Omega_{jk} \end{aligned} \quad . \tag{6.B.3}$$

Eq. (6.24) can be obtained.

The multiplication of each equation for the transported variable allows obtaining:

$$\begin{aligned} &\rho\frac{\partial}{\partial t}\left(\frac{S_{ij}S_{ij}}{2}\right)+\rho u_k\frac{\partial}{\partial x_k}\left(\frac{S_{ij}S_{ij}}{2}\right)=-\frac{1}{2}\frac{\partial}{\partial x_i}\left(S_{ij}\frac{\partial p}{\partial x_j}\right)-\frac{1}{2}\frac{\partial}{\partial x_j}\left(S_{ij}\frac{\partial p}{\partial x_i}\right)+ \\ &\frac{\partial}{\partial x_k}\left(\mu_{app}\frac{\partial}{\partial x_k}\left(\frac{S_{ij}S_{ij}}{2}\right)+S_{ij}S_{ij}\frac{\partial\mu_{app}}{\partial x_k}\right)-\mu_{app}\frac{\partial S_{ij}}{\partial x_k}\frac{\partial S_{ij}}{\partial x_k}-\frac{\partial\mu_{app}}{\partial x_k}\frac{\partial}{\partial x_k}\left(\frac{S_{ij}S_{ij}}{2}\right)+ \\ &\frac{1}{2}\frac{\partial p}{\partial x_j}\frac{\partial S_{ij}}{\partial x_i}+\frac{1}{2}\frac{\partial p}{\partial x_i}\frac{\partial S_{ij}}{\partial x_j}+S_{jj}\left(-\rho S_{jk}^2+\rho\Omega_{jk}^2+\frac{\partial}{\partial x_k}\left(\left(S_{kj}-\Omega_{kj}\right)\frac{\partial\mu_{app}}{\partial x_j}\right)\right)\delta_{ij} \end{aligned} \quad . \tag{6.B.4}$$

Finally the conservation equation for the square of the shear rate in the instantaneous form is obtained as Eq. (6.25).

C. Transport equation for $\$^2$

The transport equation for the fluctuations of the rate of deformation tensor is derived similarly to the instantaneous case. The multiplication of Eq. (6.24) for the corresponding transported variable allows writing the following equation:

$$\rho\frac{\partial}{\partial t}\left(\frac{S'_{ij}S'_{ij}}{2}\right)+\rho U_k\frac{\partial}{\partial x_k}\left(\frac{S'_{ij}S'_{ij}}{2}\right)=-\rho u'_k S'_{ij}\frac{\partial\langle S_{ij}\rangle}{\partial x_k}-\frac{1}{2}\frac{\partial}{\partial x_i}\left(S'_{ij}\frac{\partial p'}{\partial x_j}\right)-\frac{1}{2}\frac{\partial}{\partial x_j}\left(S'_{ij}\frac{\partial p'}{\partial x_i}\right)+$$
$$\frac{\partial}{\partial x_k}\left(-\rho u'_k\frac{S'_{ij}S'_{ij}}{2}+\mu_{app}\frac{\partial}{\partial x_k}\left(\frac{S'_{ij}S'_{ij}}{2}\right)+S'_{ij}S'_{ij}\frac{\partial\mu_{app}}{\partial x_k}\right)+\frac{1}{2}\frac{\partial p'}{\partial x_j}\frac{\partial S'_{ij}}{\partial x_i}+\frac{1}{2}\frac{\partial p'}{\partial x_i}\frac{\partial S'_{ij}}{\partial x_j}+$$
$$\frac{\partial}{\partial x_k}\left(+\langle\rho u'_k S'_{ij}\rangle S'_{ij}-S'_{ij}\frac{\partial}{\partial x_k}\left(\langle\mu'_{app}S'_{ij}\rangle\right)+S'_{ij}\frac{\partial}{\partial x_k}\left(\mu'_{app}\langle S_{ij}\rangle\right)\right)+ \qquad . \qquad (6.C.1)$$
$$-\left(\langle\rho u'_k S'_{ij}\rangle-\frac{\partial}{\partial x_k}\left(\langle\mu'_{app}S'_{ij}\rangle\right)+\frac{\partial}{\partial x_k}\left(\mu_{app}S'_{ij}\right)+\frac{\partial}{\partial x_k}\left(\mu'_{app}\langle S_{ij}\rangle\right)\right)\frac{\partial S'_{ij}}{\partial x_k}+$$
$$\left(-2\rho S'_{jj}S'_{jk}\langle S_{jk}\rangle+2\rho S'_{jj}\Omega'_{jk}\langle\Omega_{jk}\rangle-\rho S'_{jj}S'_{jk}S'_{jk}+\rho S'_{jj}\Omega'_{jk}\Omega'_{jk}\right)\delta_{ij}+$$
$$\left(S'_{jj}\frac{\partial}{\partial x_k}\left(-\langle\left(S'_{kj}-\Omega'_{kj}\right)\frac{\partial\mu'_{app}}{\partial x_j}\rangle+\left(S'_{kj}-\Omega'_{kj}\right)\frac{\partial\mu_{app}}{\partial x_j}+\left(\langle S_{kj}\rangle-\langle\Omega_{kj}\rangle\right)\frac{\partial\mu'_{app}}{\partial x_j}\right)\right)\delta_{ij}$$

Recalling that

$$\langle u'_x\begin{bmatrix}S'_{xx} & S'_{xy}\\ S'_{yx} & S'_{yy}\end{bmatrix}\rangle=\frac{1}{2}\frac{\partial}{\partial x}\begin{bmatrix}\langle u'_x u'_x\rangle & \langle u'_x u'_y\rangle\\ \langle u'_y u'_x\rangle & \langle u'_y u'_y\rangle\end{bmatrix}+\begin{bmatrix}0 & \frac{1}{2}\frac{\partial k}{\partial y}\\ \frac{1}{2}\frac{\partial k}{\partial y} & -\frac{\partial k}{\partial x}\end{bmatrix}, \qquad (6.C.2)$$

and

$$\langle u'_y\begin{bmatrix}S'_{xx} & S'_{xy}\\ S'_{yx} & S'_{yy}\end{bmatrix}\rangle=\frac{1}{2}\frac{\partial}{\partial y}\begin{bmatrix}\langle u'_x u'_x\rangle & \langle u'_x u'_y\rangle\\ \langle u'_y u'_x\rangle & \langle u'_y u'_y\rangle\end{bmatrix}+\begin{bmatrix}-\frac{\partial k}{\partial y} & \frac{1}{2}\frac{\partial k}{\partial x}\\ \frac{1}{2}\frac{\partial k}{\partial x} & 0\end{bmatrix}, \qquad (6.C.3)$$

the following equation is obtained

$$-\rho u'_x\left[S'\right]:\frac{\partial\langle\left[S\right]\rangle}{\partial x}-\rho u'_y\left[S'\right]:\frac{\partial\langle\left[S\right]\rangle}{\partial y}=\frac{1}{2}\left(\nabla\left[T'_R\right]:\nabla\langle\left[S\right]\rangle+2\rho\nabla k'\cdot\nabla\cdot\langle\left[S\right]\rangle\right). \qquad (6.C.4)$$

The summation of all transport equations with the square of the fluctuating rate of deformation tensor components allows obtaining Eq. (6.27) in its final form.

D. Transport equation for the dissipation rate of turbulent kinetic energy

The step by step algebra to derive the equation for the dissipation rate is the following.

D.1- First step

Multiplication of Eq. (6.C.1) by $4\frac{\mu_{app}}{\rho}$

$$\frac{2}{\rho}\mu_{app}\rho\frac{D\$^2}{Dt}=\frac{2}{\rho}\mu_{app}\nabla[T_R']:\nabla\langle[S]\rangle-4\mu_{app}\nabla k'\cdot\left(\nabla\cdot\langle[S]\rangle\right)-\frac{4}{\rho}\mu_{app}\nabla\left(\mu_{app}'\langle[S]\rangle\right):\nabla[S']-\frac{4}{\rho}\nabla\mu_{app}\cdot[S']:\nabla\left(\mu_{app}'\langle[S]\rangle\right)$$
$$\nabla\cdot\left(-\frac{4}{\rho}\mu_{app}[S']\nabla p'-\rho\vec{a}'\frac{2}{\rho}\mu_{app}\$^2+\mu_{app}\frac{2}{\rho}\mu_{app}\nabla\$^2+\frac{4}{\rho}\mu_{app}\$^2\nabla\mu_{app}\right)+$$
$$\nabla\cdot\left(\frac{4}{\rho}\mu_{app}[S']:\nabla\left(\mu_{app}'\langle[S]\rangle\right)+4\mu_{app}'[S']\nabla k-\frac{2}{\rho}\mu_{app}'[S']:\nabla\left([T_R]+[T_\mu]\right)+4\langle\mu_{app}\rangle[S']\nabla k-\frac{2}{\rho}\langle\mu_{app}\rangle[S']:\nabla\left([T_R]+[T_\mu]\right)\right)+\cdot \qquad (6.D.1)$$
$$\frac{4}{\rho}\nabla\mu_{app}\cdot[S']\nabla p'+\frac{2}{\rho}\nabla\mu_{app}\cdot\rho\vec{a}'\$^2-\frac{2}{\rho}\nabla\mu_{app}\cdot\mu_{app}\nabla\$^2-\frac{4}{\rho}\nabla\mu_{app}\cdot\$^2\nabla\mu_{app}-4\nabla\mu_{app}'\cdot[S']\nabla k+\frac{2}{\rho}\nabla\mu_{app}'\cdot[S']:\nabla\left([T_R]+[T_\mu]\right)$$
$$\frac{4}{\rho}\mu_{app}\nabla p'\cdot\left(\nabla\cdot[S']\right)-\frac{4}{\rho}\mu_{app}\nabla\left(\mu_{app}[S']\right):\nabla[S']+\frac{2}{\rho}\mu_{app}\nabla\left([T_R]+[T_\mu]\right):\nabla[S']-4\mu_{app}\nabla k\cdot\left(\nabla\cdot[S']\right)+$$
$$-4\nabla\langle\mu_{app}\rangle\cdot[S']\nabla k+\frac{2}{\rho}\nabla\langle\mu_{app}\rangle\cdot[S']:\nabla\left([T_R]+[T_\mu]\right)$$

D.2- Second step

Use the expression $\$^2=[S']:[S']$ to decompose some terms of Eq. (6.D.1)

$$\frac{2}{\rho}\mu_{app}\rho\frac{D\$^2}{Dt}=\frac{2}{\rho}\mu_{app}\nabla[T_R']:\nabla\langle[S]\rangle-4\mu_{app}\nabla k'\cdot\left(\nabla\cdot\langle[S]\rangle\right)-\frac{4}{\rho}\nabla\left(\mu_{app}'\langle[S]\rangle\right):\nabla\left(\mu_{app}[S']\right)+$$
$$\nabla\cdot\left(-\frac{4}{\rho}\mu_{app}[S']\nabla p'-\rho\vec{a}'\frac{2}{\rho}\mu_{app}\$^2+\mu_{app}\frac{2}{\rho}\mu_{app}\nabla\$^2+\frac{4}{\rho}\mu_{app}\$^2\nabla\mu_{app}\right)+$$
$$\nabla\cdot\left(\frac{4}{\rho}\mu_{app}[S']:\nabla\left(\mu_{app}'\langle[S]\rangle\right)+2[T_\mu']\nabla k-\frac{1}{\rho}[T_\mu']:\nabla\left([T_R]+[T_\mu]\right)+4\langle\mu_{app}\rangle[S']\nabla k-\frac{2}{\rho}\langle\mu_{app}\rangle[S']:\nabla\left([T_R]+[T_\mu]\right)\right)+\cdot \qquad (6.D.2)$$
$$\frac{2}{\rho}\nabla\mu_{app}\cdot\rho\vec{a}'[S']:[S']-\frac{4}{\rho}\nabla\left(\mu_{app}[S']\right):\nabla\left(\mu_{app}[S']\right)+\frac{4}{\rho}\nabla p'\cdot\left(\nabla\cdot\mu_{app}[S']\right)+\frac{1}{\rho}\nabla\left([T_R]+[T_\mu]\right):\nabla[T_\mu']-2\nabla k\cdot\left(\nabla\cdot[T_\mu']\right)+$$
$$-4\left(\nabla\cdot\langle\mu_{app}\rangle[S']\right)\cdot\nabla k+\frac{2}{\rho}\nabla\left(\langle\mu_{app}\rangle[S']\right):\nabla\left([T_R]+[T_\mu]\right)$$

D.3- Third step

The instantaneous viscosity μ_{app} needs to be summed to the turbulent one \$. The symbol $\frac{D}{Dt}$ is used for the total derivative in the conservation equation of the apparent viscosity, recalling the relation

$$\frac{\overline{D}}{\overline{D}t}=\frac{D}{Dt}+\vec{u}'\cdot\nabla. \tag{6.D.3}$$

It is then possible to write

$$\begin{aligned}&2\frac{\$^2}{\rho}\rho\frac{\partial\mu_{app}}{\partial t}+2\frac{\$^2}{\rho}\rho\vec{U}\cdot\nabla\mu_{app}+2\frac{\$^2}{\rho}\rho\vec{u}'\cdot\nabla\mu_{app}=\\&\nabla\cdot\left(-4\frac{\$^2}{\rho}C[S]\nabla p+2\mu_{app}\frac{\$^2}{\rho}\nabla\mu_{app}+4\frac{\$^2}{\rho}CS^2\nabla\mu_{app}\right)+\frac{4}{\rho}\nabla\left(C\$^2\right)\cdot\left([S]\nabla p\right)\\&-\frac{1}{C}\nabla\left(2C\frac{\$^2}{\rho}\right)\cdot\left(\mu_{app}\nabla\mu_{app}\right)-\frac{4}{\rho}\nabla\left(C\$^2\right)\cdot\left(S^2\nabla\mu_{app}\right)+4\frac{\$^2}{\rho}C\left(\nabla\cdot[S]\right)\cdot\nabla p-4\frac{\$^2}{\rho}C\nabla\left(\mu_{app}[S]\right):\nabla[S]\end{aligned}. \tag{6.D.4}$$

D.4- Forth step

Collection of the different terms

$$\begin{aligned}&2\frac{\$^2}{\rho}\rho\frac{D\mu_{app}}{Dt}=\nabla\cdot\left(-\frac{4}{\rho}C\$^2[S]\nabla p+2\mu_{app}\frac{\$^2}{\rho}\nabla\mu_{app}+\frac{4}{\rho}\$^2CS^2\nabla\mu_{app}\right)+\\&\nabla\cdot\left(\frac{4}{\rho}C\$^2[S]\right)\cdot\nabla p-\frac{4}{\rho}\nabla\left(\mu_{app}[S]\right):\nabla\left(C\$^2[S]\right)-\frac{2}{\rho}\nabla\mu_{app}\cdot\rho\vec{u}'[S']:[S']\end{aligned}. \tag{6.D.5}$$

D.5- Fifth step

Summation of Eq. (6.D.2) and Eq. (6.D.5) gives

$$\frac{2}{\rho}\mu_{app}\rho\frac{D\$^2}{Dt}+\frac{2}{\rho}\$^2\rho\frac{D\mu_{app}}{Dt}=\frac{2}{\rho}\mu_{app}\nabla[T'_R]:\nabla[S]\rangle-4\mu_{app}\nabla k'\cdot(\nabla\cdot\langle[S]\rangle)$$
$$\nabla\cdot\left(-\rho\vec{u}'\frac{2}{\rho}\mu_{app}\$^2+\mu_{app}\frac{2}{\rho}\mu_{app}\nabla\$^2+\mu_{app}\frac{2}{\rho}\$^2\nabla\mu_{app}+\frac{4}{\rho}\mu_{app}\$^2\nabla\mu_{app}+\frac{4}{\rho}\$^2C\$^2\nabla\mu_{app}\right)+$$
$$\nabla\cdot\left(\frac{4}{\rho}\mu_{app}[S']:\nabla\left(\mu'_{app}\langle[S]\rangle\right)+2[T'_\mu]\nabla k-\frac{1}{\rho}[T'_\mu]:\nabla\left([T_R]+[T_\mu]\right)+4\langle\mu_{app}\rangle[S']\nabla k-\frac{2}{\rho}\langle\mu_{app}\rangle[S']:\nabla\left([T_R]+[T_\mu]\right)\right)+. \qquad (6.D.6)$$
$$\nabla\cdot\left(-\frac{4}{\rho}\mu_{app}[S']\nabla p'-\frac{4}{\rho}C\$^2[S]\nabla p\right)-\frac{4}{\rho}\nabla\left(\mu_{app}[S']\right):\nabla\left(\mu_{app}[S']\right)-\frac{4}{\rho}\nabla\left(\mu_{app}[S]\right):\nabla\left(C\$^2[S]\right)+$$
$$-\frac{4}{\rho}\nabla\left(\mu'_{app}\langle[S]\rangle\right):\nabla\left(\mu_{app}[S']\right)+\frac{4}{\rho}\nabla p'\cdot\left(\nabla\cdot\mu_{app}[S']\right)+\nabla\cdot\left(\frac{4}{\rho}C\$^2[S]\right)\cdot\nabla p+$$
$$\frac{1}{\rho}\nabla\left([T_R]+[T_\mu]\right):\nabla[T'_\mu]-2\nabla k\cdot\left(\nabla\cdot[T'_\mu]\right)-4\left(\nabla\cdot\langle\mu_{app}\rangle[S']\right)\cdot\nabla k+\frac{2}{\rho}\nabla\left(\langle\mu_{app}\rangle[S']\right):\nabla\left([T_R]+[T_\mu]\right)$$

D.6- Sixth step

Introduction of the instantaneous dissipation rate $\frac{2}{\rho}\mu_{app}\$^2=\varepsilon'$, multiplication and division for C of the apparent viscosity gives

$$\rho\frac{D\varepsilon'}{Dt}=\frac{2}{\rho}\mu_{app}\nabla[T'_R]:\nabla[S]\rangle-4\mu_{app}\nabla k'\cdot\left(\nabla\cdot\langle[S]\rangle\right)+\frac{1}{\rho}\nabla\left([T_R]+[T_\mu]\right):\nabla[T'_\mu]-2\nabla k\cdot\left(\nabla\cdot[T'_\mu]\right)+$$
$$\nabla\cdot\left(-\rho\vec{u}'\varepsilon'+\mu_{app}\nabla\varepsilon'+2\varepsilon'\left(1+\frac{C\$^2}{\mu_{app}}\right)\nabla\mu_{app}+\frac{4}{\rho}\mu_{app}[S']:\nabla\left(\mu'_{app}\langle[S]\rangle\right)+2[T'_\mu]\nabla k-\frac{1}{\rho}[T'_\mu]:\nabla\left([T_R]+[T_\mu]\right)\right)+$$
$$\nabla\cdot\left(-\frac{4}{\rho}\mu_{app}[S']\nabla p'-\frac{4}{\rho}C\$^2[S]\nabla p+4\langle\mu_{app}\rangle[S']\nabla k-\frac{2}{\rho}\langle\mu_{app}\rangle[S']:\nabla\left([T_R]+[T_\mu]\right)\right)+\frac{4}{\rho}\nabla p'\cdot\left(\nabla\cdot\mu_{app}[S']\right)+ . \qquad (6.D.7)$$
$$\nabla\cdot\left(\frac{4}{\rho}C\$^2[S]\right)\cdot\nabla p-\frac{4}{\rho}\nabla\left(\mu_{app}[S']\right):\nabla\left(\mu_{app}[S']\right)-\frac{4}{\rho}\nabla\left(\mu_{app}[S]\right):\nabla\left(C\$^2[D]\right)-\frac{4}{\rho}\nabla\left(\mu'_{app}\langle[S]\rangle\right):\nabla\left(\mu_{app}[S']\right)+$$
$$-4\left(\nabla\cdot\langle\mu_{app}\rangle[S']\right)\cdot\nabla k+\frac{2}{\rho}\nabla\left(\langle\mu_{app}\rangle[S']\right):\nabla\left([T_R]+[T_\mu]\right)$$

D.7- Seventh step

Further algebra is necessary for the dissipation terms

$$\rho\frac{D\varepsilon'}{Dt}=\frac{2}{\rho}\mu_{app}\nabla[T'_R]:\nabla[S]\rangle-4\mu_{app}\nabla k'\cdot\left(\nabla\cdot\langle[S]\rangle\right)+\frac{1}{\rho}\nabla[T'_\mu]:\nabla\left([T_R]+[T_\mu]+2\langle\mu_{app}\rangle[S]\rangle\right)-2\nabla k\cdot\left(\nabla\cdot[T'_\mu]\right)$$
$$\nabla\cdot\left(-\rho\vec{I}\varepsilon'+\mu_{app}\nabla\varepsilon'+2\varepsilon'\left(1+\frac{CS^2}{\mu_{app}}\right)\nabla\mu_{app}+\frac{4}{\rho}\mu_{app}[S']:\nabla\left(\mu_{app}\langle[S]\rangle\right)+2[T'_\mu]\nabla k-\frac{1}{\rho}[T'_\mu]:\nabla\left([T_R]+[T_\mu]+2\langle\mu_{app}\rangle[S]\rangle\right)\right)+ \quad . \quad (6.D.8)$$
$$\nabla\cdot\left(4\langle\mu_{app}\rangle[S']\nabla k-\frac{2}{\rho}\langle\mu_{app}\rangle[S']:\nabla\left([T_R]+[T_\mu]+2\langle\mu_{app}\rangle[S]\rangle\right)-\frac{4}{\rho}\mu_{app}[S']\nabla p'-\frac{4}{\rho}CS^2[S]\nabla p\right)+\frac{4}{\rho}\nabla p'\cdot\left(\nabla\cdot\mu_{app}[S']\right)+$$
$$\nabla\cdot\left(\frac{4}{\rho}CS^2[S]\right)\cdot\nabla p-\frac{4}{\rho}\nabla\left(\mu_{app}[S]\right):\nabla\left(\mu_{app}[S']+CS^2[S]\right)-4\left(\nabla\cdot\langle\mu_{app}\rangle[S']\right)\cdot\nabla k+\frac{2}{\rho}\nabla\left(\langle\mu_{app}\rangle[S']\right):\nabla\left([T_R]+[T_\mu]+2\langle\mu_{app}\rangle[S]\rangle\right)$$

D.8- Eight step

Averaging the previous equation allows obtaining the dissipation rate equation as Eq. (6.40).

E. Order of magnitude analysis of turbulent kinetic energy

The transport group of the turbulent kinetic energy equation contains seven terms with the following orders of magnitude:

- first one $\frac{\partial}{\partial x_j}\left(\langle\rho k'u'_j\rangle\right)\sim\rho\frac{u^3}{l}$, (6.E.1)

- second one $\frac{\partial}{\partial x_j}\left(\langle p'u'_j\rangle\right)\sim\rho\frac{u^3}{l}$, (6.E.2)

- third one $\frac{\partial}{\partial x_j}\left(\langle\mu'_{app}\frac{\partial k'}{\partial x_j}\rangle\right)\sim\frac{\mu'}{l}\frac{u^2}{\lambda_\mu}\sim\rho\frac{u^3}{l}\frac{1}{\mathrm{Re}_\lambda}$, (6.E.3)

- fourth one $\frac{\partial}{\partial x_j}\left(\langle\mu_{app}\rangle\frac{\partial k}{\partial x_j}\right)\sim\frac{\mu_w}{l}\frac{u^2}{l}\sim\rho\frac{u^3}{l}\frac{1}{\mathrm{Re}_\lambda^2}$, (6.E.4)

- fifth one $\frac{\partial}{\partial x_j}\left(\langle u'_i\mu'_{app}\rangle\langle S_{ij}\rangle\right)\sim\frac{1}{l}u\mu'\frac{U}{l}\sim\rho\frac{u^3}{l}\frac{1}{\mathrm{Re}_\lambda^2}\left(\frac{U}{u}\right)\left(\frac{\lambda_\mu}{\lambda}\right)$, (6.E.5)

- sixth one $\frac{\partial}{\partial x_j}\left(\frac{\langle\mu_{app}\rangle}{\rho}\frac{\partial T_{R,ij}}{\partial x_i}\right)\sim\frac{\mu_w}{l}\frac{u^2}{l}\sim\rho\frac{u^3}{l}\frac{1}{\mathrm{Re}_\lambda^2}$. (6.E.6)

- seventh one $\frac{\partial}{\partial x_j}\left(\langle\frac{\mu'_{app}}{\rho}\frac{\partial T'_{R,ij}}{\partial x_i}\rangle\right)\sim\frac{\mu'}{l}\frac{u^2}{\lambda_\mu}\sim\rho\frac{u^3}{l}\frac{1}{\mathrm{Re}_\lambda}$, (6.E.7)

F. Order of magnitude analysis of the dissipation rate of turbulent kinetic energy

The convective term, on the left hand side of Eq. (6.37) is of the order

$$U_j\frac{\partial}{\partial x_j}(\rho\varepsilon)\sim U\frac{\rho}{L}\frac{u^3}{l}\sim\rho\frac{u^4}{l^2}. \quad (6.F.1)$$

The production group contains six terms:

- the first one can be split in two parts, which have the same order of magnitude

$$\begin{aligned}
&\frac{2}{\rho}\left(\langle\mu_{app}\frac{\partial T'_{R,ij}}{\partial x_k}\rangle\frac{\partial\langle S_{ij}\rangle}{\partial x_k}\right)=\frac{2}{\rho}\langle\mu_{app}\rangle\frac{\partial T_{R,ij}}{\partial x_k}\frac{\partial\langle S_{ij}\rangle}{\partial x_k}+\frac{2}{\rho}\langle\mu'_{app}\frac{\partial T'_{R,ij}}{\partial x_k}\rangle\frac{\partial\langle S_{ij}\rangle}{\partial x_k};\\
&\frac{2}{\rho}\langle\mu_{app}\rangle\frac{\partial T_{R,ij}}{\partial x_k}\frac{\partial\langle S_{ij}\rangle}{\partial x_k}\sim\frac{1}{\rho}\mu_w\frac{\rho u^2}{\lambda}\frac{1}{L}\frac{U}{l}\sim\rho\frac{u^4}{l^2}\frac{1}{\mathrm{Re}_\lambda};\\
&\frac{2}{\rho}\langle\mu'_{app}\frac{\partial T'_{R,ij}}{\partial x_k}\rangle\frac{\partial\langle S_{ij}\rangle}{\partial x_k}\sim\frac{1}{\rho}\mu'\frac{\rho u^2}{\lambda_\mu}\frac{1}{L}\frac{U}{l}\sim\rho\frac{u^4}{l^2}\frac{1}{\mathrm{Re}_\lambda};
\end{aligned} \quad (6.F.2)$$

- the second one can be split in two parts, which have the same order of magnitude

$$\begin{aligned}
&-4\langle\mu_{app}\frac{\partial k'}{\partial x_k}\rangle\frac{\partial\langle S_{kj}\rangle}{\partial x_j}=-4\langle\mu_{app}\rangle\frac{\partial k}{\partial x_k}\frac{\partial\langle S_{kj}\rangle}{\partial x_j}-4\langle\mu'_{app}\frac{\partial k'}{\partial x_k}\rangle\frac{\partial\langle S_{kj}\rangle}{\partial x_j};\\
&-4\langle\mu_{app}\rangle\frac{\partial k}{\partial x_k}\frac{\partial\langle S_{kj}\rangle}{\partial x_j}\sim\mu_w\frac{u^2}{\lambda}\frac{1}{L}\frac{U}{l}\sim\rho\frac{u^4}{l^2}\frac{1}{\mathrm{Re}_\lambda};\\
&-4\langle\mu'_{app}\frac{\partial k'}{\partial x_k}\rangle\frac{\partial\langle S_{kj}\rangle}{\partial x_j}\sim\mu'\frac{u^2}{\lambda_\mu}\frac{1}{L}\frac{U}{l}\sim\rho\frac{u^4}{l^2}\frac{1}{\mathrm{Re}_\lambda};
\end{aligned} \quad , \quad (6.F.3)$$

- the third one gives

$$\frac{1}{\rho}\frac{\partial T_{\mu,ij}}{\partial x_k}\frac{\partial T_{R,ij}}{\partial x_k}\sim\frac{1}{\rho}\frac{1}{l}\mu'\frac{u}{\lambda_\mu}\frac{\rho u^2}{l}\sim\frac{1}{\mathrm{Re}_\lambda}\rho\frac{u^4}{l^2}, \quad (6.F.4)$$

- the fourth one gives

$$\frac{1}{\rho}\frac{\partial T_{\mu,ij}}{\partial x_k}\frac{\partial T_{\mu,ij}}{\partial x_k} \sim \frac{1}{\rho}\frac{1}{l}\mu'\frac{u}{\lambda_\mu}\frac{1}{l}\mu'\frac{u}{\lambda_\mu} \sim \frac{1}{\mathrm{Re}_\lambda^2}\rho\frac{u^4}{l^2}, \tag{6.F.5}$$

- the fifth one gives

$$\frac{1}{\rho}\frac{\partial T_{\mu,ij}}{\partial x_k}\frac{\partial}{\partial x_k}\left(2\langle\mu_{app}\rangle\langle S_{ij}\rangle\right) \sim \frac{1}{\rho}\frac{1}{l}\mu'\frac{u}{\lambda_\mu}\frac{1}{l}\mu_w\frac{U}{l} \sim \frac{1}{\mathrm{Re}_\lambda^3}\rho\frac{u^4}{l^2}\left(\frac{U}{u}\right), \tag{6.F.6}$$

- the sixth one gives

$$-2\frac{\partial T_{\mu,ij}}{\partial x_k}\frac{\partial k}{\partial x_j} \sim \frac{1}{l}\mu'\frac{u}{\lambda_\mu}\frac{u^2}{l} \sim \frac{1}{\mathrm{Re}_\lambda}\rho\frac{u^4}{l^2}. \tag{6.F.7}$$

For non-Newtonian fluids two of the most used inelastic rheological models are considered: Herschel-Bukley

$$\mu_{app} = \frac{\tau_0}{\left(S^2\right)^{\frac{1}{2}}} + k_\tau\left(S^2\right)^{\frac{n-1}{2}} \Rightarrow C = -\frac{1}{2}\frac{\tau_0}{\left(S^2\right)^{\frac{3}{2}}} + \frac{n-1}{2}k_\tau\left(S^2\right)^{\frac{n-3}{2}} \Rightarrow$$

$$\frac{CS^2}{\mu_{app}} = -\frac{1}{2}\frac{\frac{\tau_0}{\left(S^2\right)^{\frac{1}{2}}} + (1-n)k_\tau\left(S^2\right)^{\frac{n-1}{2}}}{\frac{\tau_0}{\left(S^2\right)^{\frac{1}{2}}} + k_\tau\left(S^2\right)^{\frac{n-1}{2}}} = -\frac{1}{2} + \frac{n}{2}\frac{1}{\frac{\tau_0}{k_\tau\left(S^2\right)^{\frac{n}{2}}} + 1} \Rightarrow \begin{cases} \left|\frac{n}{2} - \frac{1}{2}\right| \le \left|\frac{CS^2}{\mu_{app}}\right| \le \frac{1}{2}; n \in [0,2] \\ \frac{1}{2} \le \left|\frac{CS^2}{\mu_{app}}\right| \le \left|\frac{n}{2} - \frac{1}{2}\right|; n \notin [0,2] \end{cases}, \tag{6.F.8}$$

and Carreau-Yassuda

$$\mu_{app} = \mu_0 + \frac{\mu_\infty - \mu_0}{\left(1 + \left(\lambda_{CY}\right)\left(S^2\right)^{\frac{n}{2}}\right)} \Rightarrow C = -\frac{n}{2}\frac{\mu_\infty - \mu_0}{\left(1 + \left(\lambda_{CY}\right)\left(S^2\right)^{\frac{n}{2}}\right)^2}\left(\lambda_{CY}\right)\left(S^2\right)^{\frac{n-2}{2}} \Rightarrow$$

$$\frac{CS^2}{\mu_{app}} = -\frac{n}{2}\left(1 - \frac{\mu_0 + \frac{\mu_\infty - \mu_0}{\left(1 + \left(\lambda_{CY}\right)\left(S^2\right)^{\frac{n}{2}}\right)^2}}{\mu_0 + \frac{\mu_\infty - \mu_0}{\left(1 + \left(\lambda_{CY}\right)\left(S^2\right)^{\frac{n}{2}}\right)}}\right) \Rightarrow 0 \le \left|\frac{CS^2}{\mu_{app}}\right| \le \left|\frac{n}{2}\right|, \tag{6.F.9}$$

with the conclusion that the ratio $\frac{CS^2}{\mu_{app}}$ can be considered constant.

Assuming

$$\frac{CS^2}{\mu_{app}} \sim \frac{n-1}{2}, \tag{6.F.10}$$

it is concluded, in agreement to [6.16], that

$$S^2 = \langle S_{ij}^2 \rangle + 2\langle S_{ij} \rangle S'_{ij} + \$^2 \approx \$^2, \tag{6.F.11}$$

The transport group contains eight terms:

- the first and the second terms, i.e. the pressure ones, can be written as

$$\frac{\partial}{\partial x_k}\left(-\frac{4}{\rho}\langle \mu_{app} S'_{kj} \frac{\partial p'}{\partial x_j}\rangle - \frac{4}{\rho}\langle C\$^2 S_{kj} \frac{\partial p}{\partial x_j}\rangle\right) \approx \frac{\partial}{\partial x_k}\left(-\frac{4}{\rho}\langle \mu_{app} S'_{kj} \frac{\partial p'}{\partial x_j}\rangle - \frac{C\$^2}{\mu_{app}}\frac{4}{\rho}\langle \mu_{app} S_{kj} \frac{\partial p}{\partial x_j}\rangle\right) \approx$$
$$\frac{\partial}{\partial x_k}\left(-\left(1+\frac{CS^2}{\mu_{app}}\right)\frac{4}{\rho}\left(\langle \mu_{app}\rangle\langle S'_{kj} \frac{\partial p'}{\partial x_j}\rangle + \langle \mu'_{app} S'_{kj} \frac{\partial p'}{\partial x_j}\rangle\right) - \frac{CS^2}{\mu_{app}}\frac{4}{\rho}\left(\langle \mu_{app}\rangle\langle S_{kj}\rangle \frac{\partial P}{\partial x_j} + \langle S_{kj}\rangle\langle \mu'_{app} \frac{\partial p'}{\partial x_j}\rangle + \langle \mu'_{app} S'_{kj}\rangle \frac{\partial P}{\partial x_j}\right)\right) \tag{6.F.12}$$

with the following orders of magnitude:

$$\frac{\partial}{\partial x_k}\left(-\left(1+\frac{CS^2}{\mu_{app}}\right)\frac{4}{\rho}\langle \mu_{app}\rangle\langle S'_{kj} \frac{\partial p'}{\partial x_j}\rangle\right) \sim \frac{1}{l}\left(1+\frac{n-1}{2}\right)\frac{\mu_w}{\rho}\frac{u}{\lambda}\frac{\rho u^2}{\lambda} \sim \left(1+\frac{n-1}{2}\right)\rho\frac{u^4}{l^2}, \tag{6.F.13}$$

$$\frac{\partial}{\partial x_k}\left(-\left(1+\frac{CS^2}{\mu_{app}}\right)\frac{4}{\rho}\langle \mu'_{app} S'_{kj} \frac{\partial p'}{\partial x_j}\rangle\right) \sim \frac{1}{l}\left(1+\frac{n-1}{2}\right)\frac{\mu'}{\rho}\frac{u}{\lambda_\mu}\frac{\rho u^2}{\lambda} \sim \left(1+\frac{n-1}{2}\right)\rho\frac{u^4}{l^2}, \tag{6.F.14}$$

$$\frac{\partial}{\partial x_k}\left(-\frac{CS^2}{\mu_{app}}\frac{4}{\rho}\langle \mu_{app}\rangle\langle S_{kj}\rangle \frac{\partial P}{\partial x_j}\right) \sim \frac{1}{l}\frac{n-1}{2}\frac{\mu_w}{\rho}\frac{U}{l}\frac{\rho U^2}{L} \sim \frac{n-1}{2}\rho\frac{u^4}{l^2}\frac{1}{\mathrm{Re}_\lambda^2}\left(\frac{U}{u}\right)^2, \tag{6.F.15}$$

$$\frac{\partial}{\partial x_k}\left(-\frac{CS^2}{\mu_{app}}\frac{4}{\rho}\langle S_{kj}\rangle\langle \mu'_{app} \frac{\partial p'}{\partial x_j}\rangle\right) \sim \frac{1}{l}\frac{n-1}{2}\frac{1}{\rho}\frac{U}{l}\mu'\frac{\rho u^2}{\lambda_\mu} \sim \frac{n-1}{2}\rho\frac{u^4}{l^2}\frac{1}{\mathrm{Re}_\lambda}\left(\frac{U}{u}\right), \tag{6.F.16}$$

$$\frac{\partial}{\partial x_k}\left(-\frac{CS^2}{\mu_{app}}\frac{4}{\rho}\langle \mu'_{app} S'_{kj}\rangle \frac{\partial P}{\partial x_j}\right) \sim \frac{1}{l}\frac{n-1}{2}\frac{1}{\rho}\mu'\frac{u}{\lambda_\mu}\frac{\rho U^2}{L} \sim \frac{n-1}{2}\rho\frac{u^4}{l^2}\frac{1}{\mathrm{Re}_\lambda}\left(\frac{U}{u}\right). \tag{6.F.17}$$

- the third term gives

$$\frac{\partial}{\partial x_k}\left(\langle \rho u_k' \varepsilon' \rangle\right) \sim \rho \frac{u^4}{l^2}, \tag{6.F.18}$$

- the forth one can be split in two, giving

$$\begin{aligned}
&\frac{\partial}{\partial x_k}\left(\langle \mu_{app} \frac{\partial \varepsilon'}{\partial x_k} \rangle\right) = \frac{\partial}{\partial x_k}\left(\langle \mu_{app} \rangle \frac{\partial \varepsilon}{\partial x_k}\right) + \frac{\partial}{\partial x_k}\left(\langle \mu_{app}' \frac{\partial \varepsilon'}{\partial x_k} \rangle\right); \\
&\frac{\partial}{\partial x_k}\left(\langle \mu_{app} \rangle \frac{\partial \varepsilon}{\partial x_k}\right) \sim \mu_w \frac{u^3}{l^3} \sim \rho \frac{u^4}{l^2} \frac{1}{\mathrm{Re}_\lambda^2}; \\
&\frac{\partial}{\partial x_k}\left(\langle \mu_{app}' \frac{\partial \varepsilon'}{\partial x_k} \rangle\right) \sim \frac{1}{l} \mu' \frac{u^3}{l \lambda_\mu} \sim \rho \frac{u^4}{l^2} \frac{1}{\mathrm{Re}_\lambda};
\end{aligned} \tag{6.F.19}$$

- the fifth one can be written as

$$\langle \varepsilon' \left(1 + \frac{CS^2}{\mu_{app}}\right) \frac{\partial \mu_{app}}{\partial x_k} \rangle \approx \left(1 + \frac{CS^2}{\mu_{app}}\right) \langle \varepsilon' \frac{\partial \mu_{app}}{\partial x_k} \rangle = \left(1 + \frac{CS^2}{\mu_{app}}\right) \left(\varepsilon \frac{\partial \langle \mu_{app} \rangle}{\partial x_k} + \langle \varepsilon' \frac{\partial \mu_{app}'}{\partial x_k} \rangle \right). \tag{6.F.20}$$

with the orders of magnitude

$$\frac{\partial}{\partial x_k}\left(2\left(1 + \frac{CS^2}{\mu_{app}}\right) \varepsilon \frac{\partial \langle \mu_{app} \rangle}{\partial x_k}\right) \sim \frac{1}{l}\left(1 + \frac{n-1}{2}\right) \frac{u^3}{l} \frac{\mu_w}{l} \sim \left(1 + \frac{n-1}{2}\right) \rho \frac{u^4}{l^2} \frac{1}{\mathrm{Re}_\lambda^2}, \tag{6.F.21}$$

$$\frac{\partial}{\partial x_k}\left(2\left(1 + \frac{CS^2}{\mu_{app}}\right) \langle \varepsilon' \frac{\partial \mu_{app}'}{\partial x_k} \rangle\right) \sim \frac{1}{l}\left(1 + \frac{n-1}{2}\right) \frac{u^3}{l} \frac{\mu'}{\lambda} \sim \left(1 + \frac{n-1}{2}\right) \rho \frac{u^4}{l^2} \frac{1}{\mathrm{Re}_\lambda} \left(\frac{\lambda_\mu}{\lambda}\right). \tag{6.F.22}$$

- the sixth one can be simplified as

$$\begin{aligned}
&\frac{\partial}{\partial x_k}\left(\frac{4}{\rho} \langle \mu_{app} S_{ij}' \frac{\partial}{\partial x_k}\left(\mu_{app} \langle S_{ij} \rangle\right) \rangle\right) = \\
&\frac{\partial}{\partial x_k}\left(\frac{4}{\rho} \langle \mu_{app} \rangle \langle S_{ij}' \frac{\partial}{\partial x_k}\left(\mu_{app}' \langle S_{ij} \rangle\right) \rangle + \frac{1}{\rho} 2 \langle \mu_{app}' S_{ij}' \rangle \frac{\partial}{\partial x_k}\left(2 \langle \mu_{app} \rangle \langle S_{ij} \rangle\right) \rangle + \frac{4}{\rho} \langle \mu_{app}' S_{ij}' \frac{\partial}{\partial x_k}\left(\mu_{app}' \langle S_{ij} \rangle\right) \rangle\right)
\end{aligned}, \tag{6.F.23}$$

with the orders of magnitude

$$\frac{\partial}{\partial x_k}\left(\frac{4}{\rho} \langle \mu_{app} \rangle \langle S_{ij}' \frac{\partial}{\partial x_k}\left(\mu_{app}' \langle S_{ij} \rangle\right) \rangle\right) \sim \frac{1}{l} \frac{1}{\rho} \mu_w \frac{u}{\lambda} \frac{1}{l} \mu' \frac{U}{l} \sim \rho \frac{u^4}{l^2} \frac{1}{\mathrm{Re}_\lambda^3} \left(\frac{U}{u}\right) \left(\frac{\lambda_\mu}{\lambda}\right), \tag{6.F.24}$$

$$\frac{\partial}{\partial x_k}\left(\frac{1}{\rho}2\langle\mu'_{app}S'_{ij}\rangle\frac{\partial}{\partial x_k}\left(2\langle\mu_{app}\rangle\langle S_{ij}\rangle\right)\right)\sim\frac{1}{l}\frac{1}{\rho}\mu'\frac{u}{\lambda_\mu}\frac{1}{l}\mu_w\frac{U}{l}\sim\rho\frac{u^4}{l^2}\frac{1}{\mathrm{Re}_\lambda^3}\left(\frac{U}{u}\right), \tag{6.F.25}$$

$$\frac{\partial}{\partial x_k}\left(\frac{4}{\rho}\langle\mu'_{app}S'_{ij}\frac{\partial}{\partial x_k}\left(\mu'_{app}\langle S_{ij}\rangle\right)\rangle\right)\sim\frac{1}{l}\frac{1}{\rho}\mu'\frac{u}{\lambda_\mu}\frac{1}{l}\mu'\frac{U}{l}\sim\rho\frac{u^4}{l^2}\frac{1}{\mathrm{Re}_\lambda^3}\left(\frac{U}{u}\right)\left(\frac{\lambda_\mu}{\lambda}\right), \tag{6.F.26}$$

- the seventh one can be split in three parts giving

$$\frac{\partial}{\partial x_k}\left(-\frac{1}{\rho}T_{\mu,ij}\frac{\partial T_{R,ij}}{\partial x_k}\right)\sim\frac{1}{l}\frac{1}{\rho}\mu'\frac{u}{\lambda_\mu}\frac{\rho u^2}{l}\sim\rho\frac{u^4}{l^2}\frac{1}{\mathrm{Re}_\lambda}, \tag{6.F.27}$$

$$\frac{\partial}{\partial x_k}\left(-\frac{1}{\rho}T_{\mu,ij}\frac{\partial T_{\mu,ij}}{\partial x_k}\right)\sim\frac{1}{l}\frac{1}{\rho}\mu'\frac{u}{\lambda_\mu}\frac{1}{l}\mu'\frac{u}{\lambda_\mu}\sim\rho\frac{u^4}{l^2}\frac{1}{\mathrm{Re}_\lambda^2}, \tag{6.F.28}$$

$$\frac{\partial}{\partial x_k}\left(-\frac{1}{\rho}T_{\mu,ij}\frac{\partial}{\partial x_k}\left(2\langle\mu_{app}\rangle\langle S_{ij}\rangle\right)\right)\sim\frac{1}{l}\frac{1}{\rho}\mu'\frac{u}{\lambda_\mu}\frac{1}{l}\mu_w\frac{U}{l}\sim\rho\frac{u^4}{l^2}\frac{1}{\mathrm{Re}_\lambda^3}\left(\frac{U}{u}\right), \tag{6.F.29}$$

- the eight one gives

$$\frac{\partial}{\partial x_k}\left(2T_{\mu,ij}\frac{\partial k}{\partial x_j}\right)\sim\frac{1}{l}\mu'\frac{u}{\lambda_\mu}\frac{u^2}{l}\sim\rho\frac{u^4}{l^2}\frac{1}{\mathrm{Re}_\lambda}. \tag{6.F.30}$$

The dissipation group contain three terms:

- the first two terms can be simplified as follows

$$\begin{aligned}&\frac{4}{\rho}\langle\frac{\partial}{\partial x_k}\left(\mu_{app}S'_{kj}\right)\frac{\partial p'}{\partial x_j}\rangle+\frac{4}{\rho}\frac{CS^2}{\mu_{app}}\langle\frac{\partial}{\partial x_k}\left(\mu_{app}S_{kj}\right)\frac{\partial p}{\partial x_j}\rangle\approx\\&\left(1+\frac{CS^2}{\mu_{app}}\right)\frac{4}{\rho}\langle\frac{\partial}{\partial x_k}\left(\langle\mu_{app}\rangle S'_{kj}\right)\frac{\partial p'}{\partial x_j}\rangle+\left(1+\frac{CS^2}{\mu_{app}}\right)\frac{4}{\rho}\langle\frac{\partial}{\partial x_k}\left(\mu'_{app}S'_{kj}\right)\frac{\partial p'}{\partial x_j}\rangle\\&\frac{2}{\rho}\frac{CS^2}{\mu_{app}}\frac{\partial}{\partial x_k}\left(2\langle\mu_{app}\rangle\langle S_{kj}\rangle\right)\frac{\partial P}{\partial x_j}+\frac{2}{\rho}\frac{CS^2}{\mu_{app}}\frac{\partial T_{\mu,kj}}{\partial x_k}\frac{\partial P}{\partial x_j}+\frac{4}{\rho}\frac{CS^2}{\mu_{app}}\langle\frac{\partial}{\partial x_k}\left(\mu'_{app}\langle S_{kj}\rangle\right)\frac{\partial p'}{\partial x_j}\rangle\end{aligned}, \tag{6.F.31}$$

with the orders of magnitude

$$\left(1+\frac{CS^2}{\mu_{app}}\right)\frac{4}{\rho}\langle\frac{\partial}{\partial x_k}\left(\langle\mu_{app}\rangle S'_{kj}\right)\frac{\partial p'}{\partial x_j}\rangle\sim\left(1+\frac{n-1}{2}\right)\frac{1}{\rho}\frac{1}{l}\mu_w\frac{u}{\lambda}\frac{\rho u^2}{\lambda}\sim\left(1+\frac{n-1}{2}\right)\rho\frac{u^4}{l^2}, \tag{6.F.32}$$

$$\left(1+\frac{CS^2}{\mu_{app}}\right)\frac{4}{\rho}\langle\frac{\partial}{\partial x_k}\left(\mu'_{app}S'_{kj}\right)\frac{\partial p'}{\partial x_j}\rangle\sim\left(1+\frac{n-1}{2}\right)\frac{1}{\rho}\frac{1}{l}\mu'\frac{u}{\lambda_\mu}\rho\frac{u^2}{\lambda}\sim\left(1+\frac{n-1}{2}\right)\rho\frac{u^4}{l^2}, \tag{6.F.33}$$

$$\frac{2}{\rho}\frac{CS^2}{\mu_{app}}\frac{\partial}{\partial x_k}\left(2\langle\mu_{app}\rangle\langle S_{kj}\rangle\right)\frac{\partial P}{\partial x_j}\sim\frac{1}{\rho}\frac{n-1}{2}\frac{1}{l}\mu_w\frac{U}{l}\frac{\rho U^2}{L}\sim\frac{n-1}{2}\rho\frac{u^4}{l^2}\frac{1}{\mathrm{Re}_\lambda^2}\left(\frac{U}{u}\right)^2, \tag{6.F.34}$$

$$\frac{2}{\rho}\frac{CS^2}{\mu_{app}}\frac{\partial T_{\mu,kj}}{\partial x_k}\frac{\partial P}{\partial x_j}\sim\frac{1}{\rho}\frac{n-1}{2}\frac{1}{l}\mu'\frac{u}{\lambda_\mu}\frac{\rho U^2}{L}\sim\frac{n-1}{2}\rho\frac{u^4}{l^2}\frac{1}{\mathrm{Re}_\lambda}\left(\frac{U}{u}\right), \tag{6.F.35}$$

$$\frac{4}{\rho}\frac{CS^2}{\mu_{app}}\langle\frac{\partial}{\partial x_k}\left(\mu'_{app}\langle S_{kj}\rangle\right)\frac{\partial p'}{\partial x_j}\rangle\sim\frac{1}{\rho}\frac{n-1}{2}\frac{1}{l}\mu'\frac{U}{l}\frac{\rho u^2}{\lambda_\mu}\sim\frac{n-1}{2}\rho\frac{u^4}{l^2}\frac{1}{\mathrm{Re}_\lambda}\left(\frac{U}{u}\right). \tag{6.F.36}$$

- the last one can be written as

$$\begin{aligned}&-\frac{4}{\rho}\langle\frac{\partial}{\partial x_k}\left(\mu_{app}S_{ij}\right)\frac{\partial}{\partial x_k}\left(\mu_{app}S'_{ij}+C\$^2S_{ij}\right)\rangle=\\&-\frac{4}{\rho}\langle\frac{\partial}{\partial x_k}\left(\mu_{app}S_{ij}\right)\frac{\partial}{\partial x_k}\left(\mu_{app}S'_{ij}\right)\rangle-\frac{4}{\rho}\langle\frac{\partial}{\partial x_k}\left(\mu_{app}S_{ij}\right)\frac{\partial}{\partial x_k}\left(C\$^2S_{ij}\right)\rangle\end{aligned}. \tag{6.F.37}$$

The first part of Eq. (6.F.37) can also be written as

$$\begin{aligned}&-\frac{4}{\rho}\langle\frac{\partial}{\partial x_k}\left(\mu_{app}S_{ij}\right)\frac{\partial}{\partial x_k}\left(\mu_{app}S'_{ij}\right)\rangle=\\&-\frac{4}{\rho}\langle\frac{\partial}{\partial x_k}\left(\left(\langle\mu_{app}\rangle+\mu'_{app}\right)\left(\langle S_{ij}\rangle+S'_{ij}\right)\right)\frac{\partial}{\partial x_k}\left(\left(\langle\mu_{app}\rangle+\mu'_{app}\right)S'_{ij}\right)\rangle=\\&-\frac{4}{\rho}\frac{\partial}{\partial x_k}\left(\langle\mu_{app}\rangle\langle S_{ij}\rangle\right)\frac{\partial}{\partial x_k}(\langle\mu'_{app}S'_{ij}\rangle)-\frac{4}{\rho}\langle\frac{\partial}{\partial x_k}\left(\langle\mu_{app}\rangle S'_{ij}\right)\frac{\partial}{\partial x_k}\left(\langle\mu_{app}\rangle S'_{ij}\right)\rangle,\\&-\frac{8}{\rho}\langle\frac{\partial}{\partial x_k}\left(\langle\mu_{app}\rangle S'_{ij}\right)\frac{\partial}{\partial x_k}\left(\mu'_{app}S'_{ij}\right)\rangle-\frac{4}{\rho}\langle\frac{\partial}{\partial x_k}\left(\mu'_{app}\langle S_{ij}\rangle\right)\frac{\partial}{\partial x_k}\left(\langle\mu_{app}\rangle S'_{ij}\right)\rangle\\&-\frac{4}{\rho}\langle\frac{\partial}{\partial x_k}\left(\mu'_{app}\langle S_{ij}\rangle\right)\frac{\partial}{\partial x_k}\left(\mu'_{app}S'_{ij}\right)\rangle-\frac{4}{\rho}\langle\frac{\partial}{\partial x_k}\left(\mu'_{app}S'_{ij}\right)\frac{\partial}{\partial x_k}\left(\mu'_{app}S'_{ij}\right)\rangle\end{aligned} \tag{6.F.38}$$

and the second one as

$$-\frac{4}{\rho}\langle\frac{\partial}{\partial x_k}\left(\mu_{app}S_{ij}\right)\frac{\partial}{\partial x_k}\left(C\$^2 S_{ij}\right)\rangle =$$

$$-\frac{4}{\rho}\langle\frac{\partial}{\partial x_k}\left(\mu_{app}S_{ij}\right)\frac{\partial}{\partial x_k}\left(\frac{CS^2}{\mu_{app}}\frac{\$^2}{S^2}\mu_{app}S_{ij}\right)\rangle \approx$$

$$-\frac{CS^2}{\mu_{app}}\frac{4}{\rho}\langle\frac{\partial}{\partial x_k}\left(\mu_{app}S_{ij}\right)\frac{\partial}{\partial x_k}\left(\mu_{app}S_{ij}\right)\rangle-\frac{CS^2}{\mu_{app}}\frac{4}{\rho}\langle\frac{\partial}{\partial x_k}\left(\mu_{app}S_{ij}\right)\frac{\partial}{\partial x_k}\left(\mu_{app}S_{ij}\right)\rangle =$$

$$-\frac{CS^2}{\mu_{app}}\frac{4}{\rho}\langle\frac{\partial}{\partial x_k}\left(\left(\langle\mu_{app}\rangle+\mu'_{app}\right)\left(\langle S_{ij}\rangle+S'_{ij}\right)\right)\frac{\partial}{\partial x_k}\left(\left(\langle\mu_{app}\rangle+\mu'_{app}\right)\left(\langle S_{ij}\rangle+S'_{ij}\right)\right)\rangle =$$

$$-\frac{CS^2}{\mu_{app}}\frac{1}{\rho}\frac{\partial}{\partial x_k}\left(2\langle\mu_{app}\rangle\langle S_{ij}\rangle\right)\frac{\partial}{\partial x_k}\left(2\langle\mu_{app}\rangle\langle S_{ij}\rangle\right)-\frac{CS^2}{\mu_{app}}\frac{1}{\rho}\langle\frac{\partial}{\partial x_k}\left(2\mu'_{app}\langle S_{ij}\rangle\right)\frac{\partial}{\partial x_k}\left(2\mu'_{app}\langle S_{ij}\rangle\right)\rangle$$

$$-\frac{CS^2}{\mu_{app}}\frac{1}{\rho}\langle\frac{\partial}{\partial x_k}\left(2\langle\mu_{app}\rangle S'_{ij}\right)\frac{\partial}{\partial x_k}\left(2\langle\mu_{app}\rangle S'_{ij}\right)\rangle-\frac{CS^2}{\mu_{app}}\frac{1}{\rho}\langle\frac{\partial}{\partial x_k}\left(2\mu'_{app}S'_{ij}\right)\frac{\partial}{\partial x_k}\left(2\mu'_{app}S'_{ij}\right)\rangle$$

$$-\frac{CS^2}{\mu_{app}}\frac{2}{\rho}\frac{\partial}{\partial x_k}\left(2\langle\mu_{app}\rangle\langle S_{ij}\rangle\right)\frac{\partial T_{\mu,ij}}{\partial x_k}-\frac{CS^2}{\mu_{app}}\frac{2}{\rho}\langle\frac{\partial}{\partial x_k}\left(2\langle\mu_{app}\rangle S'_{ij}\right)\frac{\partial}{\partial x_k}\left(2\mu'_{app}\langle S_{ij}\rangle\right)\rangle$$

$$,-\frac{CS^2}{\mu_{app}}\frac{2}{\rho}\langle\frac{\partial}{\partial x_k}\left(2\langle\mu_{app}\rangle S'_{ij}\right)\frac{\partial}{\partial x_k}\left(2\mu'_{app}S'_{ij}\right)\rangle-\frac{CS^2}{\mu_{app}}\frac{2}{\rho}\langle\frac{\partial}{\partial x_k}\left(2\mu'_{app}\langle S_{ij}\rangle\right)\frac{\partial}{\partial x_k}\left(2\mu'_{app}S'_{ij}\right)\rangle \qquad (6.F.39)$$

The order of magnitude analysis of the terms of Eq. (6.F.38) gives

$$-\frac{4}{\rho}\frac{\partial}{\partial x_k}\left(\langle\mu_{app}\rangle\langle S_{ij}\rangle\right)\frac{\partial}{\partial x_k}\left(\langle\mu'_{app}S'_{ij}\rangle\right)\sim\frac{1}{\rho}\frac{1}{l}\mu_w\frac{U}{l}\frac{1}{l}\mu'\frac{u}{\lambda_\mu}\sim\rho\frac{u^4}{l^2}\frac{1}{\mathrm{Re}_\lambda^3}\left(\frac{U}{u}\right), \qquad (6.F.40)$$

$$-\frac{4}{\rho}\langle\frac{\partial}{\partial x_k}\left(\langle\mu_{app}\rangle S'_{ij}\right)\frac{\partial}{\partial x_k}\left(\langle\mu_{app}\rangle S'_{ij}\right)\rangle\sim\frac{1}{\rho}\frac{1}{\lambda}\mu_w\frac{u}{\lambda}\frac{1}{\lambda}\mu_w\frac{u}{\lambda}\sim\rho\frac{u^4}{l^2}, \qquad (6.F.41)$$

$$-\frac{8}{\rho}\langle\frac{\partial}{\partial x_k}\left(\langle\mu_{app}\rangle S'_{ij}\right)\frac{\partial}{\partial x_k}\left(\mu'_{app}S'_{ij}\right)\rangle\sim\frac{1}{\rho}\frac{1}{\lambda}\mu_w\frac{u}{\lambda}\frac{1}{\lambda}\mu'\frac{u}{\lambda_\mu}\sim\rho\frac{u^4}{l^2}, \qquad (6.F.42)$$

$$-\frac{4}{\rho}\langle\frac{\partial}{\partial x_k}\left(\mu'_{app}\langle S_{ij}\rangle\right)\frac{\partial}{\partial x_k}\left(\langle\mu_{app}\rangle S'_{ij}\right)\rangle\sim\frac{1}{\rho}\frac{1}{l}\mu'\frac{U}{l}\frac{1}{\lambda}\mu_w\frac{u}{\lambda}\sim\rho\frac{u^4}{l^2}\frac{1}{\mathrm{Re}_\lambda^2}\left(\frac{U}{u}\right)\left(\frac{\lambda_\mu}{\lambda}\right), \qquad (6.F.43)$$

$$-\frac{4}{\rho}\langle\frac{\partial}{\partial x_k}\left(\mu'_{app}\langle S_{ij}\rangle\right)\frac{\partial}{\partial x_k}\left(\mu'_{app}S'_{ij}\right)\rangle\sim\frac{1}{\rho}\frac{1}{l}\mu'\frac{U}{l}\frac{1}{\lambda}\mu'\frac{u}{\lambda_\mu}\sim\rho\frac{u^4}{l^2}\frac{1}{\mathrm{Re}_\lambda^2}\left(\frac{U}{u}\right)\left(\frac{\lambda_\mu}{\lambda}\right), \qquad (6.F.44)$$

$$-\frac{4}{\rho}\langle\frac{\partial}{\partial x_k}\left(\mu'_{app}S'_{ij}\right)\frac{\partial}{\partial x_k}\left(\mu'_{app}S'_{ij}\right)\rangle\sim\frac{1}{\rho}\frac{1}{\lambda}\mu'\frac{u}{\lambda_\mu}\frac{1}{\lambda}\mu'\frac{u}{\lambda_\mu}\sim\rho\frac{u^4}{l^2}, \qquad (6.F.45)$$

The order of magnitude analysis of the terms of Eq. (6.F.39) gives

$$-\frac{CS^2}{\mu_{app}}\frac{1}{\rho}\frac{\partial}{\partial x_k}\left(2\langle\mu_{app}\rangle\langle S_{ij}\rangle\right)\frac{\partial}{\partial x_k}\left(2\langle\mu_{app}\rangle\langle S_{ij}\rangle\right)\sim\left(\frac{n-1}{2}\right)\frac{1}{\rho}\frac{1}{l}\mu_w\frac{U}{l}\frac{1}{l}\mu_w\frac{U}{l}\sim\left(\frac{n-1}{2}\right)\rho\frac{u^4}{l^2}\frac{1}{\mathrm{Re}_\lambda^4}\left(\frac{U}{u}\right)^2, \tag{6.F.46}$$

$$-\frac{CS^2}{\mu_{app}}\frac{2}{\rho}\frac{\partial}{\partial x_k}\left(2\langle\mu_{app}\rangle\langle S_{ij}\rangle\right)\frac{\partial}{\partial x_k}\left(2\langle\mu'_{app}S'_{ij}\rangle\right)\sim\left(\frac{n-1}{2}\right)\frac{1}{\rho}\frac{1}{l}\mu_w\frac{U}{l}\frac{1}{l}\mu'\frac{u}{\lambda_\mu}\sim\left(\frac{n-1}{2}\right)\rho\frac{u^4}{l^2}\frac{1}{\mathrm{Re}_\lambda^3}\left(\frac{U}{u}\right), \tag{6.F.47}$$

$$-\frac{CS^2}{\mu_{app}}\frac{4}{\rho}\langle\frac{\partial}{\partial x_k}\left(\langle\mu_{app}\rangle S'_{ij}\right)\frac{\partial}{\partial x_k}\left(\langle\mu_{app}\rangle S'_{ij}\right)\rangle\sim\left(\frac{n-1}{2}\right)\frac{1}{\rho}\frac{1}{\lambda}\mu_w\frac{u}{\lambda}\frac{1}{\lambda}\mu_w\frac{u}{\lambda}\sim\left(\frac{n-1}{2}\right)\rho\frac{u^4}{l^2}, \tag{6.F.48}$$

$$-\frac{CS^2}{\mu_{app}}\frac{8}{\rho}\langle\frac{\partial}{\partial x_k}\left(\langle\mu_{app}\rangle S'_{ij}\right)\frac{\partial}{\partial x_k}\left(\mu'_{app}\langle S_{ij}\rangle\right)\rangle\sim\left(\frac{n-1}{2}\right)\frac{1}{\rho}\frac{1}{\lambda}\mu_w\frac{u}{\lambda}\frac{1}{l}\mu'\frac{U}{l}\sim\left(\frac{n-1}{2}\right)\rho\frac{u^4}{l^2}\frac{1}{\mathrm{Re}_\lambda^2}\left(\frac{U}{u}\right)\left(\frac{\lambda_\mu}{\lambda}\right), \tag{6.F.49}$$

$$-\frac{CS^2}{\mu_{app}}\frac{8}{\rho}\langle\frac{\partial}{\partial x_k}\left(\langle\mu_{app}\rangle S'_{ij}\right)\frac{\partial}{\partial x_k}\left(\mu'_{app}S'_{ij}\right)\rangle\sim\left(\frac{n-1}{2}\right)\frac{1}{\rho}\frac{1}{\lambda}\mu_w\frac{u}{\lambda}\frac{1}{\lambda}\mu'\frac{u}{\lambda_\mu}\sim\left(\frac{n-1}{2}\right)\rho\frac{u^4}{l^2}, \tag{6.F.50}$$

$$-\frac{CS^2}{\mu_{app}}\frac{4}{\rho}\langle\frac{\partial}{\partial x_k}\left(\mu'_{app}\langle S_{ij}\rangle\right)\frac{\partial}{\partial x_k}\left(\mu'_{app}\langle S_{ij}\rangle\right)\rangle\sim\left(\frac{n-1}{2}\right)\frac{1}{\rho}\frac{1}{l}\mu'\frac{U}{l}\frac{1}{l}\mu'\frac{U}{l}\sim\left(\frac{n-1}{2}\right)\rho\frac{u^4}{l^2}\frac{1}{\mathrm{Re}_\lambda^4}\left(\frac{U}{u}\right)^2\left(\frac{\lambda_\mu}{\lambda}\right)^2, \tag{6.F.51}$$

$$-\frac{CS^2}{\mu_{app}}\frac{8}{\rho}\langle\frac{\partial}{\partial x_k}\left(\mu'_{app}\langle S_{ij}\rangle\right)\frac{\partial}{\partial x_k}\left(\mu'_{app}S'_{ij}\right)\rangle\sim\left(\frac{n-1}{2}\right)\frac{1}{\rho}\frac{1}{l}\mu'\frac{U}{l}\frac{1}{\lambda}\mu'\frac{u}{\lambda_\mu}\sim\left(\frac{n-1}{2}\right)\rho\frac{u^4}{l^2}\frac{1}{\mathrm{Re}_\lambda^2}\left(\frac{U}{u}\right)\left(\frac{\lambda_\mu}{\lambda}\right), \tag{6.F.52}$$

$$-\frac{CS^2}{\mu_{app}}\frac{1}{\rho}\langle\frac{\partial}{\partial x_k}\left(2\mu'_{app}S'_{ij}\right)\frac{\partial}{\partial x_k}\left(2\mu'_{app}S'_{ij}\right)\rangle\sim\left(\frac{n-1}{2}\right)\frac{1}{\rho}\frac{1}{\lambda}\mu'\frac{u}{\lambda_\mu}\frac{1}{\lambda}\mu'\frac{u}{\lambda_\mu}\sim\left(\frac{n-1}{2}\right)\rho\frac{u^4}{l^2}. \tag{6.F.53}$$

Some terms with the same order of magnitude are collected together in the final form of the equation, e.g. the dissipation terms

$$
\begin{aligned}
&-\frac{4}{\rho}\langle\frac{\partial}{\partial x_k}\left(\langle\mu_{app}\rangle S'_{ij}\right)\frac{\partial}{\partial x_k}\left(\langle\mu_{app}\rangle S'_{ij}\right)\rangle-\frac{8}{\rho}\langle\frac{\partial}{\partial x_k}\left(\langle\mu_{app}\rangle S'_{ij}\right)\frac{\partial}{\partial x_k}\left(\mu'_{app}S'_{ij}\right)\rangle+\\
&-\frac{4}{\rho}\langle\frac{\partial}{\partial x_k}\left(\mu'_{app}S'_{ij}\right)\frac{\partial}{\partial x_k}\left(\mu'_{app}S'_{ij}\right)\rangle=-\frac{4}{\rho}\langle\frac{\partial}{\partial x_k}\left(\langle\mu_{app}\rangle S'_{ij}\right)\frac{\partial}{\partial x_k}\left(\langle\mu_{app}\rangle S'_{ij}\right)\rangle+\\
&-\frac{4}{\rho}\langle\frac{\partial}{\partial x_k}\left(\langle\mu_{app}\rangle S'_{ij}\right)\frac{\partial}{\partial x_k}\left(\mu'_{app}S'_{ij}\right)\rangle-\frac{4}{\rho}\langle\frac{\partial}{\partial x_k}\left(\mu'_{app}S'_{ij}\right)\frac{\partial}{\partial x_k}\left(\langle\mu_{app}\rangle S'_{ij}\right)\rangle+\\
&-\frac{4}{\rho}\langle\frac{\partial}{\partial x_k}\left(\mu'_{app}S'_{ij}\right)\frac{\partial}{\partial x_k}\left(\mu'_{app}S'_{ij}\right)\rangle=-\frac{4}{\rho}\langle\frac{\partial}{\partial x_k}\left(\langle\mu_{app}\rangle S'_{ij}\right)\frac{\partial}{\partial x_k}\left(\mu_{app}S'_{ij}\right)\rangle+\\
&-\frac{4}{\rho}\langle\frac{\partial}{\partial x_k}\left(\mu'_{app}S'_{ij}\right)\frac{\partial}{\partial x_k}\left(\mu_{app}S'_{ij}\right)\rangle=-\frac{4}{\rho}\langle\frac{\partial}{\partial x_k}\left(\mu_{app}S'_{ij}\right)\frac{\partial}{\partial x_k}\left(\mu_{app}S'_{ij}\right)\rangle
\end{aligned}
\quad , \tag{6.F.54}
$$

The dissipation term can be written as

$$
\begin{aligned}
&-\frac{4}{\rho}\langle\frac{\partial}{\partial x_k}\left(\langle\mu_{app}\rangle S'_{ij}\right)\frac{\partial}{\partial x_k}\left(\langle\mu_{app}\rangle S'_{ij}\right)\rangle-\frac{8}{\rho}\langle\frac{\partial}{\partial x_k}\left(\langle\mu_{app}\rangle S'_{ij}\right)\frac{\partial}{\partial x_k}\left(\mu'_{app}S'_{ij}\right)\rangle\\
&-\frac{4}{\rho}\langle\frac{\partial}{\partial x_k}\left(\mu'_{app}S'_{ij}\right)\frac{\partial}{\partial x_k}\left(\mu'_{app}S'_{ij}\right)\rangle-\frac{CS^2}{\mu_{app}}\frac{4}{\rho}\langle\frac{\partial}{\partial x_k}\left(\langle\mu_{app}\rangle S'_{ij}\right)\frac{\partial}{\partial x_k}\left(\langle\mu_{app}\rangle S'_{ij}\right)\rangle+\\
&-\frac{CS^2}{\mu_{app}}\frac{8}{\rho}\langle\frac{\partial}{\partial x_k}\left(\langle\mu_{app}\rangle S'_{ij}\right)\frac{\partial}{\partial x_k}\left(\mu'_{app}S'_{ij}\right)\rangle-\frac{CS^2}{\mu_{app}}\frac{1}{\rho}\langle\frac{\partial}{\partial x_k}\left(2\mu'_{app}S'_{ij}\right)\frac{\partial}{\partial x_k}\left(2\mu'_{app}S'_{ij}\right)\rangle=\\
&-\left(1+\frac{CS^2}{\mu_{app}}\right)\frac{4}{\rho}\langle\frac{\partial}{\partial x_k}\left(\mu_{app}S'_{ij}\right)\frac{\partial}{\partial x_k}\left(\mu_{app}S'_{ij}\right)\rangle
\end{aligned}
\quad , \tag{6.F.55}
$$

Terms related to the pressure are present in the transport and the dissipation groups with different orders of magnitude. Simplifications can be obtained by adding some null term which involves the mean of the fluctuating variable, which is zero, as

$$\langle S_{kj}\rangle\langle\mu_{app}\rangle\langle\frac{\partial p'}{\partial x_j}\rangle=0\,, \tag{6.F.56}$$

$$\langle\mu_{app}\rangle\langle S_{kj}\rangle+\langle\mu'_{app}S'_{kj}\rangle=\langle\mu_{app}\rangle\langle S_{kj}\rangle+\langle\langle\mu_{app}\rangle S'_{kj}\rangle+\langle\mu'_{app}\langle S_{kj}\rangle\rangle+\langle\mu'_{app}S'_{kj}\rangle=\langle\mu_{app}S_{kj}\rangle\,, \tag{6.F.57}$$

$$\langle\frac{\partial}{\partial x_k}\left(\langle\mu_{app}\rangle\langle S_{kj}\rangle\right)\frac{\partial p'}{\partial x_j}\rangle=0\,. \tag{6.F.58}$$

Then, if $\mathrm{Re}_\lambda=O(1)$ the transport group is

$$\frac{\partial}{\partial x_k}\left(-\frac{4}{\rho}\left(\langle\mu_{app}\rangle\langle S'_{kj}\frac{\partial p'}{\partial x_j}\rangle+\langle\mu'_{app}S'_{kj}\frac{\partial p'}{\partial x_j}\rangle\right)\right)+$$

$$\frac{\partial}{\partial x_k}\left(-\frac{CS^2}{\mu_{app}}\frac{4}{\rho}\left(\langle\mu_{app}\rangle\langle S'_{kj}\frac{\partial p'}{\partial x_j}\rangle+\langle\mu'_{app}S'_{kj}\frac{\partial p'}{\partial x_j}\rangle+\langle S_{kj}\rangle\langle\mu'_{app}\frac{\partial p'}{\partial x_j}\rangle+\langle\mu_{app}\rangle\langle S_{kj}\rangle\frac{\partial P}{\partial x_j}+\langle\mu'_{app}S'_{kj}\rangle\frac{\partial P}{\partial x_j}\right)\right)=$$

$$\frac{\partial}{\partial x_k}\left(-\frac{4}{\rho}\langle\mu_{app}S'_{kj}\frac{\partial p'}{\partial x_j}\rangle\right)+\frac{\partial}{\partial x_k}\left(-\frac{CS^2}{\mu_{app}}\frac{4}{\rho}\left(\langle\mu_{app}S'_{kj}\frac{\partial p'}{\partial x_j}\rangle+\langle S_{kj}\rangle\langle\mu'_{app}\frac{\partial p'}{\partial x_j}\rangle+\langle S_{kj}\rangle\langle\mu_{app}\rangle\langle\frac{\partial p'}{\partial x_j}\rangle\right)\right)+$$

$$\frac{\partial}{\partial x_k}\left(-\frac{CS^2}{\mu_{app}}\frac{4}{\rho}\left(\left(\langle\mu_{app}\rangle\langle S_{kj}\rangle+\langle\mu'_{app}S'_{kj}\rangle\right)\frac{\partial P}{\partial x_j}\right)\right)=\frac{\partial}{\partial x_k}\left(-\frac{4}{\rho}\langle\mu_{app}S'_{kj}\frac{\partial p'}{\partial x_j}\rangle\right)+$$

$$\frac{\partial}{\partial x_k}\left(-\frac{CS^2}{\mu_{app}}\frac{4}{\rho}\left(\langle\mu_{app}S'_{kj}\frac{\partial p'}{\partial x_j}\rangle+\langle S_{kj}\rangle\langle\mu_{app}\frac{\partial p'}{\partial x_j}\rangle+\langle\mu_{app}S_{kj}\rangle\frac{\partial P}{\partial x_j}\right)\right)=$$

$$\frac{\partial}{\partial x_k}\left(-\frac{4}{\rho}\langle\mu_{app}S'_{kj}\frac{\partial p'}{\partial x_j}\rangle+\frac{\partial}{\partial x_k}\left(-\frac{CS^2}{\mu_{app}}\frac{4}{\rho}\left(\langle\mu_{app}S_{kj}\frac{\partial p'}{\partial x_j}\rangle+\langle\mu_{app}S_{kj}\rangle\frac{\partial P}{\partial x_j}\right)\right)=\right.$$

$$\frac{\partial}{\partial x_k}\left(-\frac{4}{\rho}\langle\mu_{app}S'_{kj}\frac{\partial p'}{\partial x_j}\rangle-\frac{CS^2}{\mu_{app}}\frac{4}{\rho}\langle\mu_{app}S_{kj}\frac{\partial p}{\partial x_j}\rangle\right) \quad , \qquad (6.F.59)$$

and the dissipation one

$$\left(1+\frac{CS^2}{\mu_{app}}\right)\frac{4}{\rho}\langle\frac{\partial}{\partial x_k}\left(\langle\mu_{app}\rangle S'_{kj}\right)\frac{\partial p'}{\partial x_j}\rangle+\left(1+\frac{CS^2}{\mu_{app}}\right)\frac{4}{\rho}\langle\frac{\partial}{\partial x_k}\left(\mu'_{app}S'_{kj}\right)\frac{\partial p'}{\partial x_j}\rangle+$$

$$\frac{2}{\rho}\frac{CS^2}{\mu_{app}}\frac{\partial}{\partial x_k}\left(2\langle\mu_{app}\rangle\langle S_{kj}\rangle\right)\frac{\partial P}{\partial x_j}+\frac{2}{\rho}\frac{CS^2}{\mu_{app}}\frac{\partial T_{\mu,kj}}{\partial x_k}\frac{\partial P}{\partial x_j}+\frac{4}{\rho}\frac{CS^2}{\mu_{app}}\langle\frac{\partial}{\partial x_k}\left(\mu'_{app}\langle S_{kj}\rangle\right)\frac{\partial p'}{\partial x_j}\rangle=$$

$$\frac{4}{\rho}\langle\frac{\partial}{\partial x_k}\left(\langle\mu_{app}\rangle S'_{kj}\right)\frac{\partial p'}{\partial x_j}\rangle+\frac{4}{\rho}\langle\frac{\partial}{\partial x_k}\left(\mu'_{app}S'_{kj}\right)\frac{\partial p'}{\partial x_j}\rangle+\frac{CS^2}{\mu_{app}}\frac{4}{\rho}\left(\langle\frac{\partial}{\partial x_k}\left(\langle\mu_{app}\rangle S'_{kj}\right)\frac{\partial p'}{\partial x_j}\rangle+\langle\frac{\partial}{\partial x_k}\left(\mu'_{app}S'_{kj}\right)\frac{\partial p'}{\partial x_j}\rangle\right)+$$

$$\frac{CS^2}{\mu_{app}}\frac{4}{\rho}\left(\frac{\partial}{\partial x_k}\left(\langle\mu_{app}\rangle\langle S_{kj}\rangle+\langle\mu'_{app}S'_{kj}\rangle\right)\frac{\partial P}{\partial x_j}+\langle\frac{\partial}{\partial x_k}\left(\mu'_{app}\langle S_{kj}\rangle\right)\frac{\partial p'}{\partial x_j}\rangle\right)=$$

$$\frac{4}{\rho}\langle\frac{\partial}{\partial x_k}\left(\mu_{app}S'_{kj}\right)\frac{\partial p'}{\partial x_j}\rangle+\frac{CS^2}{\mu_{app}}\frac{4}{\rho}\left(\frac{\partial}{\partial x_k}\left(\langle\mu_{app}S_{kj}\rangle\right)\frac{\partial P}{\partial x_j}\right)+$$

$$\frac{CS^2}{\mu_{app}}\frac{4}{\rho}\left(\langle\frac{\partial}{\partial x_k}\left(\mu_{app}S'_{kj}\right)\frac{\partial p'}{\partial x_j}\rangle+\langle\frac{\partial}{\partial x_k}\left(\mu'_{app}\langle S_{kj}\rangle+\langle\mu_{app}\rangle\langle S_{kj}\rangle\right)\frac{\partial p'}{\partial x_j}\rangle\right)=$$

$$\frac{4}{\rho}\langle\frac{\partial}{\partial x_k}\left(\mu_{app}S'_{kj}\right)\frac{\partial p'}{\partial x_j}\rangle+\frac{CS^2}{\mu_{app}}\frac{4}{\rho}\left(\langle\frac{\partial}{\partial x_k}\left(\mu_{app}S_{kj}\right)\frac{\partial p}{\partial x_j}\rangle\right) \quad . \qquad (6.F.60)$$

If $\mathrm{Re}_\lambda = O(10)$ transport and dissipation groups are written similarly as if $\mathrm{Re}_\lambda = O(1)$ in order to have a more compact form of the final equation, also if only one of the five terms is negligible.

Finally if $\mathrm{Re}_\lambda = O(100)$ the transport group is

$$\frac{\partial}{\partial x_k}\left(-\left(1+\frac{CS^2}{\mu_{app}}\right)\frac{4}{\rho}\langle\mu_{app}\rangle\langle S'_{kj}\frac{\partial p'}{\partial x_j}\rangle\right)+\frac{\partial}{\partial x_k}\left(-\left(1+\frac{CS^2}{\mu_{app}}\right)\frac{4}{\rho}\langle\mu'_{app}S'_{kj}\frac{\partial p'}{\partial x_j}\rangle\right)= \frac{\partial}{\partial x_k}\left(-\left(1+\frac{CS^2}{\mu_{app}}\right)\frac{4}{\rho}\langle\mu_{app}S'_{kj}\frac{\partial p'}{\partial x_j}\rangle\right), \tag{6.F.61}$$

and the dissipation one

$$\left(1+\frac{CS^2}{\mu_{app}}\right)\frac{4}{\rho}\langle\frac{\partial}{\partial x_k}\left(\langle\mu_{app}\rangle S'_{kj}\right)\frac{\partial p'}{\partial x_j}\rangle+\left(1+\frac{CS^2}{\mu_{app}}\right)\frac{4}{\rho}\langle\frac{\partial}{\partial x_k}\left(\mu'_{app}S'_{kj}\right)\frac{\partial p'}{\partial x_j}\rangle= \left(1+\frac{CS^2}{\mu_{app}}\right)\frac{4}{\rho}\langle\frac{\partial}{\partial x_k}\left(\mu_{app}S'_{kj}\right)\frac{\partial p'}{\partial x_j}\rangle. \tag{6.F.62}$$

References of Chapter 6

[6.1] F. Gori. Effects of Variable Physical Properties in Laminar Flow of Pseudo-plastic Fluids. International Journal of Heat and Mass Transfer. 1978; 21(6.2): 247-250.

[6.2] F. Gori. Variable Physical Properties in Laminar Heating of Pseudo-plastic Fluids with Constant Wall Heat Flux. Journal of Heat Transfer, ASME. 1978; 100(6.2): 220-223.

[6.3] M. Rudman and H.M. Blackburn. Direct numerical simulation of turbulent non-Newtonian flow using a spectral element method. Applied Mathematical Modelling. 2006; 30: 1229–1248.

[6.4] M. Rudman, H.M. Blackburn, L.J.W. Graham and L. Pullum. Turbulent pipe flow of shear-thinning fluids. J. Non-Newtonian Fluid Mech. 2004; 118: 33–48.

[6.5] C. D. Dimitropoulos, R. Sureshkumar, A. N. Beris. Direct numerical simulation of viscoelastic turbulent channel flow exhibiting drag reduction: effect of the variation of rheological parameters. J. Non-Newtonian Fluid Mech. 1998; 79: 433-468.

[6.6] A. N. Beris and C. D. Dimitropoulos. Pseudo-spectral simulation of turbulent viscoelastic channel flow. Comp. Methods Appl. Mech. Eng. 1990; 180: 365-392.

[6.7] R. Benzi and I. Procaccia. Simple model for drag reduction. Physical Review E. 2003; 68: 025303(6.R).

[6.8] S.M. Son and R.K. Singh. Turbulence modelling and verification for aseptically processed soybean milk under turbulent flow conditions. Journal of Food Engineering. 2002; 52: 177–184.

[6.9] W. Binxin and C. Shulin. CFD Simulation of Non-Newtonian Fluid Flow in Anaerobic Digesters Biotechnology and Bioengineering, Biotechnology and Bioengineering. 2008; 99(6.3), February 15.

[6.10] M. R. Malin. Turbulent pipe flow of power-law fluids. Int. Comm. Heat Mass Transfer. 1997; 24(6.7): 977–988.

[6.11] M. R. Malin. Turbulent pipe flow of Herschel–Bulkley fluids. Int. Comm. Heat Mass Transfer. 1998; 25(6.3): 321–330.

[6.12] P.J. Oliveira and F.T. Pinho. A qualitative assessment of the role of a viscosity depending on the third invariant of the rate-of-deformation tensor upon turbulent non-Newtonian flow. J. Non-Newtonian Fluid Mech. 1998; 78: 1–25.

[6.13] F. T. Pinho. A GNF framework for turbulent flow models of drag reducing fluids and proposal for a k–ε type closure. J. Non-Newtonian Fluid Mech. 2003; 114: 149–184.

[6.14] C.F. Li, V.K. Gupta, R. Sureshkumar and B. Khomami. Turbulent channel flow of dilute polymeric solutions: Drag reduction scaling and an eddy viscosity model. J. Non-Newtonian Fluid Mech. 2006; 139: 177–189.

[6.15] F.T. Pinho, C.F. Li, B.A. Younis and R. Sureshkumar. A low Reynolds number turbulence closure for viscoelastic fluids. J. Non-Newtonian Fluid Mech. 2008; 154: 89–108.

[6.16] G.K. Batchelor. Computation of the energy spectrum in homogeneous two-dimensional turbulence. Physics of Fluids. 1969; II: 233-9.

[6.17] R.H. Kraichnan and D. Montgomery. Two-dimensional turbulence. Reports on Progress in Physics. 1980; 43(6.5): 547-619.

[6.18] R.H. Kraichnan. Eddy viscosity in two and three dimensions. Journal of the Atmospheric Sciences. 1976; 33(6.8): 1521-36.

[6.19] R.H. Kraichnan. Statistical dynamics of two-dimensional flow. Journal of Fluid Mechanics. 1975; 67(6.1): 155-75.

[6.20] J. R. Herring, S. A. Orszag and R. H. Kraichnan, D. G. Fox. Decay of Two-Dimensional Homogeneous Turbulence. Journal of Fluid Mechanics. 1974; 66(6.3): 417-444.

[6.21] P.A. Davidson. Turbulence an introduction for scientist and Engineers. Oxford University Press 2004.

[6.22] H. Tennekes and J. L. Lumley. 1972. A First Course in Turbulence. MIT Press. Cambridge, MA.

[6.23] D.O.A. Cruz, F.T. Pinho and P.R. Resende. Modeling the new stress for improved drag reduction predictions of viscoelastic pipe flow. J. Non-Newtonian Fluid Mech. 2004; 121: 127–141

[6.24] F. Gori, A. Boghi. Two New Differential Equations of Turbulent Dissipation Rate and Apparent Viscosity for Non-Newtonian Fluids, submitted paper.

Chapter 7:

INFLUENCE OF THE NON-NEWTONIAN BEHAVIOR IN AN IMAGE-BASED COMPUTATIONAL MODEL OF FLOW DYNAMICS IN STENOSED CAROTID ARTERY

7.1 Introduction

Atherosclerotic cardiovascular disease is a leading cause of morbidity in the industrialized world. A body of evidence suggests a correlation between atherosclerosis, regions of low blood flow velocity, rotational flow and low shear stress near arteries walls [7.1-2].

However, accurate measurements of interested quantities, as shear stress, are difficult to make *in vivo*. This has led to the popularity of image-based CFD modeling, where medical imaging is used to provide patient-specific boundary conditions for CFD analysis, as a means of reconstructing the local hemodynamic environment in a patient-specific manner. With the convergence of high-resolution medical imaging, sophisticated image processing techniques and high-performance desktop workstations, image-based CFD studies of *in vivo* hemodynamic are today possible. Some studies have been carried on by Steinman et al. [7.3-7.5] concerning the carotid artery bifurcation.

Cebral e Yim [7.6] compared CFD predicted flow patterns with image data from a rigid flow-through phantom of a carotid artery with 65% degree stenosis. The results show that in a rigid flow-through phantom of the carotid bifurcation with stenosis the flow can be simulated accurately with CFD, In a normal human subject the discrepancies due to human compliance are

leading to the suggestion that coupled fluid-structure calculations were able to reproduce the significant dampening of the velocity waveform observed between different slices along the common carotid artery. The studies, concerned with the realistic modeling of an artery, showed the importance of correct modelling of the rheologic behavior of the blood.

Johnston et al. [7.7] studied pulsatile blood flow through four different right coronary arteries, reconstructed from biplane angiograms. A non-Newtonian blood model (the Generalised Power Law), as well as the usual Newtonian model of blood viscosity, is used to study the wall shear stress in each of these arteries over the entire cardiac cycle. The results show that, when studying the wall shear stress distribution for transient blood flow in arteries, the use of a Newtonian blood model is a reasonably good approximation.

In a previous study [7.8] Johnston et al. concluded that there was significant inter-individual variation in the wall shear stress distributions and that using a non-Newtonian model for blood viscosity was only important at low inlet velocities.

Completely different are the conclusions of Gijsen and Allanic [7.9] who studied numerically and experimentally unsteady entry flow in a 90° curved tube to investigate the impact of the non-Newtonian blood on the velocity distribution. A Carreau-Yasuda model was employed to accommodate the shear thinning behavior of the Xanthan gum solution. The experimental results indicate significant differences between Newtonian and non-Newtonian behaviour . The numerical results for both fluids agree well with the experimental results.

Ishikawa and Guimaraes [7.10] showed the non-Newtonian properties of blood have considerable influence on the flow even at high Reynolds number. They studied numerically a periodic blood flow through a stenosed tube, using the bi-viscosity model as a constitutive equation, and the flow as periodic, incompressible and axisymmetric.

Tu and Deville [7.11] studied the blood flow through stenoses using the incompressible generalized Newtonian model incorporating the Herschel-Bulkley, Bingham and power-law fluids. The geometry was corresponding to a rigid circular tube with a partial occlusion. Computations show the memory effects taken into account in the model affect deeply the flow compared with the Newtonian reference case.

Soulis et al. [7.12] has analyzed the capabilities and limitations of eight molecular viscosity models, in the left coronary arterial tree in terms of molecular viscosity, local and global non-Newtonian importance factors, wall shear stress (WSS) and wall shear stress gradient (WSSG). The vessel geometry was acquired using 3D IVUS. High molecular viscosity, low WSS and low WSSG values occurred at the outer walls of the major bifurcation in proximal left coronary arterial regions. The Newtonian blood flow was found to be a good approximation at mid- and high-strain rates.

Completely different is the study of Hyun et al. [7.13], concerning surgical reconstruction of diseased artery. The authors have applied the methodology of "virtual prototyping" to diseased external carotid artery. The goals were to understand the particle hemodynamic and to provide various geometric design options for improved surgical reconstruction based on the minimization of critical hemodynamic wall parameters. The fluid was supposed Casson one. The results were expressed in terms of wall shear stress, wall shear stress gradient, oscillatory shear index, near-wall residence time parameter and helicity angle difference.

The original contribution of this work is conjugating the realistic reconstruction of a patient-specific geometry and non-Newtonian feature on a real carotid artery. Lumen boundary contours were segmented using commercial image-processing software AMIRA for a 3D geometry reconstruction. High-quality tetrahedral mesh was generated using commercial mesh-

generator code GAMBIT. The 3-D unsteady, incompressible Navier-Stokes equations were solved using commercial finite volume code FLUENT. For the modeling of non-Newtonian behavior we have chose the Casson model. This study use CFD predictions to evaluate the importance of modeling the blood as non-Newtonian fluid simulating blood-flow on a real geometry.

7.2 Model construction

A subject of 60 years hold with intimal thickening 90% degree of stenosis was studied. We have acquired 120 contiguous 0.5 mm thick two-dimensional slices data from CT. In order to construct the three-dimensional model, the iso-surface of brightness of color is created to depict the surface of the carotid arterial wall using the commercial visualization software AMIRA.

The vessel diameters are: common carotid artery (CCA), 0.782 cm; anterior external carotid artery (AECA), 0.6139 cm; posterior external carotid artery (PECA), 0.2822 cm; internal carotid artery (ICA), 0.695 cm. After extraction of geometrical information, each slice is stacked up vertically to construct a three dimensional model with the surface corresponding to the iso-surface of brightness of color.

The images were processed automatically, setting a threshold value for soft-tissue, and manually to remove artifacts. The use of this threshold value does not allow to differentiate between the various tissues of the body because, except the skeletal one, all tissue are “soft”.

Great attention is needed in segmentation geometry and in removing artifacts.

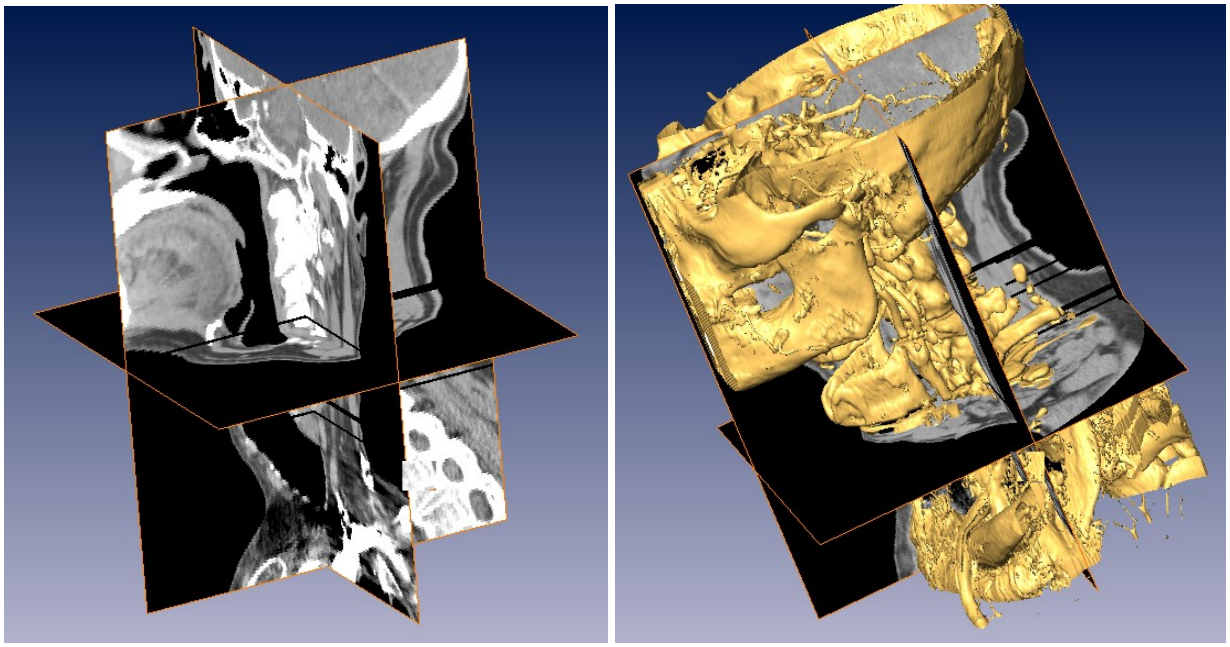

(7.a) (7.b)

Figure 7.1: Reconstruction of geometrical model using AMIRA, (7.a) three-dimensional view of the assembled slices, (7.b) creation of the iso-surfaces setting the threshold value.

An example of this procedure is shown in Figure 7.1. Based on the ICA outlet, the stenosis corresponds to a 90% area reduction. The image-processor software generates an STL data file with triangular elements which is imported on commercial mesh-generator code GAMBIT, where we have performed the smoothing operations, in order to make the surface continuous and regular, which includes elimination of singularities and spikes, filling of the holes, and a high-quality tetrahedral mesh with over four millions elements was generated.

7.3 Boundary Conditions

We have reconstructed the flow-rate-wave from literature data [7.14] in order to determine the inlet flow conditions. We have constructed a vector data containing the values of flow-rate-wave, each value correspond to a different instant of time. Applying the FFT to this

data vector, a complex vector of the Fourier coefficients was obtained, which is periodic because the impute signal is discrete. In order to avoid the aliasing, the second half of the Fourier coefficient was set equal to zero, and only the first half is used to generate the harmonic signal in time. In this way we have imposed at the inlet of CCA, a flow-rate composed by 10 harmonics wave.

The waveform is shown in Figure 7.2.

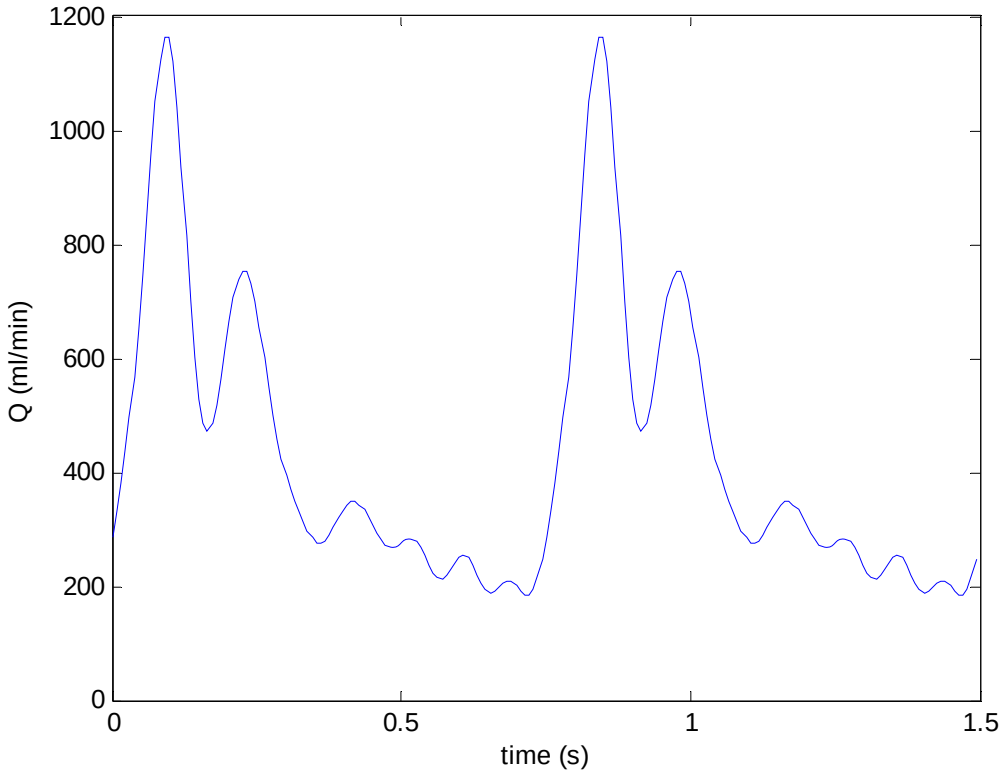

Figure 7.2: Flow-rate-wave used for computation

For the vessel wall we have imposed boundary condition of no-slip rigid wall. This assumption is realistic near the plaque because the calcium makes the plaque rigid, but could affect the solution far from the stenosis. We know that in a normal carotid artery the subdivision

of the flow is 65% of flow in ICA and 35% in ECA, but the percentage of stenosis reduce this flow-rate distribution.

A constant flow division between the ICA and ECA was kept during the cardiac cycle, assuming a 58% for ICA, 28.77% for AECA and 13.23% for PECA. Simulations under pulsatile flow conditions were conducted for 2 cardiac cycles.

7.4 Numerical methods

The governing incompressible Navier–Stokes equations were solved numerically with the finite-volume software Fluent. This solver has been successfully used in various biological fluid dynamics applications and has been extensively validated with experimental data. Second-order upwind differential scheme was used for spatial discretization and second order implicit scheme was used for time. A segregated, implicit solver was used to solve the continuity and momentum equations. As pressure–velocity coupling algorithm was employed the simple algorithm of Patankar.

The iteration steps were repeated until convergence was reached, using like convergence criterion a residual amplitude of residual equal to 10^{-6}. The steady-state solution was used as initial condition for the pulsatile simulation. The flow-rate wave was implemented in FLUENT as a boundary condition writing an UDF. We can write the equation to be solved in this form

$$\nabla \cdot \vec{v} = 0 \tag{7.1}$$

$$\rho \frac{D\vec{v}}{Dt} = -\nabla p + \nabla \cdot \left(2\mu\left(\dot{\gamma}\right)[D]\right) \tag{7.2}$$

where,

$$[D] = \frac{\left([\nabla \vec{v}] + {}^{t}[\nabla \vec{v}]\right)}{2} \tag{7.3}$$

is the rate of strain tensor and

$$\dot{\gamma} = \sqrt{2[D]:[D]} \tag{7.4}$$

is the shear rate.

If the fluid is Newtonian, the viscosity is constant and so we can obtain the Navier-Stokes equations. If viscosity is a function of the shear rate. Equation (7.2) is written in a GNF form derived from Reiner and Rivlin. We know that the viscosity of blood depends on the viscosity of plasma, in combination with the hematocrit by a complex relation. Furthermore, when velocity or shear rate increases viscosity decreases. In this work the non-Newtonian viscosity was modeled with the Casson formula.

$$\mu(\dot{\gamma}) = \left(\mu_{\infty} + 2\frac{\sqrt{\tau_0 \mu_{\infty}}}{\sqrt{\dot{\gamma}}} + \frac{\tau_0}{\dot{\gamma}} \right) \tag{7.5}$$

where τ_0 is the yield stress and μ_{∞} the asymptotic Newtonian viscosity, which are both function of hematocrit for blood.

The difficulty in using the Casson model in a numerical scheme lies in its discontinuous character in the limit of zero shear rate. We will overcome this discontinuity using the regularization technique given in [7.15].

$$\mu(\dot{\gamma}) = \left(\mu_{\infty} + 2\frac{\sqrt{\tau_0 \mu_{\infty}}}{\sqrt{\dot{\gamma}}}\left(1 - e^{-\sqrt{m\dot{\gamma}}}\right) + \frac{\tau_0}{\dot{\gamma}}\left(1 - e^{-\sqrt{m\dot{\gamma}}}\right)^2 \right) \tag{7.6}$$

when shear rate became zero we obtain

$$\mu(0) = \left(\mu_{\infty} + 2\sqrt{m\tau_0 \mu_{\infty}} + m\tau_0 \right) \tag{7.7}$$

where *m* is the Casson viscosity regularization exponent and is typically taken to be 1. Following [7.15] and [7.16] we have achieved the interest parameters for our patient, $\tau_0 = 0.01Pa$, $\mu_\infty = 0.00333Pa \cdot s$. In FLUENT the Casson viscosity model was introduced writing an UDF. In Figure 7.3 we present the variation of viscosity respect to shear rate.

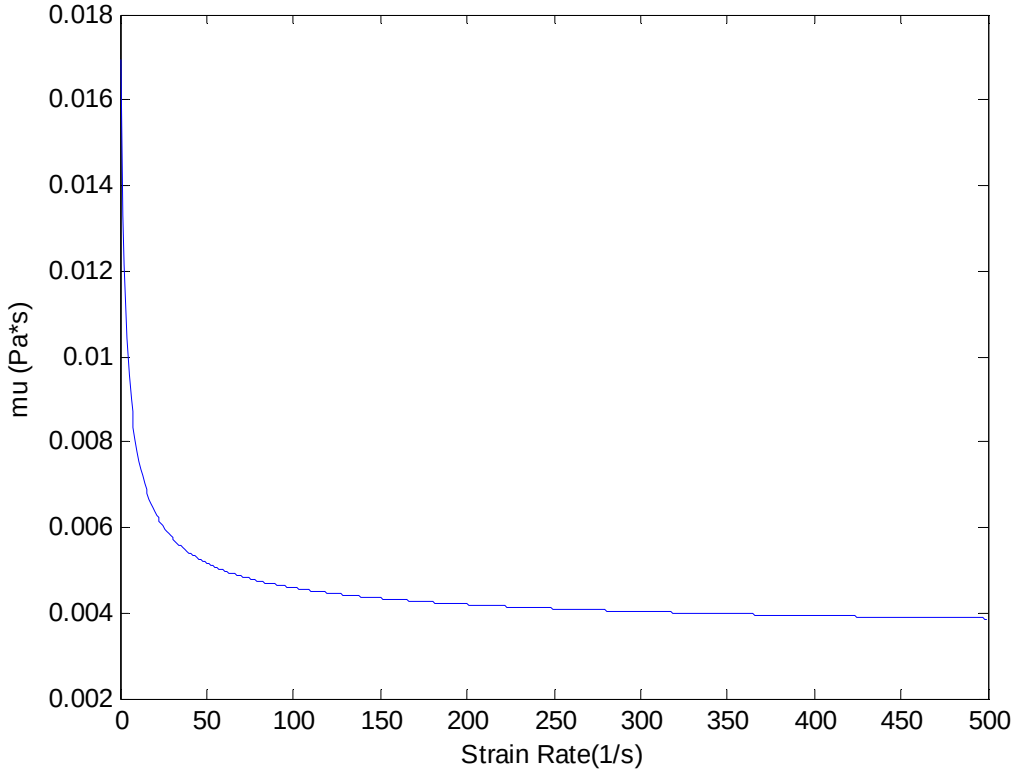

Figure 7.3: variation of viscosity respect to shear rate.

For both simulations we have imposed a density of 1060 $kg \cdot m^{-3}$. For the Newtonian case we have imposed a viscosity of $4.36 \cdot 10^{-2}$ $kg \cdot m^{-1} \cdot s^{-1}$ corresponding to the mean Casson viscosity. Each cardiac cycle required approximately 20 hours of CPU time on 4 processors.

7.5 Results

Transient simulations were performed for each rheological model described above. Each simulation was from 0 to 1.5 s, including two periods of sphigmic wave.

7.5.1 Wall Shear Stress

Figures 7.4-7.6 show the distribution of WSS at different instant of time. We have marked the Figure 7.s representing the Newtonian fluid with (7.4a) and the Casson one with (7.4b).

At the beginning of the second cardiac cycle (7.t=0.7575sec, Figure 7. 4) the distribution of WSS appears uniformly low in all region of the domain except in proximity of the stenosis. Two regions of high WSS appear at the inlet and at the small outlet. This is because these regions are influenced by the inlet-outlet boundary conditions and there is no physical reason to have an increase of WSS here. Since they are far from the plaque it does not affect the solution. There is no substantial difference in the pattern of WSS for Newtonian fluid and non-Newtonian one at this point of the cycle.

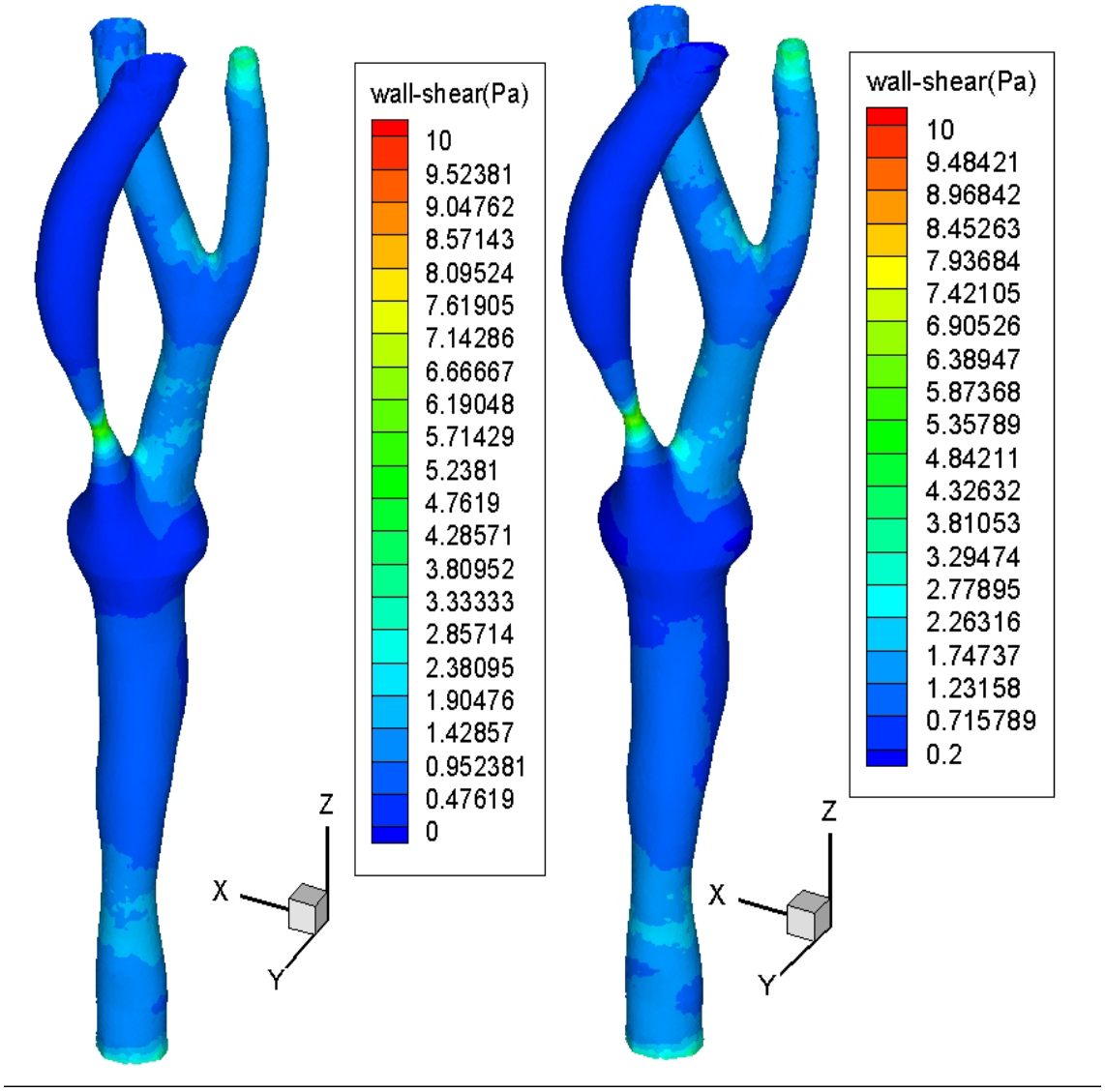

(7.4a) (7.4b)

Figure 7. 4: WSS distribution at t=0.7575s (7.a) Newtonian (7.b) Cassonian

Figure 7. 5 shows what happens three hundreds of second later. We can observe at the beginning of the CCA patches of moderate WSS, this is due to the fact that here the section became tight. In the rest of the CCA we can find region of low WSS due to the wider section. Quite a little before the bifurcation the section increases a lot allowing the presence of recirculation region. In the ICA WSS values increase rapidly because of the increasing velocity

and the presence of the stenosis, but the area of high WSS do not spread around this area. This is due to the fact that the sections downstream and upstream the stenosis are considerably high and the mean velocity in this branch decrease a lot. In the ECA immediately downstream the bifurcation we have patches of moderate WSS that disappear next to the second bifurcation of the ECA and reappear downstream the bifurcation.

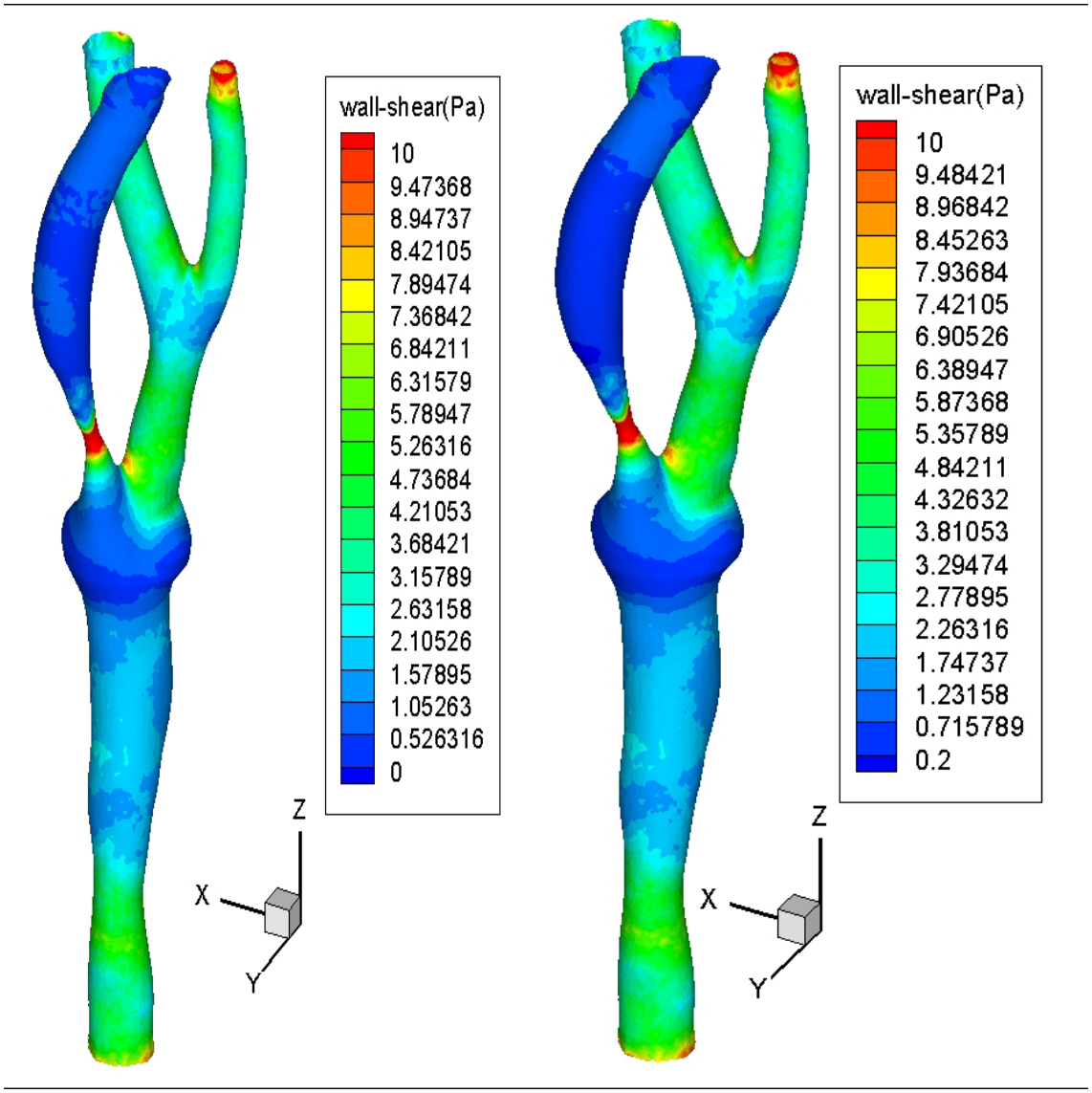

(7.5a) (7.5b)

Figure 7. 5: WSS distribution at t=0.7875s (7.a) Newtonian (7.b) Cassonian

In the two branches of ECA we have a quiet uniform distribution of WSS due to the uniform section. Some differences appear in the WSS pattern between Newtonian case and Cassonian one. In particular there the regions of high WSS for the Casson fluid show a little big spreading. In Figure 7.6 are shown the WSS patterns for the instant of highest flow rate. At this point we have the biggest values of WSS of all the cycle. At the CCA the WSS grow and the patches region became a uniform region of moderate WSS. Nevertheless this region does not spread further the constriction of CCA. In the rest of the CCA the WSS distribution present low values as far as on the bifurcation. On the stenosis the spreading of high WSS zones increase and we can observe the presence of zones, downstream and upstream of moderate WSS. In the rest of the ICA the WSS is low due to the enlargement of the section. At ECA the patches region of low WSS become a uniform region of moderate WSS with patches of high WSS at the internal side. At the bifurcation of ECA we can observe region of low WSS at the shoulders of bifurcation and region of high WSS at the internal side of the branches. This is a typical distribution of WSS in a bifurcation. The two branches of ECA show region of moderate WSS. There is no substantial difference in WSS patterns between Newtonian fluid and the Casson one at this time step.

According to the flow rate wave-form, we have a cyclic pattern of WSS. After the maximum values we have a depression in which the WSS decrease uniformly letting the moderate WSS regions became patches of low WSS and than another peak in which the pattern is quite similar to those obtained in Figure 7. 6. Next the WSS decrease uniformly with time according to flow-rate wave showing a pattern similar to that shown in Figure 7. 4. The ICA downstream the stenosis and the CCA show low WSS values at all time. During all cycle, as can be shown by Figures (7.4-7.6), the Casson fluid presents the highest values of WSS. In particular the values of

WSS are 2 or 4Pa higher than those of Newtonian one. In particular the values of WSS are 2 or 4Pa higher than those of Newtonian one.

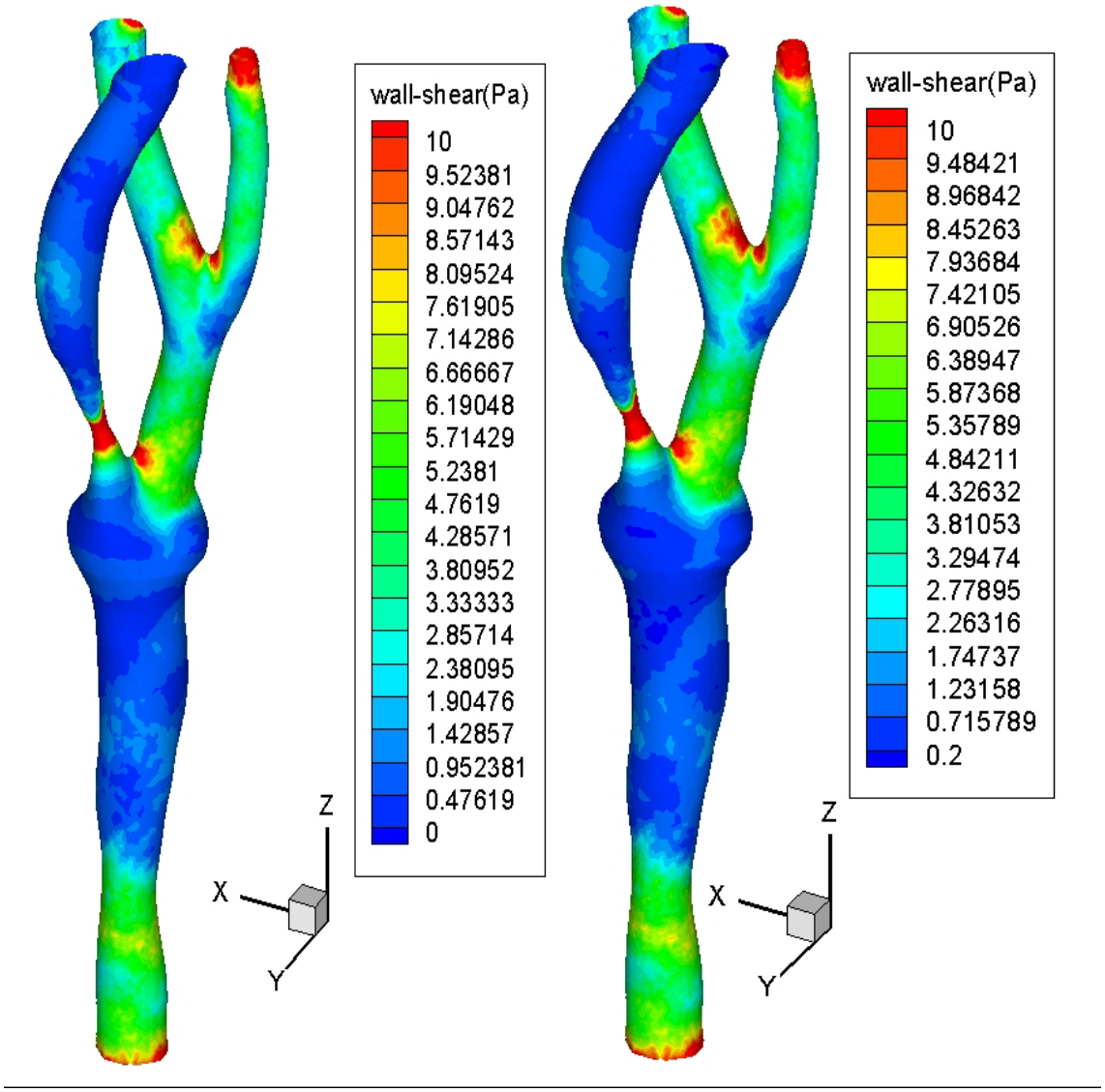

(7.6a) (7.6b)

Figure 7. 6: WSS distribution at t=0.825s (7.a) Newtonian (7.b) Cassonian

In order to discuss the importance of the non-Newtonian factor we have computed the average WSS over the plaque and over the wall. Defining

$$WSS_{N,w}(t) = \frac{1}{A_{wall}} \int_{A_{wall}} WSS_N(x,y,z,t)\,dA \tag{7.8}$$

$$WSS_{C,w}(t) = \frac{1}{A_{wall}} \int_{A_{wall}} WSS_C(x,y,z,t)\,dA \tag{7.9}$$

$$WSS_{N,p}(t) = \frac{1}{A_{plaque}} \int_{A_{plaque}} WSS_N(x,y,z,t)\,dA \tag{7.10}$$

$$WSS_{C,p}(t) = \frac{1}{A_{plaque}} \int_{A_{plaque}} WSS_C(x,y,z,t)\,dA \tag{7.11}$$

We can use these indices to evaluate the influence of the non-Newtonian factor:

$$err_{rel,w}(t) = 1 - \frac{WSS_{N,w}(t)}{WSS_{C,w}(t)} \tag{7.12}$$

$$err_{rel,p}(t) = 1 - \frac{WSS_{N,p}(t)}{WSS_{C,p}(t)} \tag{7.13}$$

$$err_{abs,w}(t) = WSS_{C,w}(t) - WSS_{N,w}(t) \tag{7.14}$$

$$err_{abs,p}(t) = WSS_{C,p}(t) - WSS_{N,p}(t) \tag{7.15}$$

The equations (7.12-7.15) define four error index, two relative and two absolute, and they are relative to the plaque and to the wall. The results in Figures 7.7-7.8 report the error pattern during cardiac cycle. The absolute error on plaque, reported in Figure 7.7, is about 2.6-5.2Pa, that for the wall is 0.8-1.65Pa. These values appear low compared to those of the legend of Figures 7.4-7.6, but it should be remembered that the WSS scale is shifted to high values due to

the presence of the plaque and that physiological values of WSS are in the order of magnitude of the unity.

The Figure 7.7 shows that the maxima differences are present where the WSS is maximum and the minima where it's minimum. With regard to the relative error indices the opposite consideration can be done. Observing Figure 7.8 we can find a relative error index in the range between 3-9.5% for the plaque and for the rest of the wall the relative errors values are between 10-26%. Moreover it must be pointed out that the maximum values of relative error indices can be found in the phase of minimum flow rate of the cycle. So the maxima values of absolute error are showed where the relatives are minima and vice versa.

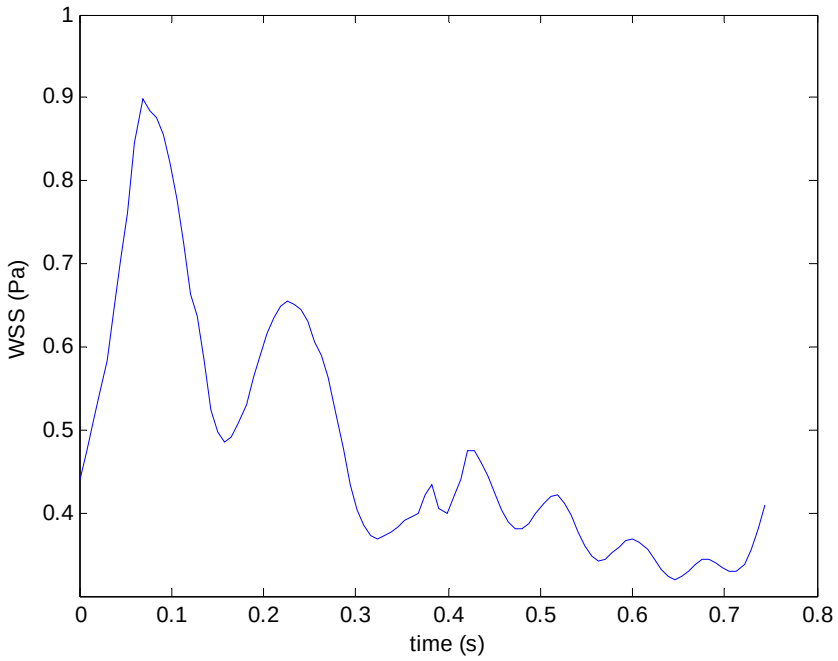

(7.7a)

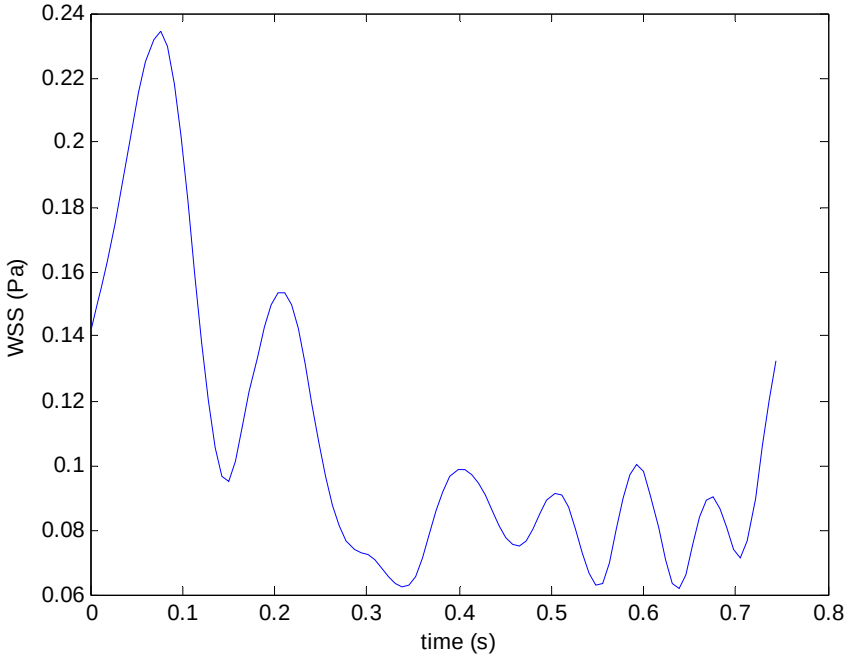

(7.7b)

Figure 7.7: Absolute error values for the plaque (7.7a) and for the wall (7.7b)

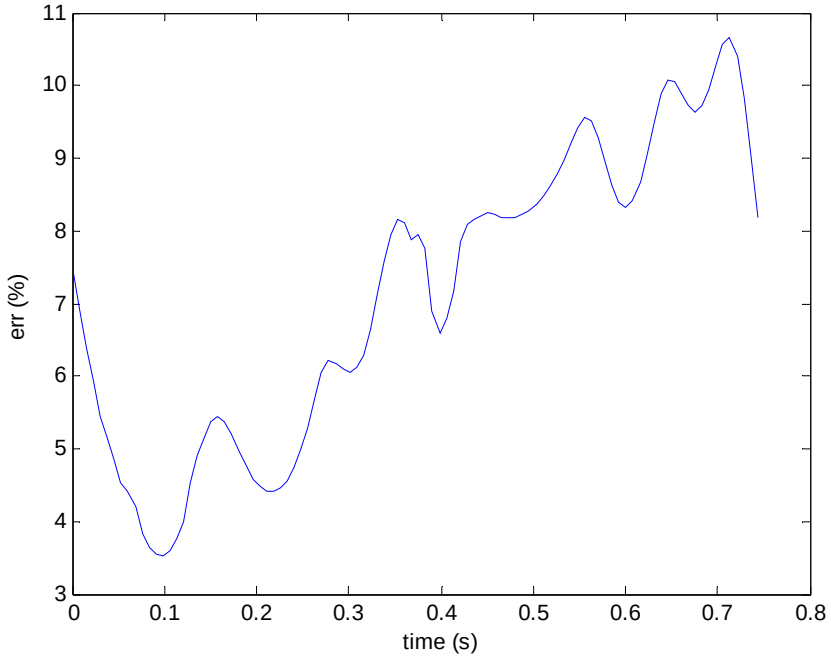

(7.8a)

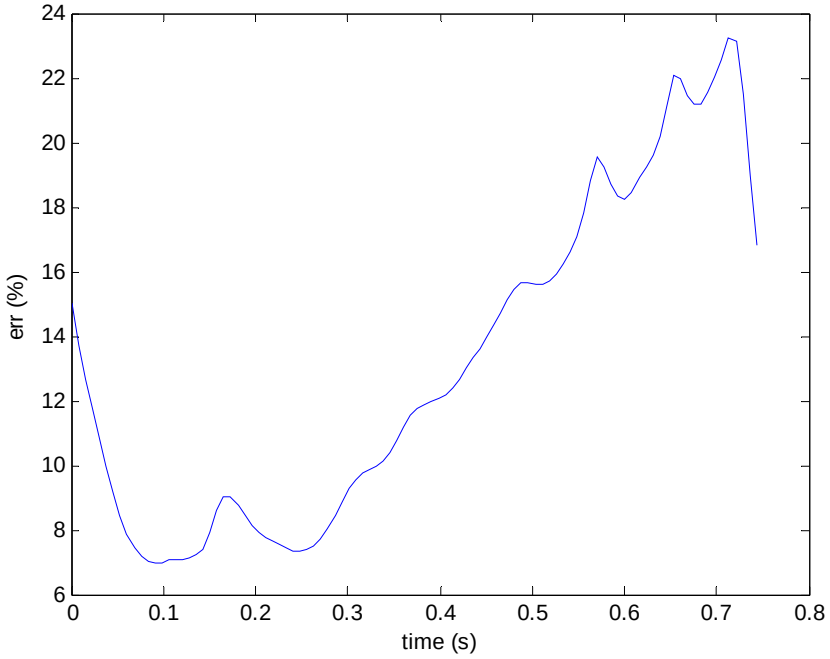

(7.8b)

Figure 7.8: Relative error values for the plaque (7.8a) and for the wall (7.8b)

7.5.2 Non-Newtonian Importance Factor

In order to quantify the effect of this non-Newtonian model on the WSS distributions, we will use the local non-Newtonian importance factor I_L, introduced by Johnston in [7.8], and defined as

$$I_L = \frac{\mu}{\mu_\infty} \tag{7.16}$$

where μ is the apparent viscosity and μ_∞ the Newtonian value for viscosity. The ratio expresses the degree of molecular viscosity deviation from Newtonian behavior. I_L is equal to one for Newtonian flow and values which are significantly different from unity indicate regions of high

Non-Newtonian behavior. Figures 7.9a, 7.9b, 7.9c show a plot of I_L for the Casson fluid at different instants of time.

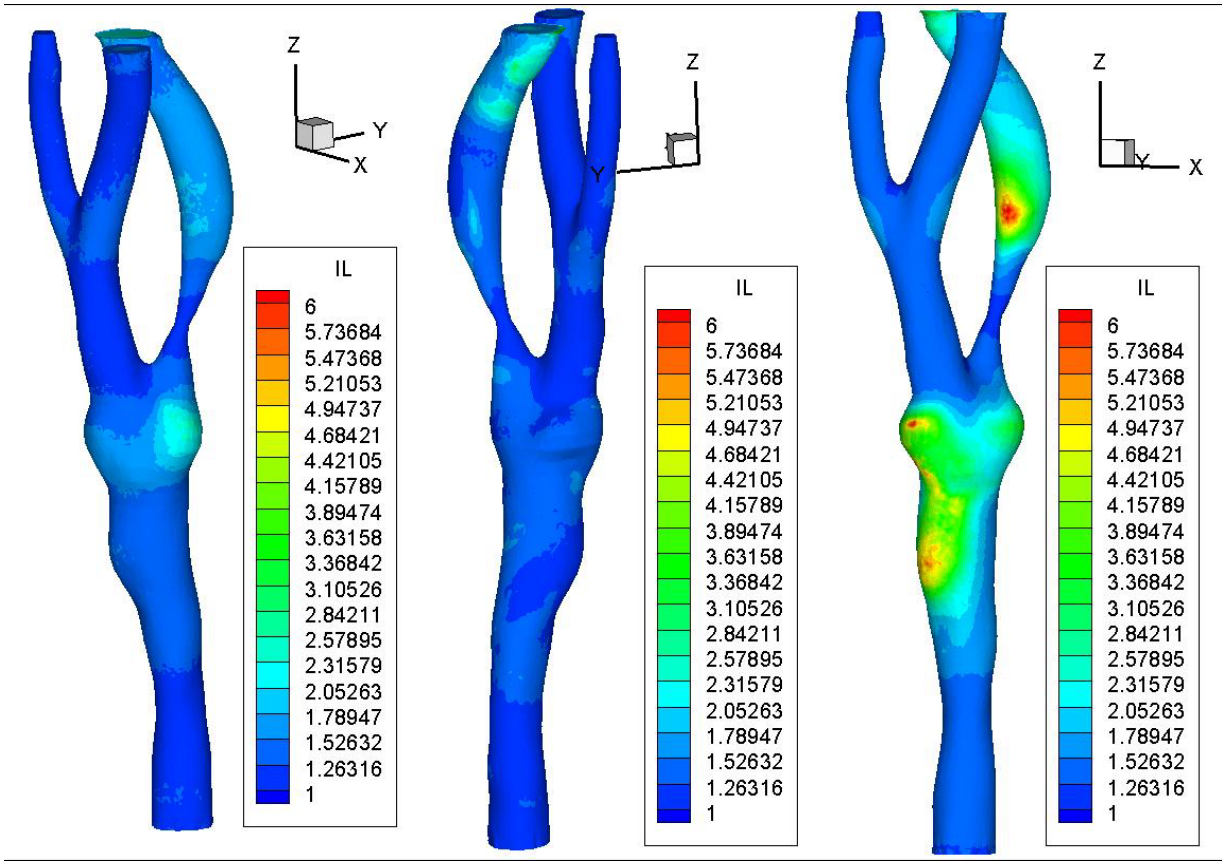

(7.9a) (7.9b) (7.9c)

Figure 7.9: Local Non-Newtonian Importance Factor: (7.9a) 0.7575 sec, (7.9b) 0.9 sec, (7.9c) 1.425 sec

It can be seen that there are patches of non-Newtonian flow before the bifurcation, where the section is bigger and the velocity slower and in the internal carotid artery because in these conditions the flow rate is very small in this branch, also in the external branch, near the second bifurcation we can see patches of non-Newtonian behavior. The I_L value raises also 6 units in diastolic part of the cardiac cycle. In Figure 7.9 are reported the I_L wall values but this variables is defined in the entire domain. The choice of showing only this part of the domain is due to the

fact that in this region the shear rate is bigger and so the non-Newtonian behavior will be less important in this region, and so the scale in Figure 7.9 underestimates the non-Newtonian behavior in the entire domain.

The plots and graphs of the WSS, shown in Figures 7.5-7.7, show that the WSS pattern of the non-Newtonian model is close to that produced by the Newtonian one and hence we would expect the value of I_G; representing the percentage difference of WSS from the Newtonian model, to be low. Here it can be seen that the model produces WSS very close to the Newtonian values.

Following the discussion of Johnston in [7.8] we also investigate the global Non-Newtonian Importance Factor

$$I_G = 100\frac{1}{N}\frac{\left[\sum_N \left(\mu-\mu_\infty\right)^2\right]^{1/2}}{\mu_\infty} \tag{7.17}$$

which is the relative difference of each value of viscosity from the Newtonian value averaged and expressed as a percentage. The I_G is evaluated only at each of the N nodes on the surface of the artery. In Figure 7.10 the plot of the I_G values versus time is reported.

As the inlet velocity value increases the I_G value tends to decrease, moreover the I_G values are in a range of 0.065-0.155 units, in accordance to the literature [7.8, 7.12]. In according to the literature [7.12] and in particular with the work of Johnston [7.8], we assume that values below 0.25 units indicate Newtonian behavior.

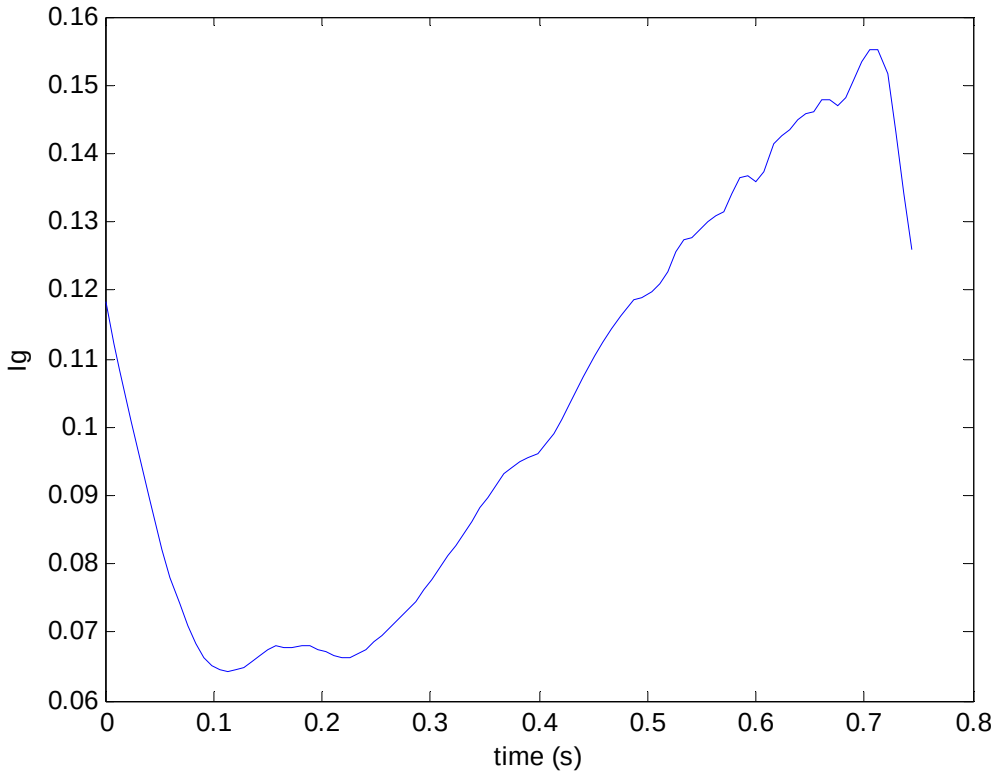

Figure 7. 10: Global Non-Newtonian Importance Factor

Since the maximum value reached during the entire cycle is 0.16 units from the non-Newtonian importance factor analysis we can affirm that the non-Newtonian features of the fluid don't play an important role in the WSS determination for a carotid artery subjected to high degree stenosis.

The reason stay in the high velocity of the fluid in the carotid artery and in the severity of the stenosis: the flow rate in the stenosed branch is reduced but due to the decreasing of the section the shear rate is still high and the behavior is completely Newtonian, downstream the stenosis, due to the decreased flow rate the non-Newtonian behavior is marked. In the external branch due to the mass conservation law the flow rate must increase than the stenosis free case, and so the shear rate will increase and the non-Newtonian features don't appear.

7.6 Discussion

The aim of this work was to assess the difference between Newtonian and non-Newtonian viscosity models of blood flow in a human high degree-stenosis coronary artery. The Casson model has been considered in describing blood viscosity. The role of viscosity in the development and progression of vascular disease is very important. Henceforth, the selection and application of an appropriate viscosity model for CFD analysis is crucial for achieving acceptable results.

Results for transient simulation of blood flow in the human right carotid artery have been presented in the previous section in terms of wall shear stress and non-Newtonian Importance factor distribution. There isn't a significant variation between the models in terms of wall shear stress distribution. The reason could be that the shear rate is significantly high in the entire domain during the cardiac cycle. This is in agreement with Jonston [7.8] that suggested that the use of non-Newtonian model is important only for low velocities leading to low shear rate.

The carotid artery is a medium artery and the velocity here is relatively high. The transient analysis is important because, as suggested by the Figures 7.4-7.6, the WSS pattern change a lot during the cycle. Jonston in [7.6] suggest that the non-Newtonian importance factors are only significant during periods where the blood flow is quite slow.

We have used the non-Newtonian importance factor as an index, our results are in accordance to this in terms of relative error (Figure 7.8) and in disagreement in terms of absolute error (Figure 7.7) where we have found big differences during periods where the blood flow is fast.

This mustn't astonish because of the nature of Casson fluid. Indeed, the WSS in a Casson fluid is inversely proportional to the shear rate, so when the shear rate increase, the viscosity tends to a constant value, that one of the Newtonian fluid, instead when the shear rate is small WSS is higher than that found for Newtonian fluid.

Since in a rigid duct flow the shear rate increase white the flow rate, at time steps in which the flow rate increase also the shear rate increase and we can find a behavior similar to the Newtonian one, instead, decreasing the flow rate, also the shear rate decrease and the WSS of Casson fluid grow up, so in this phase of the cycle will be the biggest difference between Newtonian and non-Newtonian fluid. Moreover the shear rate is a function of the geometry, so where the duct diameter is small, it will be high shear rate whereas where the diameter is high the shear rate will be small.

This implies that on the stenosis, due to the conservation of mass, we have high velocity in a little area. So in this region the shear rate will be always high especially when it will be the maximum flow rate. Indeed in this cycle phase the relative error on the plaque is about 3-5%. There is a little area at the center of the plaque section in which the shear rate is low and this implies an increase of the WSS values of 4-5Pa respect to the Newtonian case. When the flow rate decreases also the shear rate decrease on the plaque but due to the small crossing area, the shear rate is always moderately high, leading to a greatest relative error of 9.5%. So we have the lowest differences between Newtonian and non-Newtonian fluid on the plaque.

In the rest of the duct, the diameter is considerably high than that of the stenosis and this reduce the shear rate, moreover due to mass conservation, the velocity is also smaller here and this is another reason of the decrease of shear rate. So, since the shear rate is small, there will be more differences between Newtonian and Casson fluid. In the phase of the cycle in which the

flow rate increase, the shear rate increase and so the difference are less marked giving anyway to a smallest relative error in this region of 10%, instead when the flow rate decrease the relative error rise till 26%, which is a big relative error.

The Local non-Newtonian Importance Factor analysis at different instants of time show the regions of vessel wall in which the flow possessing high molecular viscosity. These regions have a different distribution respect to the wall shear stress one but even at the wall they varies in a range between 1-6 and for all the cycle there are regions in which the viscosity is always 2-6 times bigger to the Newtonian one, except the stenosis in which the values are always around the unity.

Considering the results given by the error curves and the local non-Newtonian importance factor we can surely say that on the stenosis the shear rate is too high to exhibit a non-Newtonian behavior. Otherwise in the rest of the duct the big values in terms of relative error and Local non-Newtonian Importance Factor could suggest that the non-Newtonian nature of the viscosity can influence the Wall Shear Stress distribution at the stenosis and so this feature of the flow is enough important in performing a simulation.

The variable that can disappear any doubt is the Global non-Newtonian Importance Factor. The non-Newtonian Casson model decreases the I_G value with increasing inlet velocity. The analysis has shown that I_G is always smaller than the value accepted as critical. In relation to the others data achieved we can argue that values of relative errors for the stenosis (4%-11%) and for the rest of the duct (7%-23%) are not big enough to justify the choice of a Casson viscosity model to describe the blood flow.

Anyway it must be pointed out that in the carotid artery the velocity is moderately and the presence of the stenosis increase also the shear rate. This avoids the exhibition of non-Newtonian

features by the fluid. A simulation on a low or moderate-degree stenosis carotid artery could show the importance of considering this characteristic. Moreover concerning the development of the atherosclerosis pathology an absolute error of few Pascal (0.3Pa-1Pa on the stenosis, 0.06Pa-0.24Pa on the wall), should be important in determining the percentage area subjected to critical WSS values for restenosis because values smaller than 0.5Pa are indicated by the literature [7.1, 7.17-7.18] as promoters of neo intimal hyperplasia, while values higher than 1 Pa seem to have no relation with neo intimal hyperplasia.

7.7 Conclusion

This paper has presented a transient study of blood flow in an image based right carotid artery with two different blood viscosity models. A comparison of the two models shows that the WSS distribution forms complex patterns on the artery wall which change considerably during the cardiac cycle.

It appears that low wall shear stress predominates on the CCA, and downstream the stenosis, while high wall shear stress is always present on the stenosis. In this region due to the reduction of the section we can find also high values of the shear rate. The Newtonian blood flow treatment is considered to be a good approximation at mid and high-strain rates.

The analysis in terms of relative and absolute error show that there are low discrepancies between the Newtonian and non-Newtonian case during the systolic phase of the cycle while in the diastolic one the differences are not so negligible. The high values of the local non-Newtonian Importance Factor during the diastolic phase of the cycle also allow supposing that the non-Newtonian features of the flow could have some importance.

Nevertheless the Global non-Newtonian Importance Factor analysis revealed that the I_G remains always quite below the critical value of 0.25 units. From this last result we can conclude that for a high stenosis degree carotid artery subjected to the cardiac wave the non-Newtonian features of the fluid are negligible even if the wall shear stress difference between the Newtonian and non-Newtonian model are around 20%.

These conclusions are based on simulations for a heart rate of only 60 beats per minute. Hence, for simulation purposes, to study wall shear stress a Newtonian model would be sufficient, but to study the flow in more detail, to look at mixing within the blood or stresses on individual blood cells (haemolysis) for example, the non-Newtonian behavior of the blood should be included.

These conclusions are presented under the assumption that a fixed mesh is used to study the flow. There may be some discrepancy if the simulations were performed on a model with elastic arterial walls and the artery was allowed to move with the beating heart. Moreover different geometry of the vessel could exhibit different wall shear stress pattern. A future study could investigate the influence of the geometry in predicting the wall shear stress values as in [7.7-7.8, 7.19].

References of Chapter 7

[7.1] D. N. Ku, "Blood Flow in Arteries", Annu Rev Fluid Mech, 01/1997.

[7.2] C. G. Caro, "Vascular fluid dynamics and vascular biology and Disease", Math Meth Appl Sci 24: 1311–1324. 2001.

[7.3] D. A. Steinman, J. B. Thomas, H. M. Ladak, J. S. Milner, B. K. Rutt, and J. D. Spence "Reconstruction of Carotid Bifurcation Hemodynamic and Wall Thickness Using Computational Fluid Dynamics and MRI", Magn Reson Med 47:149–159 (7.2002).

[7.4] J. B. Thomas, J. S. Milner, B. K. Rutt and D. A. Steinman, "Reproducibility of Image-Based Computational Fluid Dynamics Models of the Human Carotid Bifurcation", Ann Biomed Eng, 31: 132–141, 2003.

[7.5] M. D. Ford, G. R. Stuhne, H. N. Nikolov, D. F. Habets, S. P. Lownie, D. W. Holdsworth, and D. A. Steinman, "Virtual Angiography for Visualization and Validation of Computational Models of Aneurysm Hemodynamics", IEEE Trans Med Imaging, 24, 12, 2005.

[7.6] J. R. Cebral, P. J. Yim, R. Lohner, O. Soto, H. Marcos, P. L. Choyke, "New methods for computational fluid dynamics modeling of carotid artery from magnetic resonance angiography", Proc. SPIE, 4321, 177-87, 2001.

[7.7] B. M. Johnston, P. R. Johnston, S. Corney, D. Kilpatrick "Non-Newtonian blood flow in human right coronary arteries: Transient Simulations", J. Biomech, 39, 6, 1116-28, 2006.

[7.8] B. M. Johnston, P. R. Johnston, S. Corney and D. Kilpatrick, "Non-Newtonian blood flow in human right coronary arteries: steady state simulations", J. Biomech 37 (7.5), 709–720, 2004.

[7.9] F. J. H. Gijsen, E. Allanic, F. N. Van De Vosse, J. D. Janssen, "The influence of the non-Newtonian properties of blood on the flow in large arteries: Unsteady flow in a 90curved tube", J. Biomech, 32, 7, 705-713, 1999.

[7.10] T. Ishikawa, L. F. R. Guimaraes, S. Oshima, R. Yamanae, "Effect of Non-Newtonian property of blood on flow through a stenosed tube", Fluid Dynamics Research, 22: 251-264, 1998.

[7.11] C. Tu and M. Deville, "Pulsatile flow of Non-Newtonian fluids through arterial stenoses", J. Biomech, 29, 7, 899-908, 1996.

[7.12] Johannes V. Soulis, George D. Giannoglou, Yiannis S. Chatzizisis, Kypriani V. Seralidou, George E. Parcharidis, George E. Louridas Non-Newtonian models for molecular viscosity and wall shear stress in a 3D reconstructed human left coronary artery Medical Engineering & Physics 30 (7.2008) 9–19

[7.13] S. Hyun, C. Kleinstreurer, P.W. Longest and C. Chen, "Particle-Hemodynamic Simulations and Design Options for Surgical Reconstruction of Diseased Carotid Artery Bifurcations", J Biomech Eng, 126, 188-195, 2004.

[7.14] S. E. Lee, S.-W. Lee, P. F. Fischer, H. S. Bassiouny, F. Loth, "Direct numerical simulation of transitional flow in a stenosed carotid bifurcation", J. Biomech, 41:2551–2561, 2008.

[7.15] K. Mukundakrishnan, P. S. Ayyaswamy and D. M. Eckmann, "Finite-sized gas bubble motion in a blood vessel: Non-Newtonian effects", Phys. Rev. E 78, 036303, 2008.

[7.16] M. Sharan and A. S. Popel, "A two-phase model for flow of blood in narrow tubes with increased effective viscosity near the wall", Biorheology, 38, 415, 2001.

[7.17] Ku D.N., D.P. Giddens, C.K. Zarins, S. Glagov. Pulsatile flow and atherosclerosis in the human carotid bifurcation. Positive correlation between plaque location and low oscillating shear stress. Arteriosclerosis 5: 293-302, 1985.

[7.18] Malek A.M., S.L. Alper, S. Izumo. Hemodynamic shear stress and its role in atherosclerosis. JAMA 282: 2035-2042, 1999.

[7.19] F. Gori, A. Boghi. Image-Based Computational Fluid Dynamics in Carotid Artery. IMECE2009, November 13-19, 2009, Lake Buena Vista, Florida, USA

Chapter 8:

THREE-DIMENSIONAL NUMERICAL SIMULATION OF BLOOD FLOW IN TWO CORONARY STENT

8.1 Introduction

Atherosclerosis is one of the most common causes of death in the Western World. Stent is commonly used to restore blood flow in patients with severe coronary artery disease. Local hemodynamic variables, depending on stent geometry, have an important role in the restenosis. The new drug eluting stent reduces significantly the percentage of restenosis [8.1-8.4], also if the percent of restenosis in the long term may be similar to the classic one [8.5-8.6] and the restenosis rates may be similar to the bare metal stent [8.7-8.8]. The new drug eluting stent does not help in healing the intima damaged by prior vascular disease or stent implantation procedure and, being not applicable to all patient populations and locations within the arterial vasculature [8.9], cannot supplant the bare metal stent and avoid the fluid dynamics problems in the device designing. Local hemodynamic variables, as wall shear stress, have an important role in restenosis and are dependent on stent geometry [8.10-8.12].

Previous two-dimensional (2D) computational fluid dynamics (CFD) studies used simple stent geometry. Berry et al. [8.13] investigated the influence of mesh dimension on the flow, suggesting that a small mesh can disturb the flow more than a big one. Lanoye et al. [8.14] characterized the effect of the strut section, showing the round strut section disturbs the flow at a small extent. Seo et al. [8.15] investigated the influence of the stent design near the curvatures,

providing an understanding of the flow in the vicinity of the stent and suggesting strategies for the design optimization in order to minimize flow disturbance.

Few three-dimensional (3D) CFD studies have been carried out on stented arteries. LaDisa et al. [8.16-8.21] performed simulations to characterize the stent design, and geometrical parameters such as width, thickness and angle with the flow direction of the struts. He at al. [8.22] studied realistic strut geometry, considering three geometric parameters of the struts and demonstrating the stent design is crucial in determining the fluid flow in an artery.

Duraiswamy et al. [8.23] provided a physiologic assessment on the effects of stent geometry on platelet deposition by using actual stent. Three-Dimensional Computational Fluid Dynamic models of the stent provided flow data explaining localized platelet deposition and identifying the regions of deposition. The localized platelet deposition is dependent on flow convection, suggesting that arterial reaction to stent can be modulated in part by altering the hemodynamics associated to stent design.

The goal of the present study is to reconstruct a realistic 3D geometry of a coronary stent in order to carry out CFD simulations in physiological conditions. A comparison is carried out between two reconstructed stent, made of 12 rings and similar to the real coronary ones. The two stents differ only by the position of the struts, the first type is with parallel-connectors and the second one with transverse-connectors. The artery is modeled as a rigid cylinder and the fluid is an incompressible Newtonian fluid in laminar flow with the average physical properties of blood.

8.2 Geometry

A real 3D geometry of a coronary stent, made of sequential rings and connected with longitudinal flexible connectors, is considered. Two different connections are investigated:

regular peak to peak and mid-strut to mid-strut. The first type of stent is then with parallel-connectors and the second one with transverse-connectors [8.24], similarly to the real coronary stent. For simplicity we will call parallel-connectors stent as S1, and transverse-connectors stent as S2.The software GAMBIT is used for reconstruction and mesh generation. The two complete reconstructed stent are shown in Figure 8.1a.

Only a portion of the stent, 60° of the cylinder as shown in Fig 8.1b, is investigated because of symmetry. Each reconstructed stent is made of 12 rings; artery diameter is 2.6 mm, width 0.1 mm and total length 27.6 mm, in agreement to a stented coronary artery [8.16] and a real coronary stent [8.25]. The mesh used is made of non-uniform tetrahedrons having a minimum volume of $5.38 \cdot 10^{-16}$ m^3 and a maximum one of $4.82 \cdot 10^{-13}$ m^3, as shown in Figure 8.2.

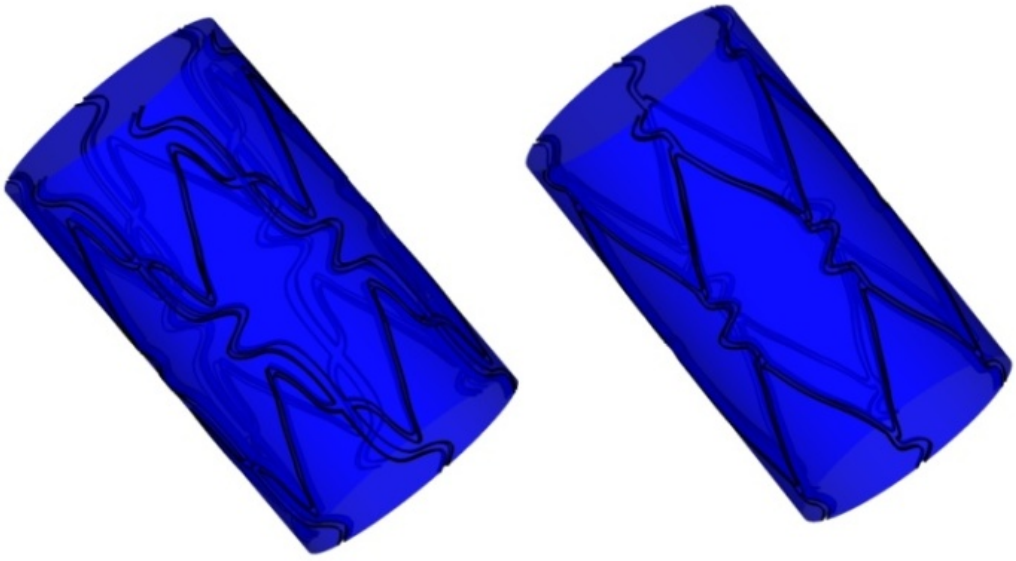

(8.1a)

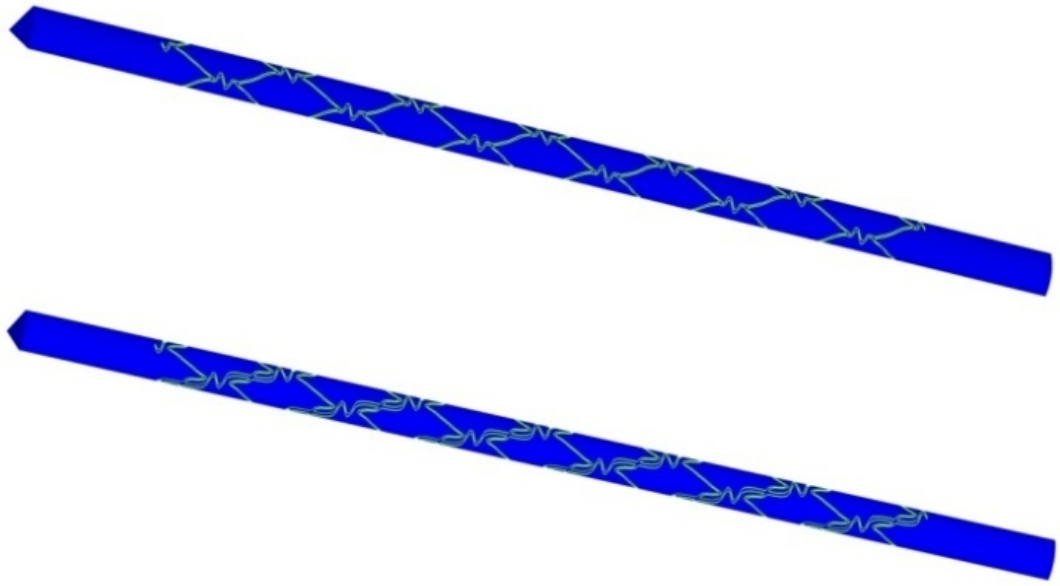

(8.1b)

Figure 8.1 - Reconstructed geometries and Meshes: (8.1a) complete stent, S2 on the left and S1 on the right, (8.1b) geometries used for numerical simulations.

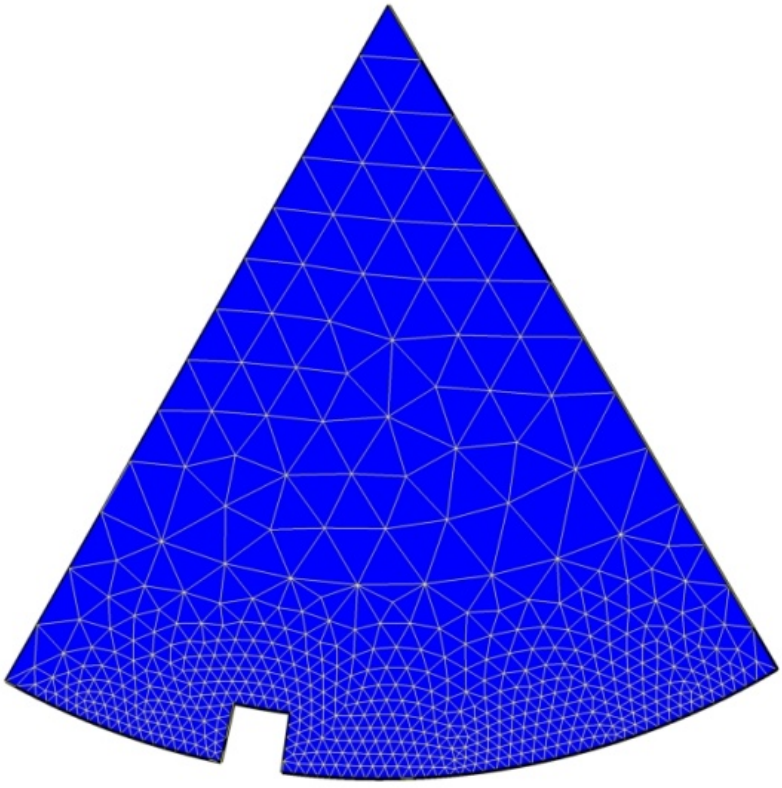

Figure 8.2 - Mesh.

8.3 Governing equations

The blood is assumed as an incompressible Newtonian fluid in laminar flow with the average properties of blood, such as ρ = 1,060 kg m^{-3}, and μ=0.003333 kg·m^{-1} s^{-1}. The conservation equations of mass and momentum are respectively:

$$\nabla \cdot \vec{v} = 0 \tag{8.1}$$

and

$$\rho \frac{D\vec{v}}{Dt} = -\nabla p + \mu \nabla^2 \vec{v} \tag{8.2}$$

Equations (8.1-8.2) are solved with the following boundary conditions: no slip on artery and stented walls, prescribed blood flow (8.constant or physiologic waveform) on the inlet and constant pressure on the outlet. The commercial computational fluid dynamic code FLUENT is used to carry out simulations in steady and unsteady states.

In unsteady state the physiological waveform of mass flux, measured by LaDisa et al. [8.16] in the proximal portion of a left anterior canine descending coronary artery, is employed, as shown in Figure 8.3. The artery diameter is the same as the diameter of the reconstructed artery. The waveform of Figure 8.3, sum of sinusoidal functions, is used as UDF input in the code FLUENT. In steady state the mean value of this waveform is employed, 104.85 kg m^{-2} s^{-1}.

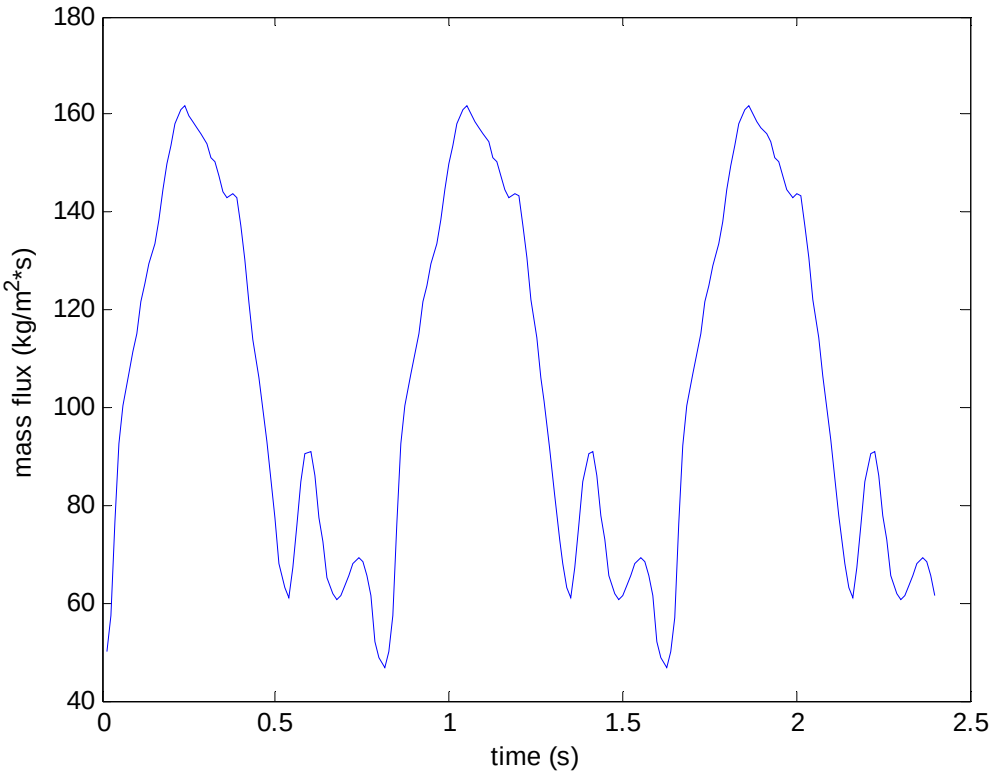

Figure 8.3 - Physiological inlet waveform of mass flux.

Simulations are carried out using a Core 2 Duo 2.2 GHz Intel Mobile Centrino with 2 GByte of RAM, running LINUX. The residuals values for mass and three velocity components, after 1000 iterations, are lower than 10^{-6} for all cases. In unsteady state the total investigated time (0.8 s) is split into 800 time steps, and 20 iterations are done for each period.

8.4 Fluid dynamics parameters

The most important fluid dynamic parameter, according to the literature, is the wall shear stress (WSS), defined, in cylindrical coordinates, by

$$WSS = \mu \sqrt{\left[\left(\frac{1}{r}\frac{\partial v_r}{\partial \vartheta} + \frac{\partial v_\vartheta}{\partial r} - \frac{v_\vartheta}{r}\right)^2 + \left(\frac{\partial v_r}{\partial z} + \frac{\partial v_z}{\partial r}\right)^2\right]}\Bigg|_{wall} \tag{8.3}$$

where v_r and v_θ are the r and θ components of the velocity, respectively. According to previous studies of the literature a low wall shear stress is below 0.5 Pa.

Another important parameter used in literature is the spatial wall shear stress gradient [8.26], WSSG, defined, in cylindrical coordinates, by

$$WSSG = \begin{bmatrix} \frac{\partial WSS_r}{\partial r} & \frac{1}{r}\frac{\partial WSS_r}{\partial \vartheta} - \frac{WSS_\vartheta}{r} & \frac{\partial WSS_r}{\partial z} \\ \frac{\partial WSS_\vartheta}{\partial r} & \frac{1}{r}\frac{\partial WSS_\vartheta}{\partial \vartheta} - \frac{WSS_r}{r} & \frac{\partial WSS_\vartheta}{\partial z} \\ \frac{\partial WSS_z}{\partial r} & \frac{1}{r}\frac{\partial WSS_z}{\partial \vartheta} & \frac{\partial WSS_z}{\partial z} \end{bmatrix} \tag{8.4}$$

where WSS_r and WSS_θ are the r and θ components of the WSS, respectively.

The modulus of this matrix is defined by:

$$MGS = \sqrt{\sum_{i=1}^{3}\sum_{j=1}^{3}\left(WSSG_{ij}\right)^2} \tag{8.5}$$

High values of magnitude of wall shear stress gradient, MGS are related to neointimal hyperplasia.

The oscillatory shear index (OSI) is defined in [8.27] as

$$OSI = \frac{1}{2}\left(1 - \frac{\int_0^T WSS_z\, dt}{\int_0^T \left\| WSS_z \right\| dt}\right) \tag{8.6}$$

where T is the period. OSI is investigated to measure the degree of deviation of the wall shear stress from its average direction during pulsatile flow.

8.5 Results

8.5.1 Mesh

Figure 8.4 presents the results of three simulations with different meshes, in order to show the spatial mesh independence of WSS, according to the proposal of Prakash et al. [8.28]. Figure 8.4 reports the average WSS for three different meshes, with about 765,000; 1,900,000 and 3,100,000 cells for both stent.

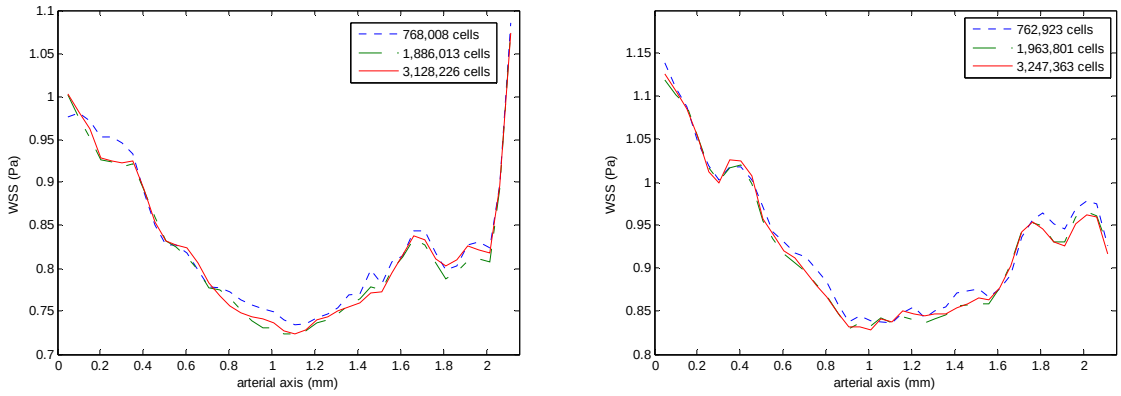

Figure 8.4 - WSS spatial distribution for different numbers of cells. S1 are on the left and S2 on the right.

Concerning the S2 stent the minimum and maximum percentage difference between 765,000 and 1,900,000 cells are about 3.46% and 0.29% while the minimum and maximum percentage difference between 1,900,000 and 3,100,000 cells are about 2.26% and 0.13%. Concerning the S1 stent the minimum and maximum percentage difference between 765,000 and 1,900,000 cells are about 2.33% and 0.03% while the minimum and maximum percentage difference between 1,900,000 and 3,100,000 cells are about 1.76% and 0.13%. The WSS distributions are enough close among the three simulations with the conclusion that a mesh with 765,000 cells is a good compromise.

8.5.2 Steady state simulations

The average WSS is reported versus the axial length in Figure 8.5, where the average is relative only to the endothelium, not to the stent. This is the reason of the low values of WSS. Figure 8.5 shows a repeating pattern of WSS being a periodic function presenting intermittent localized lower oscillations, due to the protrusion of the curved shape struts. WSS is greater in the S1 stent, as compared to the S2 one, due to the skewing of velocity profile, caused by the transverse struts of the S2 stent.

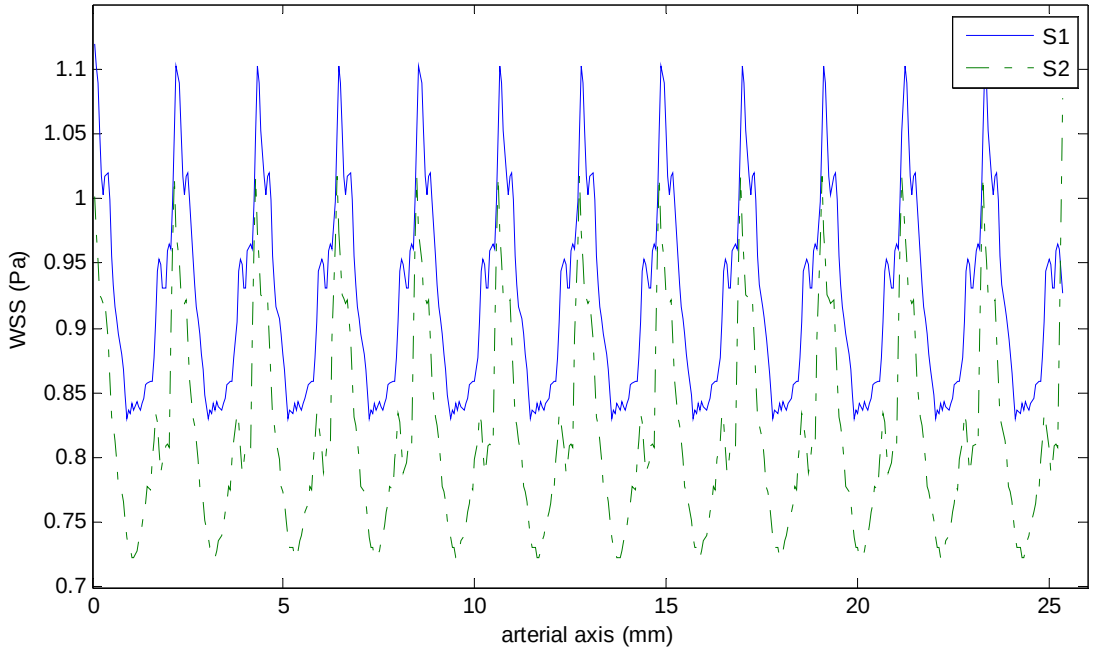

Figure 8.5 - WSS on endothelium for S1 and S2 stent.

The lowest values of WSS are due to the presence of the stagnation regions, while highest values are in the center of the cell, where the velocity vectors are parallel to the wall. The

differences between two WSS profiles are small, e.g. of the order of 0.1 Pa. Moreover, the spatial oscillations of WSS are low in each single stent, e.g. of the order of 0.35 Pa.

Distributions of WSS and MGS are presented in Figure 8.6 for each stent. Stagnation zones occurred around and between stent struts, generating lower WSS in both stent while, far from the struts, regions with higher WSS are observed. Velocity changes direction due to the stent, but, because of the small stent thickness, the occurring vortex is very small and can promote proteins deposition. The nominal diameter of the vessel is reduced on the stent surface, producing converging streamlines and higher WSS, while, after the stent struts, higher nominal diameters are present and the diverging streamlines produce lower WSS. The diverging effect is enough low to disappear in one strut diameter and to give higher WSS at the center of each repeating stent unit.

Higher WSS is present on the stent surface, not shown in Figure 8. 6 because the main interest is the endothelium effect. Lower WSS are present around the stent struts in the region of transition between vessel and stent. The conclusion is a large difference between WSS in a small region, causing high MGS.

Physiological values of WSS span between 0.5 Pa and 0.8 – 1 Pa [8.10-8.11]. Low WSS values are strongly related to endothelial permeability and can promote neointimal hyperplasia, while values higher than 1 Pa seem to have no relation with neointimal hyperplasia. Steady state WSS of both stent shows that the regions of the vessel wall surrounding the stent have a uniform WSS distribution, with values lower than 0.5 Pa. No substantial difference is reported between the two stent but these areas have a larger extension in the S2 stent.

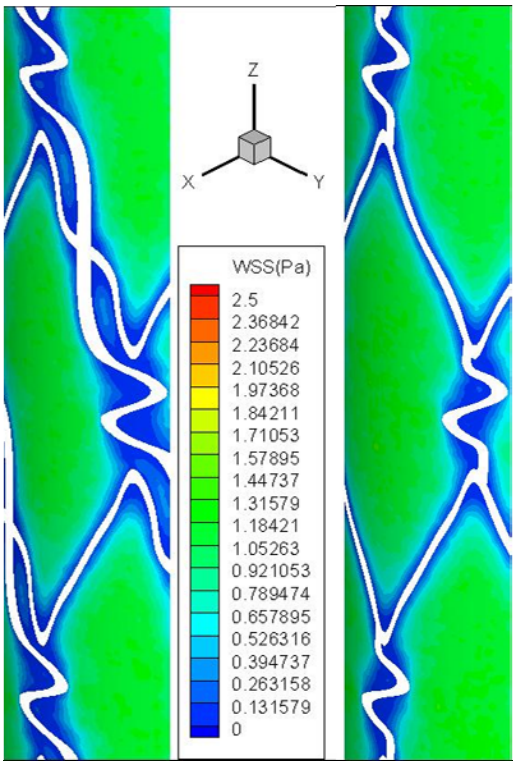

Figure 8.6 – Steady state distributions of WSS. S2 stent is on the left and S1 one on the right.

Steady state MGS are presented in Figure 8.7. MGS values on stent are less interesting because high values of MGS are related to restenosis but their range has not been established yet. Regions with higher MGS are in the zone of transition between vessel and stent, while lower MGS are present between the angled struts, where is present a region with uniform WSS, due to stagnation region. Regions opposing the mean flow are highly dangerous because hyperplasia can develop here. The S2 stent presents higher values of MGS than the S1 one.

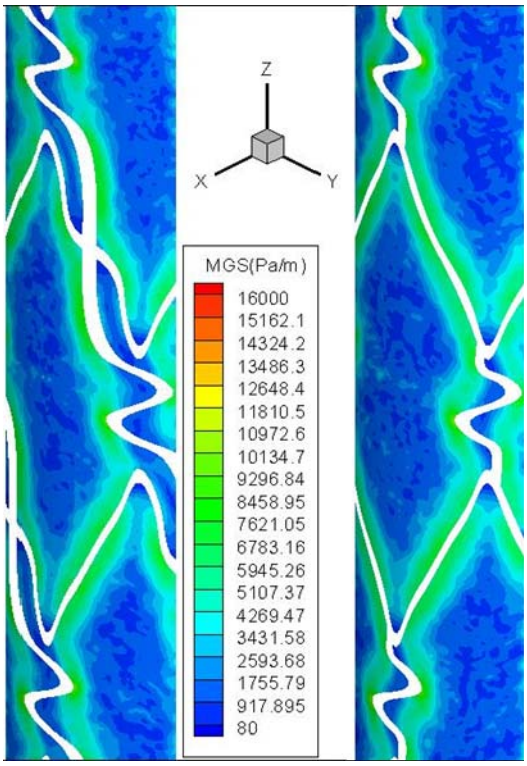

Figure 8.7 – Steady state MGS. S2 stent is on the left and S1 one on the right.

8.5.3 Unsteady state simulations

Unsteady state simulations, performed during two periods of the cardiac cycle, show large variations of WSS and MGS with time. Figure 8.8 reports the time variation of the average WSS over the endothelium, showing that average WSS of the two stent has a similar pattern but higher values are present in the S1 stent. Moreover, the differences are more significant at the systolic peak, due to stent geometry. In the S2 stent, struts of adjacent cells become parallel in proximity of the intersecting points of the struts, where the flow is trapped and WSS is quasi time-independent. The absence of these zones in the S1 stent makes the WSS increase with the flow rate more evidently leading to the differences visible in Figure 8.8.

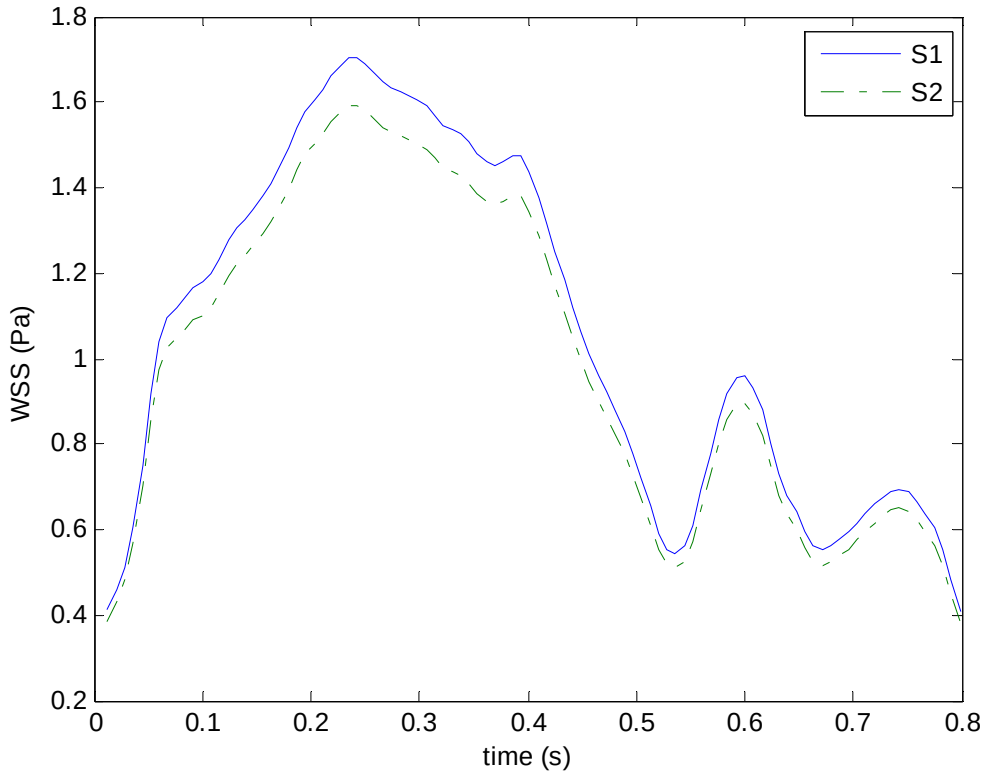

Figure 8.8 - WSS on endothelium for S1 stent and S2 one.

Figures 8.9-8.10 present WSS and MGS patterns at six different times for S1 and S2 stent. WSS and MGS increase with the systolic wave because velocity increases with the pressure, but it must be null on the stent, due to no slip condition. Stagnation zones are present for all cardiac cycles, although their extension decreases with the increase of velocity. Areas adjacent to the stent struts present low WSS values for all cardiac cycles because of stagnation regions. WSS has large variations close to the vessel wall where the velocity is free to increase. Low MGS values are present on the vessel wall during the entire cardiac cycle. WSS increases on the vessel wall with values spanning between 0 and 2.5 Pa, while MGS spans in the range between 0 and 16,000 Pa/m.

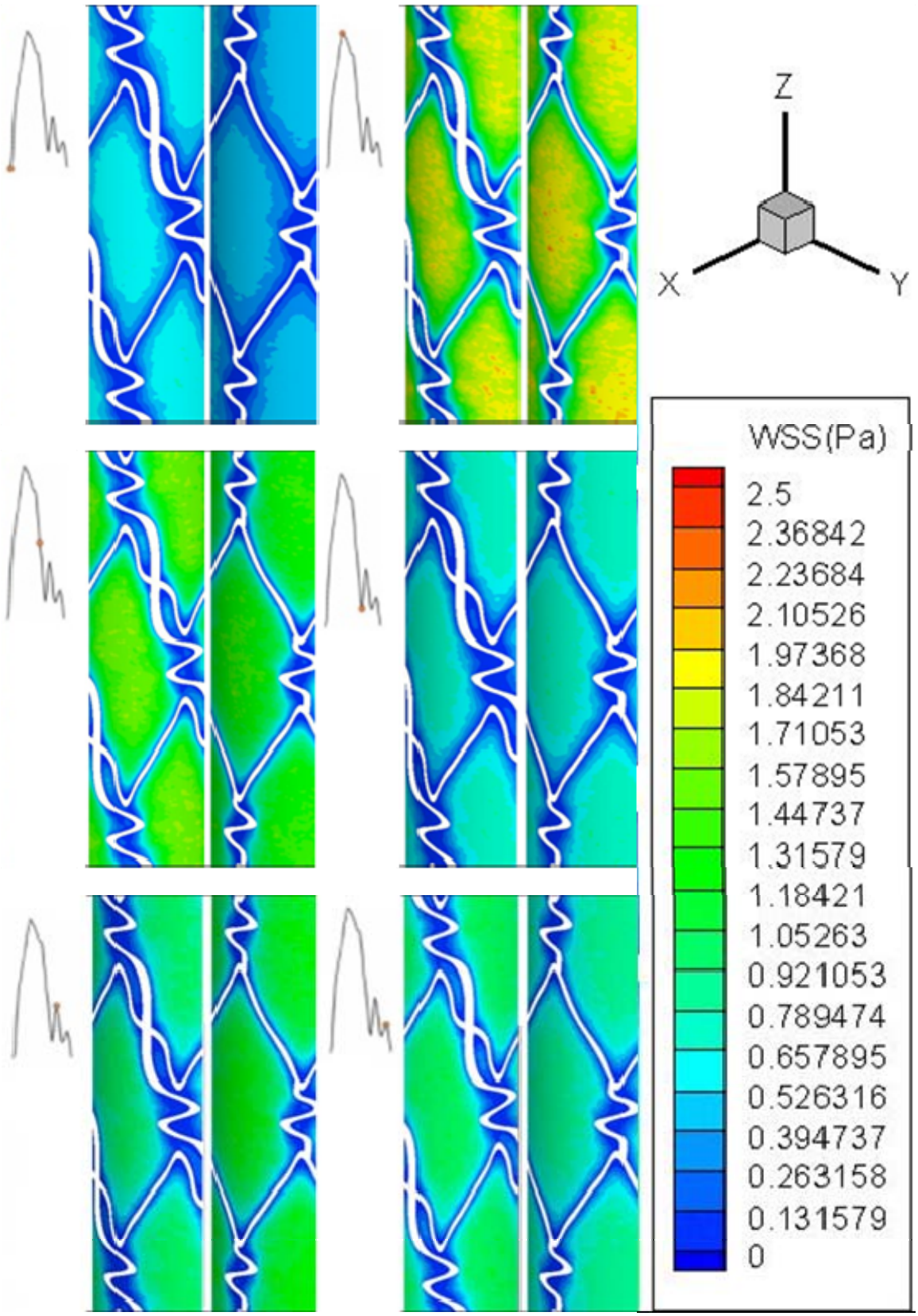

Figure 8.9 - WSS in unsteady state for S2 stent on the left and S1 one on the right.

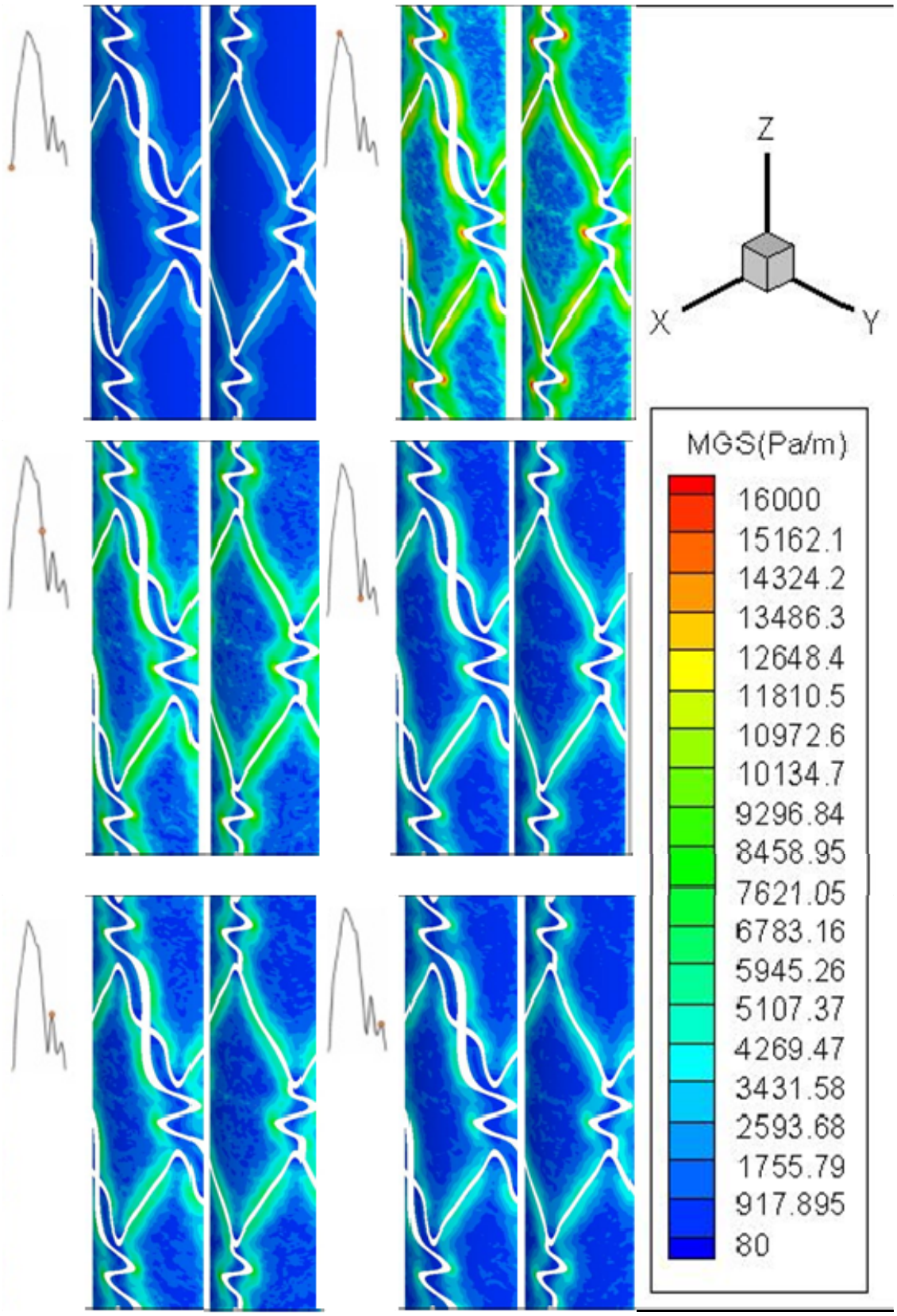

Figure 8.10 – MGS in unsteady state for S2 stent on the left and S1 one on the right.

MGS increases with the flow rate. Regions of high MGS are adjacent to the stent struts, except around the curved ones which surround the stagnation regions where uniform and low WSS can be found. Uniform values of WSS mean low MGS. A different pattern is observed on the others struts because of high WSS gradient, which increases during the flow rate, reaching a maximum on the edge of the curved struts. High increase of WSSG along the edge of the curved struts is produced, due to the strong redirection of the velocity profile, which is caused by angular struts changing WSS direction.

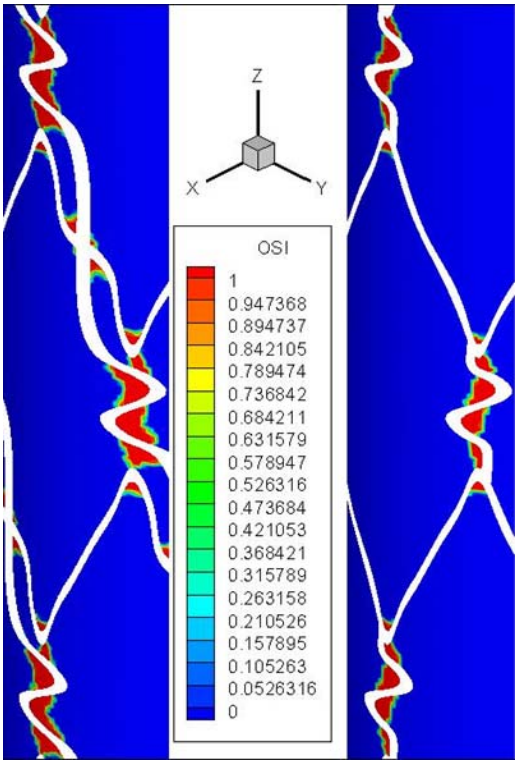

Figure 8.11 – OSI for S2 stent on the left and S1 one on the right

OSI results are presented in Figure 8.11, showing that the stent with S2 presents large regions with OSI greater than 0.5. Regions with non zero OSI are present between the handles of the struts and in the regions surrounding the points with discontinuity in the tangent. The stent with S2 has the highest curvature on the angular struts, connecting repeating stent unit, and its

axis has a transverse direction which disturbs the flow and presents larger regions with non zero OSI. In the stent with S1 the axis of the connecting struts are parallel to the flow direction, and the angular struts are longer in the stent with S2, disturbing the flow of a similar amount. The OSI parameter, which gives additional information besides WSS and MGS, shows that large differences in the fluid dynamics of the two stent are present in unsteady state.

It is also possible to estimate the percent of critical intra strut areas, P, exposed to low WSS (8.< 0.5 Pa) during the cardiac cycle, defining

$$P = percArea(\%) = 100 \frac{\int_{vesel\_wall} \frac{1}{2}\left(1 - \left(\frac{WSS - 0.5}{\|WSS - 0.5\|}\right)\right) dA}{\int_{vesel\_wall} dA} \tag{8.7}$$

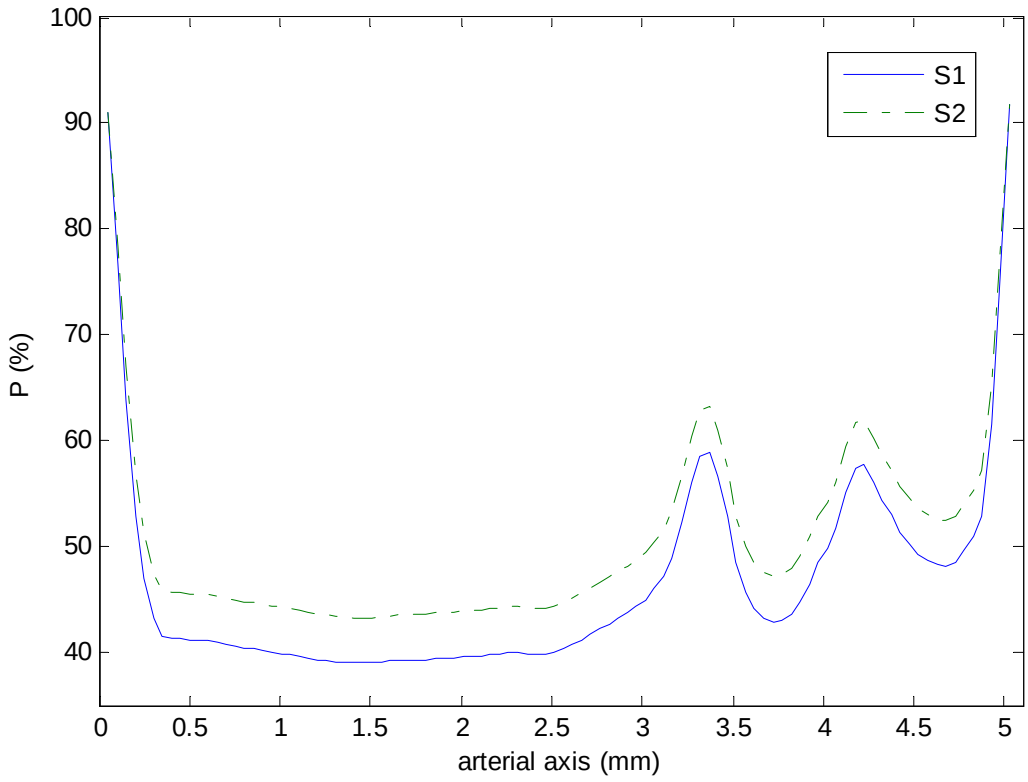

Figure 8.12 – Critical percent critical intra strut area.

Figure 8. 12 shows that the stent with S2 has lower values of percent critical intra strut area, P. The P value on the stented region, exposed to WSS smaller than 0.5 Pa, reduces as flow rate increases, reaching the minimum value at the point of the cardiac cycle corresponding to peak flow velocity. Since WSS increases with the velocity, the endothelium surface will be exposed averagely to higher WSS during the systole, decreasing the risk of developing neointimal hyperplasia.

8.6 Non-Newtonian model

Despite blood is a non-Newtonian fluid, most of the works of the literature have treated blood as Newtonian and only few studies have investigated the effect of the non-Newtonian behaviour on stent blood flow. Seo et al. [8.29] investigated the influence of the stent design close to curvatures assuming a Carreau non-Newtonian model. The study provides an understanding of the flow in the stent vicinity suggesting strategies for the optimization of the stent in order to minimize the flow disturbance. Benard et al. [8.30] investigated numerically the blood flow in 3D steady state rigid walls arteries. Non-Newtonian behaviour, based on the Carreau-Yasuda relation, in coronary stent flow seems to have important effects in the estimation of the wall shear stress on the internal surface. Amblard et al. [8.31] analyzed the phenomena of type I endoleaks in a non-invasive-stented abdominal aorta, evaluating the parietal stresses generated by the blood flow. The non-Newtonian behaviour is the Phan-Thien and Tanner models derived from the rheology of polymer solutions. This study provides an evaluation of the stresses generated by the blood flow on the aorta wall. The artery is modelled as a cylinder with rigid wall and the blood is assumed as incompressible non-Newtonian fluid in laminar flow.
Under these hypotheses the conservation equations of momentum becomes:

$$\rho \frac{D\vec{v}}{Dt} = -\nabla p + \nabla \cdot \left(2\mu\left(\dot{\gamma}\right)\left[D\right]\right) \tag{8.7}$$

The rate of strain tensor is

$$\left[D\right] = \frac{\left(\left[\nabla \vec{v}\right] + {}^{t}\left[\nabla \vec{v}\right]\right)}{2} \tag{8.8}$$

Is the rate of strain tensor and

$$\dot{\gamma} = \sqrt{2\left[D\right]:\left[D\right]} \tag{8.9}$$

is the shear rate.

In a non-Newtonian fluid, viscosity is a function of shear rate. Equation (8.7) is written in the Generalized Newtonian Fluid form, GNF, derived from Reiner and Rivlin. Viscosity of blood depends on the plasma viscosity with a complex relation with hematocrit. In this work the non-Newtonian viscosity is modelled with the Casson relation

$$\mu\left(\dot{\gamma}\right) = \left(\mu_{\infty} + 2\frac{\sqrt{\tau_0 \mu_{\infty}}}{\sqrt{\dot{\gamma}}} + \frac{\tau_0}{\dot{\gamma}}\right) \tag{8.10}$$

where τ_0 is the yield stress and μ_{∞} the asymptotic Newtonian viscosity, both function of blood hematocrit. The difficulty in using the Casson model in a numerical scheme lies in its discontinuous character to the limit of zero shear rates. In order to avoid this discontinuity it is used the regularization technique of [8.36], obtaining

$$\mu\left(\dot{\gamma}\right) = \left(\mu_{\infty} + 2\frac{\sqrt{\tau_0 \mu_{\infty}}}{\sqrt{\dot{\gamma}}}\left(1 - e^{-\sqrt{m\dot{\gamma}}}\right) + \frac{\tau_0}{\dot{\gamma}}\left(1 - e^{-\sqrt{m\dot{\gamma}}}\right)^2\right) \tag{8.11}$$

when shear rate is zero we obtain

$$\mu\left(0\right) = \left(\mu_{\infty} + 2\sqrt{m\tau_0 \mu_{\infty}} + m\tau_0\right) \tag{8.12}$$

where m is the Casson viscosity regularization exponent. According to [8.36] and [8.37] the following parameters are assumed $\tau_0 = 0.01Pa$, $\mu_\infty = 0.00333Pa \cdot s$ and $m = 100s$. The Casson viscosity model is introduced in the commercial software as a User Defined Function, UDF. Figure 8.13 presents the variation of viscosity with the shear rate.

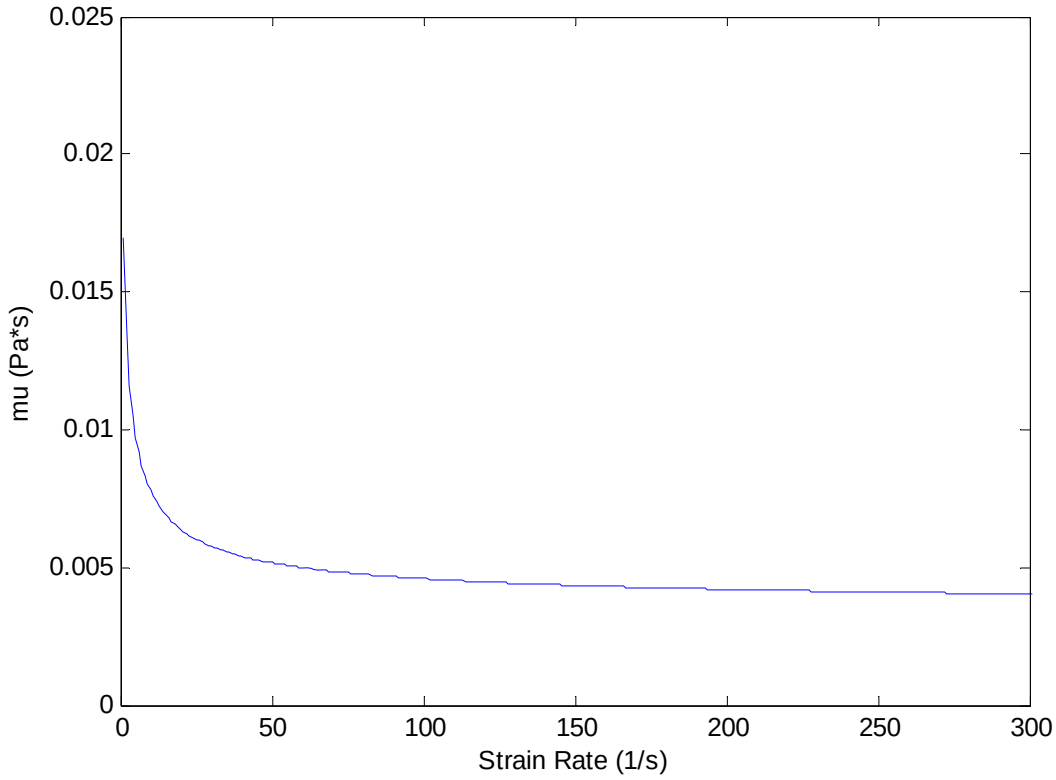

Figure 8.13 - Viscosity versus shear rate.

8.6.1 Steady State Results

Results of WSS are presented in Fig. 8.14 for each stent. Stagnation zones are present around and between stent struts with lower WSS in both stents, while, far from the struts, regions with higher WSS are present. The vessel diameter is reduced on the stent surface producing convergence of the streamlines and higher WSS, while, after the stent strut, higher diameters are present and the

diverging streamlines reduce WSS. The diverging effect is smaller and disappears in one strut diameter, with higher WSS at the centre of each repeating stent unit.

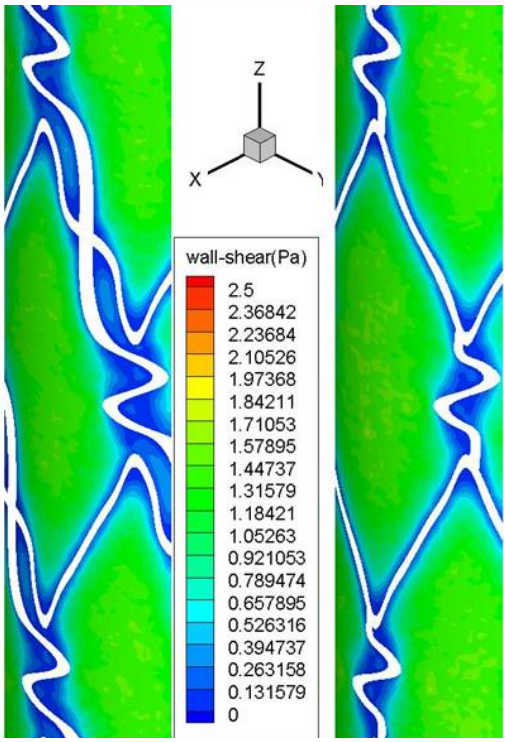

Figure 8.14 - WSS distributions in steady state.

The highest WSS is present on the stent surface and the lowest one around the stent struts, i.e. in the transition region between vessel and stent. The conclusion is a somewhat large difference between WSS in a small region.

8.6.2 Unsteady State Results

The unsteady state numerical simulations are performed during two periods of the cardiac cycle and Fig. 8.15 shows six WSS patterns at the following times: 0.84, 0.88, 1.04, 1.28, 1.44, 1.6 s.

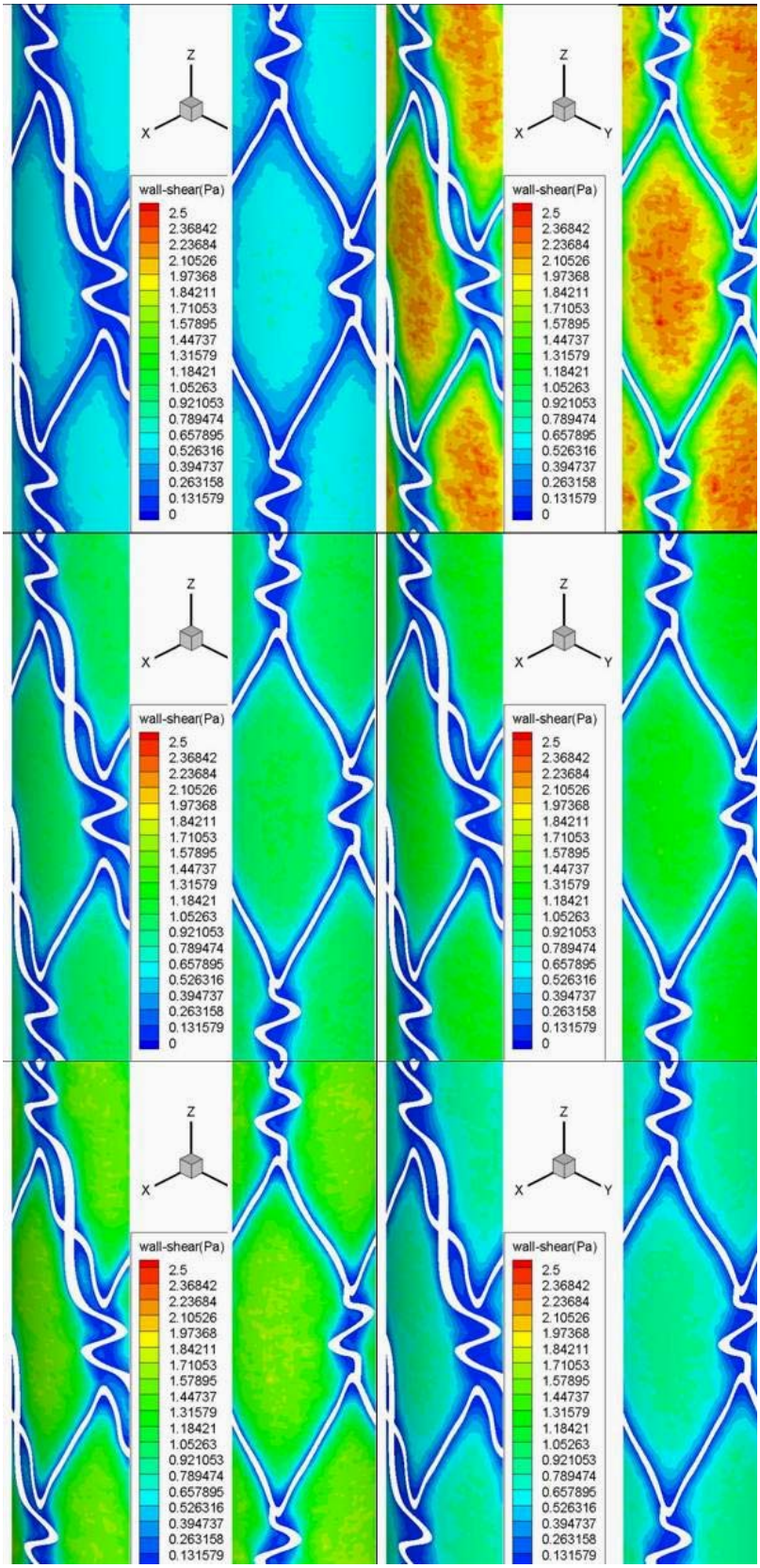

Figure 8.15 - WSS distributions in unsteady state.

Velocity increases with pressure and is zero on stent and wall, due to no slip condition. Inside the duct, velocity increases with the systolic wave causing an increase of velocity gradient and WSS. The average WSS on the wall is described by a wave with the same pattern of the systolic one.

The stent on the wall of the artery is an obstacle from the fluid-dynamics point of view, which is small as compared to the diameter of the vessel but enough large to create a stagnation zone around it. These stagnation zones are present in all cardiac cycles, while their extension decreases with the increase of velocity.

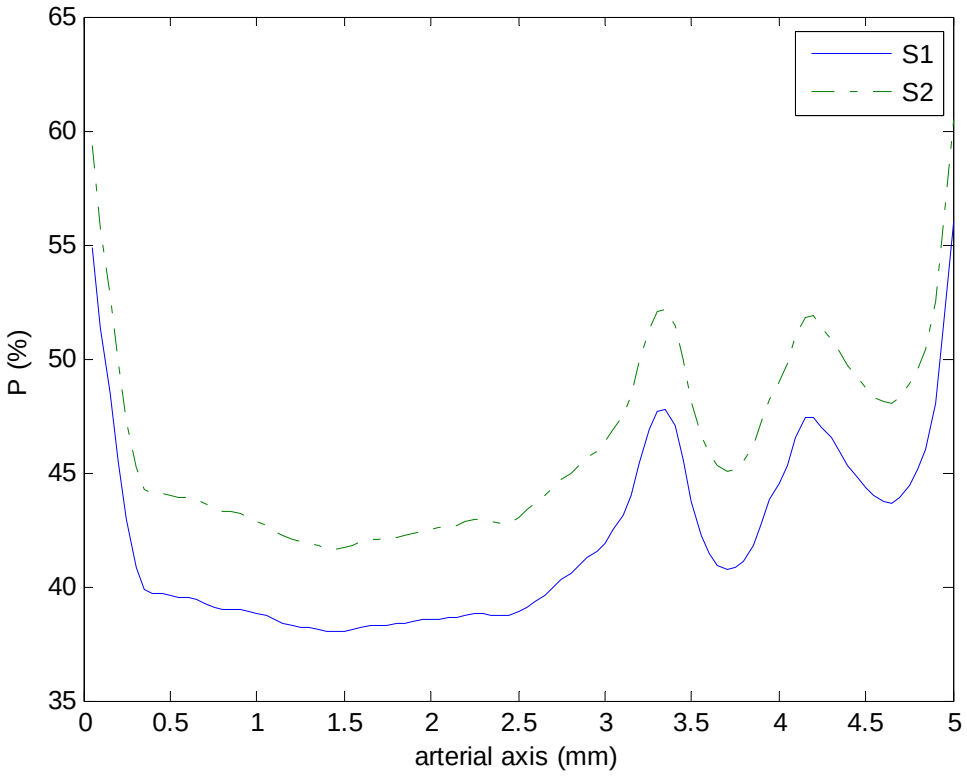

Figure 8.16 - Percent Area, P(%), with WSS lower than 0.5 Pa, versus time (s).

The areas around the stent struts present low WSS values for all cardiac cycles because of the stagnation zones while WSS has large variations, during the cycle, close to the vessel wall where WSS span from 0 to 2.5 Pa.

Non-Newtonian flow has a different behaviour near the wall as compared to the Newtonian one. Maximum WSS values are present in the centre of the stent pattern structure and minimum values on the proximal stent wire surface.

It is possible to estimate the intra strut areas exposed to low WSS (i.e. lower than 0.5 Pa) during the cardiac cycle. The percent area is evaluated for both stents and at all the time steps of the cardiac cycle. The results are presented in Fig. 8.16 showing that the stent with closed cells has a smaller percent area with low WSS.

Comparing the present results for non-Newtonian fluid with those of Newtonian fluid it can be concluded that the second one has the effect of overestimating the critical area. Results showed in Figure 8.16 indicate a significant percent area with a WSS lower than the critical value, for the two stents simulated, in agreement with those of [8.35].

8.7 Discussion

The present work investigates two stent configurations called S1 and S2. The numerical simulations show that in the S2 stent the near-wall velocity vectors are misaligned with the flow direction, contributing to generate hazardous WSS and MGS distributions. The parameters used to evaluate the stent suggest that S2 one is the worst. These conclusions are consistent with the physical intuition that optimal design should minimize changes in blood flow characteristics [8.19]. Moreover, the results of the present paper seem to confirm the experimental observations of [8.23], where, among the stent studied, the Bx Velocity stent is similar to the present S2 stent.

Indeed, it was shown in [8.23] that the nearly helically recirculating regions, near the connectors, exhibit complex fluid dynamics with more platelet deposition. The indicators employed in the present paper, for instance low WSS, high MGS and OSI, are in agreement to the predictions of the platelet deposition observed in [8.23].

Numerical simulations are carried out in order to answer to the question whether a parallel-connectors stent is preferable to a transverse-connectors one to reduce restenosis. In order to answer this question we have selected two particular stent configuration called S1 and S2. The differences of the critical WSS values are around 6.5%, while the percent of critical intra strut areas, P, increases of 4.2% in stent S2, but, more important, the great part of the stent region is subject to WSS which are lower than the critical value in both stents. The S1 stent seems slightly better from the fluid dynamics point of view than the S2 one. The results presented here are valid only for the stent examined but the results may suggest that connecting the struts with connectors parallel to the mean flow can reduce the restenosis rate.

This conclusion derives from a numerical study having limitations:

i) the left anterior descending coronary artery, where the device is embedded, is not a straight cylinder, so, simulations could be function of the axial length because of the curved geometry of the artery;

ii) simulations are not performed in a diseased artery;

iii) simulations are performed on a rigid wall, which is different from the material of elastic artery;

iv) initial conditions assumed on the blood flow are relative to proximal portion of left anterior canine descending coronary artery;

As far as the third limitation is concerned, the rigid wall should not affect significantly the results because studies on animals [8.17] assure that stent implantation reduces the vessel compliance to zero within the stented region [8.38] and wall deformability does not greatly alter the velocity field under normal conditions. Probably, the condition that could mainly affect the results is the fifth one because the waveform assumed in the simulations is relative to the left anterior canine descending coronary artery, found in literature, which may differ from a patient specific one. This waveform is assumed also because it has been employed in [8.16] as a valid boundary condition.

Despite the previous considerations it must be pointed out the potential clinical applicability of the current results, due to the growing interest in employing drug-eluting stent in order to reduce the percentage of restenosis. Local flow patterns, due to the presence of the stent, must be taken into account during stent design, in order to avoid values of fluid dynamics parameters involved in neointimal hyperplasia. An increasing number of evidences suggest that geometry and physical properties of a deployed stent may influence blood flow and alter WSS distributions after implantation, rendering certain areas of the vessel wall more susceptible to neointimal hyperplasia and restenosis [8.6, 8.8, 8.20]. This is the reason of investigating the physical parameters influencing the geometrical features that may enhance platelet and proteins deposition, thus causing pathological conditions. The physical parameters promoters of neointimal hyperplasia are low WSS, high space and time WSSG, and geometrical features as number, width and thickness of strut to struts, stent-to-artery deployment diameter, and stent scaffolding. Assessment on the influence of fluid dynamics parameters and geometrical configuration has been carried out with computational fluid dynamics models [8.26] and experimental studies [8.39], but the *in vivo* testing is still lacking.

Concerning the non-Newtonian model, the steady state results of WSS, presented in Fig. 8.14, show that in the regions of the vessel wall is present a uniform WSS which is lower than 0.3 Pa. No substantial difference is reported between the two stents but these areas have a larger extension in the stent with transverse struts. The differences in the critical values of both stents are around 5% but most part of the vessel wall is subject to WSS lower than the critical value.

The unsteady state results of Fig. 8.15 show a large variation of WSS during the cardiac cycle. The regions far from the stent have the larger variations while the regions close to the stent present the smaller variations, allowing them to be exposed permanently to critical low WSS values. The comparison of the present results with those obtained for a Newtonian fluid in [8.40], allows to conclude that the Newtonian behaviour underestimates WSS, with the clinical consequence of overestimating the restenosis risk area, in agreement to the results of [8.30].

8.8 Conclusions

Two stents with different design, the first having parallel-connectors, S1, and the second with transverse-connectors, S2, are investigated performing CFD simulations in steady and unsteady state. According to the literature, the parameters involved in the restenosis are WSS, MGS and OSI, because they are related to neointimal hyperplasia. Numerical simulations show the presence of regions close to the stent where WSS is lower than the critical value, while, close to the stent elements, opposing the flow, high MGS values are predicted. Unsteady simulations show the presence of large difference between instantaneous and mean values of WSS and MGS. Unsteady analysis suggests to use the parameter OSI, showing the presence of regions with non zero values, located in regions surrounding the angular points of the stent. It is then possible to

conclude that the S2 stent has a worst fluid dynamic behavior, compared to stent S1. These results may lead to the suggestion that the transverse connectors may increase the restenosis rate.

Moreover, the comparison of the present results for non-Newtonian behaviour, with those for a Newtonian one, allows concluding that the use of Newtonian model, in predicting WSS, leads to an overestimation of the restenosis percent.

Future investigations are required on different stent geometries involving parallel and transverse connectors. The evidence of the fluid dynamics parameters involved in restenosis suggests the importance of the hemodynamic behavior in the choice of a stent.

References of Chapter 8

[8.1] Morice M. C., Serruys P. W., Sousa J. E., Fajadet J., Ban Hayashi E., Perin M., Colombo A., Schuler G., Barragan P., Guagliumi G., Molnàr F., Falotico R. A randomized comparison of a sirolimus-eluting stent with a standard stent for coronary revascularization. N. Eng. J. Med. 2002; 346 (8.23): 1773-1780.

[8.2] Moses J. W., Leon M. B., Popma J. J., Fitzgerald P. J., Holmes D. R., O'Shaughnessy C., Caputo R. P., Kereiakes D. J., Williams D. O., Teirstein P. S., Jaeger J. L., Kuntz R. E. Sirolimus-eluting stents versus standard stents in patients with stenosis in a native coronary artery. N. Engl. J. Med. 2003; 349(8.14): 1315-1323.

[8.3] Schampaert E., Cohen E. A., Schluter M. The Canadian study of the sirolimus-eluting stent in the treatment of patients with long de novo lesions in small native coronary arteries (8.C-SIRIUS). J. Am. Coll. Cardiol. 2004; 43: 1110-1115.

[8.4] Schofer M., Gershlick A. H. Sirolimus-eluting stents for treatment of patients with long atherosclerotic lesions in small coronary arteries: double-bind, randomized controlled trial. Lancet 2003; 362: 1093-1099.

[8.5] Palmaz J.C. Intravascular stents in the last and the next 10 years. J. Endovasc. Ther. Suppl. 2004; 2, 200-206.

[8.6] Virmani R., Farb A., Guagliumi G., Kolodgie F. D. Drug-eluting stents: caution and concerns for long-term outcome. Coronary Artery Disease 2004; 15: 313-318.

[8.7] Finn A. V., Palacios I. F., Kastrati A., Gold H. K. Drug-eluting stents for diabetes mellitus: a rush to judgment? J. Am. Coll. Cardiol. 2005; 45:479-483.

[8.8] Virmani R., Farb A., Guagliumi G., Kolodgie F. D. Drug-eluting stents: caution and concerns for long-term outcome. Coronary Artery Disease 2004; 15:313-318.

[8.9] Farb, A., Tang, A. L., Shroff, S., Sweet, W., Virmani, R. Neointimal responses 3 months after ^{32}P β-emitting stent placement. International Journal of Radiation Oncology Biology Physics 2000; 48 (8.3): 889-98.

[8.10] Ku D.N., Giddens D. P., Zarins C. K., Glagov S. Pulsatile flow and atherosclerosis in the human carotid bifurcation. Positive correlation between plaque location and low oscillating shear stress. Arteriosclerosis 1985; 5: 293-302.

[8.11] Malek A. M., Alper S. L., Izumo S. Hemodynamic shear stress and its role in atherosclerosis. JAMA 1999; 282: 2035-2042.

[8.12] Ku D. N. Blood flow in arteries. Ann. Rev. Fluid Mech. 1997; 29: 399-434.

[8.13] Berry J. L., Santamarina A., Moore J. E. Jr., Roychowdhury S., Routh W. D. Experimental and computational flow evaluation of coronary stents. Annuals of Biomedical Engineering 2000; 28(8.4): 386-98.

[8.14] Lanoye L., De Beule M., Dewijngaert C., Segers P., Van Impe R., Verdonck P. The influence of the strut section shape on the flow field in a newly stented right coronary artery. The 56th National Congress of Theoretical and Applied Mechanics, NCTAM 2006.

[8.15] Seo T., Schachter L. G., Barakat A. I. Computational Study of Fluid Mechanical Disturbance Induced by Endovascular Stents. Annals of Biomedical Engineering 2005; 33(8.4), 444-456.

[8.16] LaDisa J. F. Jr., Hettrick D. A., Olson L. E., Guler I., Gross E. R., Kress T. T., Kersten J. R., Warltier D. C., Pagel P. S. Coronary stent implantation alters coronary artery hemodynamics and wall shear stress during maximal vasodilation. Journal of Applied Physiology 2002; 93: 1939-1946.

[8.17] LaDisa J. F. Jr., Guler I., Olson L. E., Hettrick D. A., Kersten J. R., Warltier D. C., Pagel P. S. Three dimensional computational fluid dynamics modeling of alterations in coronary artery wall shear stress produced by stent implantation. Annuals of Biomedical Engineering 2003; 31: 972-980.

[8.18] LaDisa J. F. Jr, Olson L. E., Guler I., Hettrick D. A., Audi S. H. Stent design properties and deployment ratio influence indexes of wall shear stress: a three dimensional computational fluid dynamics investigation within a normal artery. Journal of Applied Physiology 2004; 97(8.1): 424-30.

[8.19] LaDisa J. F. Jr., Olson L. E., Hettrick D. A., Warltier D. C., Kersten J. R. and Pagel P. S. Axial stent strut angle influences wall shear stress after stent implantation: analysis using 3D computational fluid dynamics models of stent foreshortening. BioMedical Engineering OnLine 2005; 4: 59.

[8.20] LaDisa J. F. Jr., Olson L. E., Guler I., Hettrick D. A., Kersten J. R., Warltier D. C. and Pagel P. S. Circumferential vascular deformation after stent implantation alters wall shear stress evaluated with time-dependent 3D computational fluid dynamics models. Journal of Applied Physiology 2005; 98: 947-957.

[8.21] LaDisa J. F. Jr., Olson L. E., Hettrick D. A., Warltier D. C., Kersten J., Pagel P. Alterations in regional vascular geometry produced by theoretical stent implantation influence distributions of wall shear stress: analysis of a curved coronary artery using 3D computational fluid dynamics modeling. BioMedical Engineering OnLine 2006; 5: 40.

[8.22] He Y., Duraiswamy N., Frank A. O., Moore J. E. Jr. Blood Flow in Stented Arteries: A Parametric Comparison of Strut Design Patterns in Three Dimensions. Journal of Biomechanical Engineering 2005; 127: 637-647.

[8.23] Duraiswamy N., Cesar J. M., Schoephoerster R. T. and Moore J. E. Jr. Effects of stent geometry on local flow dynamics and resulting platelet deposition in an *in vitro* model. Biorheology 2008; 45: 547–561.

[8.24] Stoeckel D., Bonsignore C., Duda S. A survey of stent designs. Min. Invas. Ther. & Allied Technol. 2002; 11: 137-147.

[8.25] Kastrati A., Mehilli J., Dirschinger J., Pache J., Ulm K., Schühlen H., Seyfarth M., Schmitt C., Blasini R., Neumann F. J., Schömig A. Restenosis after coronary placement of various stent types. Am. J. Cardiol. 2001; 87(8.1): 34-39.

[8.26] DePaola N., Gimbrone M. A. Jr., Davies P. F., Dewey C. F. Vascular endothelium responds to fluid shear stress gradients. Arterioscler. Thromb. 1992; 12: 1254-1257.

[8.27] Taylor C. A., Hughes T. J. R., Zarins C.K. Finite Element Modeling of Three-Dimensional Pulsatile Flow in the Abdominal Aorta: Relevance to Atherosclerosis Annals of Biomedical Engineering, Vol. 26, pp. 975–987, 1998

[8.28] Prakash S., Ethier C. R. Requirements for Mesh Resolution in 3D Computational Hemodynamics. Journal of Biomechanical Engineering 2001; 123(8.2):134-44.

[8.29] T. Seo, L. G. Schachter and A. I. Barakat, "Computational Study of Fluid Mechanical Disturbance Induced by Endovascular Stents", Ann. of Bio. Eng. 33, 4, 444-456, 8.2905.

[8.30] N. Benard, R. Perrault and D. Coisne "Computational Approach to Estimating the Effects of Blood Properties on Changes in Intra-stent Flow" Ann. of Bio. Eng. 34, 8, 18.349–18.351, 8.2906.

[8.31] A. Amblard, H. W. Le Berre, B. Bou-Saïd, M. Brunet "Analysis of type I endoleaks in a stented abdominal aortic aneurysm", Medical Engineering & Physics 31, 8.35–33, 8.2909.

[8.32] D. Stoeckel, C. Bonsignore and S. Duda, "A survey of stent designs", Min. Invas. Ther. & Allied Technol. 11: 137-147, 8.2902.

[8.33] A. Kastrati, J. Mehilli, J. Dirschinger, J. Pache, K. Ulm and H. Schühlen, "Restenosis after coronary placement of various stent types", Am. J. Cardiol. 87(1): 34-39, 8.2901.

[8.34] M. R. Ebeid "Balloon expandable stents for coarctation of the aorta: re
view of current status and technical considerations", Images Pediatr Cardiol. 15: 8.34-41, 8.2903

[8.35] J. Mejia, B. Ruzzeh, R. Mongrain, R. Leask and O. F. Bertrand "Evaluation of the effect of stent strut profile on shear stress distribution using statistical moments", BioMed. Eng. OnLine. 8: 8, 8.2909.

[8.36] K. Mukundakrishnan, P. S. Ayyaswamy and D. M. Eckmann, "Finite-sized gas bubble motion in a blood vessel: Non-Newtonian effects", Phys. Rev. E 78, 0368.373, 2008.

[8.37] M. Sharan and A. S. Popel, “A two-phase model for flow of blood in narrow tubes with increased effective viscosity near the wall”, Biorheology, 38, 415, 2001

[8.38] Ebeid M. R. Balloon expandable stents for coarctation of the aorta: review of current status and technical considerations. Images in Pediatric Cardiology 2003, 15: 25-41.

[8.39] Benard N., Coisne D., Donal E., Perrault R. Experimental study of laminar blood flow through an artery treated by a stent implantation: characterization of intra-stent wall shear stress. Journal of Biomechanics 2003; 36: 991–998.

[8.40] F. Gori, A. Boghi and M. Amitrano “Three-Dimensional Numerical Simulation of the Fluid Dynamics in a Coronary Stent”, IMECE8.2909, November 13-8.41, 8.2909, Lake Buena Vista, Florida, USA.

[8.41] F. Gori and A. Boghi "Three-Dimensional Numerical Simulation Of Non-Newtonian Blood In Two Coronary Stents", IHTC14-23087 August 8-13, 2010, Washington D.C., USA

[8.42] F. Gori and A. Boghi, “Three-dimensional numerical simulation of blood flow in two coronary stent”, submitted for publication.

Appendix: Published Papers

Proceedings of the ASME INTERNATIONAL
MECHANICAL ENGINEERING CONGRESS AND EXPOSITION
October 31 November 6, 2008, Boston, Massachusetts, USA

IMECE2008-66024

On a New Turbulent Energy Equation with Variable Thermal Conductivity

Fabio Gori
Department of Mechanical Engineering
University of Rome "Tor Vergata"
Rome, Italy

Andrea Boghi
Department of Mechanical Engineering
University of Rome "Tor Vergata"
Rome, Italy

ABSTRACT

The present work investigates the energy equation of a general fluid, Newtonian or non-Newtonian, with variable thermal conductivity in turbulent flow. The usual energy equation, without the dissipation terms, is taken into account with the fluctuating terms in the temperature as well as in the thermal conductivity. The energy equation is written for the average temperature, for the fluctuating temperature one as well as for the square of the fluctuating temperature. Besides the usual Reynolds stresses, a new term appears, which is the product of the fluctuation of the thermal conductivity and the gradient of the temperature fluctuation. This new term is interpreted and introduced in the energy equation where the variable is the square of the temperature fluctuation where new terms appear. A possible physical interpretation is given to the different terms. Assuming a polynomial relation between thermal conductivity and temperature it is then possible to write an expression for the average and the fluctuating thermal conductivity. The expressions are then simplified on the basis of physical and mathematical considerations. Specifically, the heat flux due to the fluctuating thermal conductivity is then expressed as the product of the derivative of the thermal conductivity with the mean temperature to the gradient of the square of the temperature fluctuation. Further considerations allow to write a new energy equation of the average temperature which include the new term. The solution of this energy equation is possible with the coupled solution of the equation for the square of the fluctuating temperature. The introduction of this new term in the energy equation can be of some importance in problems related to liquid metals flowing in turbulent flow and/or in very low temperature applications where the thermal conductivity becomes very high.

INTRODUCTION

The fluids used as cooler in thermal plants with very high heat fluxes range in a wide spectrum of Prandtl numbers. Liquid metals have been widely used after world war II as coolers in nuclear power plants. These fluids have a very low Prandtl number because their thermal conductivity is very high. One of the first approach to the liquid metals heat transfer has been the analogy between momentum transport and heat transfer with some modifications of the Reynolds analogy [1]. The classical approach to solve the problem of predicting heat transfer in liquid metals has been the use of empirical expressions, as reported in [2].

Because of the large scatter between experimental data and empirical predictions, due to the scale separation between momentum and heat transfer [3], it has been suggested to modify the turbulent Prandtl number on empirical basis [4], while several models have been reviewed in [5]. With the use of modern type computers the approach to the prediction of heat transfer to liquid metals has incorporated the use of the turbulent Prandtl number in the turbulent models. One of the approach of this kind [6] has been followed by [7-8] as reviewed recently [9].

The cooling of nuclear reactors with molten salts with high Prandtl numbers has been the subject of several papers, as reviewed in [10], due to the importance of the convective and turbulent heat transfer. The use of these molten salts is also related to the radioactive and toxic properties [11]. The enhancement of heat transfer with molten salts has been proposed in [12]. A special kind of molten salts, called Flibe, has been investigated with the DNS approach [13]. Fluids with high Prandtl number have been used in MHD, i.e. subject to magnetic fields, in order to optimize the design of MHD instruments [14]. The investigation pointed out an increase of the turbulent diffusivity close to the free surface and the increase of heat flux and temperature fluctuations with the increase of the Prandtl number.

Molten salts are actually used also in solar plants because of the economical evaluation of hybrid solar plants [15]. Molten salts are used in a Japanese project named "Solar Hybrid Fuel Project" with the solar concentration [16]. Molten salts like sodium and potassium nitrates are proposed in parabolic solar concentrators and power towers [17].

In fluids with high Prandtl number the smallest scale of the temperature fluctuation is inversely proportional to the square

root of the molecular Prandtl number, which means the temperature fluctuations increase with the Prandtl number [3]. The description of turbulence in liquid metals needs the knowledge of the temperature fluctuations which have a temporal scale different from the velocity one. The temperature fluctuations are high in fluids with high Prandtl numbers, as shown by a DNS study with different Prandtl number fluids [18]. Among the fluids with high Prandtl number, a special importance is given to non-Newtonian fluids which present a reduction in heat transfer. A recent DNS study [19] showed an increase of the temperature fluctuations and a reduction of the velocity fluctuations perpendicular to the wall.

Besides the temperature fluctuations, it is important to recall the importance of the variation of the fluid properties with the temperature, which has been usually considered in laminar flow. Only few works have dealt with this variability in turbulent flow [20-21] which has been recently investigated with a model based on the Reynolds stresses [22-25].

One of the main criticism to the previous models is that the equations are previously deduced with the assumption of constant physical properties and later on the dependence on the temperature is introduced. The present paper is aimed to study the energy equation with the thermal conductivity dependent on the temperature.

NOMENCLATURE

Latin

a_i	coefficients of the polynomial expression of $k(T)$
$k(T)$	instantaneous thermal conductivity
$\langle k(T)\rangle$	time average thermal conductivity
$k'(T)$	time fluctuating thermal conductivity
k_T	turbulent kinetic energy
$P_k(\langle T\rangle)$	polynomial expression of order k
$Q_k(\langle T\rangle)$	polynomial expression of order k
$\vec{q}_R$	time average turbulent Reynolds heat flux
$\vec{q}_R{}'$	instantaneous turbulent Reynolds heat flux
$\vec{q}_k$	average turbulent thermal conductivity heat flux
$\vec{q}_k{}'$	fluctuating turbulent thermal conductivity heat flux
T	instantaneous temperature
$\langle T\rangle$	time average temperature
T'	fluctuating temperature
u	instantaneous x-velocity component
U	time average x-velocity component
u'	fluctuating x-velocity component
v	instantaneous y-velocity component
V	time average y-velocity component
v'	fluctuating y-velocity component
x	horizontal Cartesian coordinate
y	vertical Cartesian coordinate

Greek

ε	dissipation of turbulent kinetic energy

ENERGY CONSERVATION EQUATIONS

Let consider a fluid in turbulent flow in a two dimensional domain with the thermal conductivity dependent on the temperature

$$\rho c\frac{\partial T}{\partial t}+\rho cu\frac{\partial T}{\partial x}+\rho cv\frac{\partial T}{\partial y}=\frac{\partial}{\partial x}\left(k(T)\frac{\partial T}{\partial x}\right)+\frac{\partial}{\partial y}\left(k(T)\frac{\partial T}{\partial y}\right) \tag{1}$$

Assuming the temperature is made of a time average and a fluctuating component

$$T=\langle T\rangle+T'' \tag{2}$$

Eq. (1) becomes

$$\rho c\frac{\partial}{\partial t}\left(\langle T\rangle+T''\right)+\rho c\left(U+u'\right)\frac{\partial}{\partial x}\left(\langle T\rangle+T''\right)+\rho c\left(V+v'\right)\frac{\partial}{\partial y}\left(\langle T\rangle+T''\right)=$$
$$\frac{\partial}{\partial x}\left(\left(\langle k\rangle+k'\right)\frac{\partial}{\partial x}\left(\langle T\rangle+T''\right)\right)+\frac{\partial}{\partial y}\left(\left(\langle k\rangle+k'\right)\frac{\partial}{\partial y}\left(\langle T\rangle+T''\right)\right) \tag{3}$$

Equation (3) can be split in two equations: the first one contains the time average temperature

$$\rho c\frac{\partial\langle T\rangle}{\partial t}+\rho cU\frac{\partial\langle T\rangle}{\partial x}+\rho cV\frac{\partial\langle T\rangle}{\partial y}=\frac{\partial}{\partial x}\left(\langle k(T)\rangle\frac{\partial\langle T\rangle}{\partial x}-\rho c\langle u'T''\rangle+\langle k'(T)\frac{\partial T''}{\partial x}\rangle\right)+$$
$$\frac{\partial}{\partial y}\left(\langle k(T)\rangle\frac{\partial\langle T\rangle}{\partial y}-\rho c\langle v'T''\rangle+\langle k'(T)\frac{\partial T''}{\partial y}\rangle\right) \tag{4}$$

and the second one the fluctuating temperature

$$\rho c\frac{\partial T''}{\partial t}+\rho cU\frac{\partial T''}{\partial x}+\rho cV\frac{\partial T''}{\partial y}=-\rho cu'\frac{\partial\langle T\rangle}{\partial x}-\rho cv'\frac{\partial\langle T\rangle}{\partial y}+$$
$$\frac{\partial}{\partial x}\left(-\rho cu'T''+\rho c\langle u'T''\rangle+\langle k(T)\rangle\frac{\partial T''}{\partial x}+k'(T)\frac{\partial\langle T\rangle}{\partial x}+k'(T)\frac{\partial T''}{\partial x}-\langle k'(T)\frac{\partial T''}{\partial x}\rangle\right)+$$
$$\frac{\partial}{\partial y}\left(-\rho cv'T''+\rho c\langle v'T''\rangle+\langle k(T)\rangle\frac{\partial T''}{\partial y}+k'(T)\frac{\partial\langle T\rangle}{\partial y}+k'(T)\frac{\partial T''}{\partial y}-\langle k'(T)\frac{\partial T''}{\partial y}\rangle\right) \tag{5}$$

Multiplying Eq. (5) by T' and operating the average it is obtained the equation which contains the square of the fluctuating temperature.

$$\rho c\frac{\partial}{\partial t}\left(\frac{\langle T''T''\rangle}{2}\right)+\rho cU\frac{\partial}{\partial x}\left(\frac{\langle T''T''\rangle}{2}\right)+\rho cV\frac{\partial}{\partial y}\left(\frac{\langle T''T''\rangle}{2}\right)=$$
$$-\left(\langle\rho cu'T''\rangle+\langle k'(T)\frac{\partial T''}{\partial x}\rangle\right)\frac{\partial\langle T\rangle}{\partial x}-\left(\langle\rho cv'T''\rangle+\langle k'(T)\frac{\partial T''}{\partial y}\rangle\right)\frac{\partial\langle T\rangle}{\partial y}+$$
$$\frac{\partial}{\partial x}\left(-\langle\rho cu'\frac{T''T''}{2}\rangle+\langle k'(T)\frac{\partial}{\partial x}\left(\frac{T''T''}{2}\right)\rangle+\langle k(T)\rangle\frac{\partial}{\partial x}\left(\frac{\langle T''T''\rangle}{2}\right)+\langle k'(T)T''\rangle\frac{\partial\langle T\rangle}{\partial x}\right)+$$
$$\frac{\partial}{\partial y}\left(-\langle\rho cv'\frac{T''T''}{2}\rangle+\langle k'(T)\frac{\partial}{\partial y}\left(\frac{T''T''}{2}\right)\rangle+\langle k(T)\rangle\frac{\partial}{\partial y}\left(\frac{\langle T''T''\rangle}{2}\right)+\langle k'(T)T''\rangle\frac{\partial\langle T\rangle}{\partial y}\right)+$$
$$-\langle k(T)\rangle\langle\frac{\partial T''}{\partial x}\frac{\partial T''}{\partial x}\rangle-\langle k'(T)\frac{\partial T''}{\partial x}\frac{\partial T''}{\partial x}\rangle-\langle k(T)\rangle\langle\frac{\partial T''}{\partial y}\frac{\partial T''}{\partial y}\rangle-\langle k'(T)\frac{\partial T''}{\partial y}\frac{\partial T''}{\partial y}\rangle \tag{6}$$

which can be written in compact form as in the following.

The energy equation for the time average temperature, i.e. Eq. (4), is then

$$\rho c\frac{D\langle T\rangle}{Dt}=-\nabla\cdot\left(\langle\rho cT'\vec{v}'\rangle-\langle k'(T)\nabla T'\rangle-\langle k(T)\rangle\nabla\langle T\rangle\right) \tag{7}$$

the energy equation for the fluctuating temperature, i.e. Eq. (5), is

$$\rho c\frac{DT'}{Dt}=-\rho c\vec{v}'\nabla\langle T\rangle+$$
$$-\nabla\cdot\left(\rho c\vec{v}'T'-k'(T)\nabla T'-\langle\rho c\vec{v}'T'\rangle+\langle k'(T)\nabla T'\rangle-\langle k(T)\rangle\nabla T'-k'(T)\nabla\langle T\rangle\right) \tag{8}$$

while the energy equation for the square of the fluctuating temperature, i.e. Eq. (6), is

$$\rho c\frac{D}{Dt}\left(\frac{\langle T'T'\rangle}{2}\right)=-\left(\langle\rho cT'\vec{v}'\rangle+\langle k'(T)\nabla T'\rangle\right)\nabla\langle T\rangle+$$
$$-\nabla\cdot\left(\langle\rho c\vec{v}'\frac{T'T'}{2}\rangle-\langle k'(T)\rangle\nabla\frac{T'T'}{2}\rangle-\langle k(T)\rangle\nabla\frac{\langle T'T'\rangle}{2}-\langle k'(T)T'\rangle\nabla\langle T\rangle\right)+$$
$$-\langle k(T)\rangle\langle\nabla T'\nabla T'\rangle-\langle k'(T)\nabla T'\nabla T'\rangle \tag{9}$$

The equation for the time average temperature, i.e. Eq. (7), has two terms which transfer energy from small to large scales. The first one is the classical term which couples the temperature fluctuation to the velocity fluctuation. The second one is a new term which couples the thermal conductivity fluctuation to the fluctuation of the temperature gradient.

The two terms can also be written as

$$\vec{q}_R=\langle\rho cT'\vec{v}'\rangle \tag{10}$$

and

$$\vec{q}_k=-\langle k'(T)\nabla T'\rangle \tag{11}$$

which allow to write Eq. (7) as

$$\rho c\frac{D\langle T\rangle}{Dt}=-\nabla\cdot\left(-\langle k(T)\rangle\nabla\langle T\rangle\right)-\nabla\cdot\left(\vec{q}_k+\vec{q}_R\right) \tag{12}$$

The introduction of Eqs. (10) and (11) in Eq. (8) gives

$$\rho c\frac{DT'}{Dt}=-\rho c\vec{v}'\nabla\langle T\rangle-\nabla\cdot\left(\vec{q}'_R+\vec{q}'_k-\vec{q}_R-\vec{q}_k-\langle k(T)\rangle\nabla T'-k'(T)\nabla\langle T\rangle\right) \tag{13}$$

in Eq. (9) gives

$$\rho c\frac{D}{Dt}\left(\frac{\langle T'T'\rangle}{2}\right)=-\left(\vec{q}_R-\vec{q}_k\right)\nabla\langle T\rangle+$$
$$-\nabla\cdot\left(\langle\rho c\vec{v}'\frac{T'T'}{2}\rangle-\langle k'(T)\rangle\nabla\frac{T'T'}{2}\rangle-\langle k(T)\rangle\nabla\frac{\langle T'T'\rangle}{2}-\langle k'(T)T'\rangle\nabla\langle T\rangle\right)+$$
$$-\langle k(T)\rangle\langle\nabla T'\nabla T'\rangle+\langle\vec{q}'_k\nabla T'\rangle \tag{14}$$

On the right hand side of Eq. (14) the turbulent production term is given by

$$-\left(\vec{q}_R-\vec{q}_k\right)\nabla\langle T\rangle \tag{15}$$

It can be observed that the energy transfer from the time average to the fluctuations has different sign whether is due to the velocity or the thermal conductivity fluctuation. Specifically, the turbulent production is enhanced by the velocity fluctuation and decreased by the thermal conductivity fluctuation.

The turbulent transport term is made of four components, not only two,

$$-\nabla\cdot\left(\langle\rho c\vec{v}'\frac{T'T'}{2}\rangle-\langle k'(T)\rangle\nabla\frac{T'T'}{2}\rangle-\langle k(T)\rangle\nabla\frac{\langle T'T'\rangle}{2}-\langle k'(T)T'\rangle\nabla\langle T\rangle\right) \tag{16}$$

The first component is due to the eddy transport. The second and the third component represent the contribution of the thermal conductivity, with the second one due to the fluctuations and the third one to the average. The fourth component is a new term, i.e. the product of the fluctuating thermal conductivity and the temperature fluctuation.

The turbulent dissipation term is made of two components, both negative, where the first one is linked to the average thermal conductivity while the second one to the fluctuating thermal conductivity.

$$-\langle k(T)\rangle\langle\nabla T'\nabla T'\rangle+\langle\vec{q}'_k\nabla T'\rangle \tag{17}$$

MODELLING THE FLUCTUATING THERMAL CONDUCTIVITY

The thermal conductivity can be approximated by a polynomial expression as

$$k(T)=\sum_{i=0}^{N}a_iT^i=a_0+a_1T+a_2T^2+.....+a_NT^N \tag{18}$$

Some cases are examined. The first one is the linear variation

$$k(T)=a_0+a_1T \tag{19}$$

Introducing the fluctuating temperature, Eq. (2), it is obtained for the average thermal conductivity

$$\langle k(T)\rangle=a_0+a_1\langle T\rangle \tag{20}$$

and for the fluctuating thermal conductivity

$$k'(T)=a_1T'. \tag{21}$$

The average thermal conductivity depends only on the average temperature and the fluctuating thermal conductivity on the fluctuating temperature.

If the relation is a quadratic one

$$k(T)=a_0+a_1T+a_2T^2, \tag{22}$$

the application of Eq. (2) gives for the average term

$$\langle k(T)\rangle=a_0+a_1\langle T\rangle+a_2\left(\langle T\rangle\langle T\rangle+\langle T'T'\rangle\right) \tag{23}$$

and for the fluctuating one

$$k'(T)=a_1T'+a_2\left(2\langle T\rangle T'+T'T'-\langle T'T'\rangle\right) \tag{24}$$

Equation (24) shows the interaction between average and fluctuating temperature in the quadratic case.

If the relation is a cubic one

$$k(T)=a_0+a_1T+a_2T^2+a_3T^3, \tag{25}$$

the average thermal conductivity is

$$\langle k(T)\rangle=a_0+a_1\langle T\rangle+a_2\left(\langle T\rangle\langle T\rangle+\langle T'T'\rangle\right)+$$
$$a_3\left(\langle T\rangle\langle T\rangle\langle T\rangle+3\langle T\rangle\langle T'T'\rangle+\langle T'T'T'\rangle\right) \tag{26}$$

and the fluctuating one

$$k'(T)=a_1T'+a_2\left(2\langle T\rangle T'+T'T'-\langle T'T'\rangle\right)+$$
$$a_3\left(3\langle T\rangle\langle T\rangle T'+3\langle T\rangle T'T'-3\langle T\rangle\langle T'T'\rangle+T'T'T'-\langle T'T'T'\rangle\right) \tag{27}$$

If the relation is a forth power one

$$k(T) = a_0 + a_1 T + a_2 T^2 + a_3 T^3 + a_4 T^4, \tag{28}$$

the average thermal conductivity is

$$\begin{aligned}\langle k(T)\rangle = {} & a_0 + a_1\langle T\rangle + a_2\left(\langle T\rangle\langle T\rangle + \langle T'T'\rangle\right) + \\ & a_3\left(\langle T\rangle\langle T\rangle\langle T\rangle + 3\langle T\rangle\langle T'T'\rangle + \langle T'T'T'\rangle\right) + \\ & a_4\left(\langle T\rangle\langle T\rangle\langle T\rangle\langle T\rangle + 6\langle T\rangle\langle T\rangle\langle T'T'\rangle + 4\langle T\rangle\langle T'T'T'\rangle + \langle T'T'T'T'\rangle\right)\end{aligned} \tag{29}$$

and the fluctuating one

$$\begin{aligned}k'(T) = {} & a_1 T' + a_2\left(2\langle T\rangle T' + T'T' - \langle T'T'\rangle\right) + \\ & a_3\left(3\langle T\rangle\langle T\rangle T' + 3\langle T\rangle T'T' - 3\langle T\rangle\langle T'T'\rangle + T'T'T' - \langle T'T'T'\rangle\right) + \\ & + a_4\left(4\langle T\rangle\langle T\rangle\langle T\rangle T' + 6\langle T\rangle\langle T\rangle T'T' + 4\langle T\rangle T'T' + T'T'T'T'\right) + \\ & - a_4\left(6\langle T\rangle\langle T\rangle\langle T'T'\rangle + 4\langle T\rangle\langle T'T'\rangle + \langle T'T'T'T'\rangle\right)\end{aligned} \tag{30}$$

The average and fluctuating thermal conductivity are then resumed in the following. For the constant case:

$$\langle k(T)\rangle = a_0,\ k'(T) = 0 \tag{31}$$

for the linear one

$$\langle k(T)\rangle = a_0 + a_1\langle T\rangle,\ k'(T) = a_1 T' \tag{32}$$

for the quadratic one

$$\begin{aligned}\langle k(T)\rangle &= \left(a_0 + a_1\langle T\rangle + a_2\langle T\rangle\langle T\rangle\right) + \left(a_2\langle T'T'\rangle\right) \\ k'(T) &= \left(a_1 + 2a_2\langle T\rangle\right)T' + a_2\left(T'T' - \langle T'T'\rangle\right)\end{aligned} \tag{33}$$

for the cubic one

$$\begin{aligned}\langle k(T)\rangle &= \left(a_0 + a_1\langle T\rangle + a_2\langle T\rangle\langle T\rangle + a_3\langle T\rangle\langle T\rangle\langle T\rangle\right) + \\ &\left(a_2 + 3a_3\langle T\rangle\right)\langle T'T'\rangle + \left(a_3\langle T'T'T'\rangle\right) \\ k'(T) &= \left(a_1 + 2a_2\langle T\rangle + 3a_3\langle T\rangle\langle T\rangle\right)T' \\ &+ \left(a_2 + 3a_3\langle T\rangle\right)\left(T'T' - \langle T'T'\rangle\right) + a_3\left(T'T'T' - \langle T'T'T'\rangle\right)\end{aligned} \tag{34}$$

and for the forth power case

$$\begin{aligned}\langle k(T)\rangle = {} & \left(a_0 + a_1\langle T\rangle + a_2\langle T\rangle\langle T\rangle + a_3\langle T\rangle\langle T\rangle\langle T\rangle + a_4\langle T\rangle\langle T\rangle\langle T\rangle\langle T\rangle\right) + \\ & \left(a_2 + 3a_3\langle T\rangle + 6a_4\langle T\rangle\langle T\rangle\right)\langle T'T'\rangle + \left(a_3 + 4a_4\langle T\rangle\right)\langle T'T'T'\rangle + a_4\langle T'T'T'T'\rangle \\ k'(T) = {} & \left(a_1 + 2a_2\langle T\rangle + 3a_3\langle T\rangle\langle T\rangle + 4a_4\langle T\rangle\langle T\rangle\langle T\rangle\right)T' + \\ & \left(a_2 + \left(3a_3 + 4a_4\right)\langle T\rangle + 6a_4\langle T\rangle\langle T\rangle\right)\left(T'T' - \langle T'T'\rangle\right) + \\ & a_3\left(T'T'T' - \langle T'T'T'\rangle\right) + a_4\left(T'T'T'T' - \langle T'T'T'T'\rangle\right)\end{aligned} \tag{35}$$

In conclusion, the following general expression can be assumed for the average thermal conductivity

$$\langle k(T)\rangle = k\left(\langle T\rangle\right) + \sum_{k=2}^{N} P_k\left(\langle T\rangle\right)\langle T'^k\rangle \tag{36}$$

and for the fluctuating thermal conductivity

$$k'(T) = \left.\frac{dk}{dT}\right|_{T=\langle T\rangle} \cdot T' + \sum_{k=2}^{N} Q_k\left(\langle T\rangle\right)\cdot\left(T'^k - \langle T'^k\rangle\right) \tag{37}$$

The average thermal conductivity is due to the thermal conductivity at the average temperature and of polynomials where the temperature fluctuations are present at several powers. The fluctuating thermal conductivity is due to the product of the first derivative and the fluctuating thermal conductivity and several polynomials.

The structure of the thermal conductivity can be simplified with the following expression

$$k(T) = k\left(\langle T\rangle\right) + \left.\frac{dk}{dT}\right|_{T=\langle T\rangle} \cdot \left(T - \langle T\rangle\right) + o\left(T - \langle T\rangle\right) \tag{38}$$

or

$$k(T) = k\left(\langle T\rangle\right) + \left.\frac{dk}{dT}\right|_{T=\langle T\rangle} \cdot T' + o\left(T'\right) \tag{39}$$

It is then possible to obtain for the average thermal conductivity

$$\langle k(T)\rangle \approx k\left(\langle T\rangle\right) \tag{40}$$

and for the fluctuating thermal conductivity

$$k'(T) \approx \left.\frac{dk}{dT}\right|_{T=\langle T\rangle} T' \tag{41}$$

From Eq.(36) and Eq. (40) it is possible to conclude

$$\left\|k\left(\langle T\rangle\right)\right\| >> \left\|\sum_{k=2}^{N} P_k\left(\langle T\rangle\right)\langle T'^k\rangle\right\| \tag{42}$$

and from Eq. (37) and (41)

$$\left\|\left.\frac{dk}{dT}\right|_{T=\langle T\rangle} \cdot T'\right\| >> \left\|\sum_{k=2}^{N} Q_k\left(\langle T\rangle\right)\cdot\left(T'^k - \langle T'^k\rangle\right)\right\|. \tag{43}$$

Equations (42) and (43) are confirmed by the assumption

$$\left\|\langle T\rangle\right\| >> \left\|T'\right\|. \tag{44}$$

From the physical point of view the coefficients of the polynomial expressions follow the rule

$$\left\|a_{n+1}\right\| << \left\|a_n\right\|, n > 1, \tag{45}$$

i.e. the contribution of the coefficients of higher order are less influencing the variation of the thermal conductivity. The polynomials $P_k\left(\langle T\rangle\right)$, $Q_k\left(\langle T\rangle\right)$ contain the coefficients a_n of higher order and are smaller than the thermal conductivity at the average temperature and of its derivative. On the basis of the experimental evidence that the coefficients a_n decrease of some orders of magnitude with the increase of n it is possible to conclude that Eqs. (40) and (41) are valid.

Using Eqs. (40) and (41) it is possible to obtain

$$\vec{q}_k = -\left.\frac{dk}{dT}\right|_{T=\langle T\rangle} \nabla\frac{\langle T'T'\rangle}{2} \tag{46}$$

which, substituted in Eq. (7) gives

$$\rho c\frac{D\langle T\rangle}{Dt} = -\nabla\cdot\left(\langle\rho c T'\vec{v}'\rangle - \left.\frac{dk}{dT}\right|_{T=\langle T\rangle} \nabla\frac{\langle T'T'\rangle}{2} - \langle k\left(T\right)\rangle\nabla\langle T\rangle\right) \tag{47}$$

and in Eq. (9)

$$\begin{aligned}\rho c\frac{D}{Dt}\left(\frac{\langle T'T'\rangle}{2}\right) = {} & -\left(\langle\rho c\vec{v}'T'\rangle + \left.\frac{dk}{dT}\right|_{T=\langle T\rangle} \nabla\frac{\langle T'T'\rangle}{2}\right)\nabla\langle T\rangle + \\ & -\nabla\cdot\left(\langle\rho c\vec{v}'\frac{T'T'}{2}\rangle - \left.\frac{dk}{dT}\right|_{T=\langle T\rangle} \nabla\frac{\langle T'T'T'\rangle}{3} - k\left(\langle T\rangle\right)\nabla\frac{\langle T'T'\rangle}{2} - 2\left.\frac{dk}{dT}\right|_{T=\langle T\rangle} \frac{\langle T'T'\rangle}{2}\nabla\langle T\rangle\right) + \\ & -k\left(\langle T\rangle\right)\langle\nabla T'\nabla T'\rangle - \left.\frac{dk}{dT}\right|_{T=\langle T\rangle} \langle T'\nabla T'\nabla T'\rangle\end{aligned} \tag{48}$$

Equation (48) contains a third order term of the fluctuating temperature which cannot be solved writing an equation for the cube of the temperature fluctuation because it would introduce a forth power of the fluctuating temperature and so on. It is necessary to make some assumptions to find a simple

expression for the average and the fluctuating thermal conductivity.
From Eq. (44) it is obtained

$$\left.\frac{dk}{dT}\right|_{T=\langle T\rangle}\langle T'\nabla\frac{T'T'}{2}\rangle \propto k(\langle T\rangle)\frac{T_{rms}}{\langle T\rangle}\frac{T_{rms}^2}{\delta} \prec k(\langle T\rangle)\nabla\frac{\langle T'T'\rangle}{2} \propto k(\langle T\rangle)\frac{T_{rms}^2}{\delta} \tag{49}$$

and

$$\left.\frac{dk}{dT}\right|_{T=\langle T\rangle}\langle T'\nabla T'\nabla T'\rangle \propto k(\langle T\rangle)\frac{T_{rms}}{\langle T\rangle}\frac{T_{rms}^2}{\delta^2} \prec k(\langle T\rangle)\langle\nabla T'\nabla T'\rangle \propto k(\langle T\rangle)\frac{T_{rms}^2}{\delta^2} \tag{50}$$

which allow to write the equation for the square of the fluctuating temperature as

$$\rho c\frac{D}{Dt}\left(\frac{\langle T'T'\rangle}{2}\right)=-\left(\langle\rho c\vec{v}'T'\rangle+\left.\frac{dk}{dT}\right|_{T=\langle T\rangle}\nabla\frac{\langle T'T'\rangle}{2}\right)\nabla\langle T\rangle+$$
$$-\nabla\cdot\left(\langle\rho c\vec{v}'\frac{T'T'}{2}\rangle-k(\langle T\rangle)\nabla\frac{\langle T'T'\rangle}{2}-2\left.\frac{dk}{dT}\right|_{T=\langle T\rangle}\frac{\langle T'T'\rangle}{2}\nabla\langle T\rangle\right)+ \tag{51}$$
$$-k(\langle T\rangle)\langle\nabla T'\nabla T'\rangle$$

The use of the traditional Boussinesq formulation gives for the average temperature equation

$$\rho c\frac{D\langle T\rangle}{Dt}=\nabla\cdot\left(\left(k(\langle T\rangle)+\rho c\frac{\nu_T}{\sigma_T}\right)\nabla\langle T\rangle+\left.\frac{dk}{dT}\right|_{T=\langle T\rangle}\nabla\frac{\langle T'T'\rangle}{2}\right) \tag{52}$$

and for the square of the fluctuating temperature

$$\rho c\frac{D}{Dt}\left(\frac{\langle T'T'\rangle}{2}\right)=\left(\rho c\frac{\nu_T}{\sigma_T}\nabla\langle T\rangle-\left.\frac{dk}{dT}\right|_{T=\langle T\rangle}\nabla\frac{\langle T'T'\rangle}{2}\right)\nabla\langle T\rangle+$$
$$\nabla\cdot\left(\left(\rho c\frac{\nu_T}{\sigma_T}+k(\langle T\rangle)\right)\nabla\frac{\langle T'T'\rangle}{2}+2\left.\frac{dk}{dT}\right|_{T=\langle T\rangle}\frac{\langle T'T'\rangle}{2}\nabla\langle T\rangle\right)+ \tag{53}$$
$$-2C_{2,\langle TT'\rangle}k(\langle T\rangle)\frac{\langle T'T'\rangle}{2}\frac{\varepsilon}{k}$$

where it has been used the classical closure formula for the dissipation term appearing in the second order turbulence model i.e. the dissipation term is proportional to the second order transported variable multiplied by the frequency $\frac{\varepsilon}{k}$.

In a two dimensional case the previous equations are:
for the average temperature,

$$\rho c\frac{\partial\langle T\rangle}{\partial t}+\rho cU\frac{\partial\langle T\rangle}{\partial x}+\rho cV\frac{\partial\langle T\rangle}{\partial y}=$$
$$\frac{\partial}{\partial x}\left(\left(k(\langle T\rangle)+\rho c\frac{\nu_T}{\sigma_T}\right)\frac{\partial\langle T\rangle}{\partial x}+\left.\frac{dk}{dT}\right|_{T=\langle T\rangle}\frac{\partial}{\partial x}\left(\frac{\langle T'T'\rangle}{2}\right)\right)+ \tag{54}$$
$$\frac{\partial}{\partial y}\left(\left(k(\langle T\rangle)+\rho c\frac{\nu_T}{\sigma_T}\right)\frac{\partial\langle T\rangle}{\partial y}+\left.\frac{dk}{dT}\right|_{T=\langle T\rangle}\frac{\partial}{\partial y}\left(\frac{\langle T'T'\rangle}{2}\right)\right)$$

for the square of the fluctuating temperature,

$$\rho c\frac{\partial}{\partial t}\left(\frac{\langle T'T'\rangle}{2}\right)+\rho cU\frac{\partial}{\partial x}\left(\frac{\langle T'T'\rangle}{2}\right)+\rho cV\frac{\partial}{\partial y}\left(\frac{\langle T'T'\rangle}{2}\right)=$$
$$\left(\rho c\frac{\nu_T}{\sigma_T}\frac{\partial\langle T\rangle}{\partial x}-\left.\frac{dk}{dT}\right|_{T=\langle T\rangle}\frac{\partial}{\partial x}\left(\frac{\langle T'T'\rangle}{2}\right)\right)\frac{\partial\langle T\rangle}{\partial x}+$$
$$\left(\rho c\frac{\nu_T}{\sigma_T}\frac{\partial\langle T\rangle}{\partial y}-\left.\frac{dk}{dT}\right|_{T=\langle T\rangle}\frac{\partial}{\partial y}\left(\frac{\langle T'T'\rangle}{2}\right)\right)\frac{\partial\langle T\rangle}{\partial y}+$$
$$\frac{\partial}{\partial x}\left(\left(\rho c\frac{\nu_T}{\sigma_T}+k(\langle T\rangle)\right)\frac{\partial}{\partial x}\left(\frac{\langle T'T'\rangle}{2}\right)+2\left.\frac{dk}{dT}\right|_{T=\langle T\rangle}\frac{\langle T'T'\rangle}{2}\frac{\partial\langle T\rangle}{\partial x}\right)+$$
$$\frac{\partial}{\partial y}\left(\left(\rho c\frac{\nu_T}{\sigma_T}+k(\langle T\rangle)\right)\frac{\partial}{\partial y}\left(\frac{\langle T'T'\rangle}{2}\right)+2\left.\frac{dk}{dT}\right|_{T=\langle T\rangle}\frac{\langle T'T'\rangle}{2}\frac{\partial\langle T\rangle}{\partial y}\right)+$$
$$-2C_{2,\langle TT'\rangle}k(\langle T\rangle)\frac{\langle T'T'\rangle}{2}\frac{\varepsilon}{k_T} \tag{55}$$

where the turbulent kinetic energy is given by

$$\rho\frac{Dk_T}{Dt}=[T_R]:\langle[D]\rangle+\nabla\cdot\left(\rho\left(\nu+\frac{\nu_T}{\sigma_k}\right)\nabla k_T\right)-\rho\varepsilon \tag{56}$$

and the dissipation term by

$$\rho\frac{D\varepsilon}{Dt}=C_{1,\varepsilon}\frac{\varepsilon}{k_T}[T_R]:\langle[D]\rangle+\nabla\cdot\left(\rho\left(\nu+\frac{\nu_T}{\sigma_\varepsilon}\right)\nabla\varepsilon\right)-\rho C_{2,\varepsilon}\frac{\varepsilon}{k_T}\varepsilon \tag{57}$$

DISCUSSION ON THE MODEL

The equation for the conservation of energy with the average temperature, i.e. Eq. (54) for a two dimensional case, presents two terms with a variation of the thermal conductivity. The new result of Eq. (54) is the link between the variation of the thermal conductivity and the square of the temperature fluctuation in turbulent flow, which makes the present equation a new kind of energy conservation equation. As an example the energy equation for the time average temperature, solved in [7] for turbulent steady flow, is a particular case of Eq. (54).
Also Eq. (55) is a new kind of energy equation for the square of the fluctuating temperature where two kinds of new terms are present representing the variation of the thermal conductivity with the temperature.
The solution of Eq. (54) is possible with the solution of Eq. (55), which on the other hand, requires the solution of Eqs. (56) and (57).

CONCLUSIONS

The present theoretical work is aimed to take into account the variation of the thermal conductivity of a fluid flowing in turbulent flow. The equations of the energy conservation have been studied in the form of the average temperature and the square of the fluctuating temperature. The variation of the thermal conductivity has been modelled mathematically with physical hypothesis, making possible to correlate the derivative of the thermal conductivity, with respect to the average temperature, multiplied to the space gradient of the square of the fluctuating temperature. The final equations of the average and the fluctuating temperature need to be solved together to

the turbulent kinetic energy and the energy dissipation in order to take into account the variation of the thermal conductivity. It is planned to solved the four coupled equations in the near future with DNS approach to quantify the results of the theoretical approach introduced here.

REFERENCES

[1] Martinelli, R.C. 1947. Heat transfer to molten metals. Trans. ASME, 69, 47–59.

[2] Lyon, R.N. 1951. Liquid metal heat transfer coefficients. Chem. Eng. Progr., 47, 75–79.

[3] Tennekes, H., Lumley, J.L. 1972. A First Course in Turbulence. MIT Press, Cambridge, MA.

[4] Aoki, S. 1963. A consideration on the heat transfer in liquid metal. Bull. Tokyo Inst. Tech., 54, 63–73.

[5] Reynolds, A.J. 1975. The prediction of turbulent Prandtl and Schmidt numbers. Int. J. Heat Mass Transfer, 18, 1055–1069.

[6] F. Gori, M.A. El Hadidy, and D.B. Spalding. Numerical Prediction of the Heat Transfer to Low-Prandtl Number Fluids. Numerical Heat Transfer, 2, 441-454, 1979.

[7] S. Faggiani and F. Gori. Influence of Streamwise Molecular Heat Conduction on the Heat Transfer Coefficient for Liquid Metals in Turbulent Flow between Parallel Plates. Journal of Heat Transfer, ASME, 102, 2, 292-296, 1980.

[8] M.A. El Hadidy, F. Gori and D.B. Spalding. Further Results on the Heat Transfer to Low-Prandtl Number Fluids in Pipes. Numerical Heat Transfer, 5, 107-117, 1982.

[9] Cheng X., Tak N. Investigation on turbulent heat transfer to lead–bismuth eutectic flows in circular tubes for nuclear applications. Nuclear Engineering and Design, 236 (2006) 385–393.

[10] M. Satake, K. Yuki, S. Chiba, H. Hashizume. Numerical analysis of MHD flow structure behind a square rod. Fusion Engineering and Design, 81 (2006) 525–532.

[11] L. C. Cadwallader G. R. Longhurst. FLIBE use in fusion reactors: an initial safety assessment. Idaho National Engineering and Environmental Laboratory Idaho Falls, Idaho, 83415 INEEL/EXT-99-00331, March 1999.

[12] Shin-Ya Chiba, Kazuhisa Yuki Hidetoshi Hashizume, Saburo Toda, Akio Sagara. Numerical research on heat transfer enhancement for high Prandtl-number fluid. Fusion Engineering and Design, 81 (2006) 513–517.

[13] T. Kunugi, S. Satake, A. Sagara. Direct numerical simulation of turbulent free-surface high Prandtl number fluid flows in fusion reactors. Nuclear Instruments and Methods in Physics Research A, 464 (2001) 165–171.

[14] H. Nakaharai, J. Takeuchi, T. Yokomine, T. Kunugi, S. Satake, N.B. Morley, M.A. Abdou. The influence of a magnetic field on turbulent heat transfer of a high Prandtl number fluid. Experimental Thermal and Fluid Science, 32 (2007) 23–28.

[15] Gregory J. Kolbov. Economic Evaluation of Solar-Only and Hybrid Power Towers Using Molten-Salt Technology. Solar Energy, 62, 1, 51-61, 1998.

[16] Hiroshi Hasuike, Yoshio Yoshizawa, Akio Suzuki, Yutaka Tamaura. Study on design of molten salt solar receivers for beam-down solar concentrator. Solar Energy, 80 (2006) 1255–1262.

[17] F. Donatini, C. Zamparelli, A. Maccari and M. Vignolini. High efficency integration of thermodynamic solar plant with natural gas combined cycle. 2007 International Conference on Clean Electrical Power, ICCEP '07, 2007, 770-776.

[18] Hiroshi Kawamura, Kouichi Ohsaka, Hiroyuki Abe, Kiyoshi Yamamoto. DNS of turbulent heat transfer in channel flow with low to medium-high Prandtl number fluid. International Journal of Heat and Fluid Flow, 19 (1998) 482-491.

[19] Bo Yu, Yasuo Kawaguchi. DNS of fully developed turbulent heat transfer of a viscoelastic drag-reducing flow. International Journal of Heat and Mass Transfer, 48 (2005) 4569–4578.

[20] Petukhov, B.S. Heat Transfer and Friction in Turbulent Pipe Flow with Variable Physical Properties. Advances in Heat Transfer, 6, 503-565, 1970.

[21] S. Faggiani and F. Gori. Remarks on the Heat Transfer to Gases in Turbulent Flow between Parallel Plates. The 7th International Heat Transfer Conference, Munchen, Germany , 3, 33-38 1982.

[22] E. P. Valueva. Hydrodynamics and Heat Transfer in Pulsating Turbulent Pipe Flow of a Liquid of Variable Properties. High Temperature, 43, 6, 2005, 890–899.

[23] E. P. Valueva. Hydrodynamics and Heat Transfer in Pulsating Turbulent Flow of Gas in a Heated Pipe. High Temperature, 44, 1, 2006, 120–128.

[24] E. P. Valueva. Integral Methods of Calculation of Heat Transfer and Drag under Conditions of Turbulent Pipe Flow of Liquid of Variable Properties: Steady-State and Quasi-Steady-State Flows in a Round Pipe with Constant Density of Heat Flux to the Wall. High Temperature, 2007, 45, 1, 49–57.

[25] E. P. Valueva. Integral Methods of Calculation of Heat Transfer and Drag under Conditions of Turbulent Pipe Flow of Liquid of Variable Properties: Pulsating High-Frequency Flow. High Temperature, 2007, 45, 4, 502–508.

Proceedings of the ASME INTERNATIONAL
MECHANICAL ENGINEERING CONGRESS AND EXPOSITION
October 31 November 6, 2008, Boston, Massachusetts, USA

IMECE2008-66120

On a New Passive Scalar Equation with Variable Mass Diffusivity

Fabio Gori
Department of Mechanical Engineering
University of Rome "Tor Vergata"
Rome, Italy

Andrea Boghi
Department of Mechanical Engineering
University of Rome "Tor Vergata"
Rome, Italy

ABSTRACT

The present work investigates the mass conservation equation of a Newtonian and non-Newtonian fluid in turbulent flow with variable mass diffusivity. The mass conservation equation is considered with the fluctuating terms in the concentration as well as in the mass diffusivity and is written for the average concentration, for the fluctuating concentration one as well as for the square of the fluctuating concentration. A new term appears in the form of product of the fluctuating mass diffusivity to the space gradient of the concentration fluctuation. This new term is interpreted and introduced in the mass conservation equation of the square of the fluctuating concentration where other new terms are also appearing. A possible physical interpretation is given to the different terms. Assuming several relations between mass diffusivity and concentration it is then possible to write expressions for the average and the fluctuating mass concentration which can be simplified on the basis of physical and mathematical considerations. Specifically, the mass flux is then expressed as the product of the derivative of the mass diffusivity to the gradient of the square of the mass fluctuation. Further considerations make possible to write a new mass conservation equation of the average concentration which include a new term which takes into account the space gradient of the mass flux. The mass conservation equation can be solved with the coupled solution of the equation of the square of the concentration fluctuation.

INTRODUCTION

Mass diffusion is the process of matter transfer, due to the statistical movements of molecules, analogue to heat transfer. In several cases, as in dilute solutions, mass diffusivity is almost constant while in others, e.g. heavy polymers, dyes and macro-molecules, the diffusivity is strongly dependent on the concentration [1].

Tennekes and Lumley [2] showed that the scale of fluctuations reduces increasing the Schmidt number, as in dyes and macro-molecules, with the consequent increase of the fluctuations of the passive scalar. This behaviour has been confirmed by other papers of DNS simulations, as Schwertfirm and Manhart [3], who investigated low Reynolds numbers flow with a Schmidt number ranging from 3 to 49. The numerical modelling of a passive scalar in turbulent flow is usually done using the Reynolds analogy, despite some researchers argue it is no more valid at high Schmidt numbers. Hasegawa and Kasagi [4] modelled numerically, with DNS, a fluid with high Schmidt number flowing onto a free or a solid surface. The mass transfer is shown to be dominated by velocity fluctuations at low frequency, implying the analogy between mass and momentum transfer is no more valid. Indeed, at high Schmidt numbers the eddy diffusivity of mass is different from the momentum eddy diffusivity, or, in other words, the turbulent Schmidt number is not unity.

Lin [5] extended the Sada model to reacting dyes with the hypothesis of an exponential relation between mass diffusivity and concentration obtaining better predictions than before. Tsunashima, Hashimoto, and Nakano [6] performed sedimentation measurements and dynamic light scattering determining the coefficient of mutual diffusion of a linear flexible polymer. The conclusion is that the sedimentation coefficients are not constant but function of the concentration according to a polynomial law. Kuntz and Lavallee [7] showed simplest compounds, like copper sulphate in water environment, exhibit a mass diffusivity decreasing hyperbolically with the concentration.

Among the substances that exhibit concentration-dependent diffusion coefficient there are also biological molecules like proteins. Bowen [8] has investigated the physicochemical conditions on the permeation rate in cross-flow ultra-filtration of a colloidal suspension. A numerical solution of the relative equations has been used to model the concentration polarisation and hence to predict the rate of cross-flow ultra-filtration. The model takes into account the variation of the physical properties as the mass diffusivity. The results have been compared to experimental data for the proteins bovine serum albumin and recombinant human lacto-ferrin. Good agreement between theoretical predictions and experimental cross-flow

ultra-filtration data has been obtained. The results of these calculations show that the effects of variable diffusivity are both significant and comparable in magnitude.

The insight of diffusion process of particular proteins, like fibrin and selectines in turbulent blood flow, have a critical relevance because is the first step of the thrombus formation. Blood flow set the transport of cells and proteins on the surface of implantable devices like stent. Turbulent flow conditions occur in many regions of vascular bed and aid the thrombosis. Many research focuses the attention on platelet deposition even if literature about turbulence and thrombus formation is scanty but the effort in these direction is to design new devices where the recirculation zone, where it deposits thrombi, are decreased. These aspects have been resumed in Gorbedt and Sefton [9].

Among the macromolecules that diffuse in human body, like drugs, are found aerosolized medications which include bronchodilators and corticosteroids to treat asthma, realised by biomedical devices. Deposition on lung surfaces is attractive for many reasons. For pulmonary disorders it is useful to apply medication directly to the lung surfaces, in order to increase drug concentration in the affected area without increasing total dosage. Using current aerosol drug delivery equipment, less than 10% of the aerosolized medication for jet-nebulizers and less than 20% for metered dose inhalers is deposited on the alveolar surfaces of the lungs. Gemci et al. [10] have analyzed deposition of a series of mono-disperse aerosol injections in 70/30 helium/oxygen (Heliox) and air for the larynx and trachea with Computational Fluid Dynamics (CFD) software. Flow measurements such as turbulent kinetic energy and velocity magnitude typically are different by less than 5%. The authors have implemented a k-ε turbulence model to perform the simulation for mass, momentum and energy conservation equations and stochastic particle technique to solve the spray equation.

The present work is aimed to investigate theoretically the turbulent flow taking into account a mass diffusivity variable with the concentration.

Nomenclature

C	instantaneous concentration
$\langle C\rangle$	average concentration
C'	fluctuating concentration
$D(C)$	mass diffusivity
$\langle D(C)\rangle$	average mass diffusivity
$D'(C)$	fluctuating mass diffusivity
$\vec{J}_R$	average Reynolds mass flux
$\vec{J}_R{}'$	instantaneous Reynolds mass flux
$\vec{J}_D$	average mass flux
$\vec{J}_D{}'$	instantaneous mass flux
k	turbulent kinetic energy
u	instantaneous x-velocity component
U	average x-velocity component
u'	fluctuating x-velocity component
v	instantaneous y-velocity component
V	average y-velocity component
v'	fluctuating y-velocity component
ε	dissipation of turbulent kinetic energy

MASS DIFFUSION EQUATION

Consider the mass diffusion equation in turbulent flow of an incompressible fluid without chemical reactions following the Fick law and with the mass diffusivity dependent on the concentration. Neglecting the mechanical dissipation term the final equation in a two dimensional field and unsteady state is the following

$$\frac{\partial C}{\partial t}+u\frac{\partial C}{\partial x}+v\frac{\partial C}{\partial y}=\frac{\partial}{\partial x}\left(D(C)\frac{\partial C}{\partial x}\right)+\frac{\partial}{\partial y}\left(D(C)\frac{\partial C}{\partial y}\right) \tag{1}$$

Assume any instantaneous variable, i.e. the velocity component in x direction, u, in y direction, v, the mass diffusivity, D, and the concentration, C, as the sum of an average and a fluctuating term, as, for example, for the concentration, C,

$$C=\langle C\rangle+C' \tag{2}$$

Introducing each variable into Eq. (1) it is obtained

$$\frac{\partial}{\partial t}\left(\langle C\rangle+C'\right)+\left(U+u'\right)\frac{\partial}{\partial x}\left(\langle C\rangle+C'\right)+\left(V+v'\right)\frac{\partial}{\partial y}\left(\langle C\rangle+C'\right)= \tag{3}$$
$$\frac{\partial}{\partial x}\left(\left(\langle D\rangle+D'\right)\frac{\partial}{\partial x}\left(\langle C\rangle+C'\right)\right)+\frac{\partial}{\partial y}\left(\left(\langle D\rangle+D'\right)\frac{\partial}{\partial y}\left(\langle C\rangle+C'\right)\right)$$

Equation (3) can be written as two separate equations after the time averaging is done. The time average equation is

$$\frac{\partial\langle C\rangle}{\partial t}+U\frac{\partial\langle C\rangle}{\partial x}+V\frac{\partial\langle C\rangle}{\partial y}=\frac{\partial}{\partial x}\left(\langle D(C)\rangle\frac{\partial\langle C\rangle}{\partial x}-\langle u'C'\rangle+\langle D'(C)\frac{\partial C'}{\partial x}\rangle\right)+$$
$$\frac{\partial}{\partial y}\left(\langle D(C)\rangle\frac{\partial\langle C\rangle}{\partial y}-\langle v'C'\rangle+\langle D'(C)\frac{\partial C'}{\partial y}\rangle\right) \tag{4}$$

while the fluctuating one is

$$\frac{\partial C'}{\partial t}+U\frac{\partial C'}{\partial x}+V\frac{\partial C'}{\partial y}=-u'\frac{\partial\langle C\rangle}{\partial x}-v'\frac{\partial\langle C\rangle}{\partial y}+$$
$$\frac{\partial}{\partial x}\left(-u'C'+\langle u'C'\rangle+\langle D(C)\rangle\frac{\partial C'}{\partial x}+D'(C)\frac{\partial\langle C\rangle}{\partial x}+D'(C)\frac{\partial C'}{\partial x}-\langle D'(C)\frac{\partial C'}{\partial x}\rangle\right)+$$
$$\frac{\partial}{\partial y}\left(-v'C'+\langle v'C'\rangle+\langle D(C)\rangle\frac{\partial C'}{\partial y}+D'(C)\frac{\partial\langle C\rangle}{\partial y}+D'(C)\frac{\partial C'}{\partial y}-\langle D'(C)\frac{\partial C'}{\partial y}\rangle\right) \tag{5}$$

Multiplying Eq. (5) for C' the following equation can be obtained

$$\frac{\partial}{\partial t}\left(\frac{\langle C'C'\rangle}{2}\right)+U\frac{\partial}{\partial x}\left(\frac{\langle C'C'\rangle}{2}\right)+V\frac{\partial}{\partial y}\left(\frac{\langle C'C'\rangle}{2}\right)=$$
$$-\left(\langle u'C'\rangle+\langle D'(C)\frac{\partial C'}{\partial x}\rangle\right)\frac{\partial\langle C\rangle}{\partial x}-\left(\langle v'C'\rangle+\langle D'(C)\frac{\partial C'}{\partial y}\rangle\right)\frac{\partial\langle C\rangle}{\partial y}+$$
$$\frac{\partial}{\partial x}\left(-\langle u'\frac{C'C'}{2}\rangle+\langle D'(C)\frac{\partial}{\partial x}\left(\frac{C'C'}{2}\right)\rangle+\langle D(C)\rangle\frac{\partial}{\partial x}\left(\frac{\langle C'C'\rangle}{2}\right)+\langle D'(C)C'\rangle\frac{\partial\langle C\rangle}{\partial x}\right)+$$
$$\frac{\partial}{\partial y}\left(-\langle v'\frac{C'C'}{2}\rangle+\langle D'(C)\frac{\partial}{\partial y}\left(\frac{C'C'}{2}\right)\rangle+\langle D(C)\rangle\frac{\partial}{\partial y}\left(\frac{\langle C'C'\rangle}{2}\right)+\langle D'(C)C'\rangle\frac{\partial\langle C\rangle}{\partial y}\right)+$$
$$-\langle D(C)\rangle\langle\frac{\partial C'}{\partial x}\frac{\partial C'}{\partial x}\rangle-\langle D'(C)\frac{\partial C'}{\partial x}\frac{\partial C'}{\partial x}\rangle-\langle D(C)\rangle\langle\frac{\partial C'}{\partial y}\frac{\partial C'}{\partial y}\rangle-\langle D'(C)\frac{\partial C'}{\partial y}\frac{\partial C'}{\partial y}\rangle \tag{6}$$

Equation (4), i.e. the time average concentration equation, can be written, in a more compact form, as

$$\frac{D\langle C\rangle}{Dt}=-\nabla\cdot\left(\langle C'\vec{v}'\rangle-\langle D'(C)\nabla C'\rangle-\langle D(C)\rangle\nabla\langle C\rangle\right) \tag{7}$$

Equation (5), i.e. the fluctuating concentration equation, can be written, in compact form, as

$$\frac{DC'}{Dt}=-\vec{v}'\nabla\langle C\rangle-\nabla\cdot\left(-D'(C)\nabla\langle C\rangle\right)+ \tag{8}$$
$$-\nabla\cdot\left(\vec{v}'C'-D'(C)\nabla C'-\langle\vec{v}'C'\rangle+\langle D'(C)\nabla C'\rangle-D'(C)\nabla\langle C\rangle\right)$$

Equation (6), i.e. the equation which expresses the conservation of the square fluctuating concentration, can be written, in compact form, as

$$\frac{D}{Dt}\left(\frac{\langle C'C'\rangle}{2}\right)=-\left(\langle\vec{v}'C'\rangle+\langle D'(C)\nabla C'\rangle\right)\nabla\langle C\rangle+$$
$$-\nabla\cdot\left(\langle\vec{v}'\frac{C'C'}{2}\rangle-\langle D'(C)\nabla\frac{C'C'}{2}\rangle-\langle D(C)\rangle\nabla\frac{\langle C'C'\rangle}{2}-\langle D'(C)C'\rangle\nabla\langle C\rangle\right)+ \tag{9}$$
$$-\langle D(C)\rangle\langle\nabla C'\nabla C'\rangle-\langle D'(C)\nabla C'\nabla C'\rangle$$

It is now possible to distinguish the different terms which appear in the previous equations. The time average concentration equation, Eq. (4), has a form which is very similar to the instantaneous concentration equation. The terms which transfer energy from the small to the large scales are here two:

$$\langle C'\vec{v}'\rangle-\langle D'(C)\nabla C'\rangle \tag{10}$$

The first one is due to the velocity fluctuations while the second one has the traditional form of the product of the fluctuating mass diffusivity times the gradient of the fluctuating concentration.

Let us indicate the two terms respectively as:

$$\vec{J}_R=\langle C'\vec{v}'\rangle \tag{11}$$
$$\vec{J}_D=-\langle D'(C)\nabla C'\rangle \tag{12}$$

Equation (7) can be written as:

$$\frac{D\langle C\rangle}{Dt}=-\nabla\cdot\left(-\langle D(C)\rangle\nabla\langle C\rangle\right)-\nabla\cdot\left(\vec{J}_D+\vec{J}_R\right) \tag{13}$$

while Eq. (8), with the same nomenclature, as:

$$\frac{DC'}{Dt}=-\vec{v}'\nabla\langle C\rangle-\nabla\cdot\left(\vec{J}'_R+\vec{J}'_D-\vec{J}_R-\vec{J}_D-\langle D(C)\rangle\nabla C'-D'(C)\nabla\langle C\rangle\right) \tag{14}$$

and finally Eq. (9) as:

$$\frac{D}{Dt}\left(\frac{\langle C'C'\rangle}{2}\right)=-\left(\vec{J}_R-\vec{J}_D\right)\nabla\langle C\rangle+$$
$$-\nabla\cdot\left(\langle\vec{v}'\frac{C'C'}{2}\rangle-\langle D'(C)\nabla\frac{C'C'}{2}\rangle-\langle D(C)\rangle\nabla\frac{\langle C'C'\rangle}{2}-\langle D'(C)C'\rangle\nabla\langle C\rangle\right)+$$
$$-\langle D(C)\rangle\langle\nabla C'\nabla C'\rangle+\langle\vec{J}'_D\nabla C'\rangle \tag{15}$$

The different terms of Eq. (15) can be discussed. The convective term has the form

$$\frac{D}{Dt}\left(\frac{\langle C'C'\rangle}{2}\right) \tag{16}$$

while the production term is

$$-\left(\vec{J}_R-\vec{J}_D\right)\nabla\langle C\rangle \tag{17}$$

The energy transfer from the average to the fluctuating field is enhanced by the velocity fluctuations and decreased by the fluctuating mass diffusivity. In other words, the velocity fluctuations transports energy from the average to the fluctuating field while the fluctuating mass diffusivity does the opposite.

The transport term of Eq. (15) is made of four components

$$-\nabla\cdot\left(\langle\vec{v}'\frac{C'C'}{2}\rangle-\langle D'(C)\nabla\frac{C'C'}{2}\rangle-\langle D(C)\rangle\nabla\frac{\langle C'C'\rangle}{2}-\langle D'(C)C'\rangle\nabla\langle C\rangle\right) \tag{18}$$

The first one is due to the eddy transport. The second and the third ones are due to the molecular diffusion, with a contribution due to the fluctuating mass diffusivity and the other one to the average mass diffusivity. In the last term the fluctuating mass diffusivity is linked to the fluctuating concentration.

The last term of Eq. (15) is the dissipation one, which is made of two components:

$$-\langle D(C)\rangle\langle\nabla C'\nabla C'\rangle+\langle\vec{J}'_D\nabla C'\rangle \tag{19}$$

The first one is the molecular dissipation which is linked to the average mass diffusivity and the second one to the fluctuating mass diffusivity.

MODELLING THE FLUCTUATING MASS DIFFUSIVITY

Let model the mass diffusivity taking into account different dependences on the concentration, which, in some cases, give an increase and in others a decrease. The assumption is very general because the relation is not known a priori.

Let assume the mass diffusivity is linked to the fluctuating concentration according to a linear relation:

$$D(\langle C\rangle+C')\approx D(\langle C\rangle)+\left.\frac{dD}{dC}\right|_{\langle C\rangle}C' \tag{20}$$

Then, assuming

$$\langle D(C)\rangle\approx D(\langle C\rangle) \tag{21}$$

it is obtained

$$D'(C)\approx\left.\frac{dD}{dC}\right|_{\langle C\rangle}C' \tag{22}$$

Considering the following two relations

$$D_1(C)=Ae^{BC} \tag{23}$$

and

$$D_2(C)=\frac{E}{F+C} \tag{24}$$

it can be obtained

$$D_1(C)\approx Ae^{B(C)}+ABe^{B(C)}C'=Ae^{B(C)}(1+BC'), \tag{25}$$

and

$$D_2(C)\approx\frac{E}{F+\langle C\rangle}-\frac{E}{(F+\langle C\rangle)^2}C'=\frac{E}{F+\langle C\rangle}\left(1-\frac{C'}{F+\langle C\rangle}\right) \tag{26}$$

The relative error can be defined as:

$$err=\frac{D_{exact}-D_{approx}}{D_{exact}} \tag{27}$$

Assuming Eq. (23) and substituting C' with C_{rms} the error is given by

$$err_1=\left|1-e^{-BC_{rms}}\left(1+BC_{rms}\right)\right|=\left|1-e^{-\frac{C_{rms}}{\langle C\rangle}B\langle C\rangle}\left(1+\frac{C_{rms}}{\langle C\rangle}B\langle C\rangle\right)\right| \tag{28}$$

which, under the hypothesis of a 25% of turbulence, becomes:

$$err_1=\left|1-e^{-\frac{1}{4}B\langle C\rangle}\left(1+\frac{1}{4}B\langle C\rangle\right)\right| \tag{29}$$

Assuming typical values for B and $\langle C\rangle$, as in [1], average errors lower than 10% can be found.

Assuming Eq. (24) the error is given by

$$err_2=\left|1-\left(\frac{F+\langle C\rangle+C_{rms}}{F+\langle C\rangle}\right)\left(1-\frac{C_{rms}}{F+\langle C\rangle}\right)\right|= \tag{30}$$

$$\left|1-\left(1+\frac{C_{rms}}{F+\langle C\rangle}\right)\left(1-\frac{C_{rms}}{F+\langle C\rangle}\right)\right|=\left|\frac{C_{rms}}{F+\langle C\rangle}\right|^2=\left|\frac{\langle C\rangle}{F+\langle C\rangle}\frac{C_{rms}}{\langle C\rangle}\right|^2$$

which is lower than 6% if the turbulence is 25%

$$err_2=\frac{1}{16}\left|\frac{\langle C\rangle}{F+\langle C\rangle}\right|^2 \tag{31}$$

The term given by Eq. (12) becomes, using Eq. (22)

$$\vec{J}_D=-\langle D'(C)\nabla C'\rangle=-\left.\frac{dD}{dC}\right|_{\langle C\rangle}\nabla\frac{\langle C'C'\rangle}{2} \tag{32}$$

Substitution of Eq. (32) into Eq. (13) gives

$$\frac{D\langle C\rangle}{Dt}=-\nabla\cdot\left(\langle C'\vec{v}'\rangle-\left.\frac{dD}{dC}\right|_{\langle C\rangle}\nabla\frac{\langle C'C'\rangle}{2}-D(\langle C\rangle)\nabla\langle C\rangle\right) \tag{33}$$

which becomes, using Eq. (15):

$$\frac{D}{Dt}\left(\frac{\langle C'C'\rangle}{2}\right)=-\left(\langle\vec{v}'C'\rangle+\left.\frac{dD}{dC}\right|_{\langle C\rangle}\nabla\frac{\langle C'C'\rangle}{2}\right)\nabla\langle C\rangle+$$

$$-\nabla\cdot\left(\langle\vec{v}'\frac{C'C'}{2}\rangle-\left.\frac{dD}{dC}\right|_{\langle C\rangle}\nabla\langle\frac{C'C'C'}{3}\rangle-D(\langle C\rangle)\nabla\frac{\langle C'C'\rangle}{2}-2\left.\frac{dD}{dC}\right|_{\langle C\rangle}\frac{\langle C'C'\rangle}{2}\nabla\langle C\rangle\right)+$$

$$-D(\langle C\rangle)\langle\nabla C'\nabla C'\rangle-\left.\frac{dD}{dC}\right|_{\langle C\rangle}\langle C'\nabla C'\nabla C'\rangle \tag{34}$$

It is then necessary to evaluate the square of the concentration fluctuation, i.e. to solve Eq. (34), in order to solve the average concentration, i.e. Eq. (33). Eq. (34) cannot be solved directly because it contains the cube of the fluctuating concentration and it is then necessary to make assumptions to simplify the average and fluctuating diffusivity.

Assuming

$$\|\langle C\rangle\|>>\|C'\| \tag{35}$$

it is possibile to write

$$\left.\frac{dD}{dC}\right|_{C=\langle C\rangle}\langle C'\nabla\frac{C'C'}{2}\rangle\propto D(\langle C\rangle)\frac{C_{rms}}{\langle C\rangle}\frac{C_{rms}^2}{\delta}\prec D(\langle C\rangle)\nabla\frac{\langle C'C'\rangle}{2}\propto D(\langle C\rangle)\frac{C_{rms}^2}{\delta} \tag{36}$$

and

$$\left.\frac{dD}{dC}\right|_{C=\langle C\rangle}\langle C'\nabla C'\nabla C'\rangle\propto D(\langle C\rangle)\frac{C_{rms}}{\langle C\rangle}\frac{C_{rms}^2}{\delta^2}\prec D(\langle C\rangle)\langle\nabla C'\nabla C'\rangle\propto D(\langle C\rangle)\frac{C_{rms}^2}{\delta^2} \tag{37}$$

Using these approximations it is then possible to write

$$\frac{D\langle C\rangle}{Dt}=-\nabla\cdot\left(\langle C'\vec{v}'\rangle-\left.\frac{dD}{dC}\right|_{C=\langle C\rangle}\nabla\frac{\langle C'C'\rangle}{2}-D(\langle C\rangle)\nabla\langle C\rangle\right) \tag{38}$$

and

$$\frac{D}{Dt}\left(\frac{\langle C'C'\rangle}{2}\right)=-\left(\langle\vec{v}'C'\rangle+\left.\frac{dD}{dC}\right|_{C=\langle C\rangle}\nabla\frac{\langle C'C'\rangle}{2}\right)\nabla\langle C\rangle+$$

$$-\nabla\cdot\left(\langle\vec{v}'\frac{C'C'}{2}\rangle-D(\langle C\rangle)\nabla\frac{\langle C'C'\rangle}{2}-2\left.\frac{dD}{dC}\right|_{C=\langle C\rangle}\frac{\langle C'C'\rangle}{2}\nabla\langle C\rangle\right)+ \tag{39}$$

$$-D(\langle C\rangle)\langle\nabla C'\nabla C'\rangle$$

Using the Boussinesq type relation Eq. (38) becomes

$$\frac{D\langle C\rangle}{Dt}=\nabla\cdot\left(\left(\langle D(C)\rangle+\frac{\nu_C}{\sigma_C}\right)\nabla\langle C\rangle+\left.\frac{dD}{dC}\right|_{C=\langle C\rangle}\nabla\frac{\langle C'C'\rangle}{2}\right) \tag{40}$$

and Eq. (39)

$$\frac{D}{Dt}\left(\frac{\langle C'C'\rangle}{2}\right)=\left(\frac{\nu_C}{\sigma_C}\nabla\langle C\rangle-\left.\frac{dD}{dC}\right|_{C=\langle C\rangle}\nabla\frac{\langle C'C'\rangle}{2}\right)\nabla\langle C\rangle+$$

$$\nabla\cdot\left(\left(\frac{\nu_C}{\sigma_C}+D(\langle C\rangle)\right)\nabla\frac{\langle C'C'\rangle}{2}+2\left.\frac{dD}{dC}\right|_{C=\langle C\rangle}\frac{\langle C'C'\rangle}{2}\nabla\langle C\rangle\right)+ \tag{41}$$

$$-2C_{2,\langle C'C'\rangle}D(\langle C\rangle)\frac{\langle C'C'\rangle}{2}\frac{\varepsilon}{k}$$

In a two dimensional case Eq. (40) becomes:

$$\frac{\partial\langle C\rangle}{\partial t}+U\frac{\partial\langle C\rangle}{\partial x}+V\frac{\partial\langle C\rangle}{\partial y}=$$

$$\frac{\partial}{\partial x}\left(\left(\langle D(C)\rangle+\frac{\nu_C}{\sigma_C}\right)\frac{\partial\langle C\rangle}{\partial x}+\left.\frac{dD}{dC}\right|_{C=\langle C\rangle}\frac{\partial}{\partial x}\left(\frac{\langle C'C'\rangle}{2}\right)\right)+ \tag{42}$$

$$\frac{\partial}{\partial y}\left(\left(\langle D(C)\rangle+\frac{\nu_C}{\sigma_C}\right)\frac{\partial\langle C\rangle}{\partial y}+\left.\frac{dD}{dC}\right|_{C=\langle C\rangle}\frac{\partial}{\partial y}\left(\frac{\langle C'C'\rangle}{2}\right)\right)$$

and Eq. (41)

$$\frac{\partial}{\partial t}\left(\frac{\langle C'C'\rangle}{2}\right)+U\frac{\partial}{\partial x}\left(\frac{\langle C'C'\rangle}{2}\right)+V\frac{\partial}{\partial y}\left(\frac{\langle C'C'\rangle}{2}\right)=$$
$$\left(\frac{\nu_C}{\sigma_C}\frac{\partial\langle C\rangle}{\partial x}-\left.\frac{dD}{dC}\right|_{C=\langle C\rangle}\frac{\partial}{\partial x}\left(\frac{\langle C'C'\rangle}{2}\right)\right)\frac{\partial\langle C\rangle}{\partial x}+$$
$$\left(\frac{\nu_C}{\sigma_C}\frac{\partial\langle C\rangle}{\partial y}-\left.\frac{dD}{dC}\right|_{C=\langle C\rangle}\frac{\partial}{\partial y}\left(\frac{\langle C'C'\rangle}{2}\right)\right)\frac{\partial\langle C\rangle}{\partial y}+ \quad (43)$$
$$\frac{\partial}{\partial x}\left(\left(\frac{\nu_C}{\sigma_C}+D(\langle C\rangle)\right)\frac{\partial}{\partial x}\left(\frac{\langle C'C'\rangle}{2}\right)+2\left.\frac{dD}{dC}\right|_{C=\langle C\rangle}\frac{\langle C'C'\rangle}{2}\frac{\partial\langle C\rangle}{\partial x}\right)+$$
$$\frac{\partial}{\partial x}\left(\left(\frac{\nu_C}{\sigma_C}+D(\langle C\rangle)\right)\frac{\partial}{\partial y}\left(\frac{\langle C'C'\rangle}{2}\right)+2\left.\frac{dD}{dC}\right|_{C=\langle C\rangle}\frac{\langle C'C'\rangle}{2}\frac{\partial\langle C\rangle}{\partial y}\right)+$$
$$-2C_{2,(C'C')}D(\langle C\rangle)\frac{\langle C'C'\rangle}{2}\frac{\varepsilon}{k}$$

where the turbulent kinetic energy is given by

$$\rho\frac{Dk}{Dt}=[T_R]:\langle[D]\rangle+\nabla\cdot\left(\rho\left(\nu+\frac{\nu_T}{\sigma_k}\right)\nabla k\right)-\rho\varepsilon \quad (44)$$

and the energy dissipation by

$$\rho\frac{D\varepsilon}{Dt}=C_{1,\varepsilon}\frac{\varepsilon}{k}[T_R]:\langle[D]\rangle+\nabla\cdot\left(\rho\left(\nu+\frac{\nu_T}{\sigma_\varepsilon}\right)\nabla\varepsilon\right)-\rho C_{2,\varepsilon}\frac{\varepsilon}{k}\varepsilon \quad (45)$$

DISCUSSION ON THE MODEL

The model developed theoretically allows to show the appearance of a new term in the average concentration (Eq. 32) and two new terms in the equation for the square of the fluctuating concentration, which are the following:

$$\left(-\left.\frac{dD}{dC}\right|_{C=\langle C\rangle}\nabla\frac{\langle C'C'\rangle}{2}\right)\nabla\langle C\rangle+\nabla\cdot\left(2\left.\frac{dD}{dC}\right|_{C=\langle C\rangle}\frac{\langle C'C'\rangle}{2}\nabla\langle C\rangle\right) \quad (46)$$

In the average mass flux, Eq. (32), it is possible to observe a decrease or increase of mass transfer depending on the relation between mass diffusivity and concentration. On the basis of the DNS results of Hasegawa [4], it is possible to conclude that if the mass diffusivity increases with the concentration the fluctuating mass flux increases the mass diffusion close to the wall while it decreases the mass diffusion in the rest of the fluid. Furthermore, on the same hypothesis, the fluctuating mass flux decreases the effect of the production term near the wall and increase production term in the rest of the fluid.

On the other hand the new terms of Eq. (46) reduce the production of fluctuating concentration close to the wall. and they increases it in the rest of the fluid, because, on the basis of the DNS results of Hasegawa [4], the gradient of concentration fluctuation is positive near the wall and negative in the rest of the domain.

The diffusive term of the fluctuating concentration depends on the value of the concentration fluctuation producing an increase of the fluctuating concentration which is proportional to the gradient of the average concentration, i.e. it is greater close to the wall. If the mass diffusivity decreases with the concentration the relative considerations are opposite except for the diffusive term in the equation of the fluctuating concentration.

It can be observed that in a general Reynolds transport equation an increase of the mass flux produces an increase in the production of the fluctuating concentration, while in the new term an increase of the mass flux due to fluctuating concentration implies a reduction of the fluctuations themselves.

The two new terms, Eq. (46), seem to have an opposite role from the energetic point of view. It is then difficult to define whether it is a production or a dissipation term because the production term is always positive while the dissipation term is always negative. In conclusion, these terms behave in a case as a production and in an other case as a dissipation term, or, in general, as an increase or a decrease of the production.

The numerical solution of the above mentioned equations requires the solution of an additional equation compared to the case of constant mass diffusivity.

CONCLUSIONS

The present theoretical model has investigated the variation of mass diffusivity with the concentration on the concentration distribution in a fluid in turbulent flow. Starting from the equation of instantaneous mass concentration it has been found that the application of Reynolds-type average with a variable mass diffusivity allow to introduce a new type of term in the average concentration equation and two new types of terms in the fluctuating mass concentration equation.

The mass flux due to the variation of mass diffusivity has been related to the fluctuating mass concentration. The equation for the fluctuating mass concentration has been coupled to the equation of the average mass concentration which can be solved coupled with the turbulent kinetic energy and the dissipation of kinetic energy.

REFERENCES

[1] Crank, J., 1990. The Mathematics of Diffusion. Oxford University Press, London.

[2] Tennekes, H., Lumley, J.L., 1972, A First Course in Turbulence, MIT Press, Cambridge.

[3] Schwertfirm, F., Manhart, M., DNS of passive scalar transport in turbulent channel flow at high Schmidt numbers International Journal of Heat and Fluid Flow, 28 (2007), 1204–1214.

[4] Hasegawa, Y., Kasagi, N., Effects of interfacial velocity boundary condition on turbulent mass transfer at high Schmidt numbers, International Journal of Heat and Fluid Flow, 28 (2007), 1192–1203.

[5] Lin, S. H., Concentration-dependent diffusion of dye in reactive dyeing systems, Journal of Applied Polymer Science, 44 (1992), 10, 1743 – 1749.

[6] Tsunashima, Y., Hashimoto, T., and Nakano, T., First and Second Concentration-Dependent Coefficients of Translational Diffusion and Sedimentation for Poly(R-methylstyrene) in a Good Solvent, Macromolecules, 1996, 29, 3475-3484.

[7] Kuntz, M., Lavall'ee, P., Anomalous diffusion is the rule in concentration-dependent diffusion processes, J. Phys. D: Appl. Phys., 37 (2004) L5–L8.
[8] Bowen, W.R., Williams, P.M., Prediction of the rate of cross-flow ultra filtration of colloids with concentration-dependent diffusion coefficient and viscosity theory and experiment, Chemical Engineering Science, 56 (2001) 3083-3099.
[9] Gorbet, M.B., Sefton, M.V., Biomaterial-associated thrombosis: roles of coagulation factors, complement, platelets and leukocytes, Biomaterials, 25 (2004) 5681–5703.
[10] Gemci, T., Shortall, B., Allen, G.M., Corcoran, T.E., Chigier, N., A CFD study of the throat during aerosol drug delivery using heliox and air, Aerosol Science, 34 (2003) 1175–1192.

Proceedings of the ASME INTERNATIONAL MECHANICAL ENGINEERING CONGRESS AND EXPOSITION
November 13-19, 2009, Lake Buena Vista, Florida, USA

IMECE 2009-10301

THREE-DIMENSIONAL NUMERICAL SIMULATION OF THE FLUID DYNAMICS IN A CORONARY STENT

F. Gori
Department of Mechanical Engineering,
University of Rome "Tor Vergata",
Rome, Italy.

A. Boghi
Department of Mechanical Engineering,
University of Rome "Tor Vergata",
Rome, Italy.

M. Amitrano
Department of Mechanical Engineering,
University of Rome "Tor Vergata",
Rome, Italy.

ABSTRACT

Stents are commonly used to restore blood flow in patients with severe coronary artery disease. Local hemodynamic variables, as wall shear stress, have an important role in the restenosis and their distribution depends on the stent geometry. The objective of the present study is to carry out CFD simulations in a realistic 3D geometry of a coronary stent in physiological conditions. A comparison is performed between two reconstructed stents, made of 12 rings and similar to the real coronary ones, which differ by the position of the struts, where the first type is with closed cells and the second one with open cells. The artery is modeled as a cylinder with rigid walls and the blood is assumed as incompressible Newtonian fluid in laminar flow with constant physical properties. The commercial computational fluid dynamic code FLUENT is used with a mesh composed of non uniform tetrahedrons. The simulations are performed in steady and unsteady state. Wall shear stresses, WSS, as well as its time variations, are investigated in unsteady state with the conclusion that the stent with closed cells have a better fluid dynamic behavior.

INTRODUCTION

Atherosclerosis is one of the most common causes of death in the Western World. Stents are commonly used to restore blood flow in patients with severe coronary artery disease. With the new drug eluting stent the percentage of restenosis has been significantly reduced, [1-4], but the long term percentage of restenosis is similar to the classic stent, [5-6]. Local hemodynamic variables, as wall shear stress, have an important role in the restenosis and their distribution depends on the stent geometry, [7-9].

Previous two-dimensional computational fluid dynamics simulations, 2D-CFD, have used simple stent geometry. Berry et al. [10] investigated the influence of the mesh dimension on the flow with the conclusion that a small mesh can disturb the flow at a larger extent. Lanoye et al. [11] studied the effect of the strut section with the conclusion that a round strut section can disturb the flow at a smaller extent. Seo et al. [12] investigated the influence of the stent design close to the curvatures providing an understanding of the flow in the vicinity of the stent and suggesting strategies for the stent design optimization in order to minimize the flow disturbance.

Some three-dimensional computational fluid dynamics simulations, 3D-CFD, have been carried out on stented arteries. LaDisa et al. [13-18] characterized the best stent design investigating the influence of number, width, thickness and angle of the struts on the flow direction. He at al. [19] studied a realistic strut geometry considering three geometric parameters of the struts and showing that the stent design is very important for the fluid flow in arteries.

The goal of the present study is to reconstruct a realistic 3D geometry of a coronary stent and to carry out 3D-CFD simulations in physiological conditions. A comparison is performed between two reconstructed stents made of 12 rings and similar to the real coronary ones. The two stents differ by the position of the struts, where the first type is with closed cells and the second one with open cells. The artery is modeled as a cylinder with rigid walls and the blood is assumed as incompressible Newtonian fluid in laminar flow with constant physical properties.

GEOMETRY

A real 3D geometry of a coronary stent, made of sequential rings and connected with longitudinal flexible connectors, is considered. Two different connections are investigated: regular peak to peak and mid-strut to mid-strut. The first type of stent is with closed cells and the second one with open cells [20], similarly to the real coronary stents.

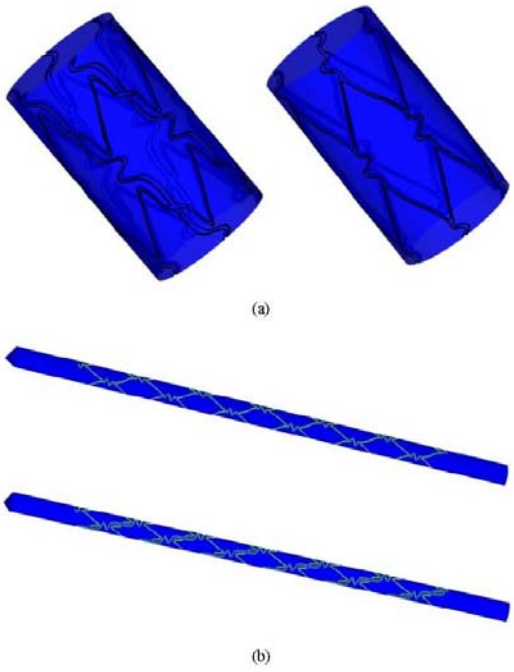

Figure 1 - Reconstruction: complete stents (a), geometries used for the numerical simulations (b).

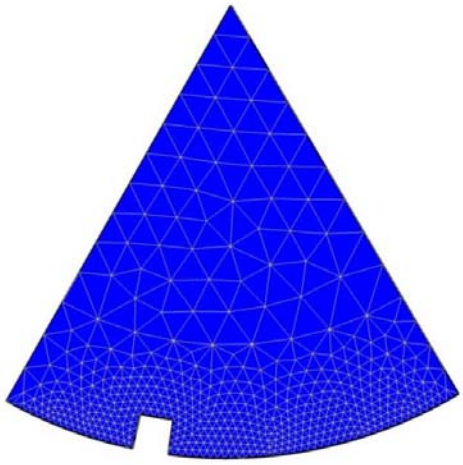

Figure 2 - Mesh.

The software GAMBIT is used for reconstruction and mesh generation. The two complete reconstructed stents are shown in Figure 1a. Only a portion of each stent, i.e. 60° of the cylinder as shown in Figure 1b, is investigated, due to symmetry.

The reconstructed stents are made of 12 rings, the diameter of the artery is 2.6 mm, the width of the stent is 0.1 mm and the total length of the stent is 27.6 mm, in agreement to a stented coronary artery [13] and a real coronary stent [21]. The mesh used, made of non-uniform tetrahedrons, is shown in Figure 2.

The arterial wall is assumed rigid as the stent. The reconstruction is relative to the stent geometry and the cylindrical arterial wall, which becomes a conjugated wall surface, i.e. the union of stent and artery endothelium. It is then possible to treat stent and artery endothelium without difference in some physical properties (e.g. stiffness), due to the non interest of this paper in describing the structural behavior. On the joint wall surface it is then possible to assign the no-slip boundary condition.

GOVERNING EQUATIONS

The blood is modeled as an incompressible Newtonian fluid with constant physical properties in laminar flow within the Reynolds number range, Re=122-440. Under these hypotheses the conservation equations of mass and momentum are respectively:

$$\nabla \cdot \vec{v} = 0 \qquad (1)$$

$$\rho \frac{\partial \vec{v}}{\partial t} + \rho(\vec{v} \cdot \nabla)\vec{v} = -\nabla p + \mu \nabla^2 \vec{v} - \rho \vec{g} \qquad (2)$$

where v is velocity, ρ (1,000 $kg \cdot m^{-3}$) density, p pressure, μ ($0.001\ kg \cdot m^{-1} \cdot s^{-1}$) fluid dynamic viscosity and g gravity.

Equations (1-2) are solved under the boundary conditions of no slip on artery and stent walls, of a prescribed mass flux per unit area (constant or physiologic waveform) on the inlet, and constant pressure on the outlet. On the two lateral surfaces of the cylinder portion the periodic boundary conditions are assumed.

The commercial computational fluid dynamic code FLUENT is used to carry on simulations in steady and unsteady states. In unsteady state the physiological waveform measured by LaDisa et al. [13] in the proximal portion of a left anterior canine descending coronary artery is employed, as shown in Figure 3. The artery diameter is the same as the diameter of the reconstructed artery. The waveform of Figure 3, obtained as the sum of sinusoidal functions, is employed as UDF input in the code. In steady state the mean value of this waveform, i.e. 104.8481 Kg m^{-2} s^{-1}, is employed.

The simulations are carried on using a Core 2 Duo 2.2 GHz Intel Mobile Centrino with 2 GByte of RAM running LINUX. The residuals, defined as the scaled residuals used in a

segregated finite volume solver, for mass and three velocity components are lower than 10^{-6} for all cases after 1000 iterations. In unsteady state the total time investigated (0.8 s) is divided into 800 time steps and 20 iterations are done for each period. In order to obtain residuals smaller than 10^{-5} only the second period is considered.

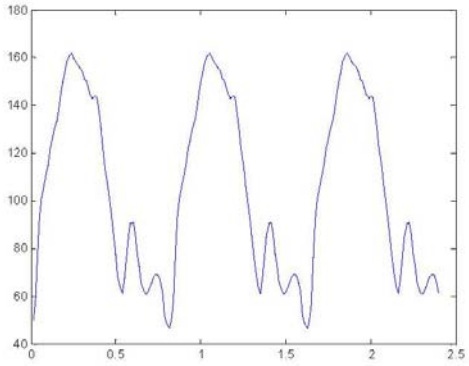

Figure 3 –Physiological inlet waveform: mass flux per unit area (kg m^{-2} s^{-1}) versus time (s).

In agreement to the literature, the most important fluid dynamics parameter is the wall shear stress (WSS), defined, in cylindrical coordinates, as:

$$WSS = \mu \sqrt{\left[\left(\frac{1}{r}\frac{\partial v_r}{\partial \vartheta} + \frac{\partial v_\vartheta}{\partial r} - \frac{v_\vartheta}{r}\right)^2 + \left(\frac{\partial v_r}{\partial z} + \frac{\partial v_z}{\partial r}\right)^2\right]} \qquad (3)$$

where v_r and v_θ are r and θ components of velocity respectively. In agreement to previous studies of the literature the wall shear stress is considered small when is below 0.5 Pa.

RESULTS

MESH INDEPENDENCE

Figure 4 presents the results of three simulations, with different mesh dimensions, in order to show the spatial mesh independence.

The WSS distributions are closer in the two simulations with 768,008 and 1,348,634 tetrahedrons, where the mean values of velocity and pressure are within the third decimal, while the mean values of the simulations with 523,859 tetrahedrons are within the second decimal. The conclusion is that a mesh with 768,008 tetrahedrons is a good compromise.

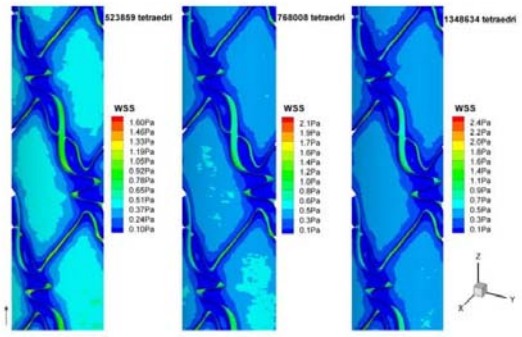

Figure 4 - WSS distribution in three simulations with different mesh dimensions.

STEADY STATE RESULTS

Distributions of WSS are presented in Figure 5 for each investigated stent. Stagnation zones occurred around and between stent struts with lower WSS in both stents, while, far from the struts, regions with higher WSS are present. The nominal diameter of the vessel is reduced on the stent surface producing convergence of the streamlines and higher WSS, while, after the stent strut, higher nominal diameters are present and the diverging streamlines are making lower WSS. The diverging effect is smaller and disappears in one strut diameter, with higher WSS at the center of each repeating stent unit.

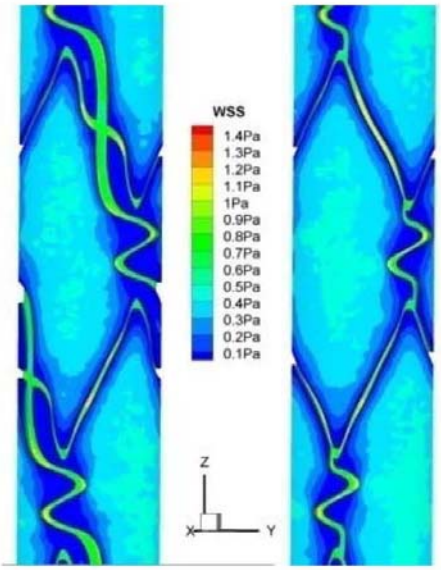

Figure 5 - WSS distributions in steady state.

The highest WSS is present on the stent surface and the lowest one around the stent struts, i.e. in the transition region between vessel and stent. The conclusion is a somewhat large difference between WSS in a small region.

UNSTEADY STATE RESULTS

The unsteady state simulations are performed during two periods of the cardiac cycle and Figure 6 shows six WSS patterns. Velocity increases with pressure and must be zero on stent and wall, due to no slip condition. Inside the duct, velocity increases with the systolic wave which causes an increase in the velocity gradient and in the WSS. The result is that the average WSS on the wall is described by a wave which has the same pattern of the systolic one.

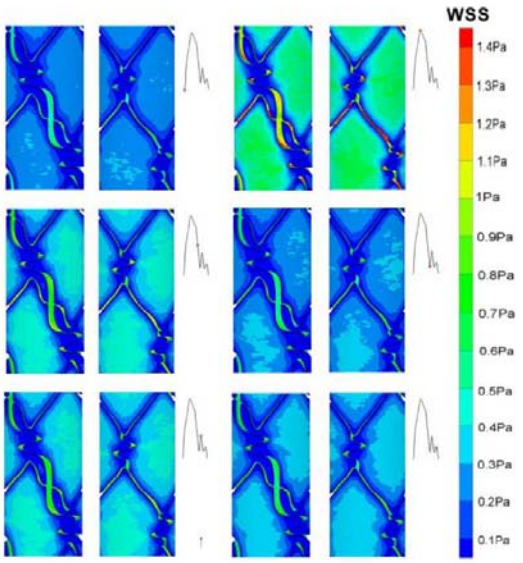

Figure 6 - WSS distributions in unsteady state.

The stent on the wall of the artery behaves as an obstacle from a fluid-dynamics point of view, which is small as compared to the diameter of the vessel but big enough to create a stagnation zone around it. These stagnation zones are present in all cardiac cycles, while their extension decreases with the increase of velocity. The areas around the stent struts present low WSS values for all cardiac cycles because of the stagnation zones while WSS has large variations, during the cycle, close to the vessel wall, where WSS span from 0 to 1.4 Pa.

It is possible to estimate the intra strut areas exposed to low WSS (< 0.5 Pa) during the cardiac cycle. The percent area is defined as the area of the vessel wall exposed to values of WSS lower than the critical value according to

$$percArea(\%) = 100 \frac{\int_{vessel\_wall} \frac{1}{2}\left(1 - \left(\frac{WSS - 0.5}{\|WSS - 0.5\|}\right)\right) dA}{\int_{vessel\_wall} dA} \quad (4)$$

This parameter is evaluated for both stents and all the time steps of the cardiac cycle. The results, presented in Figure 7, show that the stent with closed cells has a smaller percent areas with low WSS.

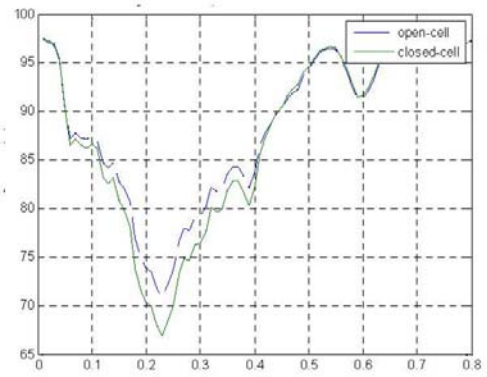

Figure 7 - Percent Area (%),with WSS lower than 0.5 Pa, versus time (s).

DISCUSSION

Physiological values of WSS span between 0.5 Pa and 0.8–1 Pa [7-9]. Values of WSS lower than 0.5 Pa are strongly correlated with endothelial permeability and can promote neo intimal hyperplasia, while values higher than 1 Pa seem to have no relation with neo intimal hyperplasia.

The steady state distribution of WSS in both stents, presented in Figure 5, show that the regions of the vessel wall have a uniform WSS distribution lower than 0.2 Pa. No substantial difference is reported between the two stents but these areas have a larger extension in the stent with transverse struts. The differences in the critical values of both stents are around 3% but most part of the vessel wall is subject to WSS lower than the critical value.

The unsteady state results of Figure 6 show a large variation of WSS during the cardiac cycle. The regions far from the stent have the largest variations while the regions close to the stent present the smallest variations, allowing them to be exposed permanently to critical low WSS values.

CONCLUSIONS

The evidence of the fluid dynamics wall shear stress involved in restenosis can support the importance of the hemodynamic behavior in the choice of a stent.

Two real stents with different design, used as drug eluting stent in the clinic practice, are investigated in steady and unsteady state with 3D-CFD simulations in order to study their fluid dynamics behavior. Numerical simulations show the presence of regions, close to the stent, where WSS is lower than the critical value. Unsteady simulations showed large differences between instantaneous and mean WSS values.

The comparisons of the WSS and the percent area of the two stents allow concluding that the stent with struts parallel to the mean flow has a better fluid dynamic behavior compared to the stent with transverse struts.

ACKNOWLEDGEMENTS

The authors thank Prof. F. Romeo for the helpful discussions about cardiological problems of stent and Dr. Clementi for the stents.

REFERENCES

[1] M. C. Morice, P. W. Serruys , J. E. Sousa, J. Fajadet, E. Ban Hayashi, "A randomized comparison of a sirolimus-eluting stent with a standard stent for coronary revascularization", New Eng. J. Med. 346(23): 1773-1780, 2002.

[2] J. W. Moses, M. B. Leon, J. J. Popma, P. J. Fitzgerald, D. R. Holmes, "Sirolimus-eluting stents versus standard stents in patients with stenosis in a native coronary artery", New Engl. J. Med. 349(14): 1315-1323, 2003.

[3] E. Schampaert, E. A. Cohen, M. Schluter, "The Canadian study of the sirolimus-eluting stent in the treatment of patients with long de novo lesions in small native coronary arteries (C-SIRIUS)", J. Am. Coll. Cardiol. 43: 1110-1115, 2004.

[4] M. Schofer, A. H. Gershlick, "Sirolimus-eluting stents for treatment of patients with long atherosclerotic lesions in small coronary arteries: double-bind, randomized controlled trial", Lancet 362: 1093-1099, 2003.

[5] J. C. Palmaz, "Intravascular stents in the last and the next 10 years", J. Endovasc. Ther. Suppl. 2, 200-206, 2004.

[6] R. Virmani, A. Farb, G. Guagliumi, F. D. Kolodgie, "Drug-eluting stents: caution and concerns for long-term outcome", Cor. Artery Dis. 15: 313-318, 2004.

[7] D. N. Ku, D. P. Giddens, C. K. Zarins, S. Glagov, "Pulsatile flow and atherosclerosis in the human carotid bifurcation. Positive correlation between plaque location and low oscillating shear stress", Arteriosclerosis 5: 293-302, 1985.

[8] D. N. Ku, "Blood flow in arteries", Ann. Rev. Fluid Mech. 29: 399-434, 1997.

[9] A. M. Malek, S. L. Alper, S. Izumo, "Hemodynamic shear stress and its role in atherosclerosis", JAMA 282: 2035-2042, 1999.

[10] J. L. Berry, A. Santamarina, J. E. Jr. Moore, S. Roychowdhury, W. D. Routh, "Experimental and computational flow evaluation of coronary stents", Ann. Biomed. Eng. 28(4): 386-98, 2000.

[11] L. Lanoye, M. De Beule, C. Dewijngaert, P. Segers, R. Van Impe, P. Verdonck, "The influence of the strut section shape on the flow field in a newly stented right coronary artery", NCTAM2006, 2006.

[12] T. Seo, L. G. Schachter and Abdul I. Barakat, "Computational Study of Fluid Mechanical Disturbance Induced by Endovascular Stents", Ann. of Bio. Eng. 33, 4, 444-456, 2005.

[13] J. F. LaDisa Jr., D. A. Hettrick, L. E. Olson, I. Guler, E. R. Gross, T. T. Kress et al. "Coronary stent implantation alters coronary artery hemodynamics and wall shear stress during maximal vasodilation", Jour. of App. Phys., 93: 1939-1946, 2002.

[14] J. F. LaDisa Jr., I. Guler, L. E. Olson, D. A. Hettrick, J. R. Kersten, D. C. Warltier et al. "Three dimensional computational fluid dynamics modeling of alterations in coronary artery wall shear stress produced by stent implantation", Ann. Biomed. Eng. 31: 972-980, 2003.

[15] J. F. LaDisa Jr, L. E. Olson, I. Guler, D. A. Hettrick, S. H. Audi, "Stent design properties and deployment ratio influence indexes of wall shear stress: a three dimensional computational fluid dynamics investigation within a normal artery", Jour. of App. Phys. 97(1): 424-30, 2004.

[16] J. F. LaDisa Jr., L. E. Olson, D. A. Hettrick, D. C. Warltier, J. R. Kersten and P. S. Pagel, "Axial stent strut angle influences wall shear stress after stent implantation: analysis using 3D computational fluid dynamics models of stent foreshortening", BioMed. Eng. On Line. 4: 59, 2005.

[17] J. F. LaDisa Jr., L. E. Olson, I. Guler, D. A. Hettrick, J. R. Kersten, D. C. Warltier et al. "Circumferential vascular deformation after stent implantation alters wall shear stress evaluated with time-dependent 3D computational fluid dynamics models", Jour. of App. Phys.. 98: 947-957, 2005.

[18] J. F. LaDisa Jr., L. E. Olson, D. A. Hettrick, D. C. Warltier, J. Kersten, P. Pagel, "Alterations in regional vascular geometry produced by theoretical stent implantation influence distributions of wall shear stress: analysis of a curved coronary artery using 3D computational fluid dynamics modeling", BioMed. Eng. On Line. 5: 40, 2006.

[19] Y. He, N. Duraiswamy, A. O. Frank, J. E. Moore Jr., "Blood Flow in Stented Arteries: A Parametric Comparison of Strut Design Patterns in Three Dimensions", Jour. of Biomech. Eng.. 127: 637-647, 2005.

[20] D. Stoeckel, C. Bonsignore, S. Duda, "A survey of stent designs", Min. Invas. Ther. & Allied Technol. 11: 137-147, 2002.

[21] A. Kastrati, J. Mehilli, J. Dirschinger, J. Pache, K. Ulm, H. Schühlen et al., "Restenosis after coronary placement of various stent types", Am. J. Cardiol. 87(1): 34-39, 2001.

Proceedings of the ASME INTERNATIONAL MECHANICAL ENGINEERING CONGRESS AND EXPOSITION
November 13-19, 2009, Lake Buena Vista, Florida, USA

IMECE 2009-10302

IMAGE-BASED COMPUTATIONAL FLUID DYNAMICS IN A CAROTID ARTERY

F. Gori
Department of Mechanical Engineering,
University of Rome "Tor Vergata",
Rome, Italy.

A. Boghi
Department of Mechanical Engineering,
University of Rome "Tor Vergata",
Rome, Italy.

ABSTRACT

Literature presents numerical simulations on image-based geometry where blood is treated as a Newtonian fluid, while others simulations assumed a non-Newtonian blood with two or three-dimensional axisymmetric geometry. The present work investigates the non-Newtonian behavior of a pulsating blood flow through a stenosed carotid artery, realistically reconstructed with the patient-specific geometry of a 60 years old man with an intimal thickening of 90% degree of stenosis. Lumen boundary contours are segmented using commercial image-processing software AMIRA for a 3D geometry reconstruction. High-quality tetrahedral mesh is generated using commercial mesh-generator code GAMBIT. The 3-D unsteady incompressible Navier-Stokes equations are solved using the commercial finite volume code FLUENT. The boundary condition is assumed from a flow-rate-wave of the literature using the FFT method and imposing a pressure sinusoidal signal with 20 harmonics.

INTRODUCTION

Atherosclerotic cardiovascular disease is a leading cause of morbidity in the industrialized world. A body of evidence suggests a correlation between atherosclerosis, regions of low blood flow velocity, rotational flow and low shear stress near arteries walls [1-2]. The image-based CFD modeling is the only mean of reconstructing the local hemodynamic conditions in a patient-specific manner, with medical imaging used to provide patient-specific boundary conditions, since accurate measurements of interested quantities, as shear stress, are difficult to make *in vivo*. Image-based CFD studies of hemodynamic are possible with high-resolution medical imaging, sophisticated image processing techniques and high-performance desktop workstations.

Some studies [3-5] were carried out on the carotid artery bifurcation, while flow patterns, predicted by CFD [6], were compared with the image data from a rigid flow-through phantom of a carotid artery with 65% degree stenosis. Johnston et al. [7] studied transient pulsatile blood flow through four different right coronary arteries, reconstructed from biplane angiograms.

Newtonian fluid model was mostly used to study the wall shear stress in the artery over the entire cardiac cycle. Newtonian fluid is a reasonably good approximation to study wall shear stress distribution in transient blood flow in arteries. Significant inter-individual variations in the steady state wall shear stress were important only at low inlet velocities, among different rheological models [8]. Different conclusions were found in a numerical and experimental study, [9], which investigated the non-Newtonian behavior on the velocity distribution in the unsteady entry flow of a 90° curved tube. A Carreau-Yasuda model was employed to accommodate the shear thinning behavior of the Xanthan gum solution showing significant differences between Newtonian and non-Newtonian models. Ishikawa et al. [10] investigated the periodic, incompressible and axisymmetric blood flow through a stenosed tube showing the non-Newtonian properties of blood have considerable influence on the flow. Tu and Deville [11] studied the blood flow, through stenoses in a rigid circular tube with a partial occlusion, using the incompressible generalized Newtonian model, incorporating Herschel-Bulkley, Bingham and power-law fluids. Computations showed the model affects the flow as compared to the Newtonian case. The investigation of Hyun et al. [12] was based on the surgical reconstruction of a diseased artery with the methodology of "virtual prototyping" to design external carotid artery. The goal of the work was the understanding of the hemodynamics of a Casson model blood in various geometries of improved surgical reconstruction.

The present work is aimed to couple the realistic reconstruction of a patient-specific geometry with the non-Newtonian model of blood in a carotid artery. Lumen boundary contours are segmented using the commercial image-processing software AMIRA for a 3D geometry reconstruction. High-quality tetrahedral mesh is employed using the commercial mesh-generator code GAMBIT. The 3-D unsteady,

incompressible Navier-Stokes equations are solved with the commercial finite volume code FLUENT using the Casson model to describe the non-Newtonian behavior of blood.

MODEL RECONSTRUCTION

The vessel of a man, 60 years old and with intimal thickening 90% degree of stenosis, is investigated with the acquisition of 120 contiguous 0.5 mm thick two-dimensional slices data from CT. The three-dimensional geometry is created by surfaces of the same color brightness to depict the carotid arterial wall using the commercial visualization software AMIRA.

The vessel diameters are: 7.82 mm for the Common Carotid Artery (CCA); 6.139 mm for the Anterior External Carotid Artery (AECA); 2.822 mm for the Posterior External Carotid Artery (PECA); 6.95 mm for the Internal Carotid Artery (ICA). After extraction of geometrical information, each slice is stacked up vertically in order to construct a three dimensional geometry with the surfaces made of the same color brightness. The images are processed automatically setting a threshold value for soft-tissue and manually removing artifacts. The threshold value does not allow differentiating among the body tissues because they are all "soft", except the skeletal one, requiring great attention to the segmentation process.

The result of the procedure is shown in Figure 1 where the stenosis corresponds to a 90% area reduction. The image-processor software generates an STL data file, with triangular elements, which is imported into the commercial mesh-generator code GAMBIT. The smoothing operations are performed on GAMBIT in order to make the surface continuous and regular, which includes eliminating singularities, spikes and filling the holes. A high-quality tetrahedral mesh with over four millions elements is generated.

BOUNDARY CONDITIONS

The flow-rate-wave, employed to determine the inlet flow conditions, was reconstructed from the literature data [13], and each data vector, containing the values of the flow-rate-wave, corresponds to a different instant of time. The application of the FFT to this data vector allows obtaining a complex vector of the Fourier coefficients, which is periodic because the input signal is discrete. The second half of the Fourier coefficients is set equal to zero to avoid aliasing and only the first half is used to generate the harmonic signal versus time, imposing on the inlet of CCA a flow-rate composed of 10 harmonics wave.

The waveform is shown in Figure 2. The boundary condition of no-slip on the vessel wall is a realistic assumption near the plaque because the calcium makes the plaque rigid. In a normal carotid artery the subdivision of the flow is 65% of flow in ICA and 35% in ECA, but the percentage of stenosis reduces this flow-rate distribution. A constant flow division between ICA and ECA is kept during the cardiac cycle, assuming 58% for ICA, 28.77% for AECA and 13.23% for PECA. Simulations under pulsatile flow conditions are carried out for 2 cardiac cycles.

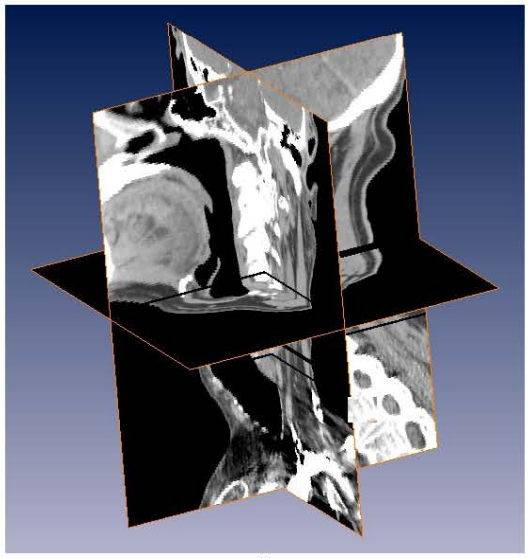

(a)

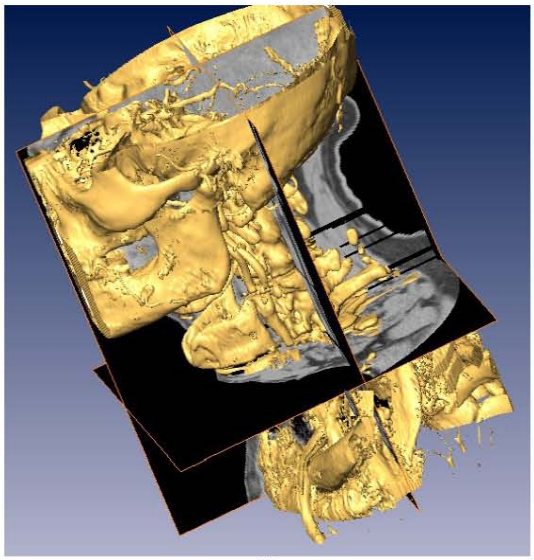

(b)

Figure1 - Reconstruction with AMIRA of the geometrical model:
(a) three-dimensional view of the assembled slices.
(b) creation of the iso-surfaces.

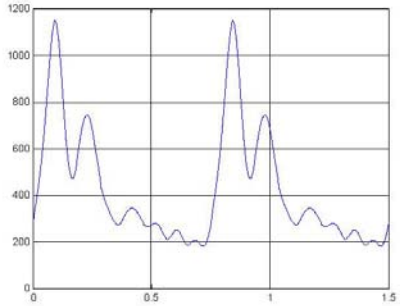

Figure 2: Flow-rate- wave (ml/min) versus time (s) used in the computations.

NUMERICAL METHODS

The incompressible Navier–Stokes equations are solved numerically with the finite-volume software FLUENT. A second-order upwind differential scheme is used for spatial discretization and a second order implicit scheme for time. A segregated, implicit solver is used to solve continuity and momentum equations. The SIMPLE algorithm of Patankar [14] is employed as the pressure–velocity coupling algorithm. The iteration steps are repeated until convergence, using the residual amplitude criterion of 10^{-6}. The steady-state solution is used as initial condition for the pulsatile simulation. The flow-rate-wave is implemented in FLUENT as boundary condition through the UDF.

The equations to be solved are

$$\nabla \cdot \vec{v} = 0 \tag{1}$$

$$\rho \frac{D\vec{v}}{Dt} = -\nabla p + \nabla \cdot \left(2\mu(\dot{\gamma})[D]\right) \tag{2}$$

where,

$$[D] = \frac{\left([\nabla \vec{v}] + {}^{t}[\nabla \vec{v}]\right)}{2} \tag{3}$$

is the rate of strain tensor and

$$\dot{\gamma} = \sqrt{2[D]:[D]} \tag{4}$$

is the shear rate.

In a non-Newtonian fluid the viscosity is function of the shear rate and Eq. (2) can be written in the GNF form derived from Reiner and Rivlin. The blood viscosity depends on the plasma viscosity with a complex relation to the hematocrit. In this work, the non-Newtonian viscosity is modeled with the Casson relation

$$\mu(\dot{\gamma}) = \left(\mu_\infty + 2\frac{\sqrt{\tau_0 \mu_\infty}}{\sqrt{\dot{\gamma}}} + \frac{\tau_0}{\dot{\gamma}}\right) \tag{5}$$

where τ_0 is the yield stress and μ_∞ the asymptotic Newtonian viscosity, both function of hematocrit for blood. The difficulty of using the Casson model in a numerical scheme lies in its discontinuous character to the limit of zero shear rate. This discontinuity is solved using the regularization technique proposed in [15]:

$$\mu(\dot{\gamma}) = \left(\mu_\infty + 2\frac{\sqrt{\tau_0 \mu_\infty}}{\sqrt{\dot{\gamma}}}\left(1 - e^{-\sqrt{m\dot{\gamma}}}\right) + \frac{\tau_0}{\dot{\gamma}}\left(1 - e^{-\sqrt{m\dot{\gamma}}}\right)^2\right) \tag{6}$$

When shear rate approaches zero it is obtained the expression

$$\mu(0) = \left(\mu_\infty + 2\sqrt{m\tau_0 \mu_\infty} + m\tau_0\right) \tag{7}$$

where m is the Casson viscosity regularization exponent, usually assumed as 1. According to [15] and [16] the parameters of interest for our patient are $\tau_0 = 0.01$ Pa, $\mu_\infty = 0.00333$ $Pa\ s$. The Casson viscosity model is introduced in FLUENT thorough UDF.

The variation of viscosity with the shear rate is presented in Figure 3.

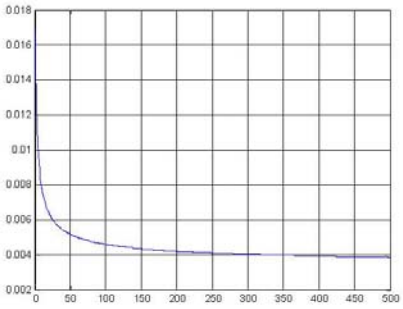

Figure3 – Casson viscosity (Pa*s) versus shear rate(1/s).

A density of 1,060 $kg \cdot m^{-3}$ and a viscosity of 0.0436 $kg \cdot m^{-1} \cdot s^{-1}$, corresponding to the mean Casson viscosity for the Newtonian case, is assumed. Each cardiac cycle requires approximately 20 hours of CPU time on a 4 processors unit.

RESULTS

Transient simulations are performed for each rheological model from 0 to 1.5 s, including two periods of systolic wave. A typical WSS pattern for a Newtonian fluid is shown in Figure 4 after 0.825 seconds. A cyclic pattern of WSS is obtained, with the presence of a depression after the maximum and a uniform WSS decrease, letting the moderate WSS regions become patches of low WSS. Downstream the stenosis ICA and CCA show low WSS values at all times.

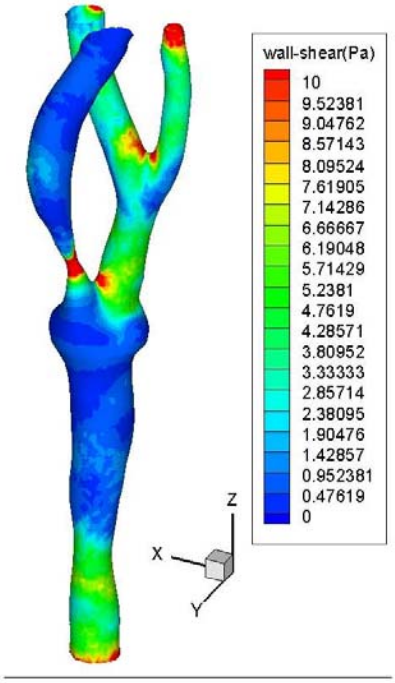

Figure 4: WSS distribution at t=0.825s for a Newtonian fluid.

The numerical simulation for a Casson fluid is presented in Figure 5 which presents the highest values of WSS, ranging from 0.5 to 0.9 *Pa* higher than for a Newtonian fluid. The importance of the non-Newtonian behavior is assessed by the average WSS over plaque and wall.

Figures 4 and 5 are similar from the qualitative point of view but the main differences are present in the regions with low WSS values. Due to the difficulty of quantifying the differences between Figures 4 and 5, some scalar indices are introduced for Newtonian and Casson fluids, on the wall and on the plaque,

$$WSS_{N,w}(t) = \frac{1}{A_{wall}} \int_{A_{wall}} WSS_N(x,y,z,t)\,dA \quad (8)$$

$$WSS_{C,w}(t) = \frac{1}{A_{wall}} \int_{A_{wall}} WSS_C(x,y,z,t)\,dA \quad (9)$$

$$WSS_{N,p}(t) = \frac{1}{A_{plaque}} \int_{A_{plaque}} WSS_N(x,y,z,t)\,dA \quad (10)$$

$$WSS_{C,p}(t) = \frac{1}{A_{plaque}} \int_{A_{plaque}} WSS_C(x,y,z,t)\,dA \quad (11)$$

The following parameters are introduced in order to evaluate the influence of the non-Newtonian behavior:

$$err_{rel,w}(t) = 1 - \frac{WSS_{N,w}(t)}{WSS_{C,w}(t)} \quad (12)$$

$$err_{rel,p}(t) = 1 - \frac{WSS_{N,p}(t)}{WSS_{C,p}(t)} \quad (13)$$

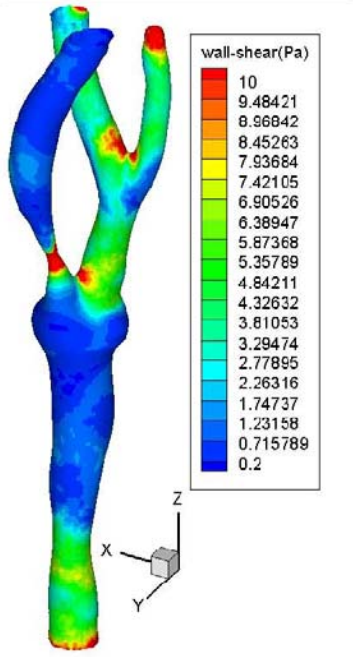

(b)

Figure 5: WSS distribution at t=0.825 s for a Casson fluid.

Equations (12-13) define two indexes (called error) which are relative to wall and plaque. The absolute error on the plaque is in the range of 0.1 - 0.9 *Pa* and that on the wall in the range of 0.24 - 0.06 *Pa*. Despite these low values, it must be remembered that physiological values of WSS are of the order of magnitude of 1 *Pa* and that the WSS scale is shifted towards high values, due to the presence of the plaque. The maximum differences are present where the WSS is maximum and the minimum values where is minimum.

As far as the error indexes are concerned the following considerations can be made. Figure 6 presents error indexes in the range of 3.5 - 10.5 % for the plaque and of 7 – 24 % for the wall. Moreover, it must be pointed out that the maximum values of the error indexes are present where is present the minimum flow rate of the cycle.

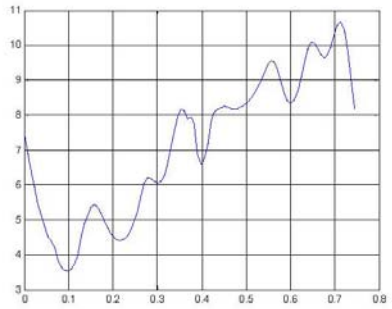

(a)

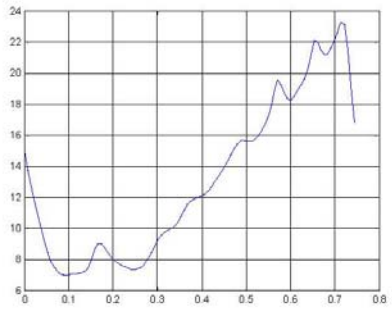

(b)

Figure 6: Error index (%) versus time (s): on stenosis (a), on wall (b).

DISCUSSION

The difference between Newtonian and non-Newtonian model of the blood is not very high as far as the wall shear stress is concerned, may be because the shear rate is significantly high in the entire cardiac cycle, in agreement with Johnston et al. [8].

The carotid artery has medium dimensions where the velocity is relatively high and the transient analysis is important because the WSS pattern changes during the cycle. Johnston et al. [7] suggested that a non-Newtonian behavior can be significant only where the blood flow is quite slow. The present results are in agreement to this conclusion in terms of error index (Figure 6). Indeed, the WSS in a Casson fluid is inversely proportional to the shear rate and the viscosity decreases to the constant value of a Newtonian fluid. On the other hand, if the shear rate is low the WSS is higher than that of a Newtonian fluid.

The shear rate increases with the flow rate inside a rigid duct, while a decrease in the flow rate reduces the shear rate and the WSS of Casson fluid increases. Then, the greater difference between Newtonian and non-Newtonian modeling is present in this phase of the cycle. Moreover, the shear rate is function of geometry and the shear rate is higher where the duct diameter is smaller whereas is smaller where the diameter is higher. On the stenosis the velocity is high in the small area and the shear rate is high, especially at the maximum flow rate. In this phase the error index on the plaque is about 3.5-5.5%. If the flow rate decreases on the plaque also the shear rate decreases but, due to the small area, the shear rate is always moderately high, leading to an error index of 9.5%. Then, the lowest difference between Newtonian and non-Newtonian fluid is present on the plaque.

In the rest of the duct, the diameter is higher than on the stenosis, and, due to mass conservation, the velocity is also smaller, reducing the shear rate, with a larger difference between Newtonian and Casson fluid. The shear rate is higher in the cycle phase where the flow rate is higher leading to less marked differences, with an error index of 10%, compared to the value of 23% where the flow rate is smaller.

CONCLUSIONS

The present paper presents a transient study of blood flow in a rigid carotid artery with two blood models, i.e. Newtonian and non-Newtonian Casson fluid. The two WSS distributions have complex patterns on the artery wall during the cardiac cycle, but low wall shear stress is prevalent on the Common Carotid Artery and downstream the stenosis for all arteries. High WSS values are present on the stenosis and on the bifurcation point while average WSS values are present on the External Carotid Artery. The WSS is small during the major part of the cardiac cycle. The conclusions are based on the simulation of a heart rate of 60 beats per minute.

One conclusion of the paper is that a Newtonian model for blood is acceptable where is present a severe stenosis while, in a less severe stenosis, the shear rate is much smaller and the differences between Newtonian and Casson models can be significant.

The investigation of the wall shear stress can be carried on with a Newtonian model enough accurately but, in

order to study the flow in more detail as, for example, to investigate the mixing within the blood or the stresses on individual blood cells (haemolysis), a non-Newtonian model of blood is necessary.

REFERENCES

[1] D. N. Ku, "Blood Flow in Arteries", Annu Rev Fluid Mech, 01/1997.

[2] C. G. Caro, "Vascular fluid dynamics and vascular biology and Disease", Math Meth Appl Sci 24: 1311–1324. 2001.

[3] D. A. Steinman, J. B. Thomas, H. M. Ladak, J. S. Milner, B. K. Rutt, and J. D. Spence "Reconstruction of Carotid Bifurcation Hemodynamic and Wall Thickness Using Computational Fluid Dynamics and MRI", Magn Reson Med 47:149–159 (2002).

[4] J. B. Thomas, J. S. Milner, B. K. Rutt and D. A. Steinman, "Reproducibility of Image-Based Computational Fluid Dynamics Models of the Human Carotid Bifurcation", Ann Biomed Eng, 31: 132–141, 2003.

[5] M. D. Ford, G. R. Stuhne, H. N. Nikolov, D. F. Habets, S. P. Lownie, D. W. Holdsworth, and D. A. Steinman, "Virtual Angiography for Visualization and Validation of Computational Models of Aneurysm Hemodynamics", IEEE Trans Med Imaging, 24, 12, 2005.

[6] J. R. Cebral, P. J. Yim, R. Lohner, O. Soto, H. Marcos, P. L. Choyke, "New methods for computational fluid dynamics modeling of carotid artery from magnetic resonance angiography", Proc. SPIE, 4321, 177-87, 2001.

[7] B. M. Johnston, P. R. Johnston, S. Corney, D. Kilpatrick "Non-Newtonian blood flow in human right coronary arteries: Transient Simulations", J. Biomech, 39, 6, 1116-28, 2006.

[8] B. M. Johnston, P. R. Johnston, S. Corney and D. Kilpatrick, "Non-Newtonian blood flow in human right coronary arteries: steady state simulations", J. Biomech 37 (5), 709–720, 2004.

[9] F. J. H. Gijsen, E. Allanic, F. N. Van De Vosse, J. D. Janssen, "The influence of the non-Newtonian properties of blood on the flow in large arteries: Unsteady flow in a 90curved tube", J. Biomech, 32, 7, 705-713, 1999.

[10] T. Ishikawa, L. F. R. Guimaraes, S. Oshima, R. Yamanae, "Effect of Non-Newtonian property of blood on flow through a stenosed tube", Fluid Dynamics Research, 22: 251-264, 1998.

[11] C. Tu and M. Deville, "Pulsatile flow of Non-Newtonian fluids through arterial stenoses", J. Biomech, 29, 7, 899-908, 1996.

[12] S. Hyun, C. Kleinstreurer, P.W. Longest and C. Chen, "Particle-Hemodynamic Simulations and Design Options for Surgical Reconstruction of Diseased Carotid Artery Bifurcations", J Biomech Eng, 126, 188-195, 2004.

[13] S. E. Lee, S.-W. Lee, P. F. Fischer, H. S. Bassiouny, F. Loth, "Direct numerical simulation of transitional flow in a stenosed carotid bifurcation", J. Biomech, 41:2551–2561, 2008.

[14] S. V. Patankar, "Numerical Heat Transfer & Fluid Flow", Hemisphere, 1980.

[15] K. Mukundakrishnan, P. S. Ayyaswamy and D. M. Eckmann, "Finite-sized gas bubble motion in a blood vessel: Non-Newtonian effects", Phys. Rev. E 78, 036303, 2008.

[16] M. Sharan and A. S. Popel, "A two-phase model for flow of blood in narrow tubes with increased effective viscosity near the wall", Biorheology, 38, 415, 2001.

ASME-ATI-UIT 2010 Conference on Thermal and Environmental Issues in Energy Systems
16 – 19 May, 2010, Sorrento, Italy

RANS MODELLING OF A NEW TURBULENT ENERGY EQUATION WITH VARIABLE AND FLUCTUATING THERMAL CONDUCTIVITY

F. Gori*, A. Boghi*

**University of Rome Tor Vergata", Dept. of Mechanical Engineering,*
Via del Politecnico 1, 00133 Rome ITALY phone: +390672597129; fax: +390672597129;
e-mail: gori@uniroma2.it, boghi@ing.uniroma2.it

ABSTRACT

This work presents numerical results for turbulent flow of a fluid with variable and fluctuating thermal conductivity. The equations solved numerically are the classical ones for the mean motion, i.e. mass conservation, turbulent kinetic energy and dissipation rate, and the new energy conservation equation. This new energy equation, obtained with mathematical and physical considerations in [1], contains a new term for heat flux due to the variation of thermal conductivity, i.e. the product of the square of fluctuating temperature and the temperature gradient of thermal conductivity. This new heat flux term, obtained in conservative form, transfers energy from large to small scales of turbulence. The present model, to be considered as a new three-equation-RANS model, has never been proposed before in the classical RANS modelling. The aim of the present paper is to investigate the influence of Prandtl number in the two-dimensional turbulent flow between parallel plates.

Introduction

Fluids used as cooler in thermal power plants span in a very wide spectrum of Prandtl numbers, e.g. from liquid metals (low Prandtl) to molten salts (high Prandtl). One of the latest approaches in the heat transfer modelling by using the analogy between momentum transport and heat transfer [2] produced large scatter between experimental data and empirical predictions, due to the scale separation between momentum and heat transfer [3]. Different values of the turbulent Prandtl number were proposed by several investigators and several models are reviewed in [4]. The use of molten salts in nuclear and solar power plants has been the subject of several papers [5-9].

A DNS approach to investigate high [10] and low to medium [11] Prandtl number fluids suggested that temperature fluctuations are high in fluids with high Prandtl number because the smallest scale of the temperature fluctuation is inversely proportional to the square root of the molecular Prandtl number, which means that the temperature fluctuations increase with the Prandtl number [3]. Among the fluids with high Prandtl number, a special importance is given to non-Newtonian fluids, which present a reduction in heat transfer, as shown in a recent DNS study [12].

Besides temperature fluctuations, it is important to recall the importance of the variation of fluid properties with temperature, mainly considered in laminar flow. Only few works investigated variable fluid properties in turbulent flow [13-15]. The problem has been recently studied with a model based on Reynolds stresses [16-19].

A common approach is to derive the conservation equations with the assumption of constant physical properties and later on to introduce temperature dependence. In a previous work of the present authors [1], the turbulent energy equation has been studied with variable and fluctuating thermal conductivity. A new term appears in the turbulent energy equation, besides the Reynolds ones, which transfers energy from large scales of turbulence to small ones. The new term is due to the product of the fluctuation of thermal conductivity and the gradient of temperature variance. The present authors proposed a closure for the new term, obtaining a system of equations where is necessary to solve one more equation, i.e. the equation for the temperature variance, in order to obtain the correct thermal field.

The aim of the present work is to solve numerically the system of equations, derived in [1], with a RANS model. The system of equations is comprehensive of the classical equations for the mean motion, i.e. turbulent kinetic energy and dissipation rate, mass and energy conservation, including the new terms of fluctuating thermal conductivity.

The new equation, derived for the transport of temperature variance, has never been used before in the classical RANS modelling but is necessary to calculate the new fluctuating thermal conductivity terms of the present model. The presence of the equation of temperature variance makes this model a three-equation-RANS model. Thermal conductivity is relative to fluids with Prandtl number spanning from low to high values because, as remarked in [1], great differences are expected for the extreme Prandtl number fluids.

Equations

The equations to be solved are the following. The continuity equation

$$\frac{\partial U_i^+}{\partial x_i^+} = 0 \tag{1}$$

The momentum equation

$$\frac{\partial U_j^+}{\partial t^+} + U_i^+ \frac{\partial U_j^+}{\partial x_i^+} = -\frac{\partial P^+}{\partial x_j^+} - \frac{2}{3}\frac{\partial k^+}{\partial x_j^+} + \frac{\partial}{\partial x_i^+}\left(2\left(1+\nu_T^+\right)S_{ij}^+\right) \tag{2}$$

The equation for turbulent kinetic energy

$$\frac{\partial k^+}{\partial t^+} + U_i^+ \frac{\partial k^+}{\partial x_i^+} = 2\nu_T^+ S_{ij}^+ S_{ij}^+ + \frac{\partial}{\partial x_i^+}\left(\left(1+\frac{\nu_T^+}{\sigma_k}\right)\frac{\partial k^+}{\partial x_i^+}\right) - \varepsilon^+ \tag{3}$$

The equation for turbulent dissipation rate

$$\frac{\partial \varepsilon^+}{\partial t^+} + U_i^+ \frac{\partial \varepsilon^+}{\partial x_i^+} = C_{1,\varepsilon} f_{1,\varepsilon} \frac{\varepsilon^+}{k^+} 2\nu_T^+ S_{ij}^+ S_{ij}^+ + \frac{\partial}{\partial x_i^+}\left(\left(1+\frac{\nu_T^+}{\sigma_\varepsilon}\right)\frac{\partial \varepsilon^+}{\partial x_i^+}\right) - C_{2,\varepsilon} f_{2,\varepsilon} \frac{\varepsilon^+}{k^+}\varepsilon^+ \tag{4}$$

The equation for energy conservation (or mean temperature equation)

$$\frac{\partial \Theta^+}{\partial t^+} + U_i^+ \frac{\partial \Theta^+}{\partial x_i^+} = \frac{\partial}{\partial x_i^+}\left(\left(\frac{1}{\mathrm{Pr}}\lambda^+\left(\Theta^+\right)+\frac{\nu_T^+}{\sigma_T}\right)\frac{\partial \Theta^+}{\partial x_i^+}\right) + \frac{\partial}{\partial x_i^+}\left(\frac{1}{\mathrm{Pr}}\frac{d\lambda^+}{d\Theta^+}\frac{\partial}{\partial x_i^+}\left(\frac{\theta^+\theta^+}{2}\right)\right) \tag{5}$$

where is present the new term for heat flux, q_λ^+, due to the variation of thermal conductivity,

$$q_\lambda^+ = -\frac{1}{\mathrm{Pr}}\frac{d\lambda^+}{d\Theta^+}\frac{\partial}{\partial x_i^+}\left(\frac{\theta^+\theta^+}{2}\right) \tag{6}$$

The equation for temperature variance

$$\frac{\partial}{\partial t^+}\left(\frac{\theta^+\theta^+}{2}\right) + U_i^+ \frac{\partial}{\partial x_i^+}\left(\frac{\theta^+\theta^+}{2}\right) = \frac{\nu_T^+}{\sigma_T}\frac{\partial \Theta^+}{\partial x_i^+}\frac{\partial \Theta^+}{\partial x_i^+} + -\frac{1}{\mathrm{Pr}}\frac{d\lambda^+}{d\Theta^+}\frac{\partial}{\partial x_i^+}\left(\frac{\theta^+\theta^+}{2}\right)\frac{\partial \Theta^+}{\partial x_i^+} + \frac{\partial}{\partial x_i^+}\left(\left(\frac{1}{\mathrm{Pr}}\lambda^+ + \frac{\nu_T^+}{\sigma_T}\right)\frac{\partial}{\partial x_i^+}\left(\frac{\theta^+\theta^+}{2}\right)\right) + \frac{\partial}{\partial x_i^+}\left(2\frac{1}{\mathrm{Pr}}\frac{d\lambda^+}{d\Theta^+}\frac{\theta^+\theta^+}{2}\frac{\partial \Theta^+}{\partial x_i^+}\right) - 2C_{2,\langle T^+T^+\rangle}\frac{1}{\mathrm{Pr}}\lambda^+\frac{\theta^+\theta^+}{2}\frac{\varepsilon^+}{k^+} \tag{7}$$

where is present also the new heat flux term.

The constant $C_{2,\langle T^+T^+\rangle}$ of Eq. (7) can be determined by the turbulence near the wall, where velocity and turbulent kinetic energy must vanish

$$\frac{\partial}{\partial x_i^+}\left(\frac{1}{\mathrm{Pr}}\lambda^+\frac{\partial}{\partial x_i^+}\left(\frac{\theta^+\theta^+}{2}\right)\right) - 2C_{2,\langle T^+T^+\rangle}\frac{1}{\mathrm{Pr}}\lambda^+\frac{\theta^+\theta^+}{2}\frac{\varepsilon^+}{k^+} \approx 0 \tag{8}$$

Dissipation rate of temperature variance balances with molecular diffusion at the wall where also the temperature fluctuation must vanish

$$\frac{\partial}{\partial x_i}\left(\frac{\theta^+\theta^+}{2}\right)\Bigg|_{wall} = 0 \tag{9}$$

The following assumptions, on the variation of the variables $k^+, \varepsilon^+, \theta^+\theta^+$, near the wall:

$$k^+ = A^+ y^{+2} + B^+ y^{+3} + O\left(y^{+4}\right) \tag{10}$$

$$\varepsilon^+ = 2A^+ + 4B^+ y^+ + O\left(y^{+2}\right) \tag{11}$$

$$\theta^+\theta^+ = A_\theta^+ y^{+2} + B_\theta^+ y^{+4} + O\left(y^{+5}\right) \tag{12}$$

allows finding the unknown constant

$$C_{2,\langle T^+T^+\rangle} \approx \frac{k^+}{\varepsilon^+}\frac{1}{\theta^+\theta^+}\left(\frac{\partial\sqrt{\theta^+\theta^+}}{\partial x_i^+}\right)^2 \tag{13}$$

Using the relation

$$\frac{k^+}{\varepsilon^+}\frac{1}{\theta^+\theta^+}\left(\frac{\partial\sqrt{\theta^+\theta^+}}{\partial y^+}\right)^2 \approx \frac{y^{+2}}{2}\frac{1}{y^{+2}} = \frac{1}{2}; \tag{14}$$

it is finally obtained

$$C_{2,\langle T^+T^+\rangle} = 0.5 \tag{15}$$

The thermal conductivity is supposed to be dependent on temperature according to the following expression, [1],

$$\lambda^+\left(\Theta^+\right) = A_\Theta^+ + B_\Theta^+\Theta^+ \tag{16}$$

The case investigated in the present paper is relative to fully developed turbulent flow between parallel plates, with constant heat flux from both walls, and thermal conductivity variable according to Eq. (16). On the inlet of the parallel plates the fluid has uniform mean temperature and temperature variance. One goal of the present numerical simulations is to investigate the influence of Prandtl number on the amplitude of the new heat flux term, q_λ^+, Eq. (6).

Boundary conditions at the wall ($y^+=0$) for U_i^+, k^+ and ε^+ are:

$$\begin{cases} U_i^+ = 0, \forall i \\ k^+ = 0 \\ \varepsilon^+\big|_w = 2\left(\partial\sqrt{k^+}/\partial x_i^+\right)^2\Big|_w \end{cases} \quad (17)$$

Thermal boundary conditions at the wall are:

$$\begin{cases} \left.\dfrac{\partial\Theta^+}{\partial x_i^+}\right|_w = \dfrac{\Pr}{\lambda^+(0)} \\ \theta^+\theta^+\big|_w = 0 \end{cases} \quad (18)$$

Numerical Model

The turbulence model is the *k-ε* proposed by Nagano and Tagawa [20]. The equations are solved using the finite volume method (FVM) with a HYBRID differential scheme for velocities, temperature and turbulent variables. A uniform staggered Cartesian grid system is used. The iterative SIMPLER algorithm is employed to relax the coupled equations. The non-linear algebraic equations over the flow domain are solved iteratively with the Thomas algorithm (TDMA) method [21-22]. Numerical simulations are carried on until fully developed temperature profiles are obtained.

Results

Numerical simulations are carried on for fully developed turbulent flow between parallel plates, at Reynolds number equal to 8,000 and three Prandtl numbers, which corresponds to liquid metal (Pr=0.44), water (Pr=4.4) and oil (Pr=44). Results of mean velocity profile in the turbulent boundary layer are presented in Fig. 1, together with the universal velocity profile. Comparison is good in the viscous sub-layer, although the logarithmic law is not fitted exactly elsewhere, in agreement to [20, 23-25], because Reynolds number is comparatively low.

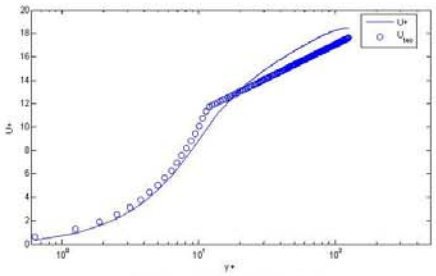

Figure 1: Mean velocity profile.

Figure 2 presents results of non-dimensional shear stresses as laminar, turbulent and total one, i.e. sum of the two. Total stress is a linear function of wall distance.

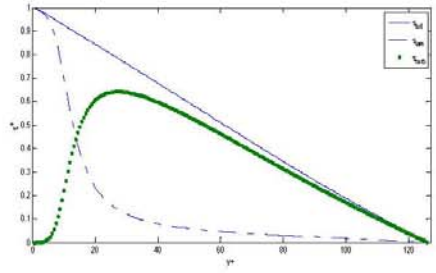

Figure 2: Non dimensional shear stresses.

Figure 3 presents the results for non-dimensional turbulent viscosity, with its typical shape.

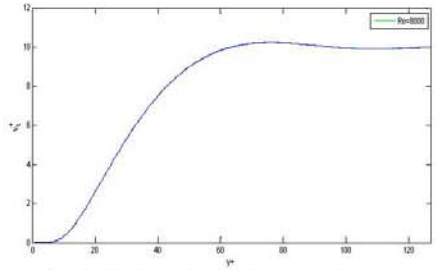

Figure 3: Non-dimensional turbulent viscosity.

Figure 4 presents the results for non-dimensional turbulent dissipation rate and Figure 5 those for non-dimensional turbulent kinetic energy, both comparable with those of [20] and [26-27].

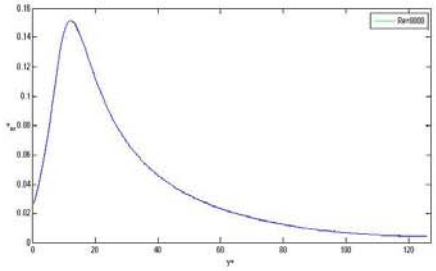

Figure 4: Non-dimensional turbulent dissipation rate.

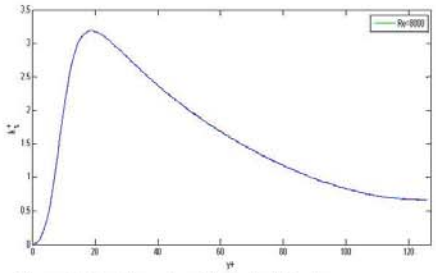

Figure 5: Non-dimensional turbulent kinetic energy.

The numerical results for the new heat flux term, is presented in Figure 6, which shows that the contribution of

the new term is important close to the wall and its importance is increasing with the increase of Prandtl number.

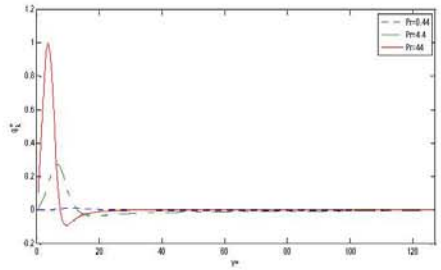

Figure 6: New heat flux term due to variation of thermal conductivity.

Figure 7 presents numerical results for heat flux contributions, i.e. total, turbulent, laminar and $\dot{q}_\lambda^+$, for a fluid with Prandtl number equal to 44. The contribution of $\dot{q}_\lambda^+$ is important mainly at the wall where is not negligible.

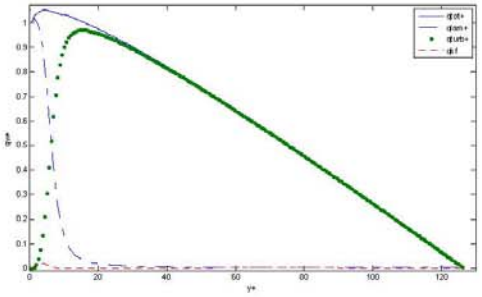

Figure 7: Heat fluxes for Pr=44.

The temperature variance profile for Pr=44 is reported in Figure 8, using the friction temperature to normalize the root-mean-square temperature variance. Temperature variance undergoes a sharp rise nearby y^+=10 in the near-wall region.

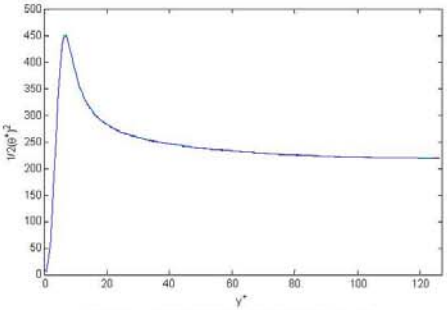

Figure 8: Temperature Variance for Pr=44.

The budget of temperature variance for Pr=44 is reported in Figure 9. The results show the influence of the new transport term, which has a similar pattern to molecular and turbulent ones, also if the amplitude is slightly smaller but with the same order of magnitude.

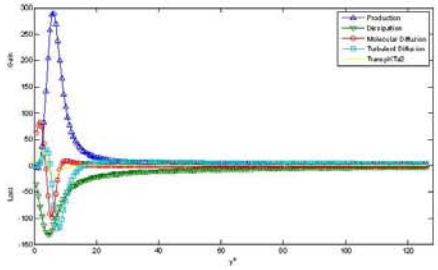

Figure 9: Budget of Temperature Variance for Pr=44.

Mean-temperature in the turbulent boundary layer for Pr=44 is reported in Figure 10. The profile is in fair agreement with the theoretical distribution, $\Theta^+ = \mathrm{Pr}\, y^+$, in the viscous sub-layer, because thermal conductivity is not constant. Moreover, it is in agreement with the law of the wall in the logarithmic region.

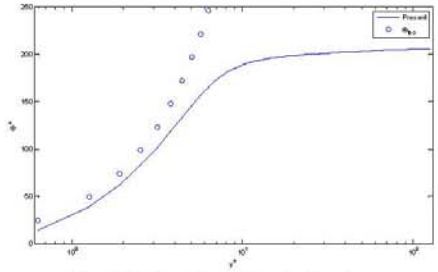

Figure 10: Mean Temperature for Pr=44.

The results presented in this work are limited to fluids with Prandtl number lower or equal than 44 because the computational time increases at large extent with the increase of Prandtl number. It can be pointed out that Prandtl number of some oil can span between $10^3 \div 4 \cdot 10^4$, when is expected a greater influence of the new term, $\dot{q}_\lambda^+$ on heat transfer.

Discussion

The contribution of the new heat flux term on heat transfer is dependent on the relation linking thermal conductivity and temperature. Greater is the variation of thermal conductivity with temperature and greater is the contribution of the new term, which can allow a decrease or an increase of heat transfer according to the relation between thermal conductivity and temperature.

The present work investigates numerically fluids with Prandtl number much smaller than, for example, a lubricant or heavy oil. A greater Prandtl number fluid implies a much thinner boundary layer and a bigger temperature gradient near the wall. The term for the production of temperature variance is proportional to the mean temperature gradient, which means that with a greater mean temperature the temperature variance is greater, as well as the new heat flux term, as shown theoretically in [3].

The new heat flux term, appearing in the transport equation for temperature variance, Eq. (7), has different influence from the energy point of view and is difficult to say whether it is a production or a dissipation term. Indeed, a

productive term is always positive while a dissipative one is always negative. Since the behaviour of the new heat flux term is dependent whether the thermal conductivity decreases or increases with temperature and is proportional to the mean temperature gradient, the new term increases if the thermal conductivity increases with temperature or decreases if the thermal conductivity decreases with temperature. In conclusion, the new term is treated as increase or decrease of production.

The boundary condition assumed in this work and the Reynolds number have a relative importance for the new heat flux term while future numerical modelling are necessary to clarify the role of the new term on diffusion processes.

Conclusion

The present numerical results, carried on for a two dimensional fully developed turbulent flow between two parallel plates, at Re=8,000 and Prandtl number equal to Pr=0.44, 4.4, 44, show the relative importance of the new heat flux term, due to the variation of thermal conductivity. Numerical simulations are limited to a relatively small Reynolds number and to a maximum value of Prandtl number equal to 44, because of the present limited computational resources. Future investigations are planned for higher Prandtl number fluids and Reynolds numbers flow.

NOMENCLATURE

Symbol	Definition	SI Unit
Latin		
c_p	Specific heat at constant pressure	J kg^{-1}K^{-1}
k	Turbulent kinetic energy	m^2·s^{-2}
P	Mean pressure	Pa
q_w	Wall heat flux	W·m^{-2}
$\langle S_{ij} \rangle$	ij-component of mean rate of shear tensor	s^{-1}
t	Time	s
$T_\tau = q_w / (\rho c_p u_\tau)$	Friction temperature	K
T_w	Wall temperature	K
$\langle T \rangle$	Mean temperature	K
T'	Fluctuating temperature	K
$\sqrt{\langle T'T' \rangle}$	Root mean square temperature	K
$u_\tau = \sqrt{\tau_w / \rho}$	Friction velocity	m·s^{-1}
U_i	i-mean velocity component	m·s^{-1}
x_i	i-coordinate	m
Greek		
ε	Turbulent dissipation rate	m^2·s^{-3}
λ	Thermal Conductivity	W·m^{-1}·K^{-1}
ν	Molecular kinematic viscosity	m^2·s^{-1}
$\nu_T = C_\mu f_\mu k^2 / \varepsilon$	Turbulent kinematic viscosity	m^2·s^{-1}
ρ	Density	kg·m^{-3}
Dimensionless		
$\begin{cases} C_{1,\varepsilon}=1.45 \\ C_{2,\varepsilon}=1.90; \\ C_\mu=0.09 \end{cases} \begin{cases} \sigma_\varepsilon=1.3 \\ \sigma_k=1.4; \\ \sigma_T=1.0 \end{cases}$	Constants of the turbulent model	
$\begin{cases} f_{1,\varepsilon}=1.0 \\ f_{2,\varepsilon}=\left(1-0.3e^{-(\mathrm{Re}_\tau/6.5)^2}\right)\left(1-e^{-y^+/6}\right)^2 \\ f_\mu=\left(1-e^{-y^+/26}\right)\left(1+4.1/\mathrm{Re}_\tau^{3/4}\right) \end{cases}$	Functions of the turbulent model	
$k^+ = k / u_\tau^2$	Turbulent kinetic energy	
$P^+ = P / (\rho u_\tau^2)$	Mean pressure	
Pr	Molecular Prandtl number	
$\dot{q}_\lambda^+$	Heat flux due to variation of thermal conductivity	
$\mathrm{Re}_\tau = k^2 / (\nu\varepsilon)$	Turbulent Reynolds Number	
$S_{ij}^+ = (\nu / u_\tau^2)\langle S_{ij} \rangle$	ij-component of mean rate of shear tensor	
$t^+ = t / (\nu / u_\tau^2)$	Time	
$U_i^+ = U_i / u_\tau$	i-mean velocity component	
$x_i^+ = x_i / (\nu / u_\tau)$	i-coordinate	
$\varepsilon^+ = \varepsilon / (u_\tau^4 / \nu)$	Turbulent dissipation rate	
$\Theta^+ = (\langle T \rangle - T_w) / T_\tau$	Mean temperature	
$\theta^+ = \sqrt{\langle T'T' \rangle} / T_\tau$	Root mean square temperature	
$\lambda^+ = \mathrm{Pr}\,\lambda / (\rho c_p \nu)$	Thermal conductivity	
y^+	Wall coordinate	

REFERENCES

[1] F. Gori and A. Boghi. On a New Turbulent Energy Equation with Variable Thermal Conductivity. *IMECE2008*, Boston, Massachusetts, USA, 2008.

[2] R.C. Martinelli. Heat transfer to molten metals. *Trans. ASME*. 1947 (69): 47–59.

[3] H. Tennekes and J. L. Lumley. *A First Course in Turbulence*. MIT Press, Cambridge, USA. 1972.

[4] A. J. Reynolds. The prediction of turbulent Prandtl and Schmidt numbers. *Int. J. Heat Mass Transfer*. 1975 (18): 1055–1069.

[5] M. Satake, K. Yuki, S. Chiba, H. Hashizume. Numerical analysis of MHD flow structure behind a square rod. *Fusion Engineering and Design*. 2006 (81):525–532.

[6] S. Y. Chiba, K. Yuki, H. Hashizume, S. Toda and A. Sagara. Numerical research on heat transfer enhancement for high Prandtl-number fluid. *Fusion Engineering and Design*. 2006 (81): 513–517.

[7] G. J. Kolbov. Economic Evaluation of Solar-Only and Hybrid Power Towers Using Molten-Salt Technology. *Solar Energy*. 1998 (62): 51-61.

[8] H. Hasuike, Y. Yoshizawa, A. Suzuki, Y. Tamaura. Study on design of molten salt solar receivers for beam-

down solar concentrator. *Solar Energy*. 2006 (80): 1255–1262.

[9] F. Donatini, C. Zamparelli, A. Maccari and M. Vignolini. High efficency integration of thermodynamic solar plant with natural gas combined cycle. *International Conference on Clean Electrical Power. ICCEP '07*. 2007: 770-776.

[10] T. Kunugi, S. Satake, A. Sagara. Direct numerical simulation of turbulent free-surface high Prandtl number fluid flows in fusion reactors. *Nuclear Instruments and Methods in Physics Research A*. 2001 (464): 165–171.

[11] H. Kawamura, K. Osaka, H. Abe, K. Yamamoto. DNS of turbulent heat transfer in channel flow with low to medium-high Prandtl number fluid. *International Journal of Heat and Fluid Flow*. 1998 (19): 482-491.

[12] B. Yu, Y. Kawaguchi. DNS of fully developed turbulent heat transfer of a viscoelastic drag-reducing flow. *International Journal of Heat and Mass Transfer*. 2005 (48): 4569–4578.

[13] B. S. Petukhov. Heat Transfer and Friction in Turbulent Pipe Flow with Variable Physical Properties. *Advances in Heat Transfer*. 1970 (6): 503-565.

[14] S. Faggiani and F. Gori. Influence of Streamwise Molecular Heat Conduction on the Heat Transfer Coefficient for Liquid Metals in Turbulent Flow between Parallel Plates. *Journal of Heat Transfer, ASME*. 1980 (102-2): 292-296.

[15] S. Faggiani, F. Gori. Remarks on the Heat Transfer to Gases in Turbulent Flow between Parallel Plates. *The 7th International Heat Transfer Conference, Munchen, Germany*. 1982 (3): 33-38.

[16] E. P. Valueva. Hydrodynamics and Heat Transfer in Pulsating Turbulent Pipe Flow of a Liquid of Variable Properties. *High Temperature*. 2005 (43-6):890–899.

[17] E. P. Valueva. Hydrodynamics and Heat Transfer in Pulsating Turbulent Flow of Gas in a Heated Pipe. *High Temperature*. 2006 (44-1):120–128.

[18] E. P. Valueva. Integral Methods of Calculation of Heat Transfer and Drag under Conditions of Turbulent Pipe Flow of Liquid of Variable Properties: Steady-State and Quasi-Steady-State Flows in a Round Pipe with Constant Density of Heat Flux to the Wall. *High Temperature*. 2007 (45-1): 49–57.

[19] E. P. Valueva. Integral Methods of Calculation of Heat Transfer and Drag under Conditions of Turbulent Pipe Flow of Liquid of Variable Properties: Pulsating High-Frequency Flow. *High Temperature*. 2007 (45-4):502–508.

[20] Y. Nagano, M. Tagawa. An improved k-ε; model for boundary layer flows. *Trans. ASME. Journal of Fluids Engineering*. 1990 (112-1): 33-39.

[21] S. V. Patankar. *Numerical Heat Transfer and Fluid Flow*. Hemisphere Publishing Corporation, 1980.

[22] H. K. Versteeg, W. Malalasekera. *Introduction to computational fluid dynamics. The finite volume method.* Longman, 1995.

[23] W. P. Jones, B. E. Launder. The calculation of low-Reynolds-number phenomena with a two-equation model of turbulence. *International Journal of Heat and Mass Transfer*. 1973 (16-6): 1119-1130.

[24] V. C. Patel, W. Rodi, G. Scheuerer. Turbulence Models for Near-Wall and Low Reynolds Number Flows: A Review. *AIAA Journal*. 1985 (23-9): 1308-1319.

[25] Y. Nagano, M. Hishida. Improved Form of the k-ε Model for Wall Turbulent Shear Flows. *Journal of Fluids Engineering, Trans.ASME*. 1987 (109-2): 156-160.

[26] K. M. Hyon, N. Kasagi. A new approach to the improvement of *k-ε* turbulence model for wall-bounded shear flows. *JSME International Journal, Series II (Fluids Engineering, Heat Transfer, Power, Combustion, Thermophysical Properties)*. 1990 (33-1): 63-72.

[27] C. K. G. Lam, K. A. Bremhorst. A Modified Form of the *k-ε* Model for Predicting Wall Turbulence. *Trans. ASME. Journal of Fluids Engineering*. 1981 (103-3): 456-460.

Proceedings of the
INTERNATIONAL HEAT TRANSFER CONFERENCE
August 8-13, 2010, Washington D.C., USA

IHTC14-23087

THREE-DIMENSIONAL NUMERICAL SIMULATION OF NON-NEWTONIAN BLOOD IN TWO CORONARY STENTS

F. Gori
Department of Mechanical Engineering,
University of Rome "Tor Vergata",
Rome, Italy.

A. Boghi
Department of Mechanical Engineering,
University of Rome "Tor Vergata",
Rome, Italy.

ABSTRACT

The objective of the present study is to carry out CFD simulations in a realistic 3D geometry of two coronary stents in physiological conditions and to assess the influence of the non-Newtonian behavior of blood, modeled as Casson fluid. The stents used are made of 12 rings and are similar to real coronary ones. Artery is modeled as a cylinder with rigid walls and the blood is assumed as incompressible non-Newtonian fluid in laminar flow. A commercial computational fluid dynamic code is used with a mesh composed of non uniform tetrahedrons. The simulations are performed in steady and unsteady state. Wall Shear Stress, as well as its time variations and the non-Newtonian behavior, are investigated in unsteady state. Results suggest that the Newtonian behavior is leading to an overestimation of the restenosis percent.

INTRODUCTION

Stents are commonly used to restore blood flow in patients with severe coronary artery disease. Local hemodynamic variables, as wall shear stress (WSS), have an important role in the restenosis and their distribution depends on the stent geometry. With the new drug eluting stent the percentage of restenosis has been significantly reduced, [1-4], but the long term percentage of restenosis is similar to the classic stent [5-6]. The distribution of local hemodynamic variables depends on the stent geometry [7-9].

Previous two-dimensional computational fluid dynamics simulations have used simple stent geometry. Berry et al. [10] investigated the influence of mesh dimensions on the flow with the conclusion that a small mesh can disturb the flow at a larger extent. Lanoye et al. [11] studied the effect of the strut section with the conclusion that a round strut section can disturb the flow at a smaller extent.

Some three-dimensional computational fluid dynamics simulations have been carried out on stented arteries. LaDisa et al. [12-17] characterized the best stent design investigating the influence of number, width, thickness and angle of the struts on the flow direction. He at al. [18] studied a realistic strut geometry considering three geometric parameters of the struts and showing that the stent design is very important for the fluid flow in arteries. The present authors have investigated numerically two coronary stents with a three-dimensional approach and considering the blood as a Newtonian fluid [19].

Despite blood is a non-Newtonian fluid, most of the works have treated blood as Newtonian and only few studies have investigated the effect of the non-Newtonian behavior on stent blood flow. Seo et al. [20] investigated the influence of the stent design close to curvatures assuming a Carreau non-Newtonian model. The study provides an understanding of the flow in the stent vicinity suggesting strategies for the optimization of the stent in order to minimize the flow disturbance. Benard et al. [21] investigated numerically the blood flow in 3D steady state rigid walls arteries. Non-Newtonian behavior, based on the Carreau-Yasuda relation, in coronary stent flow seems to have important effects in the estimation of the wall shear stress on the internal surface. Amblard et al. [22] analyzed the phenomena of type I endoleaks in a non-invasive-stented abdominal aorta, evaluating the parietal stresses generated by the blood flow. The non-Newtonian behavior is the Phan-Thien and Tanner models derived from the rheology of polymer solutions. This study provides an evaluation of the stresses generated by the blood flow on the aorta wall.

The goal of the present study is to reconstruct a realistic 3D geometry of a coronary stent and to carry out 3D-CFD simulations in physiological conditions. A comparison is performed between two reconstructed stents, made of 12 rings and similar to real coronary ones. The two stents differ from the position of the struts, where the first type, S1, is with closed

cells and the second type, S2, with open cells. The artery is modeled as a cylinder with rigid wall and the blood is assumed as incompressible non-Newtonian fluid in laminar flow.

GEOMETRY

A real 3D geometry of a coronary stent, made of sequential rings and connected with longitudinal flexible connectors, is considered. Two different connections are investigated: regular peak to peak and mid-strut to mid-strut. The first type of stent, S1, is with closed cells and the second one, S2, with open cells [23], similarly to real coronary stents.

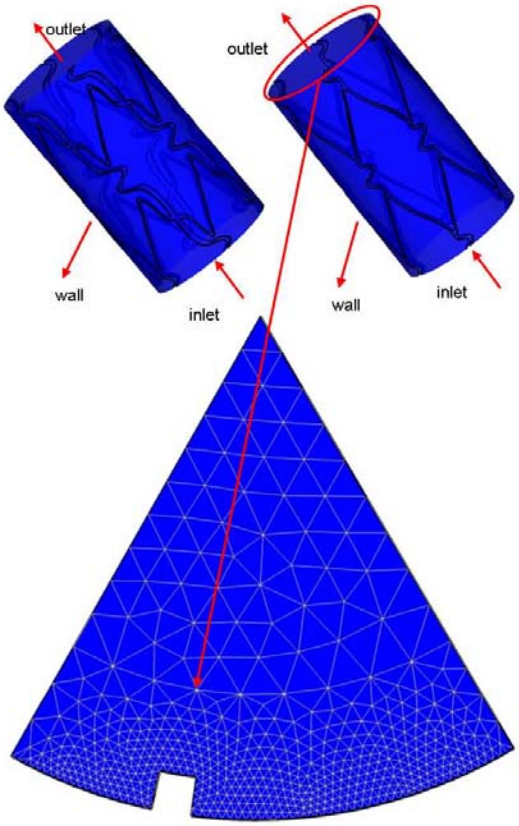

Figure 1 – Reconstruction: complete stents, S2 on the left and S1 on the right.

The software GAMBIT is used for reconstruction and mesh generation. The two complete reconstructed stents are shown in Figure 1, S2 on the left and S1 on the right. Only a portion of each stent, i.e. 60° of the cylinder, is investigated, due to symmetry. The reconstructed stents are made of 12 rings, the diameter of the artery is 2.6 mm, the width of the stent is 0.1 mm and the total length of the stent is 27.6 mm, in agreement to a stented coronary artery [12] and a real coronary stent [24]. The mesh used, made of non-uniform tetrahedrons, Figure 1, shows a detail of the mesh.

The arterial wall is rigid as the stent. This assumption does not affect significantly the results because studies on animals [13] assure that stent implantation reduces the vessel compliance to zero within the stented region [25] and wall deformability does not greatly alter the velocity field under normal conditions. The reconstruction is relative to the stent geometry and the cylindrical arterial wall, which is the union of stent and artery endothelium. On the joint wall surface is then possible to assign the no-slip boundary condition.

GOVERNING EQUATIONS

The blood is modeled as incompressible non-Newtonian fluid with ρ = 1060 Kg/m^3, in laminar flow with a Reynolds number in the range from Re = 122 to 440. Under these hypotheses the conservation equations of mass and momentum are respectively:

$$\nabla \cdot \vec{v} = 0 \tag{1}$$

$$\rho \frac{D\vec{v}}{Dt} = -\nabla p + \nabla \cdot \left(2\mu(\dot{\gamma})[D]\right) \tag{2}$$

where $\vec{v}$ is the fluid velocity, ρ the density, p the pressure.

The rate of strain tensor is

$$[D] = \frac{\left([\nabla \vec{v}] + {}^{t}[\nabla \vec{v}]\right)}{2} \tag{3}$$

and the shear rate is

$$\dot{\gamma} = \sqrt{2[D]:[D]} \tag{4}$$

In a non-Newtonian fluid, viscosity is a function of shear rate. Equation (2) is written in the Generalized Newtonian Fluid form, GNF, derived from Reiner and Rivlin. Viscosity of blood depends on the plasma viscosity with a complex relation with hematocrit. In this work the non-Newtonian viscosity is modeled with the Casson relation

$$\mu(\dot{\gamma}) = \left(\mu_\infty + 2\frac{\sqrt{\tau_0 \mu_\infty}}{\sqrt{\dot{\gamma}}} + \frac{\tau_0}{\dot{\gamma}}\right) \tag{5}$$

where τ_0 is the yield stress and μ_∞ the asymptotic Newtonian viscosity, both function of blood hematocrit. The difficulty in using the Casson model in a numerical scheme lies in its discontinuous character to the limit of zero shear rates. In order

to avoid this discontinuity it is used the regularization technique of [29], obtaining

$$\mu(\dot{\gamma}) = \left(\mu_\infty + 2\frac{\sqrt{\tau_0 \mu_\infty}}{\sqrt{\dot{\gamma}}}\left(1 - e^{-\sqrt{m\dot{\gamma}}}\right) + \frac{\tau_0}{\dot{\gamma}}\left(1 - e^{-\sqrt{m\dot{\gamma}}}\right)^2 \right) \quad (6)$$

At zero shear rate it is assumed that

$$\mu(0) = \left(\mu_\infty + 2\sqrt{m\tau_0\mu_\infty} + m\tau_0\right) \quad (7)$$

where m is the Casson viscosity regularization exponent. According to [29] and [30] the following parameters are assumed $\tau_0 = 0.0488Pa$, $\mu_\infty = 0.0333Pa \cdot s$ and $m = 100s$. The Casson viscosity model is introduced in the commercial software as a User Defined Function, UDF.

Figure 2 presents the variation of viscosity with the shear rate.

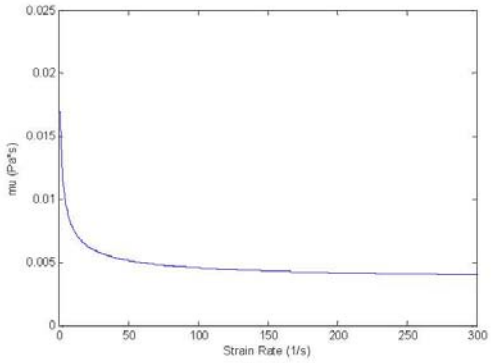

Figure 2 - Viscosity versus shear rate.

Equations (1-2) are solved under the boundary conditions of no slip on artery and stent walls, with a prescribed mass flow rate (constant or physiologic waveform) on the inlet, and a constant pressure on the outlet. The two lateral surfaces of the cylinder portion need rotational periodic as boundary conditions. The commercial computational fluid dynamic code FLUENT is used to carry on simulations in steady and unsteady states.

In unsteady state, the physiological wave form employed is shown in Fig. 4, according to the measurements of LaDisa et al. [12] in the proximal portion of a left anterior canine descending coronary artery. The artery diameter of the measurement is the same as the diameter of the reconstructed artery. The wave form of Fig. 4, sum of sinusoidal functions, is used as UDF input for the code FLUENT. In steady state the mean value of this wave form, i.e. 104.8481 Kg/(m^{2}s), is employed.

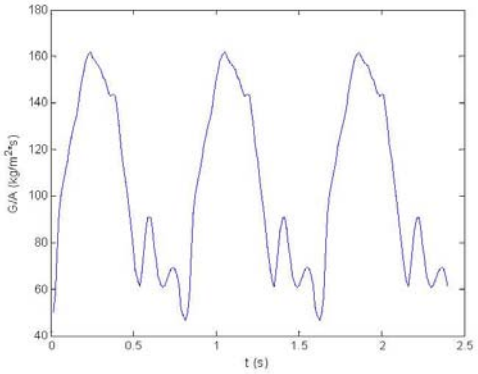

Figure 3 - Physiological inlet wave form.

RESULTS

Numerical simulations are carried on using a Core 2 Duo 2.2 GHz Intel Mobile Centrino with 2 GByte of RAM running LINUX. The residuals values after 2100 iterations, for mass and the three velocity components, are lower than 10^{-6} for all cases. In unsteady state the total investigated time (0.8 s) is split into 800 time steps and 20 iterations are done for each period. In order to obtain residual values lower than 10^{-4} only the second period is considered.

MESH INDEPENDENCE

Figure 4 presents the results of the WSS for three simulations with different mesh dimensions in order to show the spatial mesh independence. The average WSS versus axial position are shown for three meshes with 770,000, 1,900,000 and 3,130,000 elements for the stent with open cells. The WSS are enough close in the three simulations allowing to conclude that a mesh with 770,000 tetrahedrons is a good compromise.

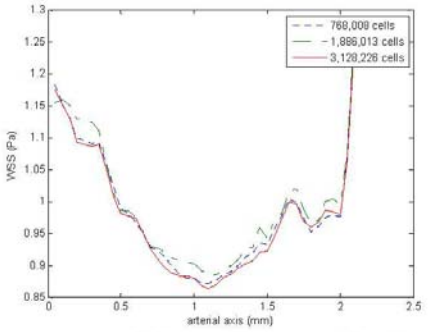

Figure 4 - WSS distributions with different mesh dimensions.

STEADY STATE RESULTS

Results of WSS are presented in Fig. 6 for each stent. Stagnation zones are present around and between stent struts with lower WSS in both stents, while, far from the struts, regions with higher WSS are present. The vessel diameter is reduced on the stent surface producing convergence of the streamlines and higher WSS, while, after the stent strut, higher diameters are present and the diverging streamlines reduce WSS. The diverging effect is smaller and disappears in one strut diameter, with higher WSS at the center of each repeating stent unit.

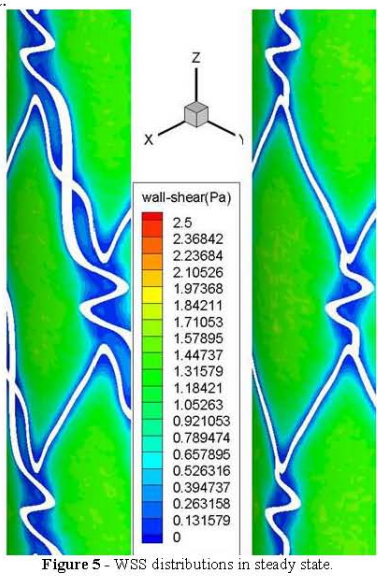

Figure 5 - WSS distributions in steady state.

The highest WSS is present on the stent surface and the lowest one around the stent struts, i.e. in the transition region between vessel and stent. The conclusion is a somewhat large difference between WSS in a small region.

UNSTEADY STATE RESULTS

The unsteady state numerical simulations are performed during two periods of the cardiac cycle and Fig. 7 shows six WSS patterns at the following times: 0.84, 0.88, 1.04, 1.28, 1.44, 1.6 s. Velocity increases with pressure and is zero on stent and wall, due to no slip condition. Inside the duct, velocity increases with the systolic wave causing an increase of velocity gradient and WSS. The average WSS on the wall is described by a wave with the same pattern of the systolic one.

The stent on the wall of the artery is an obstacle from the fluid-dynamics point of view, which is small as compared to the diameter of the vessel but enough large to create a stagnation zone around it. These stagnation zones are present in all cardiac cycles, while their extension decreases with the increase of velocity. The areas around the stent struts present low WSS values for all cardiac cycles because of the stagnation zones while WSS has large variations, during the cycle, close to the vessel wall where WSS span from 0 to 2.5 Pa.

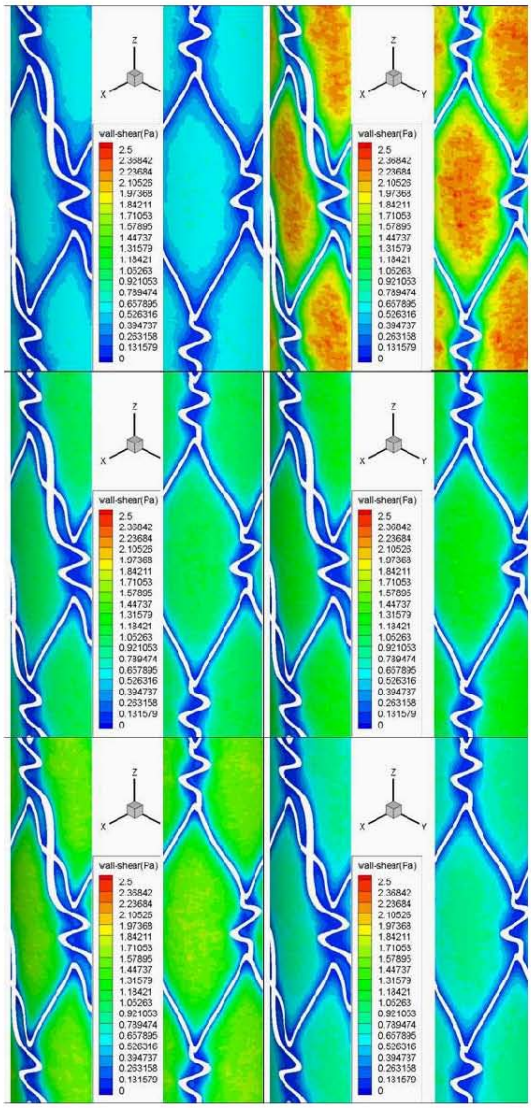

Figure 6 - WSS distributions in unsteady state.

Non-Newtonian flow has a different behavior near wall as compared to the Newtonian one [26]. Maximum WSS values are present in the center of the stent pattern structure and minimum values on the proximal stent wire surface. It is possible to estimate the intra strut areas exposed to low WSS (i.e. lower than 0.5 Pa) during the cardiac cycle.

The percent area, P, is defined as the area of the vessel wall exposed to values of WSS which are lower than the critical value, according to

$$P(\%) = 100 \frac{\int_{vessel\_wall} \frac{1}{2}\left(1 - \left(\frac{WSS - 0.5}{\|WSS - 0.5\|}\right)\right) dA}{\int_{vessel\_wall} dA} \qquad (8)$$

The percent area is evaluated for both stents and at all the time steps of the cardiac cycle. The results are presented in Fig. 8 showing that the stent with closed cells has a smaller percent area with low WSS.

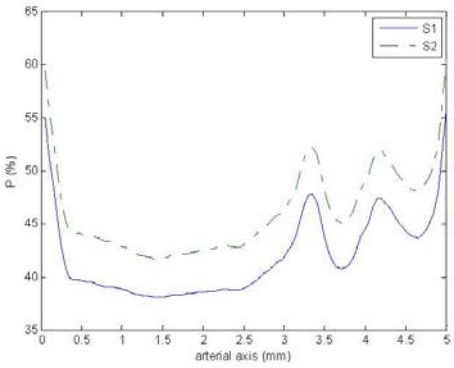

Figure 7 - Percent Area, P(%), with WSS lower than 0.5 Pa, versus time (s).

Figure 7 shows that the stent with open-cell has lower percent critical intra strut area, P. The P value on the stented region, exposed to WSS smaller than 0.5 Pa, reduces as the flow rate increases, reaching the minimum value at the point of the cardiac cycle corresponding to peak flow velocity. Since WSS increases with velocity, the endothelium surface is exposed averagely to higher WSS during the systole, decreasing the risk of developing neo-intimal hyperplasia. Comparing present results with those obtained in [26] we can conclude that the Newtonian model has the effect of overestimate the critical area. Results showed in Figure 7 indicate a significant percent area with a WSS lower than the critical value, for the two stents simulated, in agreement with those of [27].

DISCUSSION

Physiological values of WSS span between 0.5 Pa and 0.8–1 Pa [7-9]. Lower values of WSS are strongly correlated to endothelial permeability and can promote neo intimal hyperplasia, while higher values have no relation with neo intimal hyperplasia.

The steady state results of WSS, presented in Fig. 6, show that in the regions of the vessel wall is present a uniform WSS which is lower than 0.3 Pa. No substantial difference is reported between the two stents but these areas have a larger extension in the stent with transverse struts. The differences in the critical values of both stents are around 5% but most part of the vessel wall is subject to WSS lower than the critical value.

The unsteady state results of Fig. 7 show a large variation of WSS during the cardiac cycle. The regions far from the stent have the larger variations while the regions close to the stent present the smaller variations, allowing them to be exposed permanently to critical low WSS values.

The comparison of the present results with those obtained for a Newtonian fluid in [26], allows to conclude that the Newtonian behavior underestimates WSS, with the clinical consequence of overestimating the restenosis risk area, in agreement to the results of [21].

CONCLUSIONS

Two real stents with different design, used as drug eluting stent in the clinic practice, are investigated in steady and unsteady state with a 3D-CFD simulation in order to study their fluid dynamics behavior. Numerical simulations show the presence of regions, close to the stent, where WSS is lower than the critical value. Unsteady simulations show large differences between instantaneous and mean WSS values.

The comparisons of WSS and percent area of the two stents allow to state that the stent with the struts parallel to the mean flow has a better fluid dynamic behavior compared to the stent with transverse struts. Moreover, the comparison of the present results for non-Newtonian behavior, with those for a Newtonian one, [26], allows concluding that the use of Newtonian model, in predicting WSS, leads to an overestimation of the restenosis percent.

ACKNOWLEDGEMENTS

The authors thank Prof. F. Romeo for the helpful discussions about cardiological problems of stent and Dr. Clementi for the stents given.

REFERENCES

[1] M. C. Morice, P. W. Serruys , J. E. Sousa, J. Fajadet, E. Ban Hayashi, "A randomized comparison of a sirolimus-eluting stent with a standard stent for coronary revascularization", New Eng. J. Med. 346(23): 1773-1780, 2002.

[2] J. W. Moses, M. B. Leon, J. J. Popma, P. J. Fitzgerald, D. R. Holmes, "Sirolimus-eluting stents versus standard stents in patients with stenosis in a native coronary artery", New Engl. J. Med. 349(14): 1315-1323, 2003.
[3] E. Schampaert, E. A. Cohen, M. Schluter, "The Canadian study of the sirolimus-eluting stent in the treatment of patients with long de novo lesions in small native coronary arteries (C-SIRIUS)", J. Am. Coll. Cardiol. 43: 1110-1115, 2004.
[4] M. Schofer, A. H. Gershlick, "Sirolimus-eluting stents for treatment of patients with long atherosclerotic lesions in small coronary arteries: double-bind, randomized controlled trial", Lancet 362: 1093-1099, 2003.
[5] J. C. Palmaz, "Intravascular stents in the last and the next 10 years", J. Endovasc. Ther. Suppl. 2, 200-206, 2004.
[6] R. Virmani, A. Farb, G. Guagliumi, F. D. Kolodgie, "Drug-eluting stents: caution and concerns for long-term outcome", Cor. Artery Dis. 15: 313-318, 2004.
[7] D. N. Ku, D. P. Giddens, C. K. Zarins, S. Glagov, "Pulsatile flow and atherosclerosis in the human carotid bifurcation. Positive correlation between plaque location and low oscillating shear stress", Arteriosclerosis 5: 293-302, 1985.
[8] D. N. Ku, "Blood flow in arteries", Ann. Rev. Fluid Mech. 29: 399-434, 1997.
[9] A. M. Malek, S. L. Alper, S. Izumo, "Hemodynamic shear stress and its role in atherosclerosis", JAMA 282: 2035-2042, 1999.
[10] J. L. Berry, A. Santamarina, J. E. Jr. Moore, S. Roychowdhury, W. D. Routh, "Experimental and computational flow evaluation of coronary stents", Ann. Biomed. Eng. 28(4): 386-98, 2000.
[11] L. Lanoye, M. De Beule, C. Dewijngaert, P. Segers, R. Van Impe, P. Verdonck, "The influence of the strut section shape on the flow field in a newly stented right coronary artery", NCTAM2006, 2006.
[12] J. F. LaDisa Jr., D. A. Hettrick, L. E. Olson, I. Guler, E. R. Gross, T. T. Kress et al. "Coronary stent implantation alters coronary artery hemodynamics and wall shear stress during maximal vasodilation", Jour. of App. Phys., 93: 1939-1946, 2002.
[13] J. F. LaDisa Jr., I. Guler, L. E. Olson, D. A. Hettrick, J. R. Kersten, D. C. Warltier et al. "Three dimensional computational fluid dynamics modeling of alterations in coronary artery wall shear stress produced by stent implantation", Ann. Biomed. Eng. 31: 972-980, 2003.
[14] J. F. LaDisa Jr, L. E. Olson, I. Guler, D. A. Hettrick, S. H. Audi, "Stent design properties and deployment ratio influence indexes of wall shear stress: a three dimensional computational fluid dynamics investigation within a normal artery", Jour. of App. Phys. 97(1): 424-30, 2004.
[15] J. F. LaDisa Jr., L. E. Olson, D. A. Hettrick, D. C. Warltier, J. R. Kersten and P. S. Pagel, "Axial stent strut angle influences wall shear stress after stent implantation: analysis using 3D computational fluid dynamics models of stent foreshortening", BioMed. Eng. OnLine. 4: 59, 2005.
[16] J. F. LaDisa Jr., L. E. Olson, I. Guler, D. A. Hettrick, J. R. Kersten, D. C. Warltier et al. "Circumferential vascular deformation after stent implantation alters wall shear stress evaluated with time-dependent 3D computational fluid dynamics models", Jour. of App. Phys.. 98: 947-957, 2005.
[17] J. F. LaDisa Jr., L. E. Olson, D. A. Hettrick, D. C. Warltier, J. Kersten, P. Pagel, "Alterations in regional vascular geometry produced by theoretical stent implantation influence distributions of wall shear stress: analysis of a curved coronary artery using 3D computational fluid dynamics modeling", BioMed. Eng. On Line. 5: 40, 2006.
[18] Y. He, N. Duraiswamy, A. O. Frank, J. E. Moore Jr., "Blood Flow in Stented Arteries: A Parametric Comparison of Strut Design Patterns in Three Dimensions", Jour. of Biomech. Eng.. 127: 637-647, 2005.
[19] F. Gori and A. Boghi, "Three-dimensional numerical simulation of blood flow in two coronary stent", submitted for publication.
[20] T. Seo, L. G. Schachter and A. I. Barakat, "Computational Study of Fluid Mechanical Disturbance Induced by Endovascular Stents", Ann. of Bio. Eng. 33, 4, 444-456, 2005.
[21] N. Benard, R. Perrault and D. Coisne "Computational Approach to Estimating the Effects of Blood Properties on Changes in Intra-stent Flow" Ann. of Bio. Eng. 34, 8, 1259–1271, 2006.
[22] A. Amblard, H. W. Le Berre, B. Bou-Saïd, M. Brunet "Analysis of type I endoleaks in a stented abdominal aortic aneurysm", Medical Engineering & Physics 31, 27–33, 2009.
[23] D. Stoeckel, C. Bonsignore and S. Duda, "A survey of stent designs", Min. Invas. Ther. & Allied Technol. 11: 137-147, 2002.
[24] A. Kastrati, J. Mehilli, J. Dirschinger, J. Pache, K. Ulm and H. Schühlen, "Restenosis after coronary placement of various stent types", Am. J. Cardiol. 87(1): 34-39, 2001.
[25] M. R. Ebeid "Balloon expandable stents for coarctation of the aorta: review of current status and technical considerations", Images Pediatr Cardiol. 15: 25-41, 2003
[26] F. Gori, A. Boghi and M. Amitrano "Three-Dimensional Numerical Simulation of the Fluid Dynamics in a Coronary Stent", IMECE2009, November 13-19, 2009, Lake Buena Vista, Florida, USA.
[27] J. Mejia, B. Ruzzeh, R. Mongrain, R. Leask and O. F. Bertrand "Evaluation of the effect of stent strut profile on shear stress distribution using statistical moments", BioMed. Eng. OnLine. 8: 8, 2009.